Stress Corrosion Cracking of Sodium Borosilicate Amorphous Phase Separated Glasses

Weiying Feng

THÈSE DE DOCTORAT

NNT : 2022UPASP030

université PARIS-SACLAY

Stress Corrosion Cracking of Sodium Borosilicate Amorphous Phase Separated Glasses

Expériences de Corrosion sous Contrainte de Verres Borosilicates de Sodium à Séparation de Phases

Thèse de doctorat de l'université Paris-Saclay

École doctorale n° 564, Physique en Île-de-France (PIF)
Spécialité de doctorat : Physique
Graduate School: Physique. Référent : Faculté des sciences d'Orsay

Thèse préparée dans l'unité de recherche **SPEC** (Université Paris-Saclay, CEA, CNRS), sous la direction de **Cindy L. ROUNTREE**, Directrice de recherche, et le co-encadrement de **Fabrice CÉLARIÉ**, Maître de conférences

Thèse soutenue à Paris-Saclay, le 15 mars 2022, par

Weiying FENG

Composition du Jury

Matteo CICCOTTI Professeur, ESPCI	Président
Simona ISPAS Maître de conférences (HDR), Université de Montpellier	Rapporteur & Examinatrice
Lothar WONDRACZEK Professeur, Université de Jena	Rapporteur & Examinateur
Emmanuelle GOUILLART Directrice scientifique industrielle, Saint Gobin	Examinatrice
Christiane ALBA-SIMIONESCO Directrice de recherche, CEA-Saclay	Examinatrice
Cindy L. ROUNTREE Directrice de recherche, CEA-Saclay	Directrice de thèse

université PARIS-SACLAY | ÉCOLE DOCTORALE Physique en Île-de-France (PIF)

Titre : Expériences de Corrosion sous Contrainte de Verres Borosilicates de Sodium à Séparation de Phases

Mots clés : Corrosion sous contrainte, séparation de phases, verres borosilicates de sodium

Résumé : Les verres borosilicates de sodium (SBN) sont l'objet de nombreuses recherches car les trois oxydes qui les composent (SiO_2, B_2O_3 et Na_2O) font partie des principaux oxydes présents dans les verres industriels. Or il existe, dans le diagramme de phase ternaire des verres SBN, une zone où le phénomène de démixtion (ou séparation de phase amorphe) joue un rôle important. Mes recherches se sont concentrées sur les effets de cette démixtion sur la fissuration en corrosion sous contrainte (CSC) pour des verres SBN qui sont supposés avoir une démixtion en trois phases amorphes. Des traitements thermiques adéquats sur les verres parents ont permis d'engendrer cette démixtion. Plusieurs techniques ont ensuite été utilisées pour caractériser l'évolution de la structure à courte et moyenne distance qui en résulte. Des expériences de CSC ont ensuite été menées à l'aide d'un dispositif spécialement conçu à cet effet durant ma thèse. Une démixtion en petites tailles rend les verres plus sensibles à la CSC. Pourtant, celle de grandes tailles a tendance à améliorer la résistance à la CSC et, dans certains cas, ces verres ayant des séparations de phases présentent des performances supérieures à celles des verres parents.

Title: Stress Corrosion Cracking of Sodium Borosilicate Amorphous Phase Separated Glasses

Keywords: Stress corrosion cracking, amorphous phase separation, sodium borosilicate glasses

Abstract: Sodium borosilicate (SBN) glasses concern an important research topic, as the three components (SiO_2, B_2O_3 and Na_2O) are the principal oxides of many industrial glasses. Within in the ternary SBN oxide glass system, there is a region where amorphous phase separation (APS) is a dominant feature. My research focuses on how APS alters the stress corrosion cracking (SCC) behavior of SBN glasses falling within the hypothesized three-phase APS zone. Annealing pristine (as-fabricated) glasses induces APS. Various techniques were used to capture the evolution of the short- and medium-range order of the glass structure with APS. The SCC behavior in APS glasses was characterized via an in-house experimental setup designed during my thesis. Interestingly, small size APS makes the glasses more susceptible to SCC. However, larger APS structures tends to re-enhance the SCC resistance, and in some instances, the APS glass outperforms their pristine counterparts.

UNIVERSITY OF Paris-Saclay

DOCTORAL SCHOOL PIF

ToughGlasses

Stress Corrosion Cracking of Sodium Borosilicate Amorphous Phase Separated Glasses

PhD of Physics

of the University of Paris-Saclay

Defended by

Weiying Feng

Thesis Advisor: Cindy L. Rountree

Co-Advisor: Fabrice Célarié

prepared in SPEC/CEA-Saclay

defended on March 15, 2022

Jury :

Président :	Matteo Ciccotti	-	ESPCI
Reviewers :	Simona Ispas	-	University of Montpellier
	Lothar Wondraczek	-	University of Jena
Examinators :	Emmanuelle Gouillart	-	Saint-Gobain
	Christiane Alba-Simionesco	-	CEA-Saclay
Advisors :	Cindy L. Rountree	-	CEA-Saclay
	Fabrice Célarié	-	University of Rennes 1
Invited :	Paul C. M. Fossati	-	CEA-Saclay

Résumé

Les verres borosilicates de sodium (SBN) sont l'objet de nombreuses recherches car les trois oxydes qui les composent (SiO_2, Na_2O, et B_2O_3) font partie des principaux oxydes présents dans les verres industriels. Or il existe, dans le diagramme de phase ternaire des verres SBN, une zone où le phénomène de démixtion (ou séparation de phase amorphe, *APS*) joue un rôle important. Les théories, simulations et expériences révèlent le plus souvent une séparation en deux phases dans les verres SBN. Il a été par ailleurs supposé qu'il pouvait exister, pour certaines compositions chimiques, une démixtion en trois phases. De plus, la démixtion des verres est un phénomène exploité dans plusieurs procédés industriels, par exemple pour obtenir des verres résistants à l'écrasement, des verres poreux ou des vitrocéramiques. Etudier des verres démixés peut aider à améliorer les propriétés du verre, telles que les propriétés mécaniques.

Une revue concernant les théories pour expliquer l'origine de démixtion dans les verres et ses impacts sur leurs propriétés est détaillée en Chapitre 2. Selon la théorie thermodynamique, deux types de démixtion peuvent apparaître décomposition binodale (forme particulière de la phase secondaire) et spinodale (forme du réseau complexe en 3 dimension). La démixtion dans les verres entraîne une structure du verre à l'échelle nanométrique complexe et hétérogène. Selon les études existantes, ces démixtions ont un impact sur leurs propriétés physiques (la densité et les modules d'élasticité, etc.) et mécaniques (les chemins de fissure, la ténacité, la corrosion sous contrainte (CSC), *etc.*). Il convient de noter que la structure spinodale des verres SBN contribue à augmenter la ténacité. Par ailleurs, l'interaction entre le front de fissure et des phases différentes induit le changement du chemin de la fissure, modifiant ainsi la rugosité de la surface de fracture. Pourtant, le lien entre la structure des verres à séparation de phase et leurs propriétés reste difficile à interpréter, en particulier en ce qui concerne le comportement lors de la fissuration en CSC. L'objectif de ma thèse a été d'étudier les effets de la structure des verres à séparation de phase sur le comportement en CSC.

Pour effectuer ce tavail de recherche, les méthodes expérimentales, les techniques et ses principes sont détaillés au Chapitre 3. Les échantillons utilisés pendant ma thèse sont fabriqués par l'Institut de Physiques de Rennes (IPR) à l'Université de Rennes 1. Des traitements thermiques (TTs) adéquats appliqués aux verres parents dans la zone de démixtion ont permis d'engendrer des séparations de phase. Concernant des caractérisations structurelles, plusieurs techniques ont été utilisées pour caractériser l'évolution de la structure à courte et moyenne distance. La structure à courte distance des verres après séparation de phase a été caractérisée par spectroscopie en Résonance Magnétique Nucléaire (RMN) et Raman. Ces caractérisations permettent d'observer des changements des unités structurelles (anneaux et chaîne BO_3, des unités Q_n, *etc.*) avec la démixtion. Pour la structure à moyenne distance,

des images prises par microscopie à force atomique (AFM) ont permis de révéler la morphologie des phases dans ces verres après TTs, et la croissance de cette structure avec le temps (t_a) et la température (T_a) du TT. Par ailleurs, l'AFM a permis d'obtenir des images topographiques haute résolution des surfaces de rupture après des expériences de CSC. Des analyses quantitatives, sur ces images ont été faites pour comprendre les mécanismes de fracture dans les verres démixés. En plus des caractérisations structurelles, des mesures de densité par la méthode d'Archimède et de modules d'élasticité par la méthode d'échographie ont été effectuées sur les échantillons parents et démixés.

Pour la partie de CSC, des expériences ont été menées à l'aide d'un dispositif spécialement conçu à cet effet durant ma thèse. Ce dispositif utilise des échantillons de forme DCDC (*Double Cleavage Drilled Compression*) et une machine de traction compression de la marque Deben. La compression appliquée par la machine Deben sur un échantillon DCDC provoque la propagation de fissure de Mode I (Ouverture) à très basse vitesse ($10^{-12} - 10^{-5}$ m/s). Le dispositif expérimental m'a permis de suivre la propagation du front de fissure dans un environnement contrôlé (T=19 ± 1 ℃ et RH=$40.0 \pm 0.5\%$). La vitesse de fissuration v et son évolution avec le facteur d'intensité de contrainte K_I ont ensuite été déterminées. La relation entre ces deux paramètres construit la figure importante pour caractériser le comportement de CSC à très basse vitesse d'un verre, plus précisément, la limite environnementale K_E et la Région I où $log(v)$ est proportionnelle à K_I.

Mes recherches se sont concentrées sur trois compositions verrières SBN, y compris une supposée non-démixée SBN12 (Partie I), et deux supposées avoir une démixtion en trois phases amorphes après TTs à 600 ℃ - SBN42 (Partie II) et SBN96 (Partie III). En comparant mes résultats avec les études précédentes, les études sur SBN12 ont confirmé la fiabilité de dispositif expérimental pour les expériences de CSC. Des caractérisations sur les échantillons parents et démixés de SBN42 et SBN96 ont été ensuite menées pour étudier les effets de la démixtion sur la structure et le comportement en CSC.

Les caractérisations structurelles confirment que la décomposition spinodale se produit dans les échantillons SBN42 et SBN96 après TTs. Pour le SBN42, à une température de TT T_a fixée, l'évolution de la taille de la phase enrichie en Si est proportionnelle à la racine cubique du temps $t_a^{1/3}$. L'augmentation de la température accélère le processus de démixtion. De plus, des températures élevées, par exemple T_a=700 ℃, fournissent l'énergie nécessaire pour former des α-cristoballites. Des caractérisations Raman et XRD mettent en évidence cette cristallisation dans des échantillons de SBN42 après TTs à 700 ℃. Comme mon objectif était d'étudier les effets de la démixtion sur les propriétés CSC des verres SBN, les TTs à 700 ℃ n'ont pas été abordé. Cependant, ces échantillons aident à comprendre les changements structurels dans le réseau de bore. Des caractérisations RMN ont été faites sur des échantillons de SBN42. Les spectres ^{29}Si MAS (*Magic Angle Spinning*) confirment

l'hétérogénéité à l'échelle nanométrique due à la démixtion après les TTs. Les spectres ^{11}B MAS et 3QMAS révèlent une augmentation des anneaux BO_3 et une diminution des chaînes BO_3 dans les échantillons démixés. Ceci est cohérent avec la formation de phases enrichie en B due à la démixtion. Selon les expériences REDOR (*Rotational-Echo DOuble-Resonance*), les ions Na^+ restent préférentiellement dans la phase enrichie en B.

Pour SBN96, la séparation de phase se produit dans les échantillons dès leurs synthèses (sans TT). Des images d'AFM sur les échantillons après les TT avec des temps et des températures différentes ont aidé à étudier la cinétique de la séparation de phase pour SBN96. En comparant avec SBN42, la cinétique de démixtion est plus rapide dans les échantillons de SBN96. Les spectres Raman ont révélé une énorme évolution du réseau de bore dans les échantillons après les TTs. Les atomes d'oxygène non pontants peuvent apparaître dans les réseaux de bore pendant le processus de démixtion.

En général, la démixtion dans les verres s'accompagne de changements de structure à courte distance et crée l'hétérogénéité à moyenne distance ($10 - 100\ nm$). Des mesures de densités et de modules d'élasticités sur les échantillons ont été ensuite menées. D'après mes résultats, aucune tendance évidente ne peut être observée avec la variation de température ou de temps de TT. Cela est peut-être dû aux marges d'erreurs expérimentales.

Les expériences de CSC démontrent que la démixtion spinodale a un effet intéressant sur la fissuration à très basse vitesse. Au total, un groupe de SBN12, trois groupes de SBN42 et un groupe de SBN96 de forme DCDC ont été utilisés pour les expériences de CSC. Les études sur SBN12 ont confirmé la fiabilité de dispositif expérimental en comparant mes résultats avec des études précédentes. En considérant les résultats de CSC pour SBN42 et SBN96, la structure APS influence de manière significative le comportement en CSC. Dans mes travaux, les conditions de TT pour les expériences de CSC sont $T_a = 600$ ℃ et $t_a = 0$h (échantillons parents), 4h, 18h pour SBN42 et $T_a = 600$ ℃ et $t_a = 0$h (échantillons parents), 4h pour SBN96. Premièrement, la démixtion provoque un déplacement de la position de courbe de CSC $log(v) - K_I$. Pour SBN42, en comparant avec les échantillons parents, il y a un déplacement de la courbe vers la gauche pour $t_a = 4$h, ce qui signifie que les TTs de temps courts ($t_a \leq 4$h) rendent les verres plus sensibles à la CSC. Pourtant, les TTs de temps longs ($t_a \geq 18$h) ont tendance à améliorer la résistance à la CSC et induisent un déplacement de la courbe vers la droite. Dans certains cas, ces verres ayant des séparations de phases présentent des performances supérieures à celles des verres parents. Pour expliquer ce phénomène, un modèle de cinétique de démixtion spinodale a été proposé :

Etape 1 : Pour les TTs de temps courts, la démixtion démarre avec la nucléation des phases de tailles petites, ce qui est similaire à la décomposition binodale. Pendant cette période, la structure est instable et beaucoup de zones faible mécaniquement se créent dans les verres.

Ce type de morphologie avec des phases de tailles petites rend le verre plus sensible à la CSC.

Etape 2 : Pour les TTs de temps longs, il y a croissance des phases et formation du réseau complexe en 3 dimension. Pendant ce période, les phases qui sont plus résistantes à la CSC jouent un rôle d'obstacle à la propagation de fissure. Cette structure complexe aide à améliorer le comportement en CSC.

Etape 3: Pour les TTs de temps encore plus longs, la coalescence des phases se produit et la complexité de réseaux baisse. Dans ce cas, les verres deviennent plus sensibles à la CSC en comparaison avec l'**Etape 2**.

Les résultats de SBN96 ont révélé des effets similaires. Notons que les structures spinodales existent dans les échantillons parents de SBN96 (**Etape 1**), le TT à $T_a = 600$ ℃pour $t_a = 4$h provoque la formation du réseau complexe en 3 dimension (**Etape 2**) et améliore le comportement en CSC. En général, la cinétique de démixtion a un impact important sur les propriétés en CSC d'un verre. La formation d'un réseaux complexe en 3 dimension comme obstacle est la clé pour améliorer le comportement en CSC d'un verre démixé.

Deuxièmement, deux différentes parties (Région I-L pour la partie en bas et Région I-U pour la partie en haut), peuvent être observées dans la Région I pour les échantillons démixés de SBN42 et SBN96. Pour ces deux parties, la pente de Région I-L est plus raide que celle de la Région I-U. Une explication possible pour ce phénomène est que pour une propagation de fissure à vitesse plutôt faible (Région I-L), il existe différentes interactions locales lorsque le front de fissure rencontre différentes phases. Par exemple, pour un K_I fixé, l'une des phases se trouve dans la Région I alors il y a propagation de fissure ; l'autre phase est plus résistante à la CSC et il y a des effets d'épinglage empêchant la propagation de fissure. Et quand la vitesse est plus grande (Région I-U), les deux phases se trouvent à Région I alors la pente diffère de celle de la Région I-L. Cependant, d'après les résultats, aucune règle spécifique ne peut être obtenue concernant la façon dont la démixtion joue sur les pentes de la Région I.

Le comportement en CSC et la rugosité des surfaces de rupture sont liés. Les analyses post-mortem de la surface de fracture contribue à comprendre les mécanismes de fracture du verre. Après les tests CSC, des caractérisations par AFM ont été menées sur les échantillons parents et démixés. Les images montrent que les structures de démixtion ont des effets sur la rugosité des surfaces de fracture. Les surfaces de fracture des échantillons démixés sont nettement plus rugueuses par rapport aux verres homogènes. Des analyses statistiques sur ces images ont été faites pour quantifier cette évolution. Les calculs de RMS (*Root Mean Square*, Moyenne quadratique) ont été menés. Les résultats révèlent que les RMS de SBN12 sont plus petits que ceux des échantillons parents de SBN42 et SBN96. Et pour SBN42 et SBN96, le RMS augmente proportionnellement avec la taille des phases. Par conséquent, l'existence des phases secondaires peut changer le chemin de la propagation de fissure et

augmente la rugosité des surfaces de fracture. De plus, un modèle de fracture stochastique *structure function model*, a été appliqué. Ce modèle est basé sur la mécanique de la rupture élastique linéaire. Les paramètres de sortie comprennent la largeur de la microstructure ℓ, le coefficient de Poisson ν et le contraste du désordre θ. Il faut noter que mes analyses fractographiques fournissent un premier test expérimental à cette classe de modèle. Les résultats montrent que la largeur de la microstructure ℓ est liée à la structure de démixtion. Comme les calculs de RMS, ℓ de SBN12 sont plus petits que ceux des échantillons parents de SBN42 et SBN96. Et pour les échantillons démixés, ce paramètre augmente avec la taille des phases. Pourtant, les coefficients de Poisson ν obtenus par cette méthode ne fournit pas une estimation précise, mais la valeur est plutôt pour confirmer la fiabilité du modèle en restant dans l'intervalle raisonnable ($[0, 0, 5]$). De plus, aucune règle ne peut être trouvée sur l'évolution de ν et θ avec la structure de démixtion.

En conclusion, mes recherches montrent que la démixtion influence de manière significative le comportement du CSC pour des verres SBN. Cependant, la sensibilité d'un verre au CSC dépend des différents facteurs, y compris le protocole de fabrication, le protocole de TT, *etc.* La morphologie et la composition chimique locale des phases jouent un rôle important sur les propriétés du verre. Mes investigations concernent ici deux compositions dans la zone où il y a une démixtion en trois phases. Les caractérisations structurales confirment la démixtion spinodale dans ces verres après les TTs et aident à comprendre le changement dans le réseau de borate. Cependant, des expériences spécifiquement conçues (y compris la fabrication de verres enrichis en ^{29}Si pour les spectres RMN) pour capturer l'évolution du réseau de silice seraient utiles. Le manque de données sur la microstructure des phases rend difficile la compréhension des interactions locales entre le front de fissure et les différentes phases au cours de la CSC. Contrôler la morphologie de démixtion en modifiant la composition, la température et le temps de TT reste difficile. Compte tenu du diagramme SBN, il existe encore de nombreuses autres compositions chimiques et différents protocoles de TT restent à étudier. Pour améliorer les performances en CSC par la structure de démixtion, des investigations supplémentaires sont nécessaires.

Mot clés: Corrosion sous contrainte, séparation de phases, verres borosilicates de sodium

Summary

Sodium borosilicate (SBN) glasses concern an important research topic, as the three components (SiO_2, Na_2O, and B_2O_3) are the principal oxides of many industrial glasses. Within in the ternary SBN oxide glass system, there is a region where amorphous phase separation (APS) is a dominant feature. Moreover, APS has industrial relevance for crush resistant glasses, porous glasses and glass ceramics. Theory, simulations, and experiments clearly reveal two-phases. Additionally, it is hypothesized that three-phase exists for certain chemical compositions. APS inside the glasses induces complex heterogeneous structures at the nano-scale, which alter the glasses' physical and mechanical/fracture properties. However, the connection between the structure of APS glasses and their properties remains poorly understood, especially the stress corrosion cracking (SCC) behavior. Hence, in my PhD, I aim at studying the effects of APS structure on SBN glass SCC behavior.

My research focuses on SBN glasses with compositions falling within the hypothesized three-phase APS zone. Annealing pristine (as-fabricated) glasses induces APS. Various techniques were used to capture the evolution of the short- and medium-range order of the glass structure with APS. For example, Atomic Force Microscopy (AFM) images evidence spinodal decomposition in the structure, and its growth with annealing temperature and duration. The evolution of phase size is found to be proportional to the cubic root of annealing time for the fix annealing temperature. Additionally, NMR and Raman spectra help in understanding the short-range structure of the APS glasses. An increase in the fraction of BO_3-ring structural units was observed, confirming the formation of B-rich phases.

The SCC behavior in APS glasses was characterized via an in-house experimental setup designed during my thesis. This experimental setup permits me to capture the propagation of the crack front in a well-controlled environment (T=19$\pm$1 ℃ and RH=40.0$\pm$0.5%). From images captured, the crack front velocity as a function of the stress intensity factor can be rendered. These results show the inherent meso-scale structure plays on the environmental limit along with SCC Region I parameters. Interestingly, small size APS makes the glasses more susceptible to SCC. However, larger APS structures tends to re-enhance the SCC resistance, and in some instances, the APS glass outperforms their pristine counterparts. After SCC experiments, AFM imaging provides high-resolution topographical images of the fracture surfaces. Post-mortem analysis reveal that the roughness increases with the phase sizes. Additionally, the fracture surfaces of all the samples were found to fit the structure function models. These are the first results proving the reliability of structure function models with experimental fracture surfaces.

Keywords: Stress corrosion cracking, amorphous phase separation, sodium borosilicate glasses

Contents

Chapter 1

Preface and motivation

Contents

This chapter was originally written as the introduction to a review article: "Stress Corrosion Cracking in Amorphous Phase Separated Oxide Glasses: A Holistic Review of Their Structures, Physical, Mechanical and Fracture Properties" W. Feng, D. Bonamy, F. Célarié, P. C. M. Fossati, S. Gosse;, P. Houizot, C. L. Rountree, MDPI Corrosion and Materials Degradation. 2(3):412-446 (2021) DOI: 10.1039/D0SM00723D. I have made a few modifications to the text for my thesis manuscript; but for the most part, it is the same.

1.1 General introduction of glasses

Glass has existed on earth a long time ago. It can be formed naturally (*e.g.* tektite and obsidian) in the earth's crust or in meteorites or lunar rocks. Archaeological evidence shows that natural glasses have been used by man from the earliest times. Since Before the Common Era, humankind has been fabricating oxide glass for various uses. Over the years, interest in oxide glasses has grown due to advantageous optical, chemical, mechanical and electrical properties [44]. Some of these properties include optical transparency, electrical isolation, and a high melting point (between $800 - 1800$ ℃ depending on the chemical composition).

The structure of glass is an essential question in glass science. Glass was first considered to consist of crystallite [213]. In the 1932, Zachariasen, specialist in X-ray crystallography, declared the inaccuracy of this model and proposed a random network theory for the glass structure based on the crystal chemistry view of Goldschmidt [280]. According to the this theory, the formation of 3-dimensional glass networks should follow the rules: (a) No oxygen atom may be linked to more than two cations; (b) The cation coordination number is small (3 or 4); (c) Oxygen polyhedra share corners, not edges or faces; (d) at least three corners in each oxygen polyhedra must be shared. This theory is widely used for describing glass structures.

1.2 Amorphous phase separated glasses and their uses in industry

A single-phase material has a homogeneous distribution of its constituents. Multiphase materials occur when precipitates form. Each phase in these materials is homogeneous, and there is a distinctive barrier between different phases [17, 90, 80]. Liquid-liquid phase separation occurs in multi-component liquids when the Gibbs energy curve shows two distinct minimums as a function of the liquid composition. This also influences kinetic limits [130]. From a thermodynamic viewpoint, a simple binary system composed of components A and B can exist as a homogeneous mixture (attractive interactions A-B), or it might prefer to exist as a heterogeneous mixture with repulsive A-B interaction. The preference to exist as a heterogeneous mixture induces phase separation over a well-defined range of compositions, temperatures, and pressures. Phase separation processes produce a large variety of mesoscopic structures, which modifies the macroscopic behavior of the material. Theories propose different mechanisms to explain these scenarios taking into consideration the composition of the glass and the kinetic limits [130, 37].

Over the years, researchers identified metastable miscibility gaps in multiple different types of oxide glass systems [176, 142, 42], particularly those based on silica and boron oxide [87, 202, 143]. Simulation and experimental approaches aid in obtaining phase diagrams to predict the miscibility gaps. These studies [192, 25, 26, 27, 28, 178] help in understanding the short- and mid- range (micro and meso) structure of the glasses. Researchers also study how these changes scale up to variations in the overall physical and mechanical properties of phase separated glass systems [206, 97]. An industrial application of phase separated glasses and their enhanced mechanical properties concerns crush-resistant glasses [108]. Furthermore, phase diagrams have industrial significance when considering functional materials, such as glasses-ceramics and porous glasses [247, 68, 212].

Glass-ceramics [59] are oxide-based glasses with a secondary crystalline phase. Common uses for glass-ceramics include optical thermometry [281], cookware [74], dental applications [122], etc. Controlling the thermal treatments of the pristine homogeneous glass leads to nucleation and growth of crystalline phases [59, 121]. Studies suggest that APS glasses could be favorable systems in elaborating glass-ceramics, because the presence of a secondary amorphous phase could provide favorable sites for crystal nucleation [256]. Combining some observations and analyses, Uhlmann [260] proposed four effects of liquid-liquid phase separation on crystal nucleation in glass forming systems: enhanced driving force, special interfacial sites, higher atomic mobility, and enrichment of certain components after the appearance of the second phase. Tomozawa [256] attributed a higher nucleation rate to the presence of a narrow and deep diffusion zone at the interface between the minor phase and the main matrix. This provides favorable sites for crystal nucleation by lowering the interfacial energy between matrix and secondary phase. Moreover, secondary amorphous phases could themselves be a precursor to the onset of crystal nucleation [146, 118, 85]. Yet, the precise connection (if any) of these processes eludes scientists [198]. Further investigations are required to determine conclusively the mechanisms involved.

Porous glasses concern another industrial use of APS glasses [68]. Their application

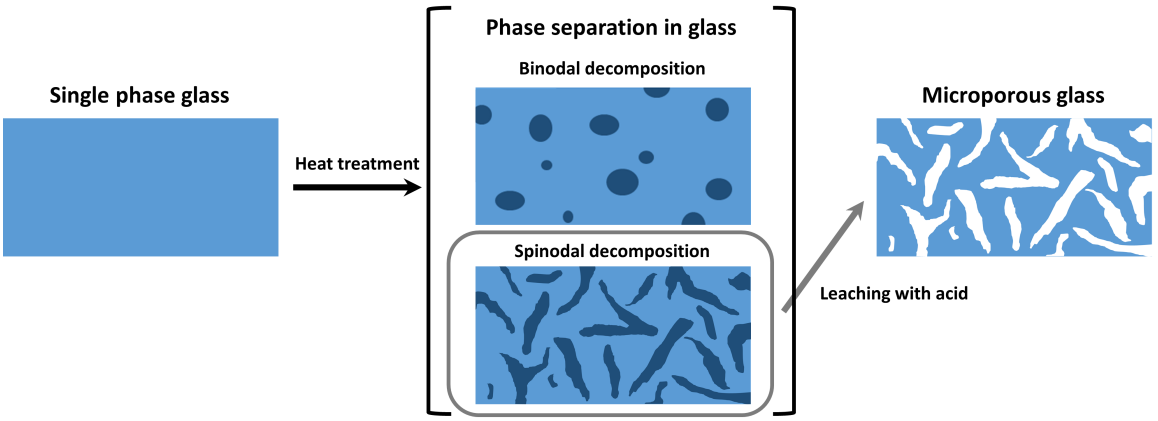

Figure 1.1: Schematic diagram of how to create porous glass using phase separation in a glass obtained from slag (Reproduced from [248]).

involved the creation of a melt that undergoes a spinodal decomposition (which will be presented in Section 2.2.2.2), followed by subsequent leaching of one or more of the phases [248, 149]. In the case of sodium borosilicate glasses [247], the alkali-rich borate phase is removed, and the nearly pure silica phase, or backbone, remains. These glasses find a multitude of different industrial applications, including ion exchange [123], membrane technology [153], chromatography [223], solid-phase biochemistry [116], and heterogeneous catalysis [120]. Furthermore, porous glasses are a base material in the preparation of zeolite/porous glass composites [60, 164].

Generally, the structure of porous glass is important for the application and macroscopic behavior of materials [68, 53]. Therefore, the glass structure should be strictly controlled to enable specific functionalities in the glasses. These functionalities are determined by (i) initial glass composition, (ii) annealing protocol (duration, temperature, number of annealing times), and (iii) leaching conditions [249]. In certain cases, the APS glass structure makes the glass more crush resistant when the leaching solution contains silica ions [171]. Similar to the case of glass-ceramics, APS controls the properties of the final products. Hence, understanding how APS, specifically size and geometry of the secondary phase, affects the structure of the glasses and subsequently the physical and mechanical (including stress corrosion cracking) behavior plays an important role in fabricating stronger glasses for future applications.

1.3 Effects of APS structure on SBN glasses properties

Oxide glasses have a major drawback: they are brittle. This limitation remains despite great efforts to overcome it. In recent years, it became apparent that solving this problem requires a detailed knowledge of how structural properties influence physical, mechanical and fracture properties in these glasses. By gaining this deep understanding, researchers will have the keys to advancing glass technology. This will ultimately benefit all kinds of industry, including high technology fields such as laser technology, energy-saving technology, and communication

Table 1.1: Chemical composition of SBN12, SBN42 and SBN96. Figure 1.2 indicates their positions in the ternary oxide diagram.

	mol%			mass%		
	SiO_2	B_2O_3	Na_2O	SiO_2	B_2O_3	Na_2O
SBN12	59.6	23.9	16.5	57.1	26.5	16.4
SBN42	70.0	23.0	7.0	67.4	25.6	7.0
SBN96	62.9	29.6	7.5	59.9	32.7	7.4

technology. Literature highlights a significant body of work concerning structural [280, 244, 31, 11, 221], physical [11, 214, 93], mechanical [221, 10, 12, 13, 166] and fracture properties [10, 261, 218, 14] of homogeneous single-phase oxide glasses, whereas multiphase glasses are less studied in literature. Thus, how APS influences the short- or medium range structure, physical and mechanical/fracture properties is not well understood. Nevertheless, some studies in literature indicate the presence of this effect. Chapter 2 provides a holistic review of the APS structures and the effects on the physical, mechanical and fracture properties. However, the existing studies are not sufficient to realize this potential, most notably for SBN glasses, which are widely used in industry. Can glass properties be optimized by controlling phase separation? More investigations should be carried out to analyze and understand their effects.

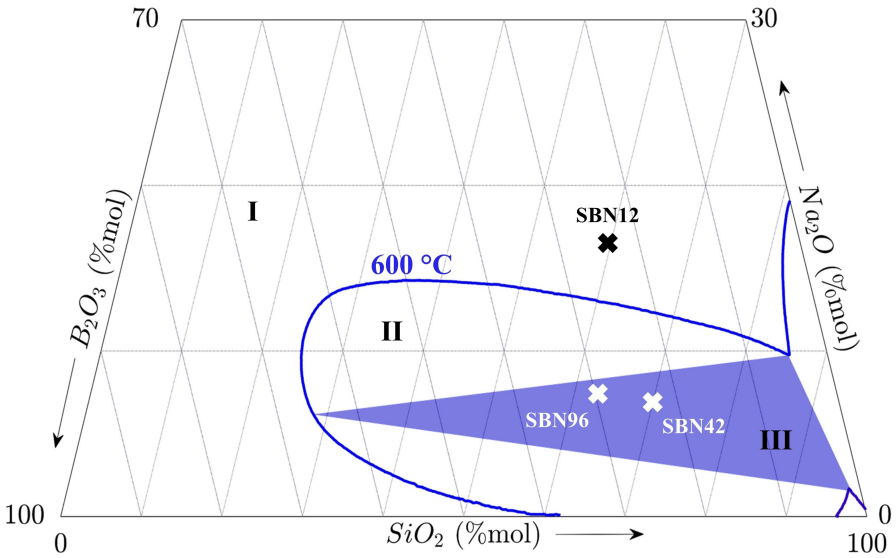

Figure 1.2: Immiscibility diagram posed by Haller [106] for SBN systems at 600 °C with the location of SBN12, SBN42 and SBN96.

Hence, in my PhD, I aim in studying the relationship between the structure (short- and medium range) and the SCC behavior changes in APS-SBN (Amorphous Phase Separated sodium borosilicate) glasses. At the beginning, the complete experimental set-up has been

built up, including a new Deben machine, humidity control system and the automatic photo capture system (Section 3.4.1). Remaining SBN12 samples from Marina Barlet's thesis [10] aid in testing the new equipment and the reliability of the set-up (Part I). Considering Haller's phase diagram [106] (Figure 1.2), SBN12 is outside the phase separation area. Then, I chose two chemical compositions inside the three phase area – SBN42 (Part II) and SBN96 (Part III), for structure characterizations (Chapter II-1 for SBN42 and Section III-1.1 for SBN96), physical characterizations (Chapter II-2 for SBN42 and Section III-1.2 for SBN96) and SCC experiments (Chapter II-3 for SBN42 and Chapter III-2 for SBN96). Annealing the pristine (as-fabricated) samples generates APS structures and leads to some changes of material behavior. Chapter 4 concerns a general discussion comparing and contrasting SCC results of three glasses. Chapter 5 summarizes the thesis and provides an outlook for the subject.

Chapter 2

APS glasses: A review of their structures and properties

Contents

This chapter was originally written as the main body of a review article: "Stress Corrosion Cracking in Amorphous Phase Separated Oxide Glasses: A Holistic Review of Their Structures, Physical, Mechanical and Fracture Properties" W. Feng, D. Bonamy, F. Célarié, P. C. M. Fossati, S. Gosse;, P. Houizot, C. L. Rountree, MDPI Corrosion and Materials Degradation. 2(3):412-446 (2021) DOI: 10.1039/D0SM00723D. I have made a few modifications to the text for my thesis manuscript; but for the most part, it is the same.

2.1 Thermodynamic interpretations of phase separation

Thermodynamic theories are some of the most widely accepted methods for explaining the origin of phase separation in materials. Section 2.1.1 reviews the case of a binary two-atom theoretical system. Section 2.1.2 turns to the more complex problem of ternary oxide systems. Section 2.1.3 addresses the special case of $SiO_2-B_2O_3-Na_2O$. It should be noted that glass is not in thermodynamic equilibrium; hence, discussions herein concern inherently metastable states.

2.1.1 Binary amorphous phase separation: a two-atom theoretical viewpoint

A simple case of phase separation concerns binary systems. Cottrell [52] and James [130] simplified the problem to a two-atom system to explain qualitatively the behavior of the two liquids. This approach is reviewed herein. For a homogeneous single-phase system, in theory, atoms A and B are considered randomly distributed on a regular lattice. The Gibbs free energy of this ideal mixing ΔG_{mix} is [130, 39, 263]:

$$\Delta G_{mix} = \Delta H_{mix} - T\Delta S_{mix} \tag{2.1}$$

where ΔH_{mix} is the enthalpy of mixing, ΔS_{mix} in the entropy of mixing, and T is the temperature. The entropy of the mixed phase is [130, 39, 263]

$$\Delta S_{mix} = -R[x_B \ln(x_B) + x_A \ln(x_A)] \tag{2.2}$$

where x_A and x_B are the mole fractions of atoms A and B (respectively), and R is the gas constant. As this is a binary system, $x_A = 1 - x_B$, the entropy of the mixed system is [130, 39, 263]

$$\Delta S_{mix} = -R[x_B \ln(x_B) + (1 - x_B) \ln(1 - x_B)] \tag{2.3}$$

The enthalpy of the system is arrived at via the quasi-chemical approach [39]. This method assumes a homogeneous mixture of A-B, A-A and B-B interatomic bonds. Moreover, the interatomic distances and bonding energies are independent of the chemical composition. In this instance, the enthalpy of mixing is [39, 263]

$$\Delta H_{mix} = \eta x_B(1 - x_B) \tag{2.4}$$

where η is

$$\eta = N_A Z[E_{AB} - \frac{1}{2}(E_{AA} + E_{BB})] \tag{2.5}$$

where E_{AA}, E_{BB} and E_{AB} are the bonding energies between atomic species, Z is the number of nearest neighbors surrounding each atom, and N_A is Avogadro's number. Finally, the Gibbs free energy of mixing is [130, 39, 263]:

$$\Delta G_{mix} = \eta x_B(1 - x_B) + RT[x_B \ln(x_B) + (1 - x_B) \ln(1 - x_B)] \tag{2.6}$$

Figure 2.1 depicts a typical miscibility gap and the Gibbs free energy curves as a function of x_B. In Figure 2.1 (a), the solid dark blue line represents the binodal curve, which is the boundary between the domain where only a single phase exists to a domain where multiple phases exist, and hence a miscibility gap. This curve is obtained from the shape variation of Gibbs free energy curves (Figure 2.1 (b) and (c)).

The temperature at the apex, T_C, is the upper consolute temperature. For temperatures greater than T_C (for example at T_1), a single phase exists for all compositions. Figure 2.1 (b) shows the Gibbs free energy as a function of the chemical composition. In this case, the

Gibbs free energy varies with chemical composition as $G = \mu_A x_A + \mu_B x_B$ [39]. The tangent to the Gibbs free energy for a specific chemical composition gives the chemical potential of A at that composition μ_A (value of the tangent at $x_B = 0$), and that of B μ_B (value of the tangent at $x_B = 1$, bearing in mind that $x_A = 1 - x_B$).

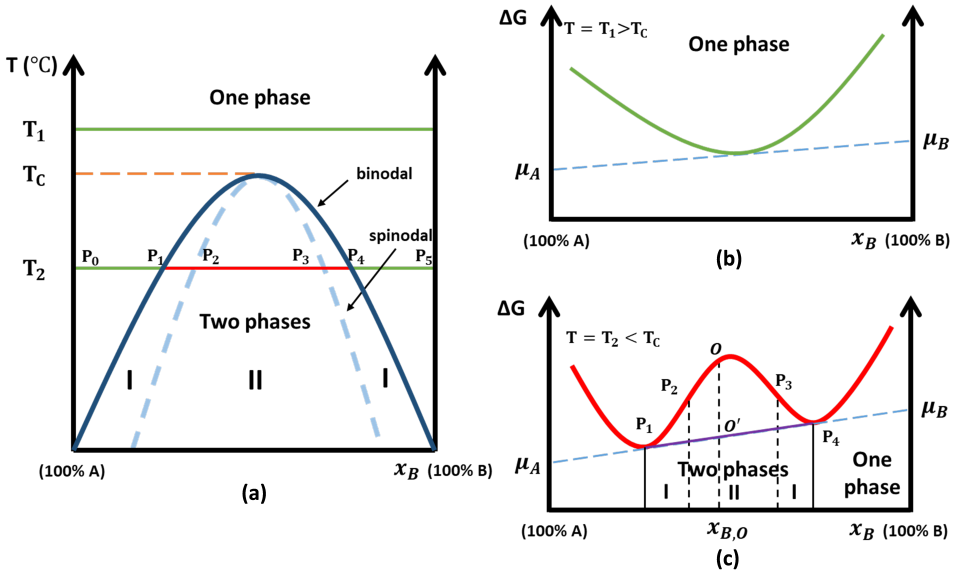

Figure 2.1: (a) Schematic two-liquid immiscibility region showing binodal and spinodal; (b) Sketch of the Gibbs free energy curve versus composition x_B (mole fraction of component B) for temperature T_1 where $T_1 > T_C$; and (c) Gibbs free energy curve versus composition x_B (mole fraction of component B) for temperature T_2 where $T_2 < T_C$.

For temperatures below T_C (Figure 2.1 (c)), the liquid can be single-phased or it can separate into two phases with different compositions. For $P_0 \leq x_B \leq P_1$ and $P_4 \leq x_B \leq P_5$, a single phase exists (Figure 2.1 (a)). However, when $P_1 \leq x_B \leq P_4$, phase separation occurs due to thermodynamic driving forces which reduces the system free energy. Within this zone, the Gibbs free energy of the mixture follows the tangent line shown in purple between P_1 and P_4 (Figure 2.1 (c)). Take a system with chemical composition $x_{B,O}$ as an example. The Gibbs free energy is marked by point O if component A and B are ideally mixed. On the other hand, point O' in Figure 2.1 (c) represents the Gibbs free energy when the system decomposes into two phases of composition x_{B,P_1} and x_{B,P_4}. The decrease of free energy from O to O' enhances the occurrence of phase separation.

Once the system equilibrates, there are two liquids co-existing, of which the chemical compositions correspond to P_1 and P_4 for atoms A and B, respectively. (It is worth noting that P_1 and P_4 are considered as *tie-lie end-members* for T_2 [107]) Furthermore, the chemical potential of each compound should be the same in different phases. For example, the chemical potential of A in the first phase α (μ_A^α) is equal to that in the second phase β (μ_A^β): $\mu_A^\alpha = \mu_A^\beta = \mu_A$. A similar phenomenon occurs for the chemical potential of B. Moreover, these values correspond to the common tangent between P_1 and P_4 which is extended to $x_B = 0$ and $x_B = 1$ (see Figure 2.1 (c)). The result of this is the coexistence of two phases with

different possible geometries and influences the physical and mechanical properties of the overall material.

Phase separation is favorable within the zone between P_1 and P_4. It is further divided into two structures, revealing itself as either binodal or spinodal decomposition. Figure 2.1 (a) and (c) identifies the different zones via the markers I and II. Moreover, the changeover from zone I ($P_1 - P_2$ and $P_3 - P_4$) to zone II ($P_2 - P_3$) corresponds to $(\partial^2 \Delta G)/(\partial x^2) = 0$ (Figure 2.1 (a) light blue dashed line).

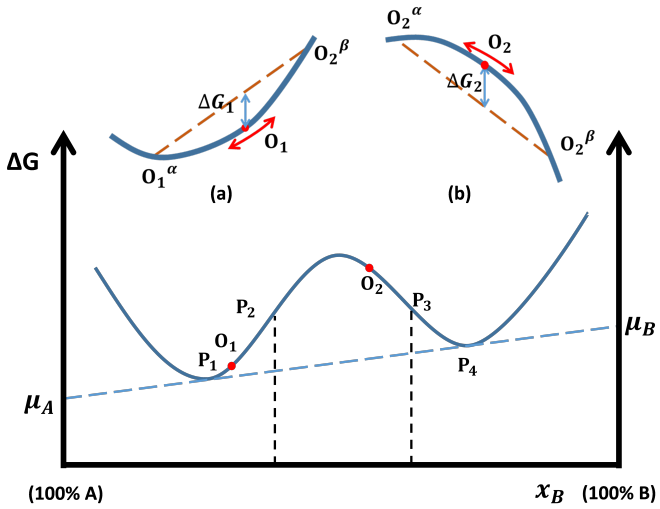

Figure 2.2: Gibbs free energy-composition diagram method for determining the driving force for phase separation.

When the system decomposes into two different phases, the free energy of both phases follow the G lines. For zone I where $(\partial^2 \Delta G)/(\partial x^2) > 0$, the Gibbs free energy curve is convex (O_1 in embedded graph (a) in Figure 2.2). A small composition fluctuation of the system O_1 situating in zone I induces composition changes into ${O_1}^{\alpha}$ and ${O_1}^{\beta}$. This results in an increase of free energy of system (brownish dashed line), so that there is a driving force to recombine them, which inhibits nucleation of a secondary phase. Hence, a stronger fluctuation is needed to overcome the energy barrier. In this case, the system is considered metastable. Once there is nucleation, the secondary phase can grow by diffusion mechanisms since the energy barrier for growth is small. This mode of phase separation has several names: *nucleation and growth*, *coarsening*, and *binodal decomposition*. A similar scenario occurs when the chemical composition falls between $P_3 - P_4$.

On the other hand, if the initial composition is between $P_2 - P_3$ (zone II) where $(\partial^2 \Delta G)/(\partial x^2) < 0$, the curve is concave ($O_2$ in embedded graph (b) in Figure 2.2). Slight fluctuations in composition implies a lower Gibbs free energy of the system, so the system is not stable. In this case, the structure changes continuously until an equilibrium is reached, and phase separation occurs. This process is called *spinodal decomposition*.

Cahn [37] constructed a mathematical model of the decomposition process using computers to produce sections through the two-phase structure. The binodal and spinodal mechanisms may be compared for isothermal separations. For binodal decompositions (Figure 2.3

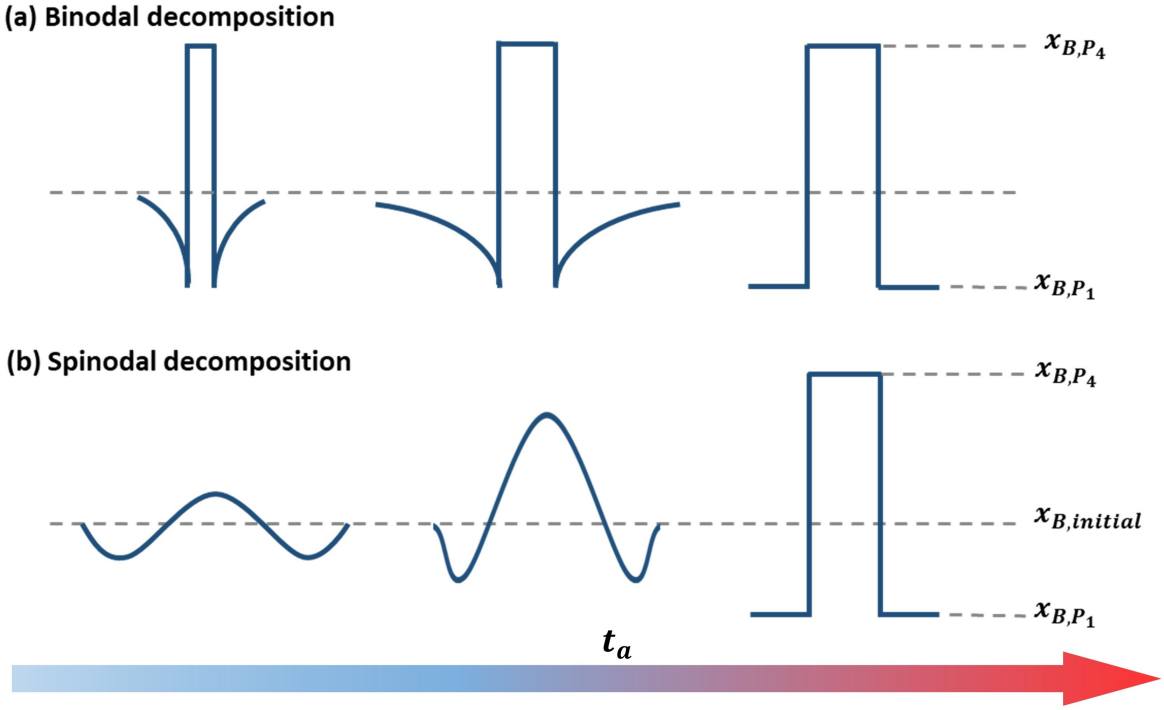

Figure 2.3: Schematic of the evolution of concentration profiles for (a) binodal and (b) spinodal decomposition. $x_{B,initial}$ represents the initial chemical composition of the glass. $x_{B,P1}$ and $x_{B,P4}$ represents the final fraction of B component in different phases in the glass. (Recreated from [263]).

(a)), the second phase composition remains constant with time. During the growth of the binodal structure, the interface sharpness between the phases remains constant. In addition, there is a tendency for spherical particles to separate; hence, the particle connectivity is low. For spinodal decomposition (Figure 2.3 (b)), there is a continuous variation of both chemical compositions in time until equilibrium compositions are reached. The interface between the phases is initially diffuse, but it sharpens and there is a tendency for high connectivity in the second phase.

2.1.2 Beyond the *two-atom* approximation

In general, the initial chemical composition of glasses along with heat treatment protocols dictates the phases in the resulting glass. Looking at binary oxide systems (specially $B_2O_3-Na_2O$, $SiO_2-B_2O_3$, and SiO_2-Na_2O), which can be analyzed as *pseudo*-binary systems even though there are three types of atoms, the problem is significantly more complex than the two-atom model presented above. All three binary oxide systems exhibit a miscibility gap depending on the chemical composition [235, 106, 107]. Haller has modified the regular mixing model for binary SiO_2-M_2O systems (where M is the alkali metal). In his studies, the main network component $[SiO_2]_m$ and a stoichiometric compound $[M_2O{\cdot}nSiO_2]$ are the limit of the miscibility gap on the alkaline oxide side [107]. Charles [43], instead of considering the ideal mixing of atoms, studies a more realistic statistical model involving

the interchange of bridging/non-bridging oxygen atoms. He compares the exothermic contribution (conversion of bridging Si – O bonds to non-bridging Si – O bonds) and endothermic contribution (Coulomb interaction energy difference between metal cations/free oxygen ions in the pure metal oxide and metal cations/non-bridging oxygen ions in the glass melt) to explain the immiscibility origin. Other explanations have been proposed for the origin of phase separation [126, 179]. Nevertheless, it is not clear if the different approaches mentioned above are consistent with one another. Considering everyday glasses, they commonly consist of more than three oxides. Thus, the structural complexity of everyday glasses is extremely high. Researchers frequently use model glasses to understand the driving phenomena. This technique will be invoked here in and I will study glasses concerning the three principle oxides (SiO_2, B_2O_3, and Na_2O) in many industrial glasses.

2.1.3 Phase diagram of SBN glasses

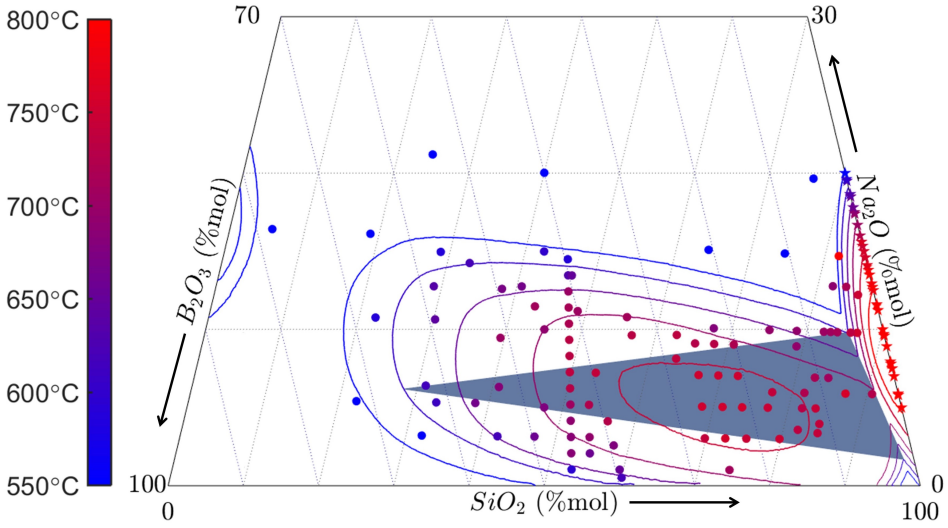

Figure 2.4: Ternary SBN oxide glass system with Haller's isothermals acquired from clearing temperatures. Data points correspond to data presented in two of Haller's papers for pseudo-ternary SBN systems (circles [106]) and SiO_2 – Na_2O systems (stars [107]). The colors correspond to the clearing temperature. The glaucous colored triangle corresponds to the predicted three-phase area for clearing temperature 600 ℃. Arrows indicate the direction of increasing mol %.

As mentioned in the previous section, the miscibility gap for binary systems is where the phase separation for a given material occurs. Nevertheless, the ternary oxide system SiO_2 – B_2O_3 – Na_2O concerns a significantly more complex system than the two-atom system presented in Section 2.1.1. One should recall that even the single-phase SBN systems are rather structurally complex, with more than nine elementary structural units existing [11, 128, 58, 76, 33]. Furthermore, Haller [106] hypothesized possible two- and three-phase separation for the SBN system. From early on, researchers realized the difficulty in identifying in-situ the onset of phase separation in oxide glasses, as the changes are rather subtle. Hence, Haller *et al.* [107] identified systemic tendencies with annealing temperature, which are more obvious. These tendencies reveal a 3-step process in regard to the transparency

of the glass: (1) The glass starts out transparent at room temperature; (2) Increasing the temperature causes the sample to become opaque; and (3) Subsequently increasing the temperature further causes the sample to regain its transparency. Researchers frequently use the clearing temperature (where a sample becomes clear again) as the upper bound of the metastable miscibility surface for SBN glasses. In some cases, the maximum opalescence is used instead of the clearing temperature; however, Haller *et al.* [107] found the maximum opalescence and clearing temperature to be nearly the same. Haller *et al.* examined a number of glasses with varying chemical composition and proposed a phase diagram. Figure 2.4 present Haller's measured clearing temperatures for the ternary oxide SBN system (circles and isothermal lines, [106]) and for the binary oxide SiO_2–Na_2O system (triangles, [107]). Furthermore, the glaucous triangle in Figure 2.4 depicts Haller's hypothesized three-phase separation zones at 600 ℃. This phase diagram is widely used to predict phase separation [248, 177, 253] in SBN glasses.

However, experimental methods have limitations. Estimating the microstructure of the glass simply by the macro-opalescence is not precise enough to point out the onset of phase separation, let alone distinguish between two or three different phases. Therefore, experimental methods require complementary numerical techniques to understand fully the dynamics of phase separation. Thermodynamic approaches using activity data [42], empirical methods [136] and Gibbs free energy [92, 23] provide an enhanced understanding of the liquid phases in phase-separated systems. Literature contains numerous thermodynamic ionic liquid models (including regular [142, 42], quasi-regular [142, 246], and sub-regular solution models [142]) used to predict the thermodynamic behavior of ternary oxide melts [226]. These predictions mostly arise from calculations of chemical activity data on binary systems or binary oxide systems. Charles used the activity data to estimate the metastable miscibility gap thermodynamically in the SiO_2–B_2O_3–Li_2O glasses [42]. In addition, Kawamoto and Tomozawa [136] developed an empirical method with the assumption that the ternary oxide alkaline earth silicate glasses separate into two phases, one of which assumed to be nearly pure silica. However, these assumptions are not considered accurate in determining the compositions of the different phases while annealing [245].

For many years, the CALPHAD (CALculation of PHAse Diagrams) method was used to provide predictions of liquid phase miscibility gaps in multiple different systems [92, 23]. This method uses the Gibbs energy to calculate phase diagrams and thermodynamic properties. Input parameters include conditions such as chemical composition, temperature and pressure. Extending CALPHAD methods to oxide glasses may give reliable estimates of the phase diagram [16], yet this is proving difficult because glass is not at equilibrium.

To sum up, for a given glass with chemical composition within the miscibility gap, annealing protocols determine: (1) the phase composition while reaching equilibrium, (2) the type of phase separation (binodal or spinodal) [106], (3) the nucleation/growth kinetics in the miscibility gaps [109, 36] and (4) the final phase compositions and phase size [32, 265, 113]. The next section focuses on different structures of some APS-SBN (Amorphous Phase Separated SBN) glasses.

2.2 The structure of SBN amorphous phase separated glasses

Industrial glasses commonly contain four or more different oxides [135, 254]. However, model glasses with only the principal oxides frequently represent these glasses. These model glasses usually consist of two glass formers, normally SiO_2 and B_2O_3 [88, 131]. Each of these glass formers reacts with alkali metal oxides [58, 76, 33]; herein, we are predominantly concerned with Na_2O. Varying the glass chemical composition alters the structure of the glass in regards to coordination number of the borate atoms and the number of non-bridging oxygen (NBO) atoms in the silicate and borate networks [11, 10, 12, 13, 218, 14]. Annealing the glasses, which have chemical compositions within miscibility gap, generates APS inside the glasses and results in structure variations at different scales. After fabrication and annealing, researchers used different techniques to probe short-, medium- and long-range structures of APS glasses. Section 2.2.1 presents the short-range order of SBN glasses and the variation after APS. Beyond the micro-scale, microscopes (AFM, TEM, *etc.*) and X-ray tomography technics aid in revealing the morphology of phases. Section 2.2.2 presents some SBN glass examples including binodal and spinodal structure. A more complicated phenomenon – secondary phase separation (which originates sometimes when an APS sample undergoes a second annealing protocol) is also presented in this section.

2.2.1 Atomic arrangement and mid-range level structure of SBN glasses

SBN ternary oxide glasses are composed of two network formers (SiO_2 and B_2O_3) and one network modifier (Na_2O) [228, 94]. Pure silica (amorphous SiO_2) and pure boron trioxide form an amorphous network with short- and mid-range orders. However, they lack long-range order. Table A.1 and Table A.2 in Appendix A.4 summarizes various structure units in SBN glasses and their nomenclature.

The short-range order of pure silica is a tetrahedron (SiO_4) with four bridging oxygen (BO) atoms. The mid-range order is the linking of the tetrahedrons to form predominantly 6-member rings (number of silicon atoms per ring; rings also contain the same number of oxygen atoms) with some ring size dispersion [264]. The short-range order of pure B_2O_3 is a planar $BO_{3/2}$ group with three BO atoms [15, 77, 189]. The mid-range order of B_2O_3 also concerns ring structure – boroxol rings. It contains 3 boron and 3 oxygen atoms per ring. It is generally thought that nearly 70-75% of boron atoms are contained in these rings, with the rest being the linkage between rings [127, 134, 243]. The following part reviews changes to the glass structure when you mix the network formers (silica and boron oxide herein) with network modifiers (sodium oxide herein).

Considering the SiO_2-B_2O_3 (SB) binary oxide glasses, boron atoms exist as planar $BO_{3/2}$ groups with three BO atoms (B[III]; the fraction of these units are f_1). Ideally, f_1 equals to 1 independent of the B_2O_3 mole fraction. Silicon atoms are four coordinated with all BO atoms [173, 262]. The fraction of these units are named Q_4, which equals to 1 in a SB glass and independent of the SiO_2 mole fraction. The interconnection of the two networks (*i.e.* populations of Si-Si, B-B and Si-B connections) plays an important role on the physical properties of material [11, 128] or even mechanical properties. However, the amount of intermixing between the two networks is still an open question and requires more

investigations to understand [61].

Contrary to SiO_2 and B_2O_3, Na_2O is an anti-fluorite crystal structure. It does not form an amorphous glass; rather, it is added to an amorphous glass to modify the glass network [14]. The structure of SBN ternary oxide glass system are more complicated than the binary SB glasses. Adding Na_2O to a SB glass leads to the appearance of different borate and silicate units (Figure A.2 (a)-(d)). The borate structures can vary in coordination, and have BO and NBO atoms. The silicate structures do not vary in coordination, but can have BO and NBO atoms on the silica tetrahedrons (Q_i where i ranges from 0 to 4 representing the number of BO atoms in SiO_4 tetrahedrons, Figure A.2 (f)-(i)). Previous literature shows how the addition of Na_2O to a SB glass modifies the network structure and the fraction of different elementary units. These elementary units concern the mol% ratio of Na_2O to B_2O_3 and of SiO_2 to B_2O_3:

$$R_{SBN} = [Na_2O]/[B_2O_3] \tag{2.7}$$

$$K_{SBN} = [SiO_2]/[B_2O_3] \tag{2.8}$$

where [ ] $\equiv$ mol%. Herein, I am only interested in relatively low R_{SBN} values ($R_{SBN} < 0.5+0.25K_{SBN}$). Below is a summary of the structural changes for $R_{SBN} < 0.5+0.25K_{SBN}$:

- $0 < R_{SBN} < 0.5$: Initially adding sodium to a SB glass does not disturb the silica network. It leads to the transformation of f_1 units (BO_3) to f_2 units (4-coordinated boron tetrahedrons B[IV] with 4 BO atoms, BO_4). These units specifically correspond to diborate groups ($Na_2O \cdot 2\ B_2O_3$). Ideally, Q_4 is 1 and NBO atoms do not exist in the glass. The ideal fractions of different borate and silicate units are as follows:

$$\left.\begin{array}{c} f_1 = 1 - R_{SBN} \\ f_2 = R_{SBN} \\ f_3 = 0 \\ f_4 = 0 \\ Q_4 = 1 \\ Q_3 = Q_2 = Q_1 = Q_0 = 0 \end{array}\right\} 0 < R_{SBN} < 0.5 \tag{2.9}$$

- $0.5 < R_{SBN} < 0.5 + 0.0625K_{SBN}$: Continuing to increase the Na_2O fraction increases the fraction of f_2 units. It also leads to the appearance of reedmergnerite units ($\frac{1}{2}(Na_2O \cdot B_2O_3 \cdot 8SiO_2)$), one four-coordinated boron bonded to 4 silica tetrahedrons. Ideally, Q_4 is 1 and no NBO atom exists in the glass. The ideal fractions of different borate and silicate units are the same as for $0 < R_{SBN} < 0.5$. Combining

equation 2.9 with this section gives the follow parameter for the equation:

$$\left.\begin{array}{c} f_1 = 1 - R_{SBN} \\ f_2 = R_{SBN} \\ f_3 = 0 \\ f_4 = 0 \\ Q_4 = 1 \\ Q_3 = Q_2 = Q_1 = Q_0 = 0 \end{array}\right\} 0.5 < R_{SBN} < 0.5 + 0.0625K_{SBN} \tag{2.10}$$

- $0.5 + 0.0625K_{SBN} < R_{SBN} < 0.5 + 0.25K_{SBN}$: Additional Na_2O in the system leads to the formation of NBO atoms on the silica units. Specially, small amounts of Na_2O causes the transformation of Q_4 to Q_3 (silica tetrahedron with 1 non-bridging oxygen atom).

$$\left.\begin{array}{c} f_1 = 0.5 - 0.0625K_{SBN} \\ f_2 = 0.5 + 0.0625K_{SBN} \\ f_3 = 0 \\ f_4 = 0 \\ Q_4 = 1 - \frac{2(R_{SBN} - (0.5 + 0.0625K_{SBN}))}{K_{SBN}} \\ Q_3 = \frac{2(R_{SBN} - (0.5 + 0.0625K_{SBN}))}{K_{SBN}} \\ Q_2 = Q_1 = Q_0 = 0 \end{array}\right\} 0.5 + 0.0625K_{SBN} < R_{SBN} < 0.5 + 0.25K_{SBN} \tag{2.11}$$

Continuing to add Na_2O into the glass results in formation of f_3, f_4, Q_i (where $i < 4$ and the number of NBO atoms is $4 - i$). Literature details estimates concerning these elementary units when $R_{SBN} > 0.5 + 0.25K_{SBN}$. Please read [11, 10, 58, 31, 165, 30, 218] for more details.

Techniques such as X-ray scattering/diffraction [19, 282], nuclear magnetic resonance (NMR, see Section 3.2.1 for a brief review) [61, 173, 262] and Raman scattering (see Section 3.2.2 for a brief review) [14, 82] provide short-range structural information of SBN glass systems. Some of the investigations evidence changes in short-range structure induced by phase separation. For example, Raman spectra reveal some APS structure changes; however they are not significant enough be qualified [83, 266]. To understand these small variations, more investigations are required.

Concerning NMR, Du and Stebbins [62] used NMR techniques to study APS-SBN glasses of chemical composition 61.5SiO_2-30.8B_2O_3-7.7Na_2O (in mol%). One dramatic effect related to the growth of heterogeneities induced by annealing is an increase in the fraction of boroxol rings. This is accompanied by a decrease in the non-ring BO_3 units. However, the BO_4 fraction remains unchanged. In addition to these changes, there is a reduction of Si-O-B connections according to ^{17}O 3QMAS spectra analysis. These results are consistent with an APS structure having Si-rich and B-rich phases. Beyond this, Na^+ ions favor the B-rich phase.

Another study [63] concerns a binary sodium borate glasses 15Na_2O-85B_2O_3 (in mol%). ^{11}B NMR analysis shows that this glass separates into two phases: $Na_2O{\cdot}9B_2O_3$ (B-rich)

phase and $3Na_2O{\cdot}B_2O_3$ (Na-rich) phase at 500 ℃. Crystallization was observed via X-ray diffraction in the annealed samples. Annealing for short durations result in crystallization of the B-rich phase, and the BO_4 fraction in the glass does not vary significantly. For Na-rich phase, when the Na_2O concentration increases to a certain value ($R_{SBN} > 0.5$), BO_3 units will begin to have one or two NBO atoms at the expense of BO_4 units. Annealing for longer times leads to the crystallization of this phase. Thus, there will be crystallization of both phases at equilibrium. These studies show the applicability of NMR technique in studying the structure changes induced by APS.

2.2.2 Morphology of APS in glasses

Ternary systems behave similarly as binary systems: they both undergo binodal and spinodal decompositions. For ternary systems, the complexity of the glass structure is so significant that the rules for binary systems via the chemical composition and annealing temperatures remain unknown. Beyond the micro-scale structure changes, APS glasses present heterogeneities ranging in sizes from 0.1 to 1 μm (medium-range). Probing medium-range ordering relies on TEM, scanning electron microscopy (SEM) and AFM imaging techniques.

2.2.2.1 Binodal decomposition in SBN glasses

As in the case of 2-atom systems (Section 2.1.1), ternary oxide SBN system undergo binodal decomposition. The mechanisms and kinetic of binodal decomposition, i.e. nucleation and growth, has been widely studied [130, 259, 38].

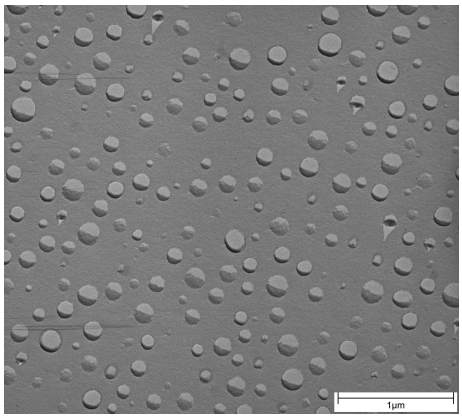

Figure 2.5: TEM replica micrograph of a glass sample thermally treated at 680 ℃ for 5 hours [113].

Binodal decomposition inside the glass reveals itself as a droplet-shaped secondary phase embedded in a matrix. Figure 2.5 shows a TEM micrograph of a SBN glass after binodal decomposition in the investigation of Häßler and Rüssel [113]. They studied a glass with the following chemical composition: $[SiO_2]$ = 60 %, $[B_2O_3]$ = 37 % and $[Na_2O]$ = 3 %, where $[\cdot]$ implies mol%. This chemical composition is found to be within the three-phase area in the ternary oxide phase diagram at 600 ℃; it clearly resides in the 2-phase area. Based on its chemical composition, one expects the structure to be Na-B-rich particles embedded in a Si-rich matrix [227]. Häßler and Rüssel subjected the samples to various annealing protocols:

annealing temperature ranges from 520 ℃ to 680 ℃ and annealing times range from 1 hour to 100 hours. Transmission electron microscopy (TEM) and Scanning electron microscope (SEM) were used to characterize the structure of samples. In their studies, EDX characterization tests show clearly the occurrence of APS in the samples. The secondary phase has a droplet like structure, consistent with the theoretical structure of binodal decomposition. These droplets have a high concentration of boron atoms and a low concentration of silicon atoms. The growth rate of the phase depends strongly on the annealing temperature. At 680 ℃, the growth rate of the droplet diameter L is approximately proportional to $t^{0.25}$, while for 620 ℃, it is close to $t^{0.08}$.

Shepilov *et al.* [238] studies another SBN glass with the following chemical composition: $[SiO_2]$ = 50.1 %, $[B_2O_3]$ = 36.0 % and $[Na_2O]$ = 13.9 %, where $[\cdot]$ implies mol%. The samples were heat-treated at 610 ℃ for 5 and 10 h. These glasses display a binodal structure after annealing. The distribution of the particle radius, and its mean were obtained by electron micrograph analysis. According to Shepilov *et al.* [238], the mean particle radii of this APS-SBN glass are 22.7 nm and 33.8 nm for 5h and 10h of annealing, respectively.

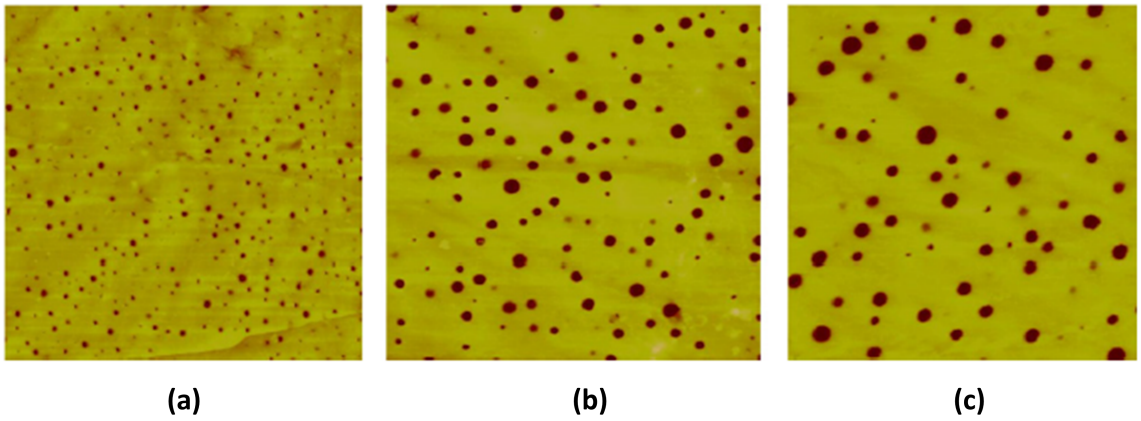

Figure 2.6: AFM images of Corning 7070 glass after heat treatment at 700 ℃ for (a) 1h, (b) 8h, and (c) 24h. All scans are 2×2 μm^2. (Reprinted from [265].)

Apart from the SBN glasses, many other systems concern binodal decomposition. Wheaton and Clare [265] studied a complex commercial material based on borosilicate oxide glass Corning 7070. This glass also has a binodal decomposition with well-formed droplets. Figure 2.6 displays AFM images after annealing at 700 ℃ for 1, 8 and 24 hours, panels a, b, and c respectively. Clearly, the droplets grow during this time period. Wheaton found the average radius of the droplet is proportional to the cubic root of the time for a given isothermal annealing temperature. Another system concerns $PbO-B_2O_3$ glasses, which is widely studied as the typical example of binodal structures concerning mechanical properties (see Section 2.4).

2.2.2.2 Spinodal decomposition in SBN glasses

Spinodal decomposition induces a complex 3-D distributed network in the glass. Researchers used different technical tools to evidence and characterize this structure in SBN glass system

[106, 67, 55, 225].

Haller [106] studied the glass with chemical compositions: [SiO_2] = 60.0%, [B_2O_3] = 30.5% and [Na_2O] = 9.5% (in mol%). Electron micrographs of this glass displays spinodal structure after annealing at 550 ℃, 600 ℃ and 650 ℃, but a binodal structure at 700 ℃. Fan and Chen [75] performed a different investigation on APS-SBN glass of chemical composition $65SiO_2$-$27B_2O_3$-$8Na_2O$ (not indicated as mol% nor wt% in original document). This glass is supposed to be within the three-phase area according to Haller's investigation [106] in Figure 2.4. The glasses annealed at 600 ℃, 620 ℃ and 640 ℃ display spinodal structures via TEM. The size of the interconnecting phases was found to be proportional to the cubic root of the annealing time $t_a^{1/3}$ at 600 ℃. Moreover, the TEM micrographs evidenced the three phases in the samples, and the sequence of phase separation was proposed as: (1) the glasses separate into a Si-rich phase and a Na-B-rich phase (annealing time from 1 h to 8 h at 600 ℃); (2) the Na-B-rich phase separates into B-rich and Na-rich phase (after annealing for 8h at 600 ℃).

In recent years, AFM imaging after chemical etching of surfaces has been widely used for characterizing spinodal structures in APS glasses [55, 265, 119]. In APS-SBN glasses, B-rich phases and alkali-rich phases (if exists) are more susceptible to acid attack [257, 167]. Hence, a controlled acid treatment removes the B-rich and/or alkali-rich phases (if exists) in the near-surface area, and the residual surface roughness reveals the APS morphology [249]. To avoid polishing effects and to capture bulk properties, AFM characterizations concern fracture surfaces.

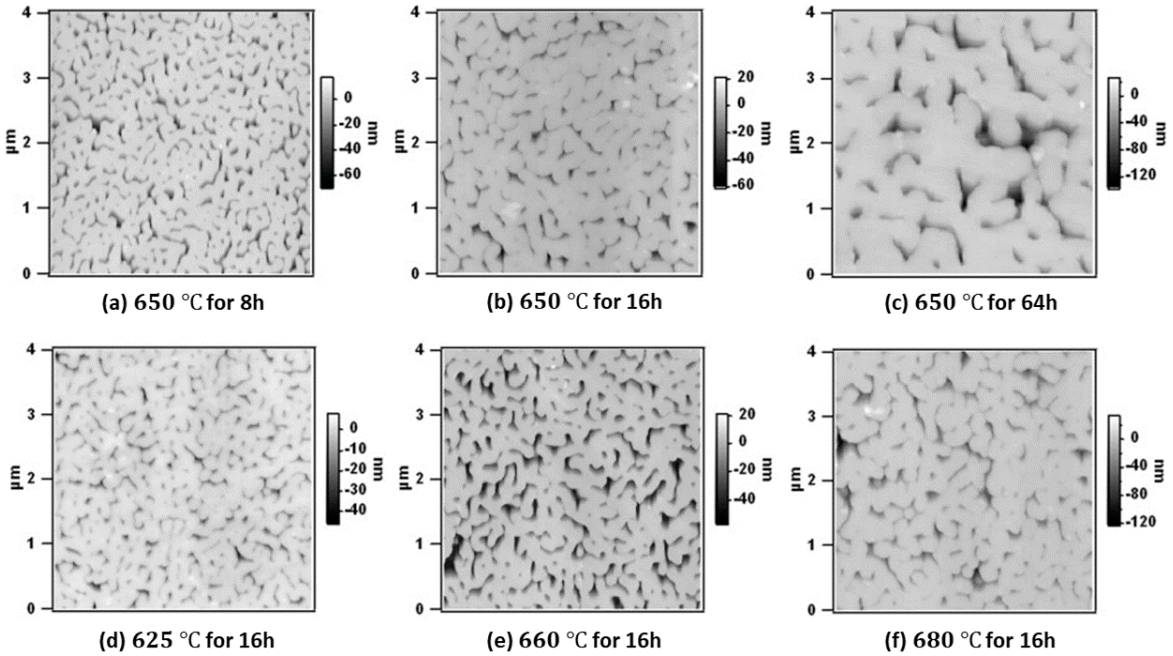

Figure 2.7: AFM height images of borosilicate glass samples (SiO_2 73.2%, B_2O_3 22.6%, Na_2O 2.5%, K_2O 1.7% in mol%) after annealing: for (a) 8 h, (b) 16 h, (c) 64 h at 650 ℃; for 16 h at (d) 625 ℃, (e) 670 ℃, (f) 680 ℃. (Reprinted from [55].)

Dalmas *et al.* [55] investigated a system of chemical composition: [SiO_2] = 73.2%, [B_2O_3]

= 22.6%, [Na_2O] = 2.5% and [K_2O] = 1.6% (in mol%). The glasses were annealed at different temperatures for different times. Then, they were etched via a slight acid solution ($pH \approx 5$) to remove the alkali borate rich phases. Figure 2.7 shows Dalmas *et al.* [55] series of AFM images of the annealed glasses. Clear spinodal structures form during annealing, and the phases grow significantly with increasing annealing time at 650 ℃. Dalmas *et al.* have done quantitative analysis on these images. They used an average auto-correlation function to obtain the characteristic correlation lengths L_{corr} of different glasses. Their investigation shows that the correlation lengths are proportional to $t_a^{1/3}$ when annealing at 650 ℃. This is consistent with the conclusion of Fan [75]. Concerning the effects of annealing temperature, the data shows a reasonable tendency between L_{corr} and annealing temperature T_a compared with Arrhenius diffusion prediction: $\log L_{corr}$ can be fitted linearly to $1/T_a$. From this relation, Dalmas *et al.* [55] was able to obtain a rough estimation of the activation energy for inter-diffusion for the glasses.

Wheaton and Clare [265] have also done a quantitative analysis by AFM on the phase growth in the glass with chemical compositions: [SiO_2] = 82.5%, [Na_2O] = 17.5% (in mol%). Before the analysis, they used 0.5% hydrofluoric acid to etch the samples' fracture surfaces for 1 min, followed by a 30 s rinse in saturated boric acid, a quick rinse in ethyl alcohol and then dried with compressed are. With an AFM, they also found similar conclusions as Fan's investigation [75] for the phase growth during the coarsening stage at 650 ℃: the area of inhomogeneity increases linearly with $t_a^{1/3}$; the interface area between different phases decreases linearly with increasing $t_a^{1/3}$.

In recent years, another non-destructive technique, X-ray micro-tomography [225], was used to capture *in-situ* microstructural changes. The absorption contrast of different chemical compositions reveals the phase separation in samples via 3D visualization schemes. For example, Bouttes *et al.* [25, 27, 26] monitored the coarsening dynamics of barium borosilicate melts (predicted to separate into Si-rich and Ba-rich phases) during phase separation with this method. Image reconstruction provides the evolution of the volumes, mean surfaces, Gaussian curvatures and phase sizes changes as a function of time at various temperatures. Furthermore, this technique can also be used during mechanical tests to monitor the formation of crack systems in some disordered materials [154, 276]. With the availability of third generation synchrotron sources and the development of new detectors, nowadays the spatial resolutions can reach a micrometer range routinely [35]. However, investigations of phase separation in SBN glasses remain outside the scope of X-ray micro-tomography (and other techniques including Raman) as the scale of phase separation is approximately 10 nm.

2.2.2.3 Secondary phase separation

With the aid of an electron microscopy, researchers evidenced and characterized highly disperse structures co-existing within the main phase(s) in phase separated systems, including fluid mixtures [250], alloys [110] and glasses [25, 234, 233, 265]. It is hypothesized that this arises due to natural fluctuations [79] or a special type of phase separation, coined micro-separation [84]. Combining the observations from several studies, Shaw [234] ($PbO-B_2O_3$ glass system) and Porai-Koshits *et al.* [203] (SiO_2-Na_2O glass systems) link this phenomenon to an asymmetric miscibility gap, leading to the over-saturation of one component at lower

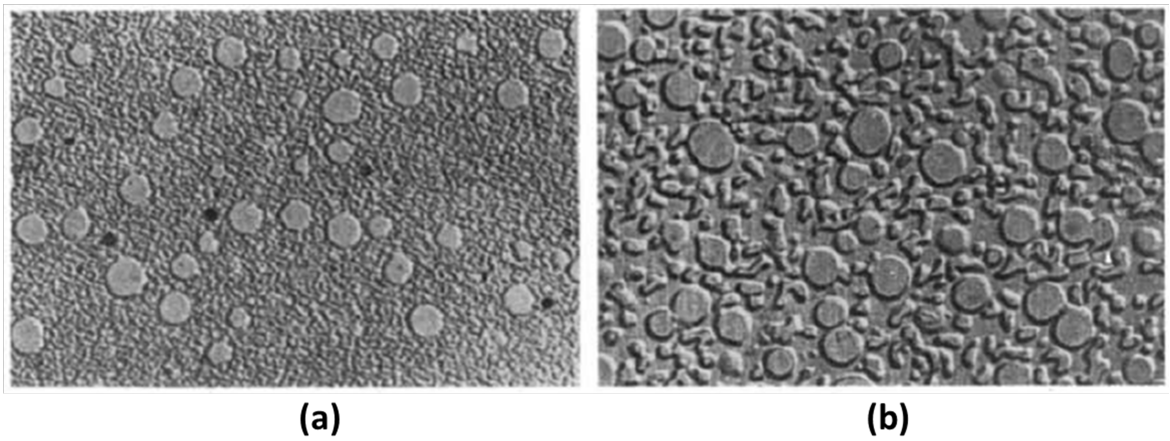

Figure 2.8: The secondary separation of SiO_2–Na_2O glass with 12.5 mole% Na_2O. The samples were annealed for 2 hours at 777 ℃ (a) and subsequently reheated at 668 ℃ for 2 hours (b). ×18900. [203].

temperature in one of the phases after the primary phase separation, thus, calling it *secondary phase separation*.

Secondary phase separation may occur in a glass that has already undergone phase separation once and the sample is reheated. The second annealing produces permits one of the phases to undergo another separation [203]. Figure 2.8 [203] shows an example of sodium silicate glasses with 12.5 mol% Na_2O. After annealing at 777 ℃ for 2 hours, binodal phase separation occurred in the sample, with the matrix phase enriched in sodium (Figure 2.8 (a)). Then the sample was heat treated at 668 ℃ for 2 hours. At this temperature, silica is over-saturated in the alkali-rich phase, resulting in a secondary phase separation in the matrix (Figure 2.8 (b)). Lead borate glasses have also been investigated, and phases rich in boron have a higher tendency to be produced due to a secondary phase separation according to the shape of immiscibility gap [234].

Generally, APS glasses may possess a large variety of structures depending on the initial chemical compositions and annealing protocols. These structures alter material properties, some of which will be discussed in the following sections.

2.3 Physical properties

The inherent structure of the glass and its amorphous phase separated counterpart could play a role in altering physical and mechanical glass properties. In this section, I take a closer look at how the APS structure of the glasses plays on the physical properties where the next section concentrates on the mechanical properties.

For homogeneous SBN glasses, first order mixing laws can be used to estimate the physical properties of SBN glasses [11, 128, 76, 33]. These mixing laws commence with an estimate of the number of basic structural units (see Section 2.2.1) in the SBN system. Then the physical properties can be calculated by accumulating those values depending on the chemical composition of the glass. From these structural units, Inoue *et al.* [128] developed a

series of equations to estimate multiple physical properties: molar volume, refractive index, mean dispersion, coefficient of thermal expansion, and glass transition temperature of SBN glasses. These equations provide an estimate of the physical properties to within 10% of the experimental data [11, 128]. This includes estimates in the immiscibility zones; yet, they ignore the possibly of spatial structure heterogeneities in the material.

APS produces a large variety of structures in glasses. This affects physical properties, such as the density, the moduli, *etc.* Burnett and Douglas' [36] investigations found that phase separation consists of two distinctive stages: (i) the decomposition stage when the developing phases gradually reaches the equilibrium composition; and (ii) the coarsening stage when the size of the phase separation regions increases without considerable changes in phase composition. At the end of the first stage, the dimension of phase-separated regions are usually significant enough to neglect the interfacial effects between different phases [175]. In this case, a two-phase glass can be considered as a composite material consisting of two different homogeneous substances, *i.e.* the *tie-line end-members*.

2.3.1 Density

Firstly, we take a closer look at how APS affects the glass density, and how it can be predicted using a model by knowing the parameters of end members. Returning to the ideal A-B binary system, researchers [175, 236, 237] use numerical models to estimate the properties of two-phase materials. Now, let us consider the zone of phase separation between P_1 and P_4 ($T_2 < T_C$ in Figure 2.1) where the glass separates into phase α and phase β. Recalling phase α corresponds to the phase at P_1 in Figure 2.1, and phase β corresponds to the phase at P_4. According to the conservation of mass, the total mass (m_T) of the system shall be the sum of two phases or equivalently the components (for all the parameters used herein, superscripts α or β relate to the phases; subscripts A or B relate to the components):

$$m = m^{\alpha} + m^{\beta} = m_A + m_B \tag{2.12}$$

where m^{α} and m^{β} are the masses of phases α and β, m_A and m_B are the masses of component A and B, respectively. Knowing the density (ρ) of the system (i.e. mass divided by volume), one can substitute this into equation 2.12 to get

$$\rho V = \rho^{\alpha} V^{\alpha} + \rho^{\beta} V^{\beta} \Longrightarrow \rho = \frac{1}{V}(\rho^{\alpha} V^{\alpha} + \rho^{\beta} V^{\beta}) \tag{2.13}$$

where ρ^{α} and ρ^{β} are the densities of phases α and β, V^{α} and V^{β} are the volumes of phases α and β, respectively. If one assumes that mixing α and β conserves the system volume, then the volume (V) is just the sum of the volume of each phase:

$$V = V^{\alpha} + V^{\beta} \tag{2.14}$$

Combining equations 2.13 and 2.14 gives:

$$\rho = \rho^{\alpha} + \frac{V^{\beta}}{V}(\rho^{\beta} - \rho^{\alpha}) \tag{2.15}$$

Equations (2.12)-(2.15) assume uniform mixing. The lever rule permits a calculation of the mass fraction of each phase, w_B^α for phase α and w_B^β for phase β, with respect to the mass fraction of component B, w_B.

$$w^\alpha = \frac{w_B - w_B^\beta}{w_B^\alpha - w_B^\beta} = \frac{m^\alpha}{m} \qquad (2.16)$$

$$w^\beta = \frac{w_B - w_B^\alpha}{w_B^\beta - w_B^\alpha} = \frac{m^\beta}{m}$$

The lever law permits one to extrapolate the volumetric fraction $V^\beta V$ in equation (2.15).

$$\frac{V^\beta}{V} = \frac{\rho^\alpha (w_B - w_B^\alpha)}{(w_B - w_B^\alpha)(\rho^\alpha - \rho^\beta) + (w_B^\beta - w_B^\alpha)\rho^\beta} \qquad (2.17)$$

Likewise, the lever law permits one to access the density [236]:

$$\rho = \frac{\rho^\alpha \rho^\beta}{\left[(w_B - w_B^\alpha)/(w_B^\beta - w_B^\alpha)\right](\rho^\alpha - \rho^\beta) + \rho^\beta} \qquad (2.18)$$

The first and secondary derivatives of equation (2.18) with respect to w_B are [236]

$$\frac{\partial \rho}{\partial w_B} = \frac{-\rho^\alpha \rho^\beta (\rho^\alpha - \rho^\beta)/(w_B^\beta - w_B^\alpha)}{\left\{\left[(w_B - w_B^\alpha)/(w_B^\beta - w_B^\alpha)\right](\rho^\alpha - \rho^\beta) + \rho^\beta\right\}^2} \qquad (2.19)$$

$$\frac{\partial^2 \rho}{\partial {w_B}^2} = \frac{2\rho^\alpha \rho^\beta \left[(\rho^\alpha - \rho^\beta)/(w_B^\beta - w_B^\alpha)\right]^2}{\left\{\left[(w_B - w_B^\alpha)/(w_B^\beta - w_B^\alpha)\right](\rho^\alpha - \rho^\beta) + \rho^\beta\right\}^3} \qquad (2.20)$$

From the above equations, the sign of first derivative does not change with w_B, and it depends on the quantitative comparison between ρ^α and ρ^β. Additionally, the second derivative is always positive. This shows that the curve of ρ as a function of one component's initial weight fraction is convex.

A binary oxide glass system can be analyzed in a similarly fashion as the above model. Shaw *et al.* [234, 236] compared and contrasted experimental and theoretical results concerning the density of $PbO–B_2O_3$ glass systems. The zone of phase separation is estimated to extend from 0.31 mol% PbO (1 PbO wt%) to 19.68 mol% PbO (44 PbO wt%). In this case, the phase parameters in the above equations correspond to these two chemical composition for this system. Figure 2.9 (a) presents Shaw's experimental data [236] (blue triangles) in comparison with the theoretical estimates (solid orange line) from equation (2.18), which concern how the density varies with respect to the weight fraction of PbO (w_B). Likewise, Figure 2.9 (b) presents Shaw's experimental data [234] (blue triangles) in comparison with the theoretical estimates (solid orange line) from equation (2.15) for how the density varies with respect to the volume fraction of the Pb-rich phase (V^β/V).

Figure 2.9 (a) shows the experimental density data compares favorably with estimations (equation 2.18) as a function of the PbO weight fraction. However, understanding how

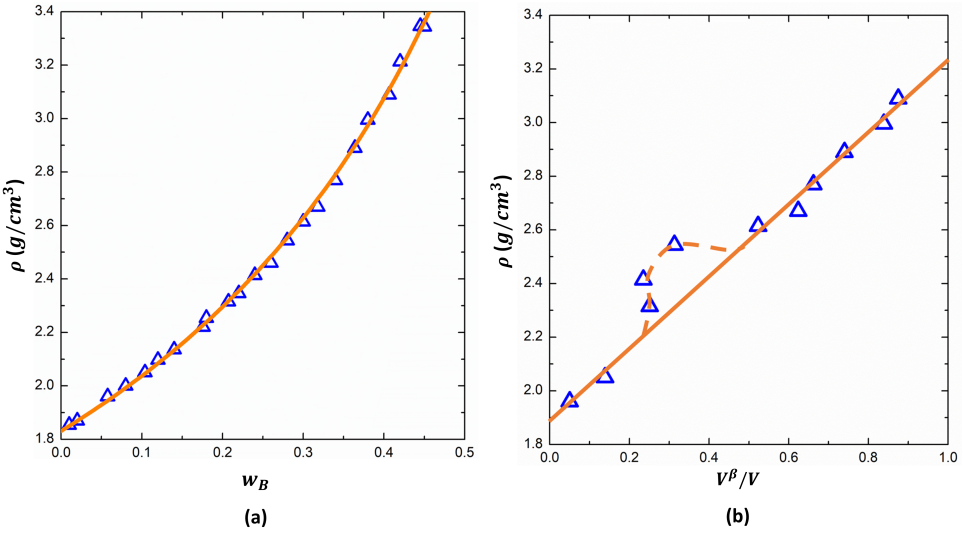

Figure 2.9: Variation of density with (a) weight fraction of PbO w_B and (b) volume fraction of PbO rich phase V^β/V in PbO–B_2O_3 glass system. Data points in blue triangle and fitting lines in orange. Recreated from [234] and [236].

the density varies with respect to the volume fraction of the PbO rich phase requires some additional insight. Figure 2.9 (b) shows that the density of different PbO–B_2O_3 phase separated glasses as a function of the Pb-rich phase volume fraction (V^β/V). Apart from a distinct region, the experimental results display a clear linear relation, which is consistent with the theoretical analysis equation (2.15). The region where the linear relation is not valid corresponds to secondary phase separation. According to Shaw [234], the corresponding PbO weight fractions lie close to the critical point (PbO fraction corresponding to T_C in Figure 2.1 (a)). Hence, they have a higher tendency to undergo secondary phase separation. In this case, secondary Pb-rich phases occur in the B-rich phase, which are too small to be measured. This leads to an underestimation of Pb-rich phase volume fraction and the deviation between experimental data points and theoretical analysis.

The comparison between experiments and theory shows the wide usability of equations (2.15) and (2.18). This analysis is also valid for ternary and higher-order systems in a two-phase region. In these regions, the above equations are valid if one follows the tie-lines at constant temperature [237].

2.3.2 Elastic modulus

Considering the two-phase system, some theories have been proposed for the variation of elastic moduli [237]. Researchers encountered difficulties in obtaining the exact expressions while considering the mutual interaction of many secondary phase inclusions. In this case, models predict the upper (E^U) and the lower (E^L) bounds of moduli values in regards to end-member phase parameters. The Voigt model assumes constant strain for the entire system and provides an upper bounds [237] for the Young's modulus E^U_{Voigt}. The Voigt estimation of Young's modulus is formulated as follows

$$E^U_{Voigt} = \left(1 - \frac{V^\beta}{V}\right) E^\alpha + \frac{V^\beta}{V} E^\beta \tag{2.21}$$

where E^α and E^β are the Young's moduli of different phases, V^β/V can be expressed by equation (2.17).

On the other hand, the Reuss model assumes a constant stress for the entire system and provides a lower bounds for the Young's modulus E^L_{Reuss} [237]. The Reuss' estimation of the Young's modulus is formulated as follows

$$E^L_{Reuss} = \frac{1}{\frac{1-V^\beta/V}{E^\alpha} + \frac{V^\beta/V}{E^\beta}} \tag{2.22}$$

By using the principle of minimum potential energy and minimum complementary energy, Hashin and Shtrikman [112] proposed an alternative model (coined HS model herein). The predictive ranges of the bulk (K) and shear (G) moduli concern the case when $K^\beta > K^\alpha$ and $G^\beta > G^\alpha$. The upper (K^U_{HS}, G^U_{HS}) and lower (K^L_{HS}, G^L_{HS}) bounds for the bulk and shear moduli are calculated as follows:

$$K^U_{HS} = K^\beta + \frac{1 - V^\beta/V}{\frac{1}{K^\alpha - K^\beta} + \frac{3V^\beta/V}{3K^\beta + 4G^\beta}} \tag{2.23}$$

$$G^U_{HS} = G^\beta + \frac{1 - V^\beta/V}{\frac{1}{G^\alpha - G^\beta} + \frac{6(K^\beta + 2G^\beta)V^\beta/V}{5G^\beta(3K^\beta + 4G^\beta)}} \tag{2.24}$$

$$K^L_{HS} = K^\alpha + \frac{V^\beta/V}{\frac{1}{K^\beta - K^\alpha} + \frac{3(1-V^\beta/V)}{3K^\alpha + 4G^\alpha}} \tag{2.25}$$

$$G^L_{HS} = G^\alpha + \frac{V^\beta/V}{\frac{1}{G^\beta - G^\alpha} + \frac{6(K^\alpha + 2G^\alpha)(1-V^\beta/V)}{5G^\alpha(3K^\alpha + 4G^\alpha)}} \tag{2.26}$$

where K^α and K^β are bulk moduli of the different phases, G^α and G^β are shear moduli of the different phases, V^β/V can be expressed by equation 2.17. Invoking these equations and the standard equation to calculate the Young's modulus from K and G by $E = 9KG/(3K + G)$, one obtains the Hashin and Shtrikman [112] bounds E^U_{HS} and E^L_{HS} for the Young's modulus.

Considering boron based glasses, a noteworthy series of experiments [237, 193, 182, 183, 184] compare and contrast mechanical properties of PbO–B_2O_3 glass systems. Mechanical properties studied in the series of papers include the variation of Young's modulus (E), fracture toughness (K_C) and fracture surface energy (Γ) with glass chemical composition. Recalling PbO–B_2O_3 glass systems undergo a binodal decomposition structure, the zone of phase separation is estimated to extend from 0.31 mol% PbO (1 PbO wt%) to 19.68 mol% PbO (44 PbO wt%). Miyata and Jinno [183] estimated these *tie-line end-members* mechanical properties. With the density and moduli of the *tie-line end-members*, the ranges of E for PbO–B_2O_3 glass systems are estimated with equations (2.21)-(2.26) and shown in Figure 2.10 for the APS zone. Figure 2.10 also shows experimental data points for APS [237, 182, 183] and non-APS zone [193]. Generally, the experimental results are reasonably

consistent with the predictive models. All the data points are within the Voigt-Reuss range. More precisely, the results are slightly lower than the lower bound of the HS model and higher than Reuss bound. These two bounds constitute the predictive range of Young's modulus for $PbO-B_2O_3$ glass system in the APS zone.

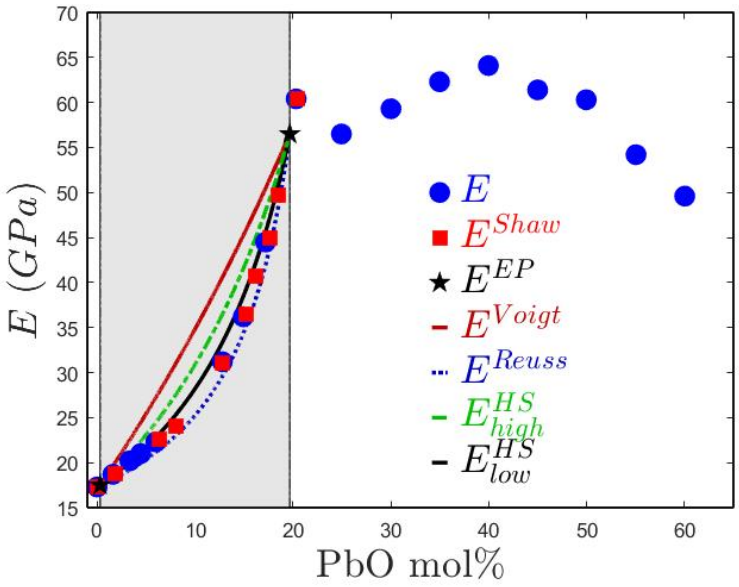

Figure 2.10: Plot of Young's moduli of $PbO-B_2O_3$ glasses as a function of the PbO mol%. Experimental data of Young's moduli of $PbO-B_2O_3$ glasses with mole fraction composition are presented in blue points from [193, 183], red squares from [237], black stars for end-members from [183]). Predictive ranges of different models within the APS zone (gray section): solid red line for Voigt upper bound, blue dotted line for Reuss lower bound, green dashed line for HS upper bound and black solid line for HS lower bound [237].

2.4 Fracture properties of APS glasses

In terms of material fracture, any cracking state can be reduced to a combination of three independent modes – opening mode (Mode I), sliding mode (Mode II) and tearing mode (Mode III) [4]. In this project, I am interested in Mode I cracking. At the continuum level, Linear Fracture Mechanics (LEFM) is commonly used to predict the failure properties of materials. Figure 2.11 (a) depicts a simple model of a crack in an infinitely large material. In this ideal system, the stress is applied at infinity. LEFM [219, 4] predicts the stress to concentrate around the crack front, in polar coordinates, as:

$$\sigma_{i,j}(r,\theta) \cong \frac{K_I}{\sqrt{2\pi r}} f_{i,j}(\theta) \tag{2.27}$$

where r is the distance from the crack front to the point of interest, θ is the angle between the direction of propagation and the point of interest, K_I is the stress intensity factor, $f_{i,j}$ is a parameter that depends on the loading conditions.

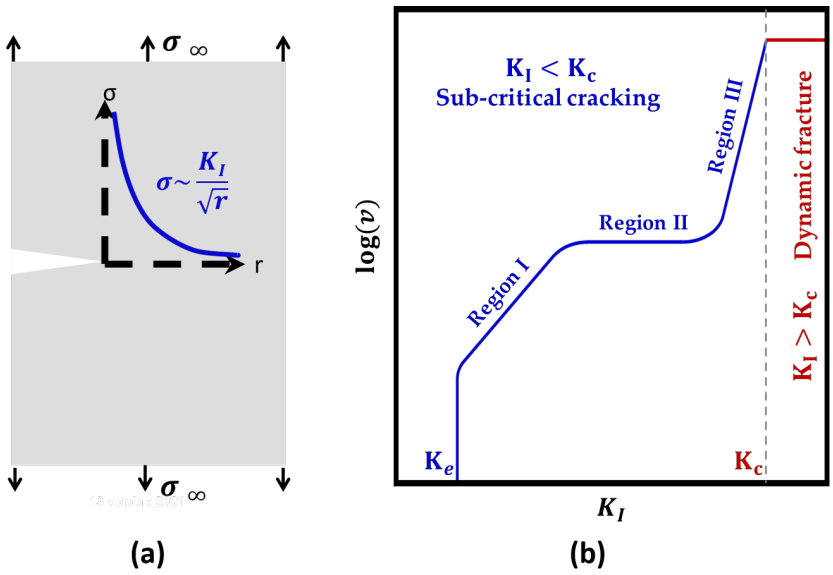

Figure 2.11: (a) Sketch of opening mode (Mode I) cracking; (b)Schematic of the log of the velocity ($log(v)$) as a function of the stress intensity factor (K_I) depicting the three regions of sub-critical cracking ($K_I < K_C$).

Equation (2.27) indicates a singularity at the crack tip, which implies that the area close to the crack tip is not linear elastic. The area where the LEFM is not applicable is called the fracture process zone. This process zone aids in shielding the crack front and its vicinity (the enclave) from the global stress intensity factor [158].

In the early 2000's, Atomic Force Microscopy (AFM) experiments tracked in-situ the crack front on the free surface of a glass samples. The investigations [99, 21, 170, 41, 22] indicated that the crack tip does not propagate regularly, but through the nucleation, growth and coalescence of damage areas ahead of the crack front. These initial AFM studies assumed an ideal Hookean material. As such, the height of the free surface, u_z, should be proportional to $r^{-0.5}$, and the departure from the $r^{-0.5}$ tendency was equated to the size of the fracture process zone [99, 21, 170, 41, 22, 220]. This overestimated the size of the process zone, yet it stirred a number of subsequent research initiatives ([111, 101, 103, 102, 100, 272, 273, 160, 161, 196, 216, 220], see [219] for a recent review). For example, Han *et al.* [111] pointed out that the hypothesized 2-D plane stress during the initial AFM studies was not relevant considering the displacement scale. Used Integrated Digital Image Correlation (IDIC) techniques, they captured both the in-plane and out-of-plane displacements [111, 215]. From these studies, they found the process zone to be less than 10 nm for a crack propagating at 7×10^{-10} m/s. Now days, the process zone of pure silica is commonly accepted to be larger than the atomic bond length (Si-O bond length $\sim$ 1.6 Å) and on the order of 100 Å(10 nm) [219].

Beyond the process zone, LEFM is reliable for stress concentration analysis, and K_I can be calculated. K_I depends on the loading applied on the system and sample geometry (including the shape and size of defects and of sample). In a vacuum, a material should not fail unless the stress intensity factor is greater that the fracture toughness (K_C) of the

material, which is considered a material parameter [239]. Needless to say in real materials, cracks propagate for $K_I < K_C$. In this instance, crack propagation is sub-critical and aided by environmental factors [240, 210]. Figure 2.11 shows a sketch of the logarithm of the crack tip velocity ($log(v)$) as a function of the stress intensity factor (K_I). There are commonly 3 zones associated with stress corrosion cracking [49]. For stress intensity factors slightly less than K_C, the velocity falls in what is commonly called Region III of the stress corrosion cracking curve. In this region, the velocity of the crack front increases exponentially with an increasing stress intensity factor:

$$v^{III} = v_0^{III} \exp(Z^{III} K_I) \tag{2.28}$$

where v_0^{III} and Z^{III} are empirical constants fitted to data [268, 271]. Researchers agree the dynamics in this section are independent of water concentration [268, 271] but other environmental conditions (temperature [270], nitrogen gas, methyl alcohol [271], etc.) do play a role in the fracture dynamics in Region III [268, 271, 49]. Decreasing the stress intensity factor further causes the crack velocity to stabilize and reach a plateau where it is independent of K_I. This zone is frequently referred to as Region II. The height of the $log(v)$ plateau depends on the amount of water in the environment, increasing the humidity shifts the plateau upwards [268]. Hence, Region II depends on the time the water takes to reach the crack front [268, 271, 49, 269]. Further decreasing the stress intensity factor causes the velocity to reach Region I. In this region, the velocity of the crack front decreases with decreasing stress intensity factor. Two different models were proposed for linking v^I and K_I, including Wiederhorn's exponential rule [268, 49]:

$$v^I = Z_1 \left(\frac{p_{H_2O}}{p_0}\right)^{Z_2} \exp(-\frac{\Delta E_a - Z_2 K_I}{RT}) = v_0^I \exp(Z^I K_I) \tag{2.29}$$

and Maugis' power rule [174, 105]:

$$v^I = v_0^{I'} (K_I/K_0)^n \tag{2.30}$$

where p_{H_2O} is the partial pressure of vapor phase in the environment, p_0 is the total atmospheric pressure, R is the gas constant, T the temperature, ΔE_a is related to the activation energy, and n is called the fatigue parameter [105]. Z_1, Z_2, Z_3, v_0^I, Z^I, ΔE_a, $v_0^{I'}$, n and K_0 are fitting parameters that depend on the glasses' composition. The significant difference between Region I and Region III: Region I depends strongly on the amount of water in the surrounding environment and temperature as shown in the above equation [268, 49]. Increasing the humidity at constant temperature in this region causes the $log(v)$ versus K_I curve to shift upwards maintaining a constant slope. The propagation of the crack front in Region I is controlled by the time for water to chemically react with the stretched bonds at the crack tip. Reducing the stress intensity factor further renders an environmental limit (K_E) below which the crack front does not propagate anymore, and it is also called Region 0.

To sum up, the position of K_E and Region I, II, III and the slope of Region I and III depend on parameters such as environmental factors and glass type. However, what

is less understood is how phase separation alters the mechanical behaviors of the glasses. This section reviews current literature concerning the effects of phase separation on dynamic fracture ($K_I > K_C$) as well as sub-critical cracking ($K_I < K_C$).

2.4.1 Dynamic fracture in multi-phase microstructure

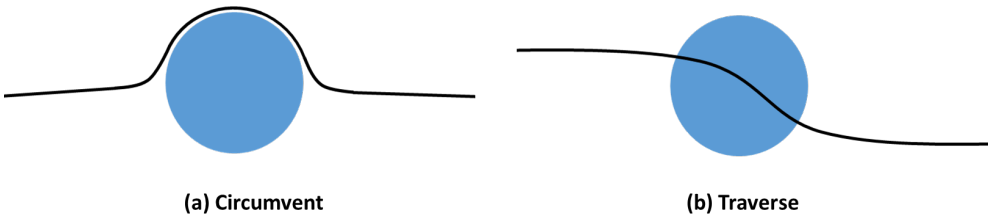

Figure 2.12: Schematic of possible crack paths when a crack (advancing from left to right) interacts with a second-phase particle: (a) crack front circumvents the particle or (b) crack front traverses the particle.

As mentioned above, fracture can be divided into two types: dynamic cracking and sub-critical cracking. This section focuses on dynamic fracture, when the crack propagation is too fast for environment factors to interact with the crack tip. In this case, theory suggests that secondary phase dispersion in brittle materials can influence the crack path, leading to variations in the fracture strength [241, 156].

The presence of a secondary phase can yield toughening via different mechanisms, which can be separated into two main classes [70]. First, crack wake processes occur in the wake of a propagating crack front and reduce crack front driving forces. A common crack wake process is crack bridging [8, 34], which occurs when a secondary crack nucleates ahead of a tough inclusion. This gives way to unbroken material ahead of the crack front [22]. Thus, stress will concentrate not only right ahead of the crack front but also around these damage areas. Hence, the applied stress intensity factor at the crack front decreases. Secondly, crack propagation processes also influence the crack tip dynamics. In this case, toughening comes from direct interactions of the crack front with the secondary phase inclusions. Several studies tried to establish the crack path motion by considering the crack front as an elastic line interacting with obstacles in the system, including crack pinning [156, 89], crack trapping [86, 29, 188] and crack deflection [72, 73]. Extension to these mechanism concerns avalanches of the crack front [157, 169]. Figure 2.12 provides an oversimplified schematic of the interaction between the second phase and the crack. When an obstacle (the secondary phase herein) occurs ahead of the crack front, the crack front can circumvent the obstacle (Figure 2.12 (a)) or traverse it (Figure 2.12 (b)). The circumstances under which either occurs depend on multiple factors.

The first factor, which should be considered in predicting the crack path, is the fracture surface energy (Γ) for both the matrix (Γ_m) and for the particles (Γ_p). The fracture surface energy concerns the energy needed to create the fracture surface. A smaller fracture surface energy implies that it is easier to break the material. Like the fracture toughness (K_C), fracture surface energy defines a material's resistance to fracture. Moreover, these two material

constants are related: $\Gamma = {K_c}^2/E$ where E refers to the Young's modulus. Considering the case where $\Gamma_p > \Gamma_m$, the particle pins the crack front. Thus, this leads to an overall increase of the fracture surface energy [156, 69, 183]. Likewise, soft particles can also lead to higher fracture surface energies due to crack blunting [183, 3, 95, 96].

Now take into consideration residual stress fields. The formation of APS glasses potentially leads to residual stresses, which depend on the local chemical composition. Due to phase separation (i.e. variations in the meso-scale chemical composition), the thermal expansion is potentially non-homogeneous throughout the glass. Consider first the simple case of one precipitate (often considered a particle or inclusion in fracture mechanics) in an otherwise homogeneous matrix/system, where the coefficient of thermal expansion for the matrix and the particle, α_m and α_p respectively, are different. As the system begins to cool, the difference in the coefficients of thermal expansion of the two phases leads to the formation of residual stresses around the particle.

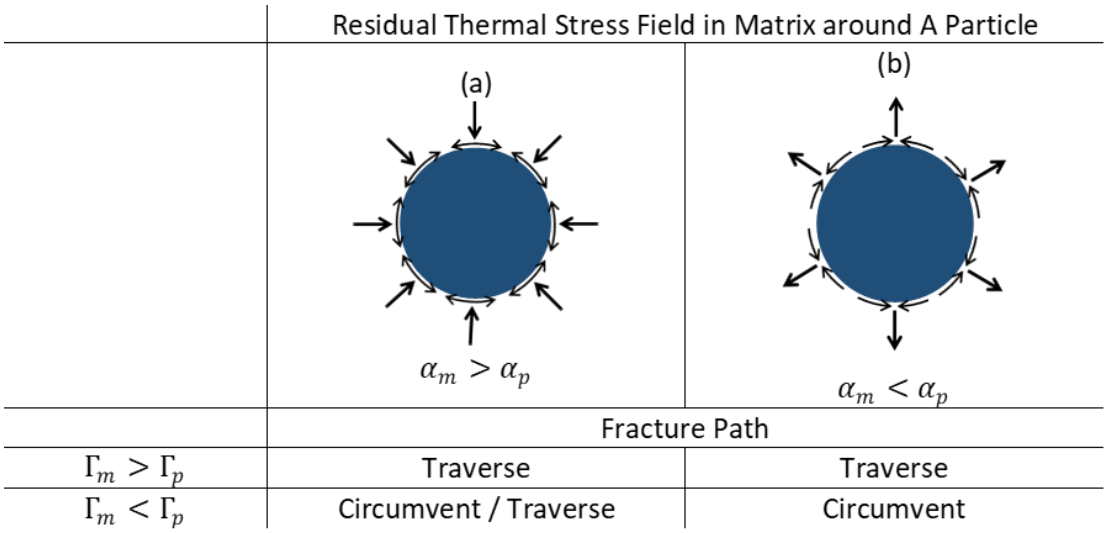

Figure 2.13: Schematic of residual stresses around a single particle embedded in a matrix, which arise due to thermal expansion mismatches during cooling. In the schematic, coefficient of thermal expansion for the matrix and the particle are α_m and α_p, respectively, a non-equivalent. Panel a depicts the scenario when $\alpha_m > \alpha_p$, and Panel b depicts the scenario when $\alpha_m < \alpha_p$ (recreated from [183]).

Selsing [231] provides theories concerning the development of stress during cooling based on differences in the coefficient of thermal expansion. Figure 2.13 depicts the orientation of the stress fields around a particle, along with the crack path, and how the crack path depends on the coefficient of thermal expansion and the fracture surface energy. When the coefficient of thermal expansion for the matrix α_m is greater than that of the particles α_p ($\alpha_m > \alpha_p$), the matrix has a tendency to shrink more than the particle during cooling. This in turn puts the particle under compressive stresses. Meanwhile, the matrix is under radial compressive and tangential tensile stress [183, 231]. On the other hand, when $\alpha_m < \alpha_p$, the matrix has a tendency to shrink less than the particle during cooling. This shrinkage will

put the particle under tensile stresses. However, the matrix will be under radial tensile and tangential compressive stress [183, 231]. These differences in thermal stresses can lead to micro-damage.

Comparing and contrasting residual stress occurring due to the thermal expansion differences with the fracture surface energy provides researchers with an idea as to whether a crack front will cut a particle in two or avoid it. Figure 2.13 recalls Miyata's [183] works. In general, radial damage around or inside the particles will facilitate crack propagation and the crack tends to traverse the particles [183]. Hemispherical damage in the matrix around the particles will repel the approaching crack front [183]. For $\Gamma_m > \Gamma_p$, independent of the residual stresses (i.e. $\alpha_m > \alpha_p$ or $\alpha_m < \alpha_p$) , the crack front will have a tendency to traverse the particle. For $\Gamma_m < \Gamma_p$ and $\alpha_m < \alpha_p$, the crack front will have a tendency to bypass the particle. However, for $\Gamma_m < \Gamma_p$ and $\alpha_m > \alpha_p$, the crack front path is uncertain; it can either circumvent or traverse the particle. Hence, the residual thermal stresses play an important role in predicting the crack path as shown in Figure 2.13.

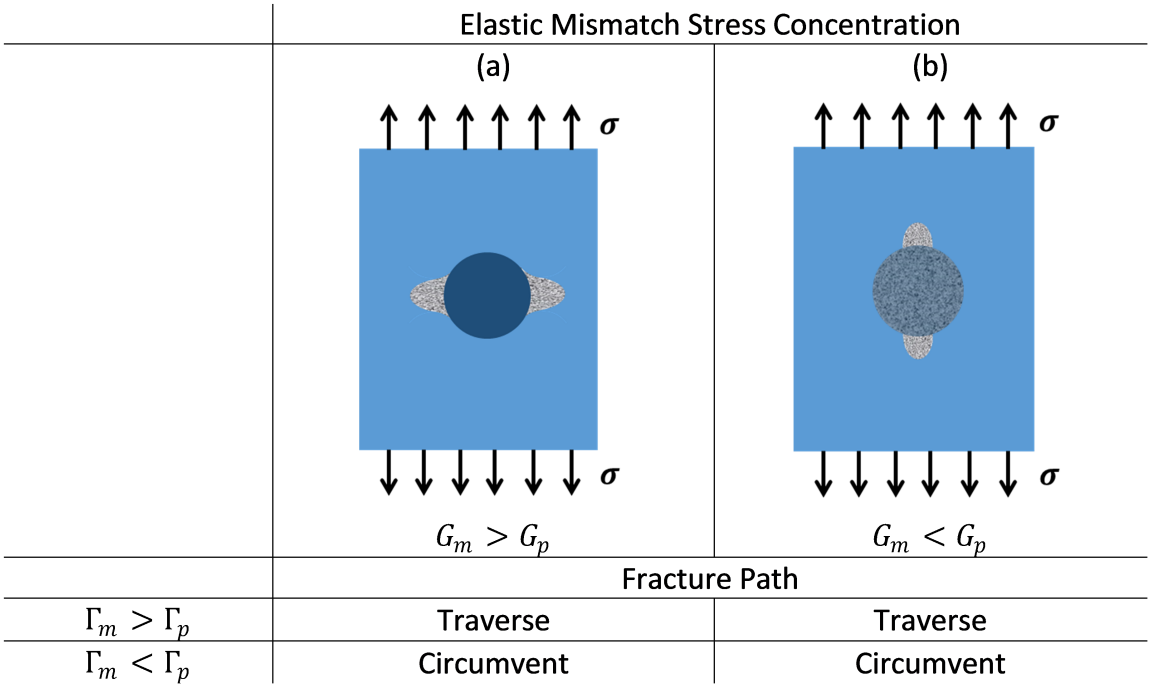

Figure 2.14: Schematic of stress concentration around a single particle embedded in a matrix, which arise due to elastic mismatches. In the schematic, shear moduli for the matrix and the particle are G_m and G_p, respectively, a non-equivalent. Column a depicts the scenario when $G_m > G_p$, and Column b depicts the scenario when $G_m < G_p$ [183].

Putting these theories together, Miyata *et al.* [183] studied Pb-rich particles in a B-rich matrix (i.e. $\alpha_m > \alpha_p$). Recall, the fracture surface energy is lower in the particles than the matrix ($\Gamma_m > \Gamma_p$). Also, there is an elastic mismatch between the particles and the matrix: the Young's modulus is greater in the particle ($E_m < E_p$). With all the theoretical analysis above, Miyata *et al.* [183] propose that the crack passes through the particles in this system. It should be noticed that this scenario is in stark contrast with sub-critical cracking, which

will be addressed in Section 2.4.3.1: The particles inhibit crack growth thus pin the crack front during slow crack propagation [185].

Likewise, Miyata *et al.* [183] studied B-rich particles in a Pb-rich matrix (i.e. $\alpha_m < \alpha_p$, $\Gamma_m < \Gamma_p$ and $E_m > E_p$). With all the theoretical analysis above, Miyata *et al.* [183] propose that the crack passes around the particles in this system.

To predict the fracture path for a real binodal phase separated glass system, many factors come into play, only a few of which have been detailed here. Other factors include phase morphology [145, 229], interfacial interaction between the different phases [209, 155], *etc.*

2.4.2 Effects on fracture toughness

As stated above, APS in glasses alters crack propagation at the micro-scale and meso-scale. Hence, structural variations should influence macroscopic fracture properties [181]. It has been widely considered that the presence of phase separation systematically increases the fracture toughness of the glass [182, 229]. Several toughening mechanisms have been proposed to explain how heterogeneous inclusions affect the fracture behavior as mentioned in Section 2.4.1 (crack pinning, deflection, trapping, etc.).

In addition, the toughening mechanisms due to the secondary phase have been studied using Finite Elements methods. In these simulations, Tang *et al.* [251] modeled the crack behavior in an APS glass containing some spherical nano-inclusions. In most cases, phase separation leads to an increase in the fracture energy of the glass. It also contributes to crack deflection, the effective cohesion of the phase-separated glass, the existence of plastic energy dissipation, and the roughness of the fracture surfaces.

Experimentally, fracture toughness investigations frequently rely on 3-points or 4-points bending tests or indentation tests. Indentation tests reveal a wealth of information concerning not only the hardness but also other interesting mechanical parameters, such as fracture toughness, cracking patterns, cracking probability, plastic deformation, irreversible deformation, etc. [13, 154, 141, 200].

Cheng *et al.* [48] distinguished two different phase separation effects on crack behavior using a TEM to analyze cracking patterns after indentation. For borosilicate glasses with a B-rich secondary phase, the medial/radial crack lengths are short since the precipitates limit the crack propagation. On the other hand, for soda-lime-silica glass consisting of a spinodal structure where one phase was relatively weaker, cracks forming at the corners of the indent propagate outside the area of observation. Hence long radial/medium cracks form.

Beyond cracking patterns, indentation investigations highlight the effects of phase separation on fracture toughness of SBN glasses. Both Haller *et al.* [106] and Seal *et al.* [229] studied annealed glasses (annealing temperature and duration shown in Figure 2.15) with the following chemical composition: [SiO_2] = 60%, [B_2O_3] = 30% and [Na_2O] = 10%. According to Seal's investigation [229], the interconnectivity between different phases in the glasses, which was obtained by TEM images, accounts for at least some of the changes in the fracture toughness. Samples annealed at 600 ℃ for 64h present the highest indentation fracture toughness (K_C^{ind}). Seal conjectured that phase separation interfaces (which are highly interconnected formed by annealing) restrains crack propagation. This in turn leads to an increase in K_C^{ind}. At higher temperatures, the APS structure becomes spherical [106].

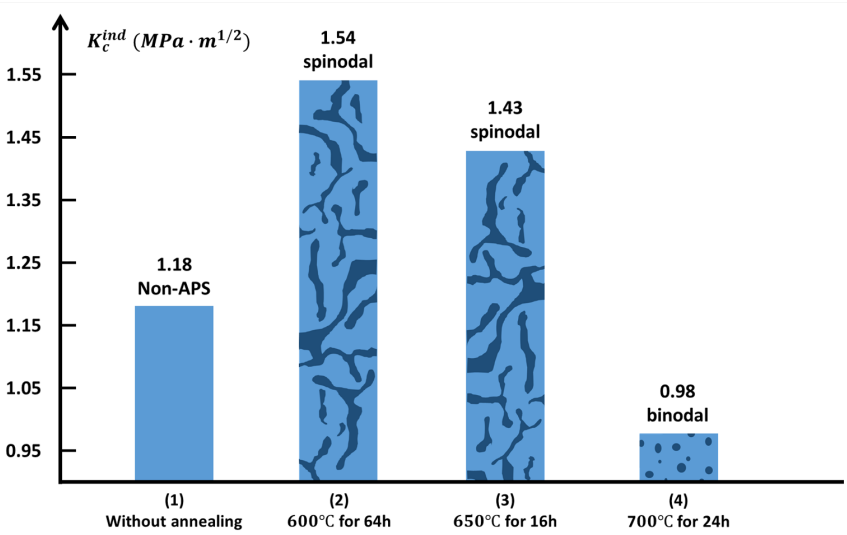

Figure 2.15: Comparison of indentation fracture toughness K_C^{ind} values for the same glass composition annealed at different temperatures for different durations: (1) Without annealing; (2) 600 ℃ for 64h; (3) 650℃ for 16h; (4) 700℃ for 24h (Data from [229]).

This transformation results in the reduction of the energy barrier for stopping the crack propagation. Thus, K_C^{ind} decreases. Seal [229] concluded that phase separation with high interconnect potentially increases the fracture toughness.

As seen above, indentation tests do provide a measure for K_C^{ind}. Moreover, indenters are commonly available in many labs and are applicable to many types of samples; thus, researchers frequently use the technique to acquire K_C^{ind} measurements (see [71, 207, 255]). However, indentation tests do have a number of limitations (see [194] for more details); and when feasible, 3-point or 4-point bending tests provide more favorable measurements. Häßler and Rüssel [113] invoked the 4-point bending test to examine the fracture toughness (K_C) for the binodal decomposition ($[SiO_2]$ = 60%, $[B_2O_3]$ = 37% and $[Na_2O]$ = 3%; presented in Section 2.2.2.1. With a strong mismatch between the thermal expansion coefficients of the two phases, the stress formed around the secondary phase during cooling is considered responsible for increasing K_C.

In summary, the structure of APS glass have some influences on fracture toughness, yet it depends on different factors (interconnectivity, comparison of physical parameters between different phases, residual stress, *etc.*). It is rather difficult to determine the toughening effects, especially for spinodal decomposed APS glasses with complicated secondary phase geometry. More experimental research and simulation work should be carried out to understand these effects.

2.4.3 Sub-critical cracking of APS glasses

Recalling Wiederhorn's works ([268, 271, 269] reviewed at the beginning of Section 2.4), dynamic fracture (see Section 2.4.1) concerns $K_I \geq K_C$, but sub-critical cracking occurs when $K_I < K_C$. For sub-critical crack propagation, chemical interactions between the

environment and the crack front becomes relevant. Hence, environmental factors should be taken into consideration to determine the crack path. Now turning to APS systems, mesoscopic heterogeneities alter SCC behavior of the material. This section takes a closer look at how APS affects SCC behavior, more specifically, the interaction between crack front and secondary phase as well as the $\log(v) - K_I$ curve.

2.4.3.1 Crack front interaction with second particulate phase

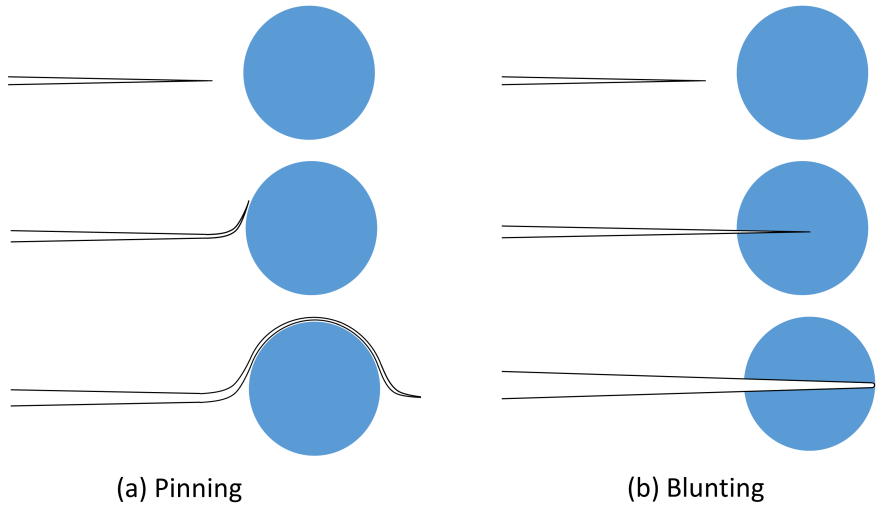

Figure 2.16: Schematic illustration successive positions of crack front upon interaction with array of second-phase particles, expected for (a) glasses consisting of Pb-rich particles/B-rich matrix, and (b) glasses consisting of B-rich particles/Pb-rich matrix [185].

Binodal structures can have either a pinning or a blunting effect on the crack front's movement according to the differences in stress corrosion resistances between the matrix and the particles [185]. The $PbO-B_2O_3$ glass system is a typical example of this kind of structure, which contains Pb-rich and B-rich phases after binodal phase separation.

Since crack growth is slow, the fracture surface energy is no longer the most important factor in predicting the crack front orientation. Instead, resistance to SCC dominates the interaction between the crack front and the precipitates and determines whether the crack pass through the precipitate, or not. Figure 2.16 (a) is a schematic illustrating the interaction between a growing crack and a particle in its wake predicted for Pb-rich particles/B-rich matrix glasses [185]. For this system, Pb-rich particles, which are supposed to be easier for the crack to pass through in dynamic fracture ($\alpha_m > \alpha_p$ and $\Gamma_m > \Gamma_p$ [183]), are more resistant to stress corrosion cracking. Hence, the crack favors circumventing the particles in sub-critical cracking. Thus, it can be said that the particle works as an obstacle to inhibit the crack growth in the B-rich matrix. Figure 2.16 (b) shows the opposite configuration, with a B-rich particle in a Pb-rich matrix. In this case, the crack penetrates into the B-rich particle. Then, it blunts locally at the particle-matrix interface. This occurs because the matrix is not as easily broken due to its high corrosion resistance. This phenomenon inhibits

the propagation of the crack front. Thus, the volume fraction of the secondary particles should impede the crack front propagation.

The two mechanisms above demonstrate how the existence of secondary particle can modify the SCC behavior of an APS glassy system. Moreover, this suggests that the APS structure has the potential to increase the resistance to SCC in glassy systems. Similar mechanisms have been proposed for other material systems to explain the influence of structural heterogeneities on SCC [3, 81].

2.4.3.2 Effects on SCC curves

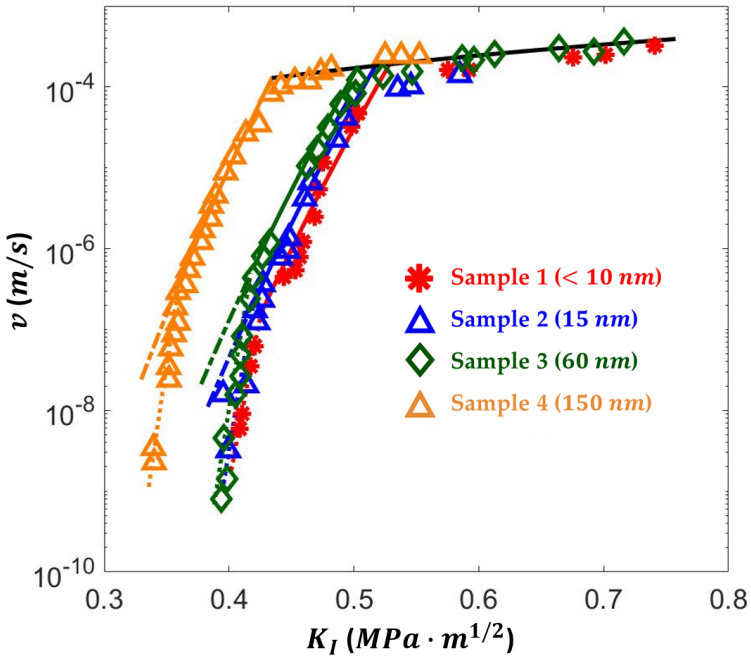

Figure 2.17: Crack growth data for sodium-borosilicate glass after varying degree of phase separation. Sample 1 (red star): annealed at 55 ℃ for 6.5 h, phase size $< 10\ nm$; Sample 2 (blue triangle): annealed at 620 ℃ for 0.5 h, phase size $\sim 15\ nm$; Sample 3 (green diamond): annealed at 620 ℃ for about 35 h, phase size $\sim 60\ nm$; Sample 4 (yellow triangle): annealed at 650 ℃ for about 90 h, phase size $\sim 150\ nm$. Recreated from [241].

Recalling Figure 2.11, cracks can grow unstably ($K_I > K_C$) or sub-critically ($K_I < K_C$). Section 2.4.2 reviews results concerning the fracture toughness K_C of APS glasses. Concerning sub-critical crack propagation ($K_I < K_C$) in APS oxide glasses, data is significantly more limited. Thus, how APS influences sub-critical crack propagation behavior is not well understood.

Nevertheless, some studies in literature indicate the presence of this effect. Figure 2.17 shows the SCC curves for an APS SBN glass by Simmons *et al.* [241]. The chemical composition of the glass is $[SiO_2] = 70\%$, $[B_2O_3] = 23\%$ and $[Na_2O] = 7\%$. These glasses are verified to have a spinodal structure. Different thermal treatment conditions (temperature and duration) were used to change the microstructure sizes. The glasses depicted in Fig-

ure 2.17 underwent four different thermal treatment protocols: Sample 1 (red star) annealed at 550 ℃ for 6.5 h, phase size < 10 nm; Sample 2 (blue triangle) annealed at 620 ℃ for 0.5 h, phase size ~ 15 nm; Sample 3 (green diamond) annealed at 620 ℃ for about 35 h, phase size ~ 60 nm; and Sample 4 (yellow triangle): annealed at 650 ℃ for about 90 h, phase size ~ 150 nm. For Region II sub-critical cracking, all four cases have the same velocity value on the plateau. This is consistent with the theoretical analysis at the beginning of this section: this value depends on the environmental water quantity. Thus, differences in the microstructure does not significantly affect the height of plateau in Region II. However, shifts of the curve exists in Region I. This implies that the dynamics in Region I significantly depend on the mesoscale structural arrangement. As the secondary phase increases in size, Figure 2.17 depicts a shift to lower values of the stress intensity factor. Sample 4 with the largest secondary phase displays the greatest susceptibility to SCC since its curves lie on the far left side of the other three samples. Simmons [241] considered that the increase of sodium concentration in the silica rich phase after high temperature annealing induces a huge decrease of chemical durability in this phase, decreasing the glass resistance to corrosion and facilitating crack propagation. The mechanism of crack propagation in Region I is controlled by the changes in composition and durability of the Si-rich phase.

2.4.4 Fracture surface roughness investigation

The sections above talks about the interactions between a single particle of a second phase and the crack front during dynamic fracture or SCC at the mesoscopic scale. Comparing the simple model presented above (single particle in an infinite field) to the complex network shape after spinodal decomposition, the stress distribution of the later is much more complex to analyze. However, the interaction between the crack front and the precipitates can still be predicted by analogy with the previous stress field analysis and by post-mortem fracture surface analysis via line models [98]. These planar line models provide insight on how the crack front propagates in such media. In these models, the crack front is considered as an elastic line, which moves through a set of randomly distributed obstacles, and its dynamics depend on long-range elastic interactions along the rough crack front [54, 24]. Moreover, the fracture surface roughness depends on the crack propagation speed, which is linked to the stress intensity factor K. When K is less than a threshold value K^*, the crack front stops propagating due to pinning effects [54]. If K is large enough, the front can overcome the obstacles and propagate. However, the velocity varies due to the obstruction. There is a competition between a roughening effect due to the randomly distributed secondary phase, and a smoothing effect due to elastic interactions along the front. The balance between these effects leads to a rich phenomenology.

It is difficult to access these phenomena experimentally [219]. Hence, researchers turn to post-mortem fracture surfaces [98]. A number of studies have been carried out to investigate the fracture surface of glasses, mostly by AFM [50, 274, 56, 197]. At the nanometer scales, these surfaces exhibits self-affine morphological features: the root mean square roughness RMS as well as the roughness exponent (or Hurst exponent) ζ. For a given topography image, the relationship between them can be expressed as [197]

$$RMS(L_0) = Z_4 l^{1-\zeta} L_0^{\zeta} \tag{2.31}$$

where Z_4 is a constant close to 1 mostly independent of the image resolution, L_0 is the image size, l is topothesy (a characteristic length-scale of the self-affine surface). The two parameters ζ and l provide a consistent characterization of the self-affine surface roughness, which is independent of the image size used to evaluate it. It is worth emphasizing here that these self-affine morphological scaling features are observed at small scales only (about $10\mu m$) [160].

Dalmas *et al.* [56] looked at fracture surfaces at large scales in a phase-separated glass ($[SiO_2]$ = 70%, $[B_2O_3]$ = 25%, $[Na_2O]$ = 2.5%, $[K_2O]$ = 2.5%). Specifically, the study concentrated on the out-of-plane roughness parallel to the direction of crack propagation in glass with domain sizes ranging from 20 to 100 nm via heat treatment, i.e. controlling annealing temperature and duration [55]. Post-mortem fracture surfaces were generated by SCC tests of DCDC (Double Cleavage Drilled Compression) samples. Their experimental results show that, at length scales larger than the phase size L, the height difference Δh increases logarithmically with the in-plane distance Δx parallel to the crack propagation direction. The relationship between Δh and Δx follows the equation [56]

$$\frac{\Delta h(\Delta x)}{\Delta h(L)} = Z_5 log(\frac{\Delta x}{L}) + Z_6 \tag{2.32}$$

where Z_5 and Z_6 are constants. This logarithmic roughness is compatible with theoretical [211] and numerical predictions [9] obtained in the framework of line models.

In Dalmas' study, the roughness disorder is not a direct reflection of the structural disorder due to the lack of information at the length scale of the process zone. Moreover, AFM tip geometries may cause interference in the measurements at small scales [160, 103]. Hence, depinning models of SBN oxide glasses currently provide limited information on the process zone size. Additional models should be used to supplement the existing results.

Another investigation [9] concerns Random Toughness Continuum Mechanics (RT-CM) approach considering the crack propagation in a solid with spatially distributed toughness. It is used to predict crackling dynamics in inhomogeneous solids via rough fracture surfaces. A random spatially distributed component is introduced in a homogeneous solid to simulate the effects of material heterogeneities. The existence of this component leads to a change in the fracture surface energy and the crack front distortion. Griffith criterion and principle of local symmetry [91] combined with an asymmetric estimation of the perturbation in the loading induced by the front distortion describes the crack growth. With some assumptions/hypothesis (see [9] for more details), the fracture surface roughness $h(x, z)$ can be characterized by computing the structure functions in the two directions available on a post-mortem fracture surface: x crack front propagation direction and z parallel to the crack front. The structure functions of a fracture surface depend on the Poisson's ratio ν, microstructure length scale ℓ, and disorder strength θ (the standard deviation of the Gaussian function for simulating the random spatially distributed component in a solid) [9]:

$$S(\Delta x) = \langle (h(x + \Delta x) - h(x))^2 \rangle \approx \frac{0.32}{A(\nu)} \theta^2 \ell^2 log(4.8A(\nu)\Delta x/\ell) \tag{2.33}$$

$$S(\Delta z) = \langle (h(z+\Delta z) - h(z))^2 \rangle \approx \frac{0.32}{A(\nu)} \theta^2 \ell^2 log(4.2\Delta z/\ell) \tag{2.34}$$

where $A(\nu) = (2-3\nu)/(2-\nu)$. In APS glasses, the microstructure length scale ℓ corresponds approximately to the phase size L. These functions allow one to infer the microstructure parameters from post-mortem fracture surface analysis.

Chapter 3

Experimental methods and techniques

Contents

3.1 Sample elaboration and annealing protocols

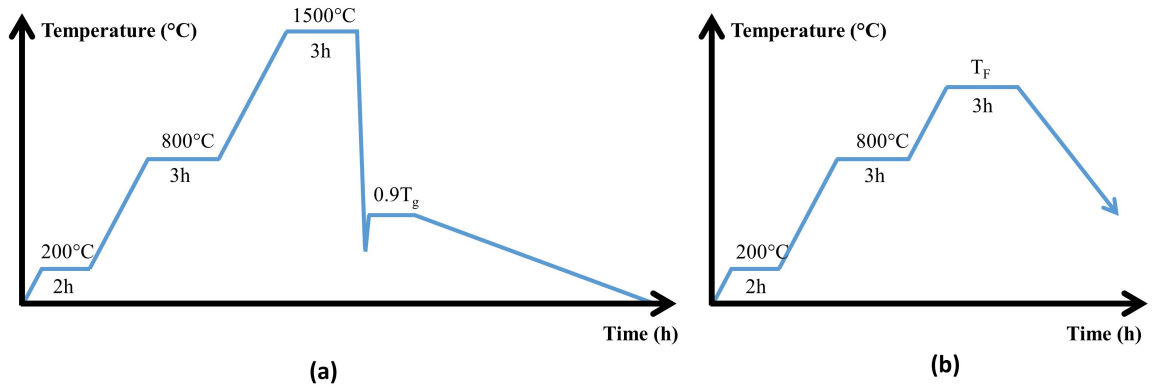

Figure 3.1: Thermal cycle of SBN glasses' elaboration: (a) Protocol A (by Rémy Baniel and Patrick Houizot); (b) Protocol C (by Marina Barlet)

In this project, the samples for APS tests were fabricated at IPR (*Institut de physique de Rennes*) in the University of Rennes by an internship student (Rémy Baniel) and a research engineer (Patrick Houizot). Sample elaboration protocols concern a ToughGlass research objective. The goals were the fabrication of homogeneous glass samples, without bubbles and residual stresses. Hence, some trials and errors were required and are detailed below. For clarity, the sample names, chemical compositions, and their corresponding protocols will be detailed at the beginning of each part before presenting the results.

Elaboration of SBN glasses requires various raw materials – silica, orthoboric acid (H_3BO_3) and sodium carbonate (Na_2CO_3) powders. They are manually homogenized and put in a platinum-rhodium crucible. Then the crucible is put into a furnace for melting. Table 3.1 details the two different glass formation protocols used for sample fabrication at IPR: Protocol A (Figure 3.1 (a)) and Protocol B (where T_g represents the transition temperature of glasses).

Table 3.1: Thermal treatment procedure of Protocol A and Protocol B

Protocol A	**Protocol B**
1. Ramp the temperature up to 200 ℃ over 30min, maintain for 2h; 2. Ramp the temperature up to 800 ℃ over 2h, maintain for 2h; 3. Ramp the temperature up to 1450 ℃ over 1h, maintain for 1h; 4. Pour the material from the crucible onto a plat in Inconel pre-heated at $0.9T_g$; 5. Put the ensemble into the furnace for tempering at $0.9T_g$ for 1h15min; 6. Lower the temperature to ambient temperature over 5h.	1. Ramp the temperature up to 900 ℃ over 5h, maintain for 2h; 2. Ramp the temperature up to 1500 ℃ over 3h, maintain for 1h; 3. Cool down the material to room temperature in the crucible; 4. Remove the glass from the crucible and grind it into pieces; 5. Put the material into a small crucible; 6. Put the crucible in the furnace pre-heated at 1500 ℃, maintain for 1h; 7. Repeat step 3 and 4; 8. Repeat step 6; 9. Perform step 4-6 in **Protocol A**.

To track samples within this thesis, I have developed a sample nomenclature. As fabricated samples are called pristine samples and are catalogued as follows:

SBN**XX**-pristine-**YY**-**Z**

where

- **XX** signals the chemical composition,
- **YY** signals the ordering number,

- **Z** signals the geometry of samples: "p" for powder, "d" for disks, "s" for small size samples, "t" for special prepared TEM samples, and blank for DCDC samples.

Table 1.1 provides the target chemical composition for the glasses studied herein along with their SBN names. After elaboration, some pristine samples undergo annealing. The nomenclature is rather similar as for the pristine samples. It is as follows:

SBN**XX**-**TTT**C-**HH**h-**YY**-**Z**

where

- **TTT** indicates the annealing temperature,
- **HH** indicates the annealing time in hours.

The annealing procedure can be divided into four steps:

- Increase of temperature (heating rate 10 ℃/min) to desired annealing temperature **TTT** ℃;
- When the temperature in the furnace becomes stable at **TTT** ℃, put the samples directly in the furnace;
- Maintain the temperature (**TTT** ℃) for desired **HH** hours;
- Take the sample out of the furnace and introduce it in another furnace pre-heated at $0.9T_g$ for 1h;
- Cool down slowly to room temperature over a period of 5h (cooling rate <2 ℃/min).

For comparison purposes, old samples, fabricated during M. Barlet's thesis [10], are also used. These samples were fabricated in SECM (*Service d'Etude et Comportement des Matériaue de conditionement*) in CEA-Marcoule via Protocol C. Figure 3.1 (b) illustrates the thermal protocol. T_F is the glass fusion temperature ranging from 1100 to 1300 ℃. For more elaboration details, please see Section 2.1 in [10].

3.2 Structure characterization

Section 2.2.1 reviews the theoretical structure of SBN glass systems. Despite vast experimental efforts to unveil borosilicate glass structures [279, 61, 82, 282, 10], many basic aspects of their short- and/or medium-range order remain debated [279], especially the APS structures [125, 259]. NMR, RAMAN and XRD techniques can aid in understanding these structural arrangements. This section presents these tools and experimental protocols.

3.2.1 NMR spectroscopy principles

Nuclear Magnetic Resonance (NMR) spectroscopy is a spectroscopic technique to observe local magnetic fields around atomic nuclei. This spectroscopic tool takes advantages of the nuclear spin of atom. Each nucleus possesses a dipole magnetic moment $\vec{\mu}$ which is linked to the nuclear spin by

$$\vec{\mu} = \hbar\gamma_n \vec{I} \tag{3.1}$$

where γ_n is the nuclear gyromagnetic ratio (different for every nucleus) and $\vec{I}$ is the nuclear spin. If $I = 0$, the nucleus carries no magnetic dipole moment, and NMR measurements cannot be performed on these isotopes. Common NMR-active nuclei are "light" ones such as ^{1}H, ^{11}B, ^{13}C, ^{17}O, ^{23}Na, *etc.* This technique has been widely used to studying the atomic local environments in various materials, including biological material [133], glasses [278, 65], liquid crystals [222], *etc.* This section presents the NMR principles.

The principle of NMR is to measure the interactions of the nuclear spin (of the probed nucleus) with its local environment in the presence of a strong external magnetic field $\vec{B_0}$ [46]. The application of this magnetic field generates a macroscopic magnetization arising from the ensemble of nuclei in the sample. Additionally, it sets the frequency f_L for measuring the signals of the nucleus N (Larmor frequency) by the equation

$$2\pi f_L = \gamma_N B_0 \tag{3.2}$$

Under the magnetic field $\vec{B_0}$, a radiofrequency (RF) magnetic field pulse oscillating at the Larmor frequency $\vec{B_{RF}} = 2B_1 cos(2\pi f_L t)$ is applied perpendicularly to $\vec{B_0}$. This will rotate the macroscopic magnetization away from its equilibrium position (along $\vec{B_0}$) to the transverse plane, where the Larmor precession can be observed. This generates an oscillating signal, so-called Free Induction Decay (FID), at Larmor frequency, *i.e.* the NMR signal. By Fourier transformation, the oscillating signal can be transformed into frequency domains.

For glass investigations, NMR techniques provide insight on the intricacies of short-range structures and aid in revealing changes in mid-range structures [66]. For example, the network connectivity, non-bridging oxygen (NBO) atoms, and coordination number can be precisely evaluated by investigating the NMR-active nuclei in the glass systems. In SBN glass systems, the interesting nuclei include ^{11}B, ^{23}Na, and ^{29}Si. Among the NMR-active nuclei, they can be further divided into two types:

- $I = 1/2$ – ^{29}Si. The nuclear charge distribution is spherically symmetric and the quadrupolar electric moment Q is 0.
- $I > 1/2$ – ^{11}B and ^{23}Na. $Q \neq 0$. These nuclei are named quadrupolar nuclei and are sensitive to local electric field gradients (EFG).

$I = 1/2$ nuclei are simpler to study, while the quadrupolar nuclei are more difficult to manipulate [191]. For the quadrupolar nuclei, NMR signals contain a central transition (CT, transitions for $I = 1/2$ and $I = -1/2$) and satellite transitions (ST, all other transitions). Herein, only CT spectra were used for investigations since they are narrower and more sensitive.

NMR characterizations include different kinds of spectra according to nuclear spin interactions, including chemical shift interactions, dipolar interactions, quadrupole interactions, *etc.* [64]. The use of RF pulses of different durations, frequencies, or pulse sequences allows the NMR spectroscopist to extract different types of information concerning the atomic arrangements in a sample. Magic angle spinning (MAS) is widely used to obtain higher resolution NMR spectra. This technique consists in spinning the samples around the magic angle θ_M (54.74°, defined by $3cos(\theta_M)$-1=0) with respect to the magnetic field $\vec{B_0}$ [46]. Indeed, for symmetry reasons related to the rotation properties of NMR interactions, anisotropic effects

(which are responsible for a broadening of the NMR peaks) average out over one rotation period of the sample under MAS. For quadrupolar nuclei, MAS only reduce partially the second-order quadrupolar broadening of CT. During my these, I invoked the following NMR spectra measurements:

- MAS for ^{11}B, ^{23}Na and ^{29}Si: MAS experiments provide high resolution NMR spectra, which probe the local environment of B, Na and Si in the samples;
- Multi-Quantum MAS (MQMAS, *i.e.* 3QMAS) for ^{11}B: MQMAS is a 2D measurement, which provides high-resolution NMR spectra for quadrupolar nuclei by removing the signal from second-order quadrupolar interactions in a (indirect) second dimension.
- Double-Quantum MAS (DQMAS) for ^{11}B-^{11}B correlation: direct ^{11}B-^{11}B spatial interactions can be revealed basing on the homonuclear magnetic dipolar interactions.
- ^{11}B$\{^{23}$Na$\}$ and ^{23}Na$\{^{11}$B$\}$ REDOR: these experiments aim at observing the spatial proximity between ^{11}B and ^{23}Na basing on the heteronuclear magnetic dipolar interactions.

to capture the structure of SBN glasses.

NMR experiments were done in collaboration with Thibault Charpentier in NIMBE/CEA-Saclay with a Bruker 500WB Solid-State NMR spectrometer operating at a magnetic field of 11.72 T. Herein, the MAS spin rate is 12500 Hz. The samples for NMR characterizations concern power samples and small disks of which the diameter is 2.9 mm and the thickness is approximately 0.9 mm. The samples were packed in ZrO_2 rotors (with external diameter 4 mm and internal diameter 3 mm). Experiments invoke one disk for each type of samples since the amount of sample is limited. Compared to disk samples, powder samples are grinded from the offcut material and provide larger amount of material for characterizations, thus more efficient.

3.2.2 Raman principles

Raman analysis (named after Indian physicist Chandrasekhara Venkata Raman) is a widely used spectroscopic technique for determining vibrational modes of molecules in materials [159, 242]. It is commonly used in chemistry to provide a structural fingerprint by which molecules can be identified. Photons from a monochromatic light laser are shined on a sample, scattering either elastically (Rayleigh scattering, 99.999%) or inelastically (Raman scattering, 0.001%). Raman spectroscopy employs the latter phenomenon [129]. For Raman scattering, there is an exchange of energy between the photons and the material molecules, resulting in the shift of scattered photon wavelength. When the scattered photon has less energy compared to the primary photon, it is called Stokes scattering; when the scattered photon has more energy, it is called anti-Stokes scattering [129]. Shifts in the photon frequency contain information about the vibrational and rotational modes along with transitions in the system. The Raman spectrum of a SBN glass displays the bending & stretching modes of Si−O−Si, danburite groups ($2B_2O_3{\cdot}3SiO_2$, see Appendix A.4 for more details), Q_i units, *etc.* [83, 266, 82, 18]. Specifically, these structures respond to the monochromatic light at particular wavelengths. Below is a summary of some of the reported structures in

low sodium content glasses ($R_{SBN} < 0.5 + 0.25K_{SBN}$, see Section 2.2.1) along with their associated wavelengths:

- $450 - 550\ cm^{-1}$: This broad band implies a mixed stretching-bending motion across the Si-O-Si bridging oxygen [267] as well as mixed Si-O-B bonds of the 3-D network [82].
- $630\ cm^{-1}$: This peak has been attributed to danburite units [20] and metaborate rings [82, 150].
- $703\ cm^{-1}$: This peak is attributed to metaborate units [57].
- $770\ cm^{-1}$: This peak corresponds to the vibrations of the six-membered borate rings with one or two B[IV] [82, 277].
- $805\ cm^{-1}$: This peak is related to symmetric vibration of boroxol rings [82].
- $900 - 1200\ cm^{-1}$: This wavelength range is linked to the stretching of Q_i structure units: Q_1 for $900 - 920\ cm^{-1}$, Q_2 for $950 - 980\ cm^{-1}$, Q_3 for $1050 - 1100\ cm^{-1}$, Q_4 for $1120 - 1200\ cm^{-1}$ [180].
- $1260 - 1540\ cm^{-1}$: This broad peak corresponds to B[III], including the BO_3 triangle units in boroxol rings or loose BO_3 units [277].

In this project, Raman analysis are done in two different laboratories, IPR (*Institute de physique de Rennes*) in University of Rennes and NIMBE (*Nanosciences et Innovation pour les Matériaux, la Biomédecine et l'Énergie*) in CEA-Saclay. The wavelength of laser is 532 *nm*, concerning a beam of visible green light. The analysis are done in ambient condition. The samples used for Raman characterizations are the small samples as well as the DCDC samples before/after SCC experiments. Either fracture or polished surfaces can be characterized and no sample preparation is required.

3.2.3 X-ray diffraction analysis

X-ray diffraction (XRD) analysis is a characterization technique for verifying the crystallinity in a material and for determining the crystallographic structures. Recalling crystals are regular arrays of atoms. The X-ray wavelength is often on the same order of magnitude as the spacing between the crystal planes. When X-rays shine on a crystal material, they mostly scatter and cancel each other out through destructive interference. However, they add constructively in a few specific directions. The diffraction patterns appearing on these specific directions contains information about the crystal structures. A careful analysis of the diffraction patterns or by using specific XRD settings provides information concerning the crystal orientation, shape and size, internal elastic stress and strains at different levels, *etc.* [1].

3.3 Physical Properties

Materials are frequently characterized by several physical properties including their density and the elastic moduli. Herein, I will do the same. Section 3.3.1 details techniques used

to measure the density of glasses. The elastic moduli are calculated based on the velocities of longitudinal and transverse acoustic waves herein. Section 3.3.2 details the techniques to measure the velocities of longitudinal and transverse acoustic waves. Then it presents how to calculate the moduli and Poisson's ratio from them.

3.3.1 Density measurement

Archimedes' principle is widely used for calculating the density of a solid material. When a body is immersed in a fluid, the upward buoyant force exerted on the body is equal to the weight of the fluid that the body displaces: $F_{buoyant} = \rho_{fluid} V g = mg - m_{influid} g$ (m and V the mass and the volume of body, $m_{influid}$ the mass of body in fluid, ρ_{fluid} the density of liquid, g the acceleration of gravity). Assuming conservation of volume, measuring the weight of a sample in air (m_a) and in water m_w gives an estimate of the density ρ of the sample via the following equation:

$$\rho = \frac{m_a \rho_w - m_w \rho_a}{m_a - m_w} \approx \frac{m_a \rho_w}{m_a - m_w} \tag{3.3}$$

Herein, density measurements invoked a homemade equipment (of which the photo is shown in Appendix A.1) and are done at room temperature (about 20 °C). The scale used to weight the samples was a Satorius balance with an accuracy of 0.1 mg. Additionally, some of the measurements were done in University of Rennes I with Explorer Analytical Analytical Balance EX124 with a density kit (Appendix A.1). For the two equipment, errors due to different factors cannot be avoided, including differences between manipulations, ambient condition variations, equipment accuracy, *etc.* The standard deviations of different measurements were averaged, and density measurement error with the homemade equipment is estimated to be 0.05 g/cm^3.

3.3.2 Moduli calculations

Bulk, Shear and Young's moduli along with Poisson's ratio are some of the most common properties considered for a material. The definitions of these four parameters are as follows:

- Bulk modulus (K) – the ratio of hydrostatic stress on an object with respect to the volumetric strain, which is also the ratio of volume change to the initial volume [139].
- Shear modulus (G) – the ratio of shear stress with respect to the shear strain, which is also called the rigidity modulus [138].
- Young's modulus (E) – the ratio of principal stress in one direction with respect to the elastic strain in the same direction [137].
- Poisson's ratio (ν) – the ratio of lateral strain with respect to the axial strain [140].

These four parameters can be linked by the following equations [124]:

$$E = \frac{9KG}{3K + G} \qquad \nu = \frac{3K - 2G}{2(3K + G)} \tag{3.4}$$

In practicality, it is not easy to access the three moduli and Poisson's ratio experimentally. Ultrasonic echography techniques provide a simple and reliable method for accessing the elastic moduli of many materials [151]. This method based on the elastodynamic of a solid material. Specifically, the moduli and Poisson's ratio are calculated using with the following equations [151]:

$$K = \rho(v_L^2 - 4/3v_T^2) \tag{3.5}$$

$$G = \rho v_T^2 \tag{3.6}$$

$$E = \rho \times \frac{3v_L^2 - 4v_T^2}{(v_L/v_T)^2 - 1} \tag{3.7}$$

$$\nu = \frac{v_L^2 - 2v_T^2}{2(v_L^2 - v_T^2)} \tag{3.8}$$

where ρ is the material density, v_L is the propagation velocities of longitudinal acoustic waves inside the material, and v_T is the propagation velocities of transverse waves inside the material.

A computer controlled ultrasonic pulser-receivers (PANAMETRICS-NDT Model 5800) accompanied with transducers (M116 for transverse waves and V222 for longitudinal waves) are used for transmitting and receiving the acoustic pulse waves. The wave frequency of is 1 kHz. To perform the measurements, the sample must have two parallel surfaces and the distance between them know. During my thesis, I measured the thickness of the samples with a digital caliper (FACOM, with an accuracy of 0.01 mm). Afterwards, one of the transducers is stuck to the sample surface with liquid honey (used to fill the gap between the sample and transducer). An acoustical wave is then transmitted from the transducer into the sample. This wave propagates trough the sample, reflects off the opposite surface and then returns to the transducer (coined echo). Additionally, the wave can undergo multiple reflections and the transducer can detect these multiply reflected waves. An oscilloscope (Tektronix TDS3054B) records these transmitted and received waves as a function of time. Figure 3.2 shows the signal of transmitted and registered waves by the oscilloscope. The first peak is the transmitted wave and the rests are echoes. The time difference Δt between two adjacent echoes indicates the time for the wave to make a round trip propagation inside the sample. Average of different pairs of adjacent peaks reduces the error. The velocity of the wave is simply the ratio of distance propagated to the time. The M116 transducer provides a means to calculate the transverse wave speed v_T, and the V222 transducer a means to calculate the longitudinal wave speed v_L. These velocities provide a means to evaluate the elastic moduli via equation (3.7) - (3.6). These calculations have an error associated with them. It originates from errors in measuring the transverse and longitudinal wave speeds (δv_T and δv_L, respectively) and the density ($\delta\rho$). Appendix A.2 provides the estimations of moduli errors based on statistical error analysis [252].

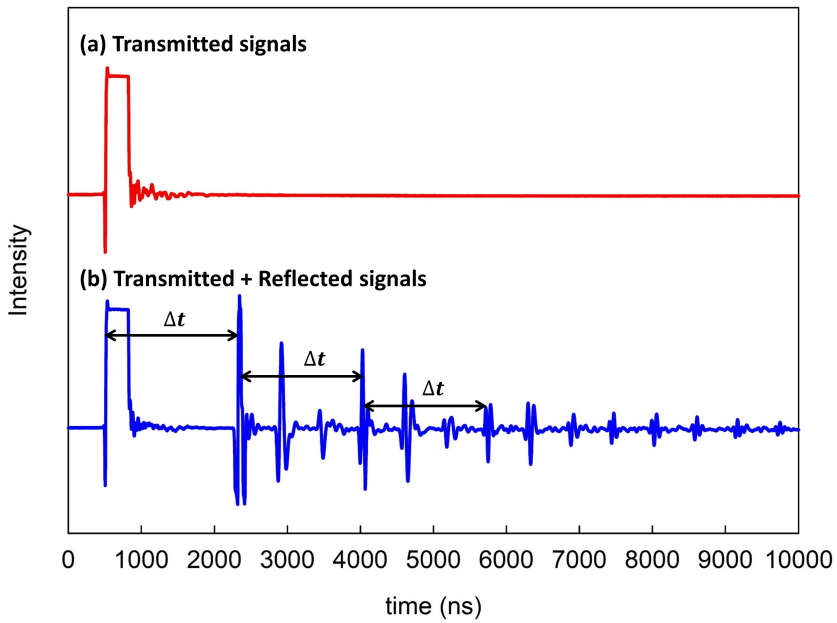

Figure 3.2: Transmitted longitudinal acoustic waves signals (no sample on the transducer V222) (a) and a typical signal with transmitted and echo waves (b) for measuring the v_L.

3.4 Fracture Properties

3.4.1 Stress corrosion cracking experiment via Deben machine

Conducting a SCC test requires an extended time period (from 2 weeks to 2 months) due to the velocity of the crack front (10^{-12} to 10^{-6} m/s). As seen above, SCC depends on different environmental factors, including the environmental temperature and humidity. During my thesis, I developed and tested an environmental chamber, which regulates the environmental humidity. An air conditioner regulates the room temperature. SCC tests were conducted in the environmental chamber. This section first details the SCC test using a Deben machine and then the environmental chamber around the Deben machine. Afterwards, it shows the tracking of the crack front. Finally, it details post-mortem analysis of fracture surfaces using an AFM.

3.4.1.1 DCDC sample and Deben machine

The SCC tests herein employ a dual screw Deben Microtest MT5000DL loading stage. Figure 3.3 middle panel shows the experimental setup. The sample geometry is a Double Cleavage Drilled Compression (DCDC) samples (Figure 3.3 left panel): a rectangular parallelepiped with a circular hole drilled through the center of the large facet. This technique is widely used for investigating SCC behavior of brittle materials because of the stability of the crack propagation [195, 40, 10, 114]. Samples used in this project concern two different sizes: $4 \times 4 \times 25$ mm^3 and $5 \times 5 \times 25$ mm^3 both with holes of 1 mm diameter.

To aid in positioning the sample, two sets of jaws were specifically designed for the two different DCDC samples. The jaws are designed to be about 1 mm larger and wider than

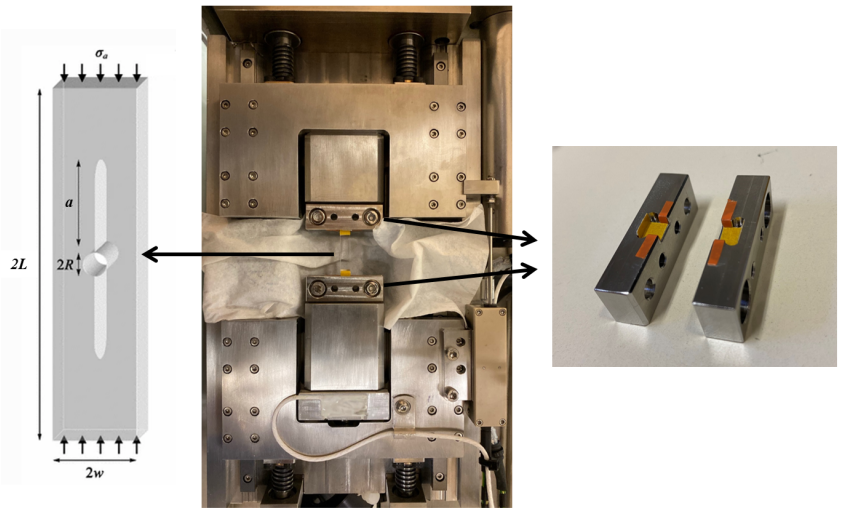

Figure 3.3: (Left) Sketch of the DCDC sample with a crack of length a. (Middle) Dual screw Deben machine for SCC tests. (Right) Jaws for mounting the samples with the tapes for protection.

the sample sections. This avoids sample pinning during loading and permits self-alignments during the pre-load. Additionally, the jaws are lined with tape (Figure 3.3 right panel) to protect the sample edges during loading and to aid in applying a more uniform load.

The force is specifically applied via a displacement of the jaws towards one another. It is applied on the $4 \times 4\ mm^2$ (or $5 \times 5\ mm^2$) facets. In other words, the sample undergoes a compressive stress. However, due to the DCDC geometry, these compression stresses provoke the initiation of two Mode I symmetric cracks (schematic in Figure 3.3 left panel). Subsequent adjustments to the applied stress provokes the propagation of the crack fronts. Recalling from Section 2.4, the stress concentration on the crack front is a geometrical parameter. 2D Finite Element (FE) simulations based on linear elasticity provide a means to calculate K_I [195]. Several researchers have provided equations to calculate K_I. Herein, I will use the Pallares *et al.* equation, which was parametrized for $2.5 \leq \frac{w}{r} \leq 5$. K_I is calculated with the following equation:

$$\frac{\sigma\sqrt{\pi r}}{K_I} = [0.3156+0.7350\times\frac{w}{r}+0.0346\times(\frac{w}{r})^2]+[-0.4093+0.3794\times\frac{w}{r}-0.0257\times(\frac{w}{r})^2]\frac{a}{r} \quad (3.9)$$

where σ is the compression stress applied on the $4 \times 4\ mm^2$ (or $5 \times 5\ mm^2$) facets, r is the radius of hole, w is the half width of sample, and a is the real-time crack length.

As stated above, SCC tests require an extended time period (from 2 weeks to 2 months) as the velocity of the crack front ranges from 10^{-11} to $10^{-5}\ m/s$. The double screw structure of the Deben machine provides a stable and uniform force application to the sample. To manage the force applied to the glass, a PC drives the Deben machine via the Microtest software (a proprietary software developed by the makers of the Deben machine to drive it). The Microtest software actually controls the displacement of the jaws, and the Deben machine has a 5k N load cell to capture the force imposed on the sample. The Microtest software

displays this force F. This allows me to calculate the stress imposed via $\sigma = F/A$, where A is the area of the facets where the force is imposed. It should be noted that controlling the stage movement via the Microtest software alters simultaneously the stress imposed on the sample and the crack front velocity. Monitoring the crack front displacement and other environmental parameters require additional equipment and software.

3.4.1.2 Automatic acquisition of crack front images

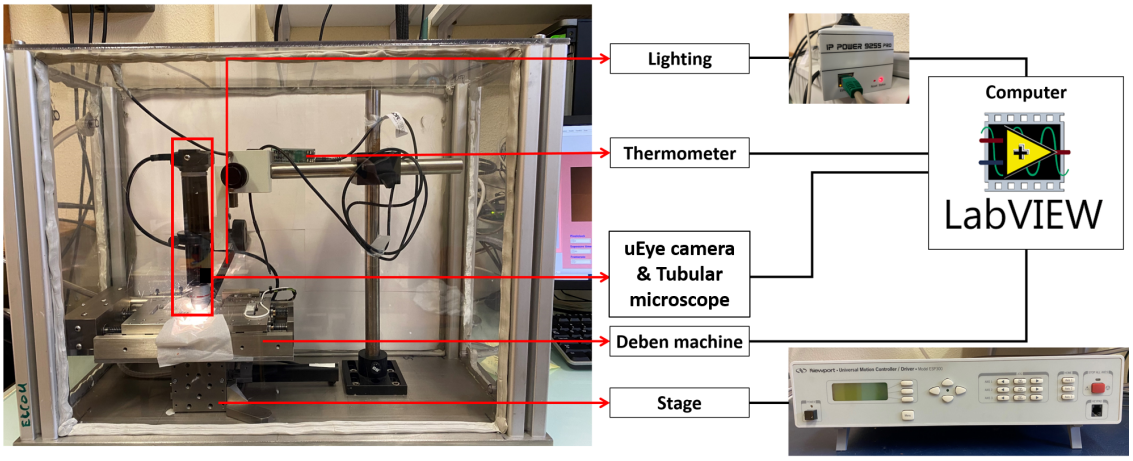

Figure 3.4: Schematic of the experimental equipment and isolation chamber.

As stated above, a stress corrosion cracking experiment takes between 2 weeks and 2 months, depending on the velocity of the crack front. Moreover, calculating K_I and v require monitoring the crack front position in real time. In order to maximize time availability, a LabVIEW program has been designed to control the image acquisition (described in this section) along with the environmental humidity (see Section 3.4.1.3), 24h/day, 365days/year.

Figure 3.4 depicts a schematic of the experimental imaging equipment. A tubular microscope (an uEye camera (UI-1465LE-C), Single Tube DIN and a 4X objective) in conjunction with a Pinion Focusing (coarse and fine motion focusing) focusses on the top surface of the glass sample (Figure 3.4). A LabVIEW program controls image acquisition. However, ambient lighting is not sufficient. Hence, a lamp (Edmund Fiber-Lite MI-152) provides additional lighting. The lamp sits outside of environmental chamber, and a fiber optic light guide is ran into the chamber. Placing the lamp outside of the chamber aids in reducing the heating in the chamber. To avoid additional heating of the sample during the experiment, the light needs to be automatically turned off and on. This is realizable by connecting the lamp's power plug to an IP Power 9255Pro power source, which is controllable by a LabVIEW program.

As stated above, a LabVIEW program manages the operation of the camera and lighting 24 h/day 365 days/year. Moreover, it allows the camera and the tubular microscope to work in tandem. When the LabVIEW program turns on (off) the light, the LabVIEW program begins (stops) to collect images. The duration the light is on (Δt_{on}) and off (Δt_{off}) is

set when the LabVIEW program is launched. The program works as follows (schematic in Figure 3.5 (a)):

1. The camera turns on for some time duration Δt_{on} set by the user. During the time the light is on, the camera acquires images;
2. Once Δt_{on} has elapsed, the light turns off and images stop recording;
3. Once Δt_{off} has elapsed, the program returns to the first step and repeats the cycle until the user stops the program.

By repeating these steps, the system is able to acquire images automatically, regularly and continuously day and night.

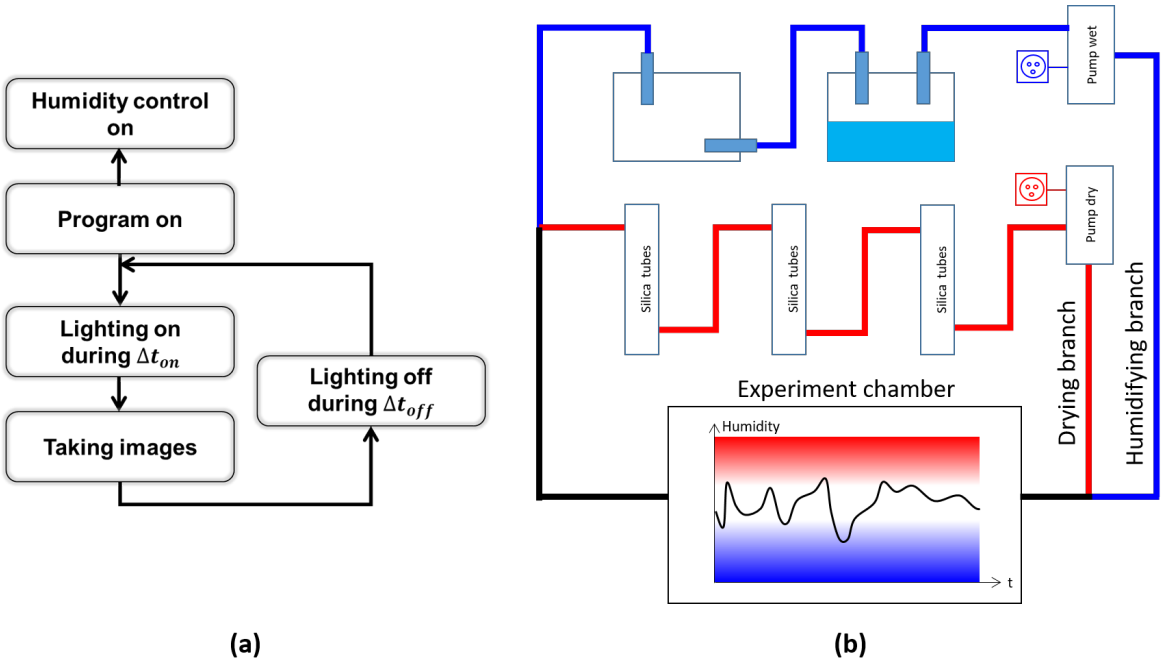

Figure 3.5: (a) LabVIEW program schema; (b) Humidity control system

3.4.1.3 Build-up of experimental chamber and humidity control system

As shown in Section 2.4, environmental factors including temperature and humidity alter a glass's SCC behavior. In order to obtain more precise experimental data, these two parameters need to be controlled during testing. This section details the experimental chamber plus control humidity system.

Figure 3.4 depicts the isolation chamber. It is made of Plexiglas planks and butyl tape seals off the chamber from the outside environment. A LabVIEW program adjusts the humidity inside the chamber to a desired range via an experimental setup modeled after Lesaine *et al.* [162] and summarized below.

A digital Thorlabs thermometer/hygrometer (TSP01 - USB Temperature and Humidity Data Logger) is placed inside the chamber for measuring temperature and humidity. It is

connected to the computer and drivers are integrated into the LabVIEW program. This permits real-time acquisition of the chamber humidity and temperature. A feedback system is then implemented to control the humidity (Figure 3.5 (b)). The humidity control feedback system consist of two branches: a "drying branch" with three columns of silica gels (DRIERITE gas drying unit), and a "wet branch" with a bottle of Millipore water and an empty bottle (to prevent water droplets from entering the chamber). Each branch has its own pump, which circulates the air through the branch. The pumps are plugged into an IP Power 9255Pro power source, which is controllable by a LabVIEW program. This permits the pumps to be turned on and off via the LabVIEW program like the lamp in Section 3.4.1.2.

During the experimental setup, the LabVIEW program requests the upper and lower threshold values of the humidity. Throughout the experiment, the humidity is captured in real time. If the humidity exceeds the upper humidity threshold, the system is "too humid". Hence, the LabVIEW program turns on the pump of the "drying branch", which pulls air from the chamber and forces it to flow through the silica gel columns and back into chamber. When the humidity drops below the upper threshold, the LabVIEW program turns off the pump. On the other hand, when the humidity drops below the lower humidity threshold, the LabVIEW program turns on the pump of the "wet branch", forcing air through the water bottle. When the real time humidity is within the expected range, both pumps stop working. This system can adjust the humidity into the expected range (RH=40%) within 3 minutes and maintains the humidity with an error of less than 0.5%.

For controlling the temperature, the laboratory where the experimental chamber sits is equipped with an air-conditioner. The temperature in the room is set to 18℃. Nevertheless, there are some seasonal differences: 19.5 ± 0.5 ℃ in summer and 18.5 ± 0.5 ℃ in winter. Thus, the temperature range during SCC experiments is 19 ± 1 ℃.

It is worth noting the chamber hinders camera position adjustments. For example, opening the chamber introduces a variation in the humidity during an on-going experiment. To solve this problem, the Deben machine sits on a stage that is controlled by a driver (Newport ESP300 Motion Controller/Driver) outside the chamber (Figure 3.4). The stage moves the Deben machine so that the crack front remains under the camera without opening the chamber.

3.4.1.4 Experiment procedure

With the experimental setup and the above information, the manipulations of SCC test are listed as follows:

1. Sample stabilization: A new sample is placed on the Deben machine between the jaws (which have tape). The jaws move towards each other at a velocity of 0.1 mm/min until they touch the sample and the force starts to increase (up to $10N$). Subsequently, the sample undergoes a constant load of $30N$. This (along with the tape) permits the self-alignment of the sample. The constant load protocol is repeated at $50N$ and $100N$. Then the force is increased to $100N$, $200N$, and $500N$ in a step wish process. Between each increase, the jaws are locked in place to stabilize the sample. The stabilization permits to extrude the tape.

2. Sample pre-crack: Once the stabilization is complete, the pre-crack procedure is implemented. The jaws are slowly brought together at a rate of 0.03mm/min. This in turn increases the force on the sample, which is monitored via the Microtest software. Once the cracks appear on both sides of the hole, the force is decreased. It should be noted, the force corresponding to the pre-crack depends on different factors, including hole geometry, sample geometry, the tape status, *etc.*). The pre-crack is allowed to grow until it reaches a length of approximately 1 mm. Step one and two are done without closing the chamber in order to properly focus the tubular microscope.

3. Stable crack propagation: At this point, the chamber is closed up and sealed with butyl tape. The LabVIEW program commences and stabilizes the humidity in the chamber. After which, the force applied via the Microtest software is adjusted to commence the propagation of the crack front. During this process, the applied force can be changed to obtain the desired crack propagation velocity. Post-processing of data points reveals the SCC curve. The LabVIEW program runs 24h/day to capture crack front images. The duration of "lighting on" and "lighting off" are adjusted according to the crack propagation velocity. Equation (3.9) along with the crack length a and the applied force F provides K_I. To change the crack front velocity, the force is unloaded and then reloaded. This provides distinctive backlash marks on the fracture surfaces and enables post-mortem studies of different velocity zones.

4. Breaking of sample: When the crack lengths reach 5 mm, I increase the force slowly until the cracks propagation reaches the end of sample. At this point, I unload the sample and remove it from the Deben machine for further analysis. Samples are stored in plastic boxes filled with silica desiccant gel between the time they are removed from the Deben machine and the time undergo additional analysis. This limits ambient water from interacting with the fracture surfaces after SCC tests.

3.4.1.5 Crack front image treatment

As mentioned in the above sections, the optical system captures the crack front images automatically during the experiments. These images are analyzed to obtain the position and velocity of the crack front. Due to minor drifts during the experiment and the displacement of the stage to ensure the crack tip position remains in the field of view, image correlations are required. With the large image size and the slow crack speed, regions with dust particles far away from the crack are considered unaltered by the crack propagation. These dust particles become reference points for positioning between images. By knowing the positions of chosen dust particles on different images, one can obtain the shifting between these images. By repeating this along the whole crack front, from the hole to the tip, the length of the crack front can be obtained and used for calculating the crack velocity.

A Matlab program aids in locating the crack tip positions in the images. Figure 3.6 along with the description below details the principles and procedures of this program.

1. Filters are applied to the original images for enhancing the contrast between the cracks and the background. Figure 3.6 (a) is the original image, and Figure 3.6 (b) is the treated image.

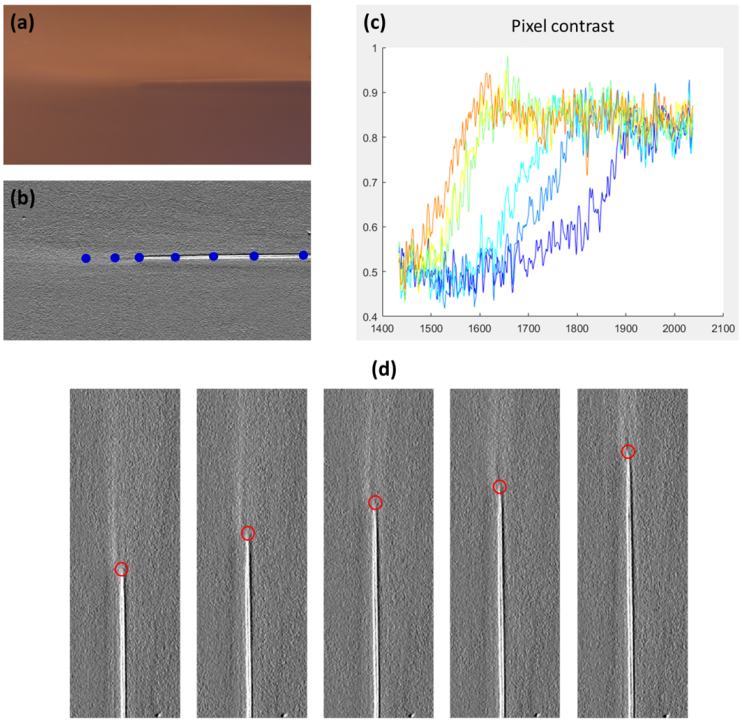

Figure 3.6: Crack front image treatment procedure: (a) Original crack front image by camera; (b) Enhancement of contrast and determination of crack path (blue circles); (c) Contrast analysis along crack path and threshold definition for crack front judgement; (d) Crack front determination.

2. The crack path needs to be determined manually (blue circles in Figure 3.6 (b)). For this step, the image should contain the wake of the crack front.
3. Figure 3.6 (c) shows the color contrast analysis along the path. The color difference between the background and the crack allows the automatic determination of crack tip position in the images.

This image treatment depends on the lighting and surface conditions. If the program is unable to judge correctly the crack tip positions, a manual override is available. If the manual override is required, the above protocol has three additional steps:

4. The automatic judgment by the program is displayed on the images.
5. The user manually verifies the positions, either accepting it or rejecting it.
6. If the position is rejected, the user chooses another position by clicking on the image to identify the tip of the crack front.

Once these steps are complete, the crack tip position are displayed in a series of image, as shown in Figure 3.6 (d). The Matlab program also creates a file containing the coordinates (in pixel number) of the crack front along with the time stamp on the image used to identify the positioning. Combining the absolute distance of dust particles from the hole and the crack tip positions on the images, one can obtain the absolute distance of crack tips from the

hole, *i.e.* the crack length. Subsequently, knowing the distance the crack front propagated over a time period gives the crack front velocity.

3.4.2 Fracture surface analysis

3.4.2.1 AFM principles

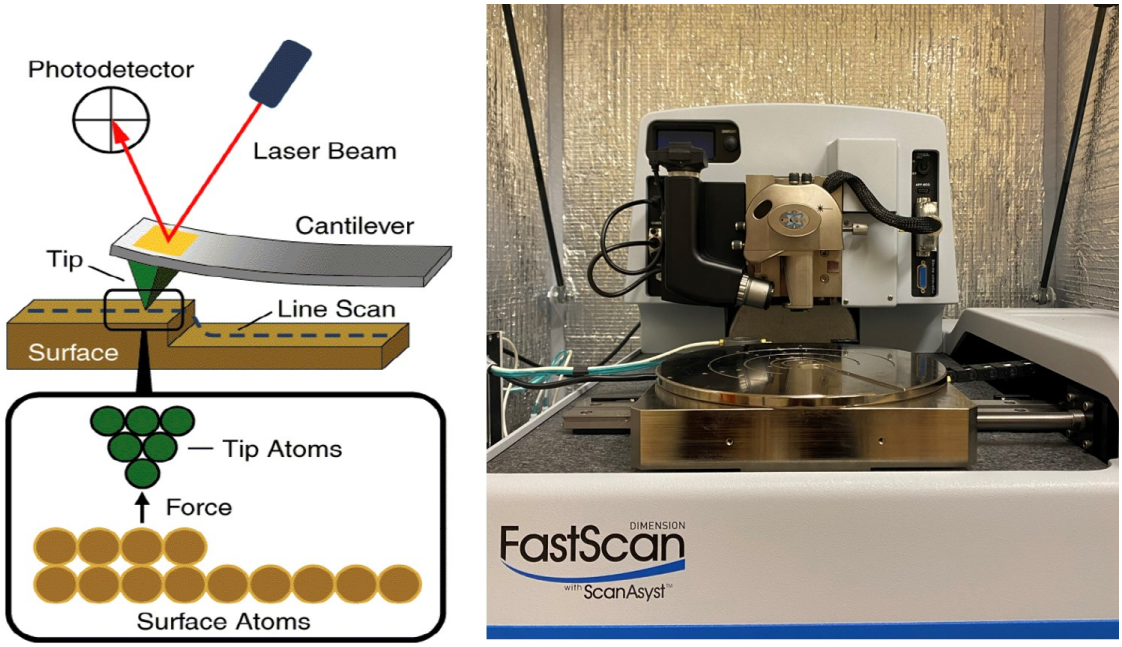

Figure 3.7: (a) Principle of AFM [2]; (b) Photo of Dimension FastScan AFM of Bruker.

The Atomic Force Microscope (AFM) is widely used to quantify topological surface properties of materials [117], including glass surfaces [5, 208]. Beyond topographies, it also provides nano-mechanical information. In general, an AFM is based on the atomic interaction between the tip and the sample surface. Figure 3.7 provides a simplified sketch of the AFM. Before bringing the tip in contact with the surface, it must be set up. The AFM tip sits on the end of a cantilever. A laser shines on the cantilever and then reflects onto a photodiode. Manual adjustments of the laser positioning maximizes the signal on the photodiode. Subsequent adjustments of the photodiode ensures the central positioning of the laser on the photodiode.

Once the tip is setup, sample mounting takes place. To study a fracture surface, the sample is placed on the metal stage and held in place by a vacuum. The stage allows for the (x,y) positioning of the sample under the AFM tip. An optical microscope in conjunction with an (x,y) positioning system permits a mapping of the surface, which allowed me to select a region of interest. Subsequently, the tip is brought in contact with the sample.

The detection of the surfaces properties relies on the tip's interaction with the surface. As the tip moves over the surface, the position of the laser spot on the photodiode moves. To

maintain its central location on the photodiode, a feedback loop controls the vertical extension or contraction of the piezoelectric ceramic scanner where the AFM tip plus cantilever is mounted. Depending on the tip/surface interaction and the nature of the probe motion, the AFM can be operated in a number of modes, including contact mode, tapping mode, and PeakForce(PF)-Tapping.

The Interdisciplinary Multiscale Atomic Force Microscope Platform (IMAFMP) provides high-resolution topographies of the surfaces. This platform is based on a Bruker Dimension V FastScan/Icon AFM. Figure 3.7 (b) depicts the AFM setup with the ICON head used herein. Experiments herein employ the PF-Tapping mode with SCANASYST-AIR probes by Bruker, which has a normal tip radius of $2nm$. The spring constant of the cantilever is $0.4N/m$. The PF-Tapping mode controls the force excreted on the sample by the tip at every pixel and captures a force curve. These curves reveal not only the topography but also nano-mechanical material properties such as reduced modulus, adhesion, indentation, *etc.* It should be noted that the PF-Tapping mode with SCANASYST-AIR tips on glasses do not aid significantly in revealing nano-mechanical properties as the cantilever is rather soft compared to glass. Nevertheless, this operation mode is extremely favorable as a soft cantilever causes less damage to the tip. This is due to lower applied forces between the tip and the surface during scanning.

To study a fracture surface, several different AFM image sizes were taken to find the best size in revealing the phase separation and the statistical surface properties. In the end, it was decided that $500 \times 500\ nm^2$ images reveal the phase separation well and $10 \times 10\ \mu m^2$ images work well for measuring statistical surface properties. For each image, the pixel number is 512×512. Post treatment of AFM images relies on the software Nanoscope Analysis by Bruker and in-house Matlab programs. Second order plane fit and second order flatting are applied on each image for optimizing the clarity of microstructure.

3.4.2.2 RMS calculation

The calculation of RMS originates from its definition - the standard deviation of the height of the surface (h_i) from the average height of the plane (h^{fit}):

$$RMS = \sqrt{\frac{1}{N} \times \sum_{i=1}^{N} (h_i - h^{fit})^2}. \tag{3.10}$$

The calculations are done by Nanoscope Analysis on the AFM images of size $10 \times 10\ \mu m^2$ after second order plane fit.

3.4.2.3 Structure function of fracture surface

As reviewed in Section 2.4.4, equations (2.33) and (2.34) are structure functions of the fracture surfaces in inhomogeneous solids. They characterize fracture surfaces after crack propagation in a heterogeneous solid. $10 \times 10\ \mu m^2$ AFM height sensor images are used for obtaining the structure function parameters, namely Poisson's ratio ν, microstructure length scale ℓ and disorder strength θ. These two functions evidence a linear relationship between

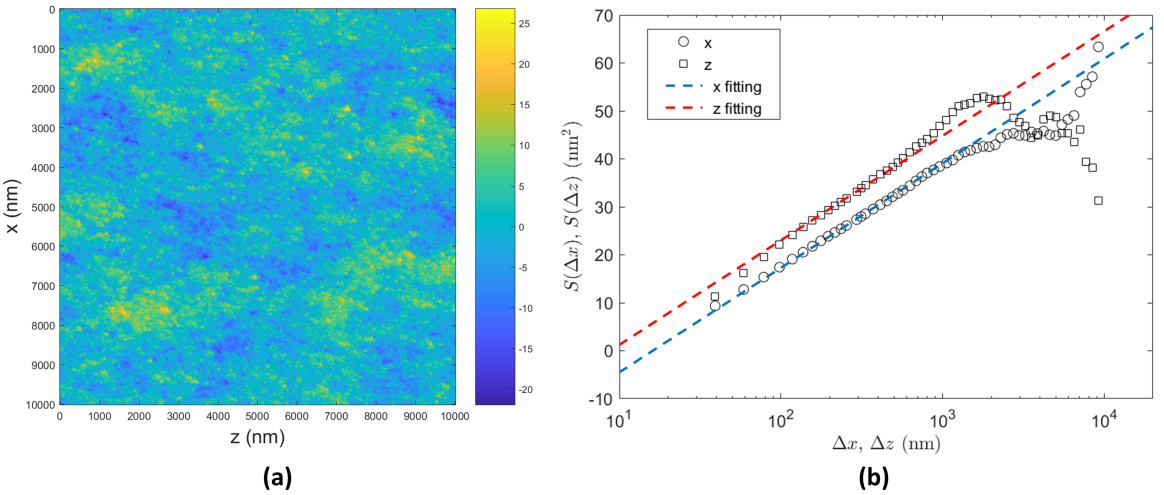

Figure 3.8: (a) Typical AFM image of a fracture surface after a parabola plane. Image of size $10 \times 10\ \mu m^2$; (b) Computation of the structure function on a fracture surface and fitting curves on data points. x direction is parallel to the crack propagation direction; and z direction is parallel to the crack front.

$S(\Delta x)$ and $S(\Delta z)$ with $log(x)$ and $log(z)$, respectively.

The structure functions are calculated as follows. First, the raw AFM height sensor data are exported to a *txt* file via Nanoscope Analysis. A Matlab program developed by Daniel Bonamy (SPEC/CEA-Saclay) reads the *txt* file and picks up the height sensor data. Data is treated with either a first order plane fit or a parabola plane fit. Figure 3.8 (a) displays a typical fracture surface after a parabola plane fit. Figure 3.8 (b) shows its structure function (curve fitting in the $10^2 - 5 \times 10^2\ nm$ length scale range). For small-length scales, the heterogeneity disturbs the computation. On the other hand, large-length scales are distorted by the data fits. Between the two scales (normally the curve fitting is done between $10^2 - 5 \times 10^2\ nm$) linear fits are possible for both $S(\Delta x)$ and $S(\Delta z)$. These two fits should be parallel and, hence, have the same slope. This allows us to invoke the theoretical structure function model from [9] (see Section 2.4.4) on real experimental fracture surfaces. Fitting the surfaces to these equations provides 3 constants: ν, ℓ and θ. The value of ℓ is an estimation of phase size L in an APS glass.

Subsequently, Part I is primarily dedicated to the validation of the experimental setup. Nonetheless, it does provide a homogeneous glass to compare APS-SBN glasses with. Hence, in this spirit, I will first review previous data concerning physical and mechanical properties of SBN 12. Afterward, it presents SCC tests on SBN12 to validate the experimental setup.

Part I

Testing experimental setup on SBN12 samples

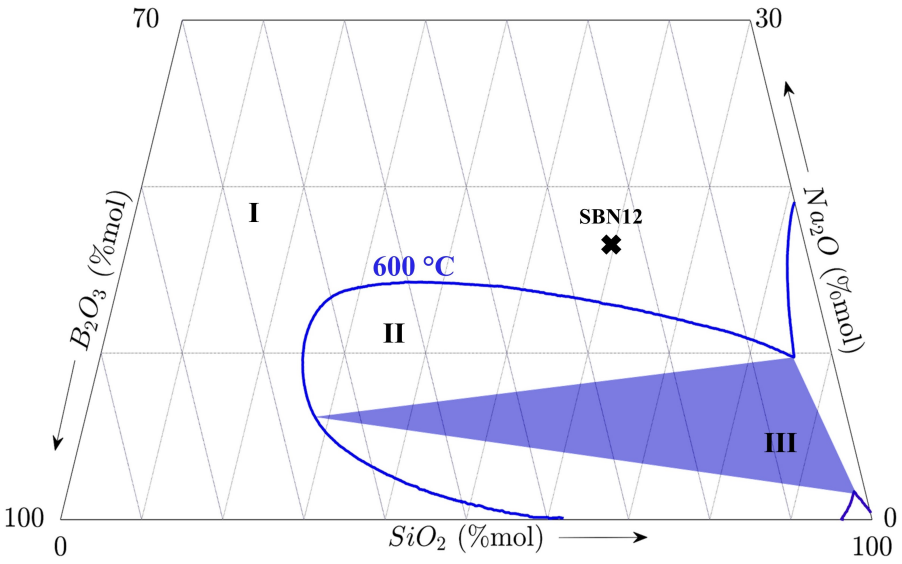

Figure I.1: Immiscibility diagram posed by Haller [106] for SBN systems at 600 °C with the location of SBN12 marked by the black cross.

At the beginning of my PhD, I built up the experimental set-up for SCC experiments, including the humidity control system and the automatic image capture system. In order to test the equipment, some surplus SBN samples from M. Barlet's thesis [10] were used. Out of the remaining samples, I selected SBN12, of which the chemical composition tested by ICP-AES (Inductively Coupled Plasma Atomic Emission Spectroscopy) is 59.6SiO_2-23.9B_2O_3-16.5Na_2O (in mol%). This sample was selected over others for the following reasons:

- The amount of Na_2O was relatively low compared to other samples.
- It is near the phase-separated zone for 600 °C, but not in it. Figure I.1 shows the positioning of SBN12 with Haller's immiscibility diagram.
- There were more SBN12 samples available, compared to the other chemical compositions.

Concerning the last point, SCC tests require high quality samples (minimal visual bubbles and waves). M. Barlet selected the best samples for her SCC tests by visual examination. I too selected the best SBN12 samples for testing the experimental setup, but the samples are somewhat of poorer quality. These results will be presented herein and compared to M. Barlet's works for testing the equipment setup. In short, SBN12 provided a means for testing the experimental setup; additionally, they provided a homogeneous glass (as compared to heterogeneous APS glasses in subsequent parts) to test fracture surface analysis.

Recalling the goal of this thesis is to study APS glasses, which require annealing protocols to provoke phase separation. Concerning SBN12, it is located outside of the phase-separated zone; one does not expect phase separation; and the leftover samples are of lesser quality. Nonetheless, for assessment purposes, SBN 12 underwent annealing. Annealing protocols were selected based on tests concerning APS samples (detailed in Part II). The same thermal treatments were performed on SBN12 samples as APS samples: T_a=600 °C for t_a=4h and

Table I.1: Sample list of SBN12

Sample name	Fabrication protocol	Characterizations
SBN12-pristine SBN12-600C-04h SBN12-600C-18h	Protocol C	Density, Elastic moduli, SCC, AFM
SBN12-L SBN12-S	Protocol C	SCC by M. Barlet [10]

18h. Table I.1 provides a list of samples used herein and characterizations performed on them. After annealing and SCC, it was determined that the samples were in much poorer condition than originally thought. Hence, due to the poor quality of the samples, SCC curves for annealed samples are out of reach. Appendix A.6 does detail the results for completeness. Tests did provide a few useable regions to examine post-mortem fracture surfaces; these results are presented herein.

Part I–SBN12 is arranged as follows. Section I-1.1 reviews the structural characterizations know in literature concerning SBN12 pristine samples, including Raman spectrum [14, 10] and NMR [10] spectra. Section I-1.2 presents the density and elastic moduli results. Section I-2.1 shows the SCC curves of SBN12-pristine in comparison with the previous results [14, 10]. Section I-2.2 presents post-mortem fracture surface as revealed by AFM imaging. This last section is broken into two sub-sections revealing characterization results of the surfaces concern RMS techniques (Section I-2.2.1) and the structure function model (Section I-2.2.2).

Chapter I-1

Structural characterizations and physical properties of SBN12

Contents

SBN12 structural and physical properties were analyzed in detail during M. Barlet's thesis [10] and will be reviewed herein. Since the chemical composition of SBN12 is outside the phase separation area, annealing the SBN12 pristine samples should not have a meso-scale phase separation. Thus, the structural characterizations and physical properties of SBN12 pristine samples should be representative of the SBN12 annealed samples.

I-1.1 Structural characterizations of SBN12: a review

Figure I-1.1 shows the Raman spectrum of SBN12 pristine samples from [10]. The contribution of different structures on the Raman spectra in low sodium content listed in Section 3.2.2 can be identified in this spectrum, as indicated by the blue dashed lines. It is worth noting that R_{SBN} (R_{SBN}=[Na_2O]/[B_2O_3]) of SBN12 is slightly greater than $0.5 + 0.0625K_{SBN}$. Thus, SBN12 should have NBO atoms on the silica units, *i.e.* the formation of Q_3 units (equation (2.11)). Additionally, the peak at 700 cm^{-1} indicates the formation of metaborate units in SBN12, signifying that NBO atoms exist in borate units. Changing the chemical composition can result in peak position shifting and line shape changes [82]. For a more detailed analysis, please see the investigation by M. Barlet where she varied the R_{SBN} value for a fixed K_{SBN} value [10, 14].

Figure I-1.2 (a) depicts the ^{11}B MAS NMR spectrum for SBN12. Analyzing the area under the curves provides details about the boron coordination (Section II-1.4.1.1 details the decomposition of the spectrum). ^{11}B MAS spectrum of SBN12 (Figure I-1.2 (a)) indicates about 60% of boron in the glass consists of B[IV] and 40% of the glass concerns B[III]. Additionally comparing the amount of Na^+ ions in the glass to the number of B[IV] provides an idea of the number of NBO atoms in the glass. SBN12 is unlike the two other chemical compositions investigated herein (Part II and Part III) as a few NBO atoms are expected, about 2.1%. Ideally, as $0.5 + 0.0625K_{SBN} < R_{SBN} < 0.5 + 0.25K_{SBN}$, these NBO atoms should be isolated to the silica network, *i.e.* forming Q_3 units [58]. Theoretical calculations

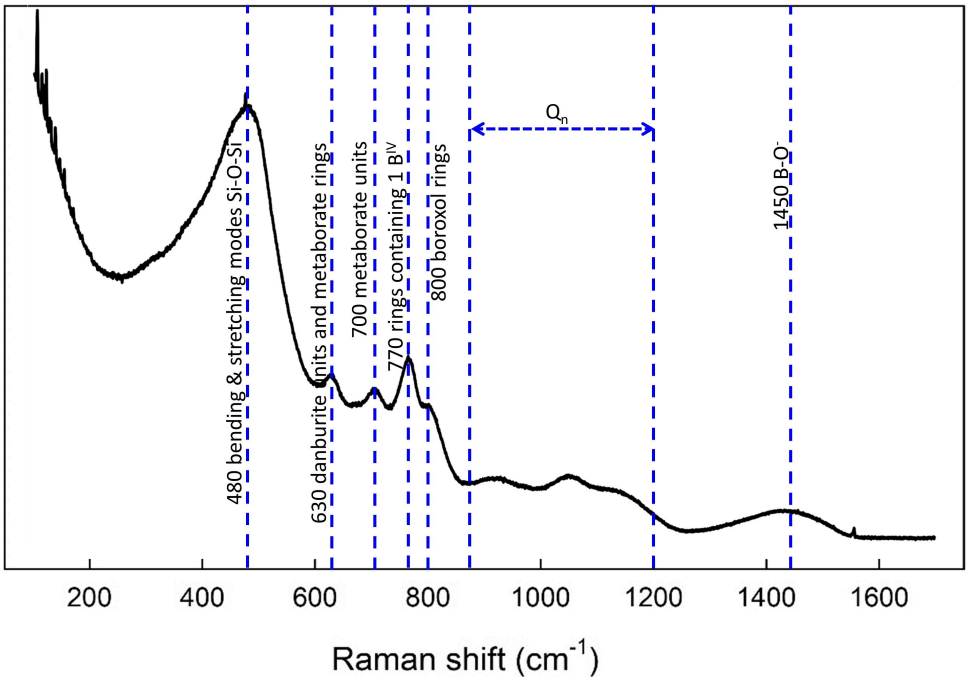

Figure I-1.1: Raman spectrum on SBN12 pristine samples from [10] with the position of peaks and bumps (blue dashed lines).

(equation (2.11)) with the chemical composition of SBN12 estimate that the fraction of Q_3 is about 2.8%. Hence, experimental values are rather consistent with theoretical calculations.

Figure I-1.2 (b) shows the ^{23}Na MAS NMR spectrum [10]. The peak position of the ^{23}Na MAS spectra indicates if Na^+ ions are acting as charge compensators (negative peak in the chemical shift) or network modifiers (moderately negative to positive values in the chemical shift). For SBN12, the peak of ^{23}Na MAS NMR spectrum is around -19 *ppm*, which indicates that the Na^+ ions are acting as charge compensators. For a more detailed analysis, please see the investigation by M. Barlet where she varied the R_{SBN} value for a fixed K_{SBN} value [10, 14].

I-1.2 Physical properties of SBN12

SBN12 physical properties were analyzed in detail during M. Barlet's thesis [10]. Nevertheless, fluctuations of chemical compositions between batches, or even in the same batch due to imperfect mixing, cannot be avoided. This can lead to minor variations in the material behavior. As these experiments are rather short, they will be redone herein. Subsequently, they are compared and contrasted with M. Barlet's results. The methods used for the measurements by M. Barlet and me are the same: Archimedes' method for density measurements (Section 3.3.1) and ultrasonic echography techniques for elastic moduli measurements (Section 3.3.2). However, she used hydrostatic balance specifically designed for density measurements; I used the same but a homemade setup (see Appendix A.1). Hence, her results should be more accurate.

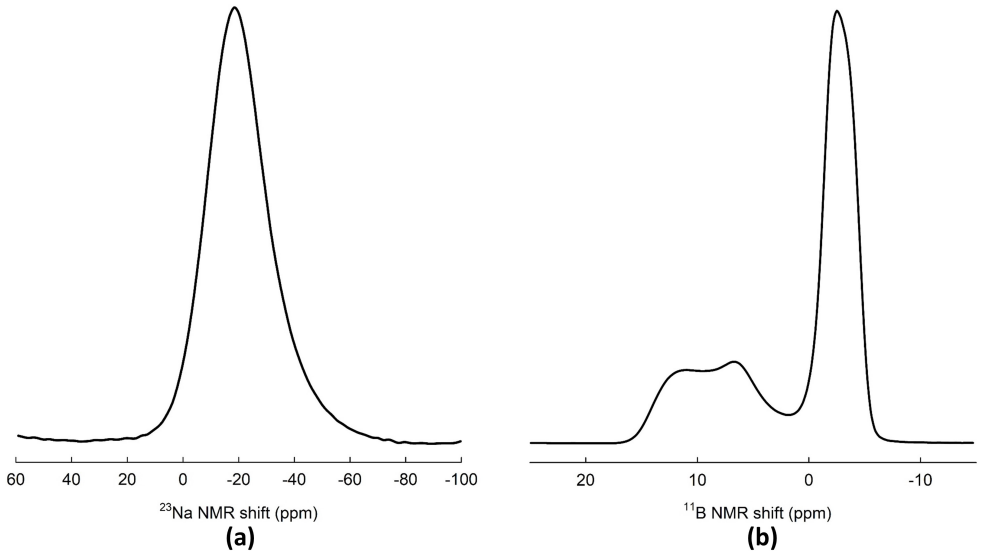

Figure I-1.2: (a) ^{11}B MAS and (b) ^{23}Na MAS spectra of SBN12. [10]

Table I-1.1: Density and elastic moduli of SBN12 DCDC samples. Uncertainties for moduli and Poissons ratio are calculated based on propagation of uncertainties (see Appendix A.2).

Sample names	ρ (g/cm^3)	K (GPa)	G (GPa)	E (GPa)	ν
SBN12-pristine	2.53 ± 0.05	48 ± 2	32.3 ± 0.4	79 ± 2	0.223 ± 0.007
SBN12-600C-04h	2.53 ± 0.05	48 ± 2	31.6 ± 0.9	78 ± 2	0.232 ± 0.011
SBN12-600C-18h	2.37 ± 0.05	44 ± 2	30.5 ± 1.1	74 ± 3	0.218 ± 0.016
SBN12-Barlet [10]	2.4619 ± 0.0003	-	-	80.10 ± 0.03	0.208 ± 0.06

Table I-1.1 lists my results for the density and elastic moduli measurements on SBN12 samples along with the results from M. Barlet [10]. Recalling that SBN12 is outside the phase separation area. Thus, annealing should not induce differences between the physical properties of SBN12 pristine and annealed samples. Considering the results, the densities, Young's moduli, and Poisson's ratio of SBN12-pristine, SBN12-600C-04h and SBN12-Barlet are rather similar considering the measurement uncertainties, while the value of SBN12-600C-18h stands out. Additionally, SBN12-600C-18h clearly had issues with bubbles (see Appendix A.6), which were seen after fracture, which lead to an underestimation of the density.

It is worth noting that experimental differences could lead to fluctuations in data. There are several factors that could lead to these variations: (1) equipment differences, (2) difference in sample sizes, (3) difference in sample batches, and (4) small sample defects (although I tried to avoid small defects). Concerning the samples sizes, M. Barlet used a large cylindrical samples (30 mm in diameter and 10 mm in height) specifically designed for Young's modulus measurements and density measurements. I used the DCDC samples after fracture (about $2.5 \times 5 \times 25$ mm^3). The larger samples depend less on small defects (although I tried to avoid small defects). Based on previous measurement and considering the sample sizes, the

measurements by Archimedes' methods herein have estimated uncertainties of about 0.05 g/cm^3 (see Section 3.2.1). Additionally, SBN12-600C-18h clearly had issues with bubbles (see Appendix A.6), which were seen after fracture. In addition, a big sample batch with visible wavy lines may be a signal that the material did not mix well due to the viscosity, which leads to minor differences in properties after cutting into different pieces. In general, the fluctuations of density and elastic moduli are considered reasonable due to measurement uncertainties.

Chapter I-2

Stress corrosion cracking of SBN12

Contents

This chapter concerns the stress corrosion cracking of SBN12 samples, which aids in confirming the experimental setup. Additionally, it will present post-mortem analysis concerning SBN12 pristine and annealed samples. Stress corrosion cracking (SCC) experiments have been performed on SBN12 pristine and annealed samples. However, as mentioned at the beginning of Part I, these samples are remaining from M. Barlet's thesis. I selected the best SBN12 sample for testing the experimental setup. Like mentioned previously, a few of the remaining samples underwent annealing protocols; however, the samples were of poorer quality than originally thought. For example, samples exploded (underwent fast fracture in an inappropriate way) during SCC test or had damage which prevented SCC tests. Nevertheless, I attempted to analyze the annealed samples SCC behavior before they exploded. Unlike a normal SCC curve (see Figure 2.11) of SBN glasses, large fluctuations and shifting in the SCC curves occurred for annealed SCC curves of SBN12 (see Appendix A.6 for details). The determinations of slopes and K_E become impossible. Hence, all annealed SCC curves were rejected for SBN12. Consequently, the SCC data points of annealed SBN12 samples (SBN12-600C-04h and SBN12-600C-18h) will not be presented in the main text. For completeness, they are found in Appendix A.6.

Nevertheless, the fracture surfaces of these samples after SCC can still be used for post-mortem analysis. The existence of unexpected damages, impurities, bubbles or residual stresses changes the stress concentration around crack front. However, my fracture surfaces analysis techniques concern the interactions between crack front and material at nanometer scale. Hence, I hypothesized that the deviation of stress concentration due to these large-scale defects has minor effects at small scale. Post-mortem analysis will be performed on SBN12-pristine, SBN12-600C-04h and SBN12-600C-18h samples.

I-2.1 SCC experiments on SBN12

Figure I-2.1 shows my experiment results for SBN12 pristine (blue circles) and the results from M. Barlet's thesis. During her thesis [10], two different DCDC sample sizes were used:

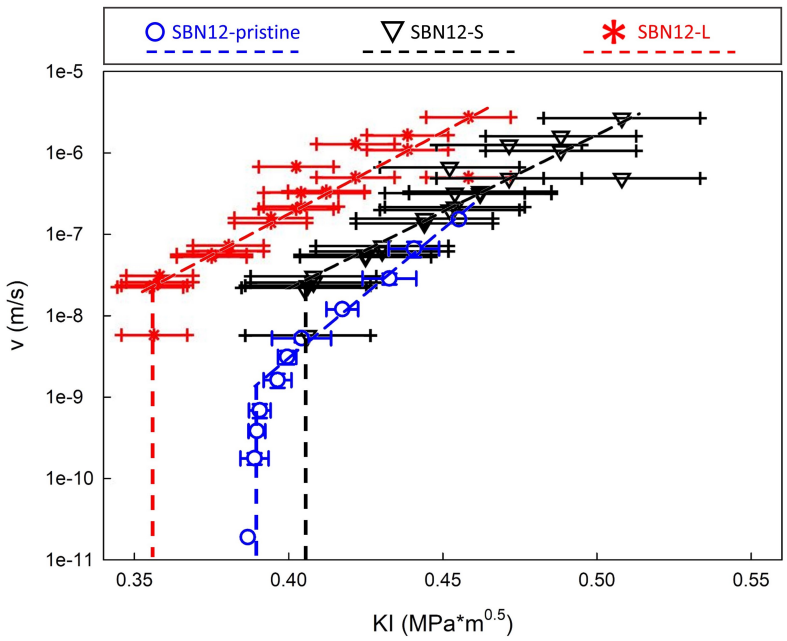

Figure I-2.1: Stress corrosion cracking curves of SBN12-pristine (blue circles) and the results from M. Barlet's thesis – SBN12-L (red stars) and SBN12-S (black inverted triangles) along with the error bars and the fitting curves along with the environmental limit (vertical line) shown by dashed lines.

SBN12-L for large SBN12 samples of size $5 \times 5 \times 25\ mm^3$ (red stars) and SBN12-S for small SBN12 samples of size $2 \times 0.8 \times 25\ mm^3$ (inverted black triangles). Data in Figure I-2.1 exemplifies the two lowest regions of a SCC curve – Region 0 (K_E) and Region I in Figure 2.11.

Region 0, or K_E, provides the environmental threshold limit of the stress intensity factor (*i.e.* for $K < K_E$, the stress on the crack front is not sufficient for the crack front to interact with the environment; hence, the crack front will not propagate). Table I-2.1 presents the values of K_E for SBN12. Considering K_E of SBN12-L and SBN12-S [10], there is a horizon shifting of $0.05\ MPa \times m^{0.5}$ between them. Between these two samples, there were a number of difference: (1) sample sizes, (2) the small sample required a guide to prevent buckling, (3) different batches, (4) minor differences (especially concerning the tape) between experimental setup, *etc.* Nonetheless, they were deemed similar and the difference should be just the error between runs. Clearly, the environmental limit of SBN12-pristine is between SBN12-L and SBN12-S. Although more experiments are needed to quantify the uncertainties between experimental setups, the time of a single experiment makes this difficult. Hence, the environmental limit of all three samples should be considered within the error of the calculations and/or experimental setup. Additionally, the standard deviation between these experiments ($\delta K_E = 0.025\ MPa \times m^{0.5}$) aids in judging if experimental setups should be considered the same in subsequent analysis.

Turning to Region I, two different models are commonly used to evaluate the relationship between v and K_I, including Wiederhorn's exponential law (equation (2.29)) and Maugi's power law (equation (2.30)). Fitting these data points allow one to obtain

Table I-2.1: Estimated values of β (exponential laws), n (power laws) and K_E from the data points in Figure I-2.1.

Sample name	β	n	$K_E(MPa \times m^{0.5})$
SBN12-pristine	31 ± 2	31 ± 2	0.389 ± 0.001
SBN12-L	20 ± 2	19 ± 2	0.357 ± 0.001
SBN12-S	19 ± 2	20 ± 2	0.406 ± 0.001

the slopes β $(d(log(v))/dK_I)$ for exponential laws [268, 49] and the fatigue parameters n $(d(log(v))/d(log(K_I)))$ for power laws [174, 105]. Table I-2.1 presents the fitting parameters β and n in Region I for the different samples. Comparing different samples reveals a difference in the slopes. The slope of SBN12-pristine is higher than SBN12-L and SBN12-S; however, the data points between SBN12-pristine and SBN12-S are clearly in the same region. A number of differences between M. Barlet's experimental setup and mine can influence this:

- My experiments were done in an active temperature controlled environment via an air-conditioning unit ($T = 18.5 \pm 0.5$ ℃). M. Barlet's was done in ambient conditions (an underground room within the center of the building, $T = 28 \pm 3$ ℃ [14]);
- My experiments were done in an active humidity controlled environment via a home-made feedback chamber ($RH = 40.0 \pm 0.5\%$). M. Barlet's was done in ambient conditions (an underground room within the center of the building, $RH = 45 \pm 7\%$ [14]);
- My experiments were done with a dual-screw Deben machine. M. Barlet's was done with a single-screw Deben machine.

Expanding on the last point, the new Deben loading machine with dual screws provides a better loading of the sample via a more parallel force application. Hence, the crack propagation at low velocities is more stable. Beyond experimental setup differences, data treatment methods (see Appendix A.3) varied between the two setup, which leads to the reduction of error bars in my experiments. This deviation is acceptable as the data points stay in the same area as the previous results.

In conclusion, the equipment changes have minor influences on experiment results. Nonetheless, my experimental data points remain in the same area as the previous results [10]. It confirms the reliability of experimental set-up.

I-2.2 Post-mortem analysis on fracture surfaces

After SCC experiments, the samples are broken into two pieces. These surfaces can then be analyzed via RMS calculations and statistical tools [9]. AFM imaging provides high-resolution topographical images of the fracture surfaces. Figure I-2.2 concerns the fracture surfaces characterized via the AFM height sensor. The images are of size 500×500 nm^2 (top row) and 10×10 μm^2 (bottom row) on the pristine (left column), SBN12-600C-04h (center column) and SBN12-600C-18h (right column) samples. With the same color scale, these images display similar topographies. Post processing these images provides quantitative information, including the RMS calculation and the structure function analysis [9].

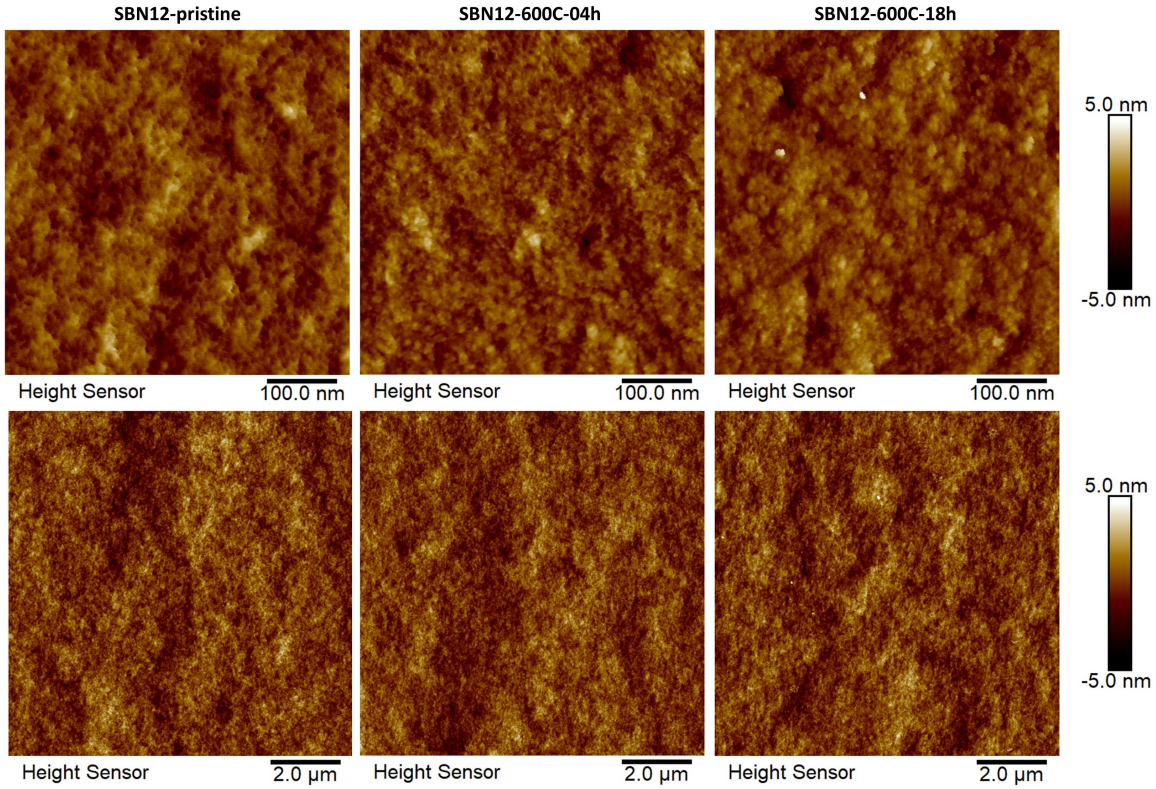

Figure I-2.2: AFM height sensor images of SBN12 fracture surfaces for pristine and annealed samples. The sizes of images are 500×500 nm^2 for the first row and 10×10 μm^2 for the second row. The color bars remain the same for all images.

I-2.2.1 Evolution of fracture surface roughness

RMS calculations were performed on the 10×10 μm^2 AFM images of the three samples: SBN12-pristine, SBN12-600C-04h and SBN12-600C-18h. Table I-2.2 presents the results. Results here concern the average of at least four sets of images for statistics. The samples have RMS values separated by less than two standard deviations; hence, one cannot eliminated that they are the same.

Recalling that SBN12 is outside the phase separation area, annealing should not lead to significant micro- nor meso- scale structural changes. Thus, the local interaction between crack front and material remains similar for the pristine and annealed samples. The similar

Table I-2.2: RMS and structure function analysis on 10×10 μm^2 AFM images of SBN12 pristine and annealed samples.

Sample name	RMS (nm)	ℓ (nm)	ν	A	θ
SBN12-pristine	1.13 ± 0.04	12.5 ± 1.4	0.33 ± 0.04	0.61 ± 0.05	0.12 ± 0.02
SBN12-600C-04h	1.06 ± 0.01	10 ± 3	0.35 ± 0.04	0.57 ± 0.05	0.15 ± 0.05
SBN12-600C-18h	1.07 ± 0.09	15 ± 4	0.34 ± 0.02	0.58 ± 0.04	0.10 ± 0.03

RMS values confirm this assumption. Hence, my hypothesis that deviation of stress concentration due to large-scale defects (bubbles and other defects) has minor effects at the small scale is valid. Thus, the structural function analysis will be performed on all SBN12 samples.

I-2.2.2 Structural function analysis on fracture surfaces

Let us recall glasses are homogeneous at the continuum; however, as one scales down, glasses can no longer be considered homogeneous (see Section 2.2.1). This length scale is to some extent revealed by the process zone ahead of the crack front. Literature shows that the process zone length-scale is on the order of a few nanometers to tens of nanometers [219, 196, 220]. These length scales are difficult to access. To date, AFM imaging of post-mortem fracture surfaces along with characterization of these fracture surfaces remains one of the most feasible methods to measure the process zone length-scale. Section 2.4.4 reviewed structure function models to characterize small-scale inhomogeneous solids. These models will be used herein on SBN12, a traditionally homogeneous material (*i.e.* no phase separation expected). These results will be compared and contrasted to APS (*i.e.* SBN42 (Section II-3.3) and SBN96 (Section III-2.2)) samples in Section 4.2.

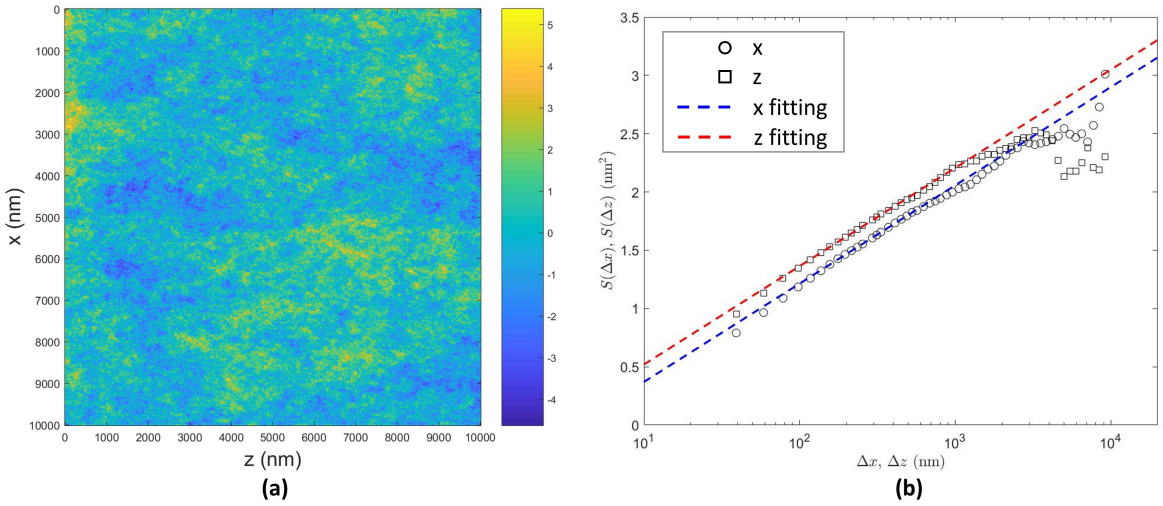

Figure I-2.3: (a) AFM image on SBN12-pristine fracture surface after parabolic fitting (x direction is parallel to crack propagation, z direction is parallel to the crack line). (b) Computation of the structure function on (a) and fitting curves on data points.

In general, SBN12 glasses can be considered as an inhomogeneous solid for the structure function analysis. The structure function of a fracture surface depends on Poisson's ratio ν (or A as a function of ν, equation (I-2.1)), microstructure length scale ℓ, and disorder strength θ [9]. Specially, the structure function is calculated on AFM images of fracture surfaces. As output, the calculations provide these parameters. Herein, I used the 10×10 μm^2 AFM height sensor images for calculating the structure functions. Section 3.4.2.3 details the analysis procedure. To validate the technique, fracture surfaces need to fit the structure function models (equation (2.33) and (2.34)). Figure I-2.3 depicts (a) a typical AFM image after parabolic fitting obtained for SBN12-pristine and (b) structure function model applied

on panel (a). Recall low length scales are influenced by the heterogeneity in glasses and large by data fits. Clearly, the two lines are parallel between 10^2 and 10^3 nm. Additionally, the values of ℓ, ν, A and θ are outputs of the procedure. Table I-2.2 presents the average values computed with more than 4 AFM images for each sample. These are the first results proving the reliability of these structure function models on experimental fracture surfaces.

Like the RMS calculations, SBN12 pristine and annealed samples have similar values, within the error bars, for ℓ, ν and θ. (All average values are the same within 1.25σ.) It further confirms that annealing the SBN12 samples does not change the general interaction of the crack front with the material at micrometer scale. Recalling that the meso-structure length scale ℓ represents the size of heterogeneities. For SBN12 samples, the heterogeneity comes from potentially two different sources: (1) ring size dispersion [264] or (2) the imperfect mixture of the silicate and borate network. The exact origins remains outside of the scope of techniques studied herein. Hence, the results herein shows that the scale of the medium-range order in SBN12 is about $10 - 15$ nm.

Considering the Poisson's ratio ν, the values estimated from the structure functions are universally higher than the values measured by ultrasonic echography (Section I-1.2, about 0.22). Nonetheless, the values estimated herein are still considered reasonable, as the calculation of the Poisson's ratio ν via the structural function models invokes several hypothesis and are idealistic [9]. Different assumptions proposed during the calculations can increase errors. Another noteworthy difference is Poisson's ratio ν estimations using fracture surfaces concern micrometer length-scales, while echography measurements are macro-scale. In summary, ultrasonic echography techniques are a standard method for measuring elastic moduli, while post-mortem fracture surface analysis provides a reasonable value for ν (within the range [0,0.5]) to confirm the reliability of structural function models.

For the parameter A, it can be calculated from ν:

$$A = (2 - 3\nu)/(2 - \nu)) \in [1/3, 1] \tag{I-2.1}$$

as the values of ν should lie in $[0, 0.5]$. When A is close to 1, *i.e.* ν is close to 0, the surface seems to be statistically isotropic while as A decreases, the surface appears more elongated in the direction of z [9]. Herein, the values of A are approximately 0.6, about the middle of the range $[1/3, 1]$. This implies some kind of anisotropy of samples. While for the parameter θ, the standard deviation of the Gaussian function for simulating the random spatially distributed component of a solid, it affects the range swept by the roughness. The values of θ can be up to 4 [9]. Herein, for the three samples, the values of θ are around 0.1, which is rather small. It indicates that the micro-structure distributions are rather random in SBN12 samples.

In conclusion, SBN12 is a homogeneous material down to length scales approximately $10 - 15$ nm. This is slightly larger than the process zone of pure silica (~ 10 nm [219]). As SBN12 is slightly more complex than pure silica due to the addition B_2O_3 and Na_2O, it is not surprising that the meso-structure length scale ℓ is only slightly larger than the process zone in pure silica. In the subsequent parts, we will see how this meso-structure length scale ℓ varies when we alter the glass structure through amorphous phase separation (APS).

To conclude this part, the experimental setup developed herein is able to control the humidity and temperature well throughout the year. SCC tests on SBN12 compared reasonably with previous tests on a different experimental setup. The fracture surfaces provide first proof of the reliability of structure function models. In the subsequent parts, we will see how material properties vary with APS in SBN glasses.

Part II

Investigations on SBN42 samples

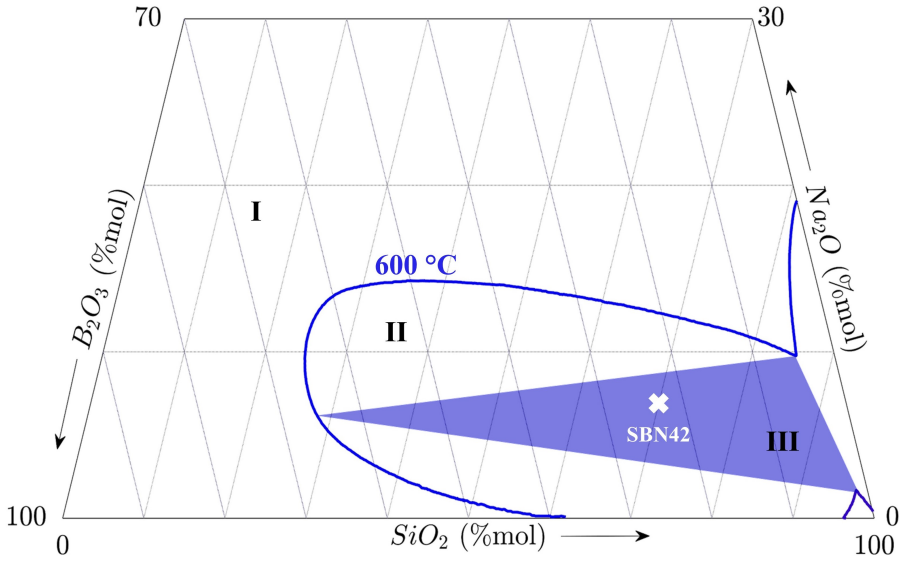

Figure II.1: Immiscibility diagram posed by Haller [106] for SBN systems at 600 ℃ with the location of SBN42 marked by the white cross.

In this part, I am going to present the results of SBN42, of which the chemical composition is 70SiO_2-23B_2O_3-7Na_2O (in mol%). As indicated in Figure II.1, this glass system is supposed to be within the hypothesized three-phase area at 600 ℃. SBN42 is the principal glass composition investigated during my PhD. Investigations on synthesizing SBN42 glasses and some preliminary characterizations were carried out by R. Baniel in University of Rennes [7]. Sample elaboration protocols concern a ToughGlass research objective. Hence, different elaboration protocol were invoked for fabricating SBN42 samples. My work focuses on detailed structural characterizations (Chapter II-1), physical properties (Chapter II-2) and SCC experiments (Chapter II-3) of SBN42 pristine and annealed samples. Table II.1 lists the nomination, fabrication protocol, batch number and the corresponding characterizations of SBN42 samples.

The next chapter details structure characterizations. AFM and TEM images reveal the spinodal tomography in the APS-SBN42 samples at meso-scale (Section II-1.1). Subsequently, XRD characterizations (Section II-1.2) and Raman analysis (Section II-1.3) confirm that annealing the SBN42 pristine samples at high temperatures for long times leads to crystallization of α-cristobalite. Concerning the short-range structure, NMR spectra evidenced some boron structural unit transversions (Section II-1.4).

Based on structure analysis, pristine samples along with two different annealing conditions (T_a=600 ℃ for t_a=4h and 18h) have been chosen for the investigations of SCC behavior. The SCC experiments invoke DCDC samples from four batches – **Batch 0 - Batch 3** (Table II.1). Some of the results were rejected due to incorrect manipulations or the occurrence of unexpected damage during the experiments. As the SCC behavior depends on the minor differences during elaboration or even the annealing process, the SCC results will be analyzed batch by batch (Section II-3.1). Post-mortem fracture surfaces as revealed by AFM imaging were performed on SBN42 DCDC samples after SCC experiments. Characterization pro-

cedures of the surfaces concern RMS techniques (Section II-3.2) and the structure function model (Section II-3.3).

Table II.1: Sample list of SBN42 along with characterization techniques samples underwent.

Sample name	Fabrication protocol	Characterizations
Small samples		
SBN42-600C-XXh-s SBN42-650C-XXh-s SBN42-700C-XXh-s (XX=2h, 4h, 6h, 18h, 24h)	Protocol A	Density, Elastic moduli, Raman, AFM
SBN42-700C-24h-s	Protocol A	XRD
TEM sample		
SBN42-pristine-t SBN42-600C-18h-t	Protocol A	TEM
Disk samples		
SBN42-pristine-d SBN42-600C-0.5h-d SBN42-600C-02h-d SBN42-600C-18h-d	Protocol A	NMR
Powder samples		
SBN42-pristine-p SBN42-600C-18h-p	Protocol A	NMR
SBN42-700C-24h-p	Protocol A	NMR, XRD
DCDC samples		
SBN42-pristine-1 SBN42-pristine-2	Protocol A, **Batch 0**	SCC (poor humidity control), AFM
SBN42-pristine-3	Protocol A	SCC (sample damaged)
SBN42-pristine-4 SBN42-600C-18h-1	Protocol A, **Batch 1**	SCC, AFM
SBN42-pristine-5 SBN42-600C-04h-1 SBN42-600C-04h-2 SBN42-600C-18h-2	Protocol A, **Batch 2**	SCC, AFM
SBN42-pristine-6	Protocol B	SCC, AFM
SBN42-pristine-7	Protocol B, **Batch 3**	SCC (long pre-crack), AFM
SBN42-pristine-8 SBN42-600C-04h-3 SBN42-600C-18h-3	Protocol B, **Batch 3**	SCC, AFM

Chapter II-1

Structural characterizations on SBN42

Contents

To better understand SCC results, the general morphology at the micro- and meso-scales of APS-SBN samples needs to be considered. This section first examines a series of samples used to quantify and qualify the general morphology of the phase-separated zone in SBN42. These studies will invoke optical microscopy imaging (Section II-1.1), atomic force microscopy (AFM) imaging (Section II-1.1.1), and Transmission Electron Microscopy (TEM) imaging (Section II-1.1.2). Subsequent sections turn to a more micro-scale imaging to aid in revealing the atomic connectivity in the glasses along with how it changes with phase separation.

II-1.1 Morphology of SBN42 APS samples

To examine the general morphology of SBN42 APS samples and how it evolves with annealing protocols, a number of small samples were fabricated initially. These small samples were fabricated with Protocol A (Section 3.1) by R. Baniel in University Rennes I (see [7] for more details). After fabrication, they were cut into small pieces and each pieces underwent a specific annealing protocol. An individual sample's annealing temperature T_a was set to either 600 ℃, 650 ℃ or 700 ℃, and annealing duration t_a was also prescribed: 2h, 4h, 6h, 18h or 24h. Samples underwent a single annealing procedure. It should be recalled, these samples have a "-s" to indicated "small samples".

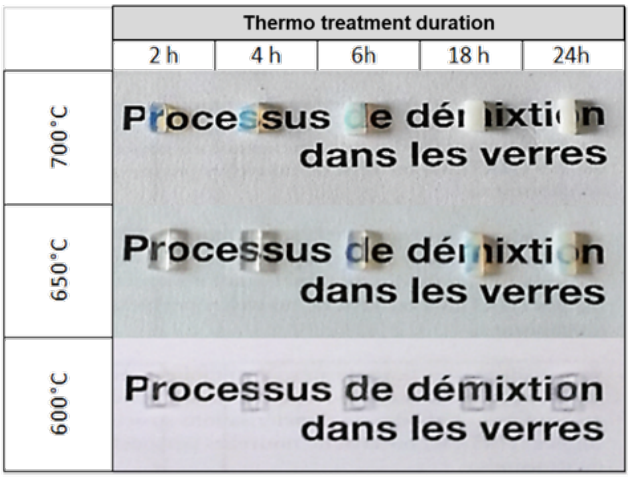

Figure II-1.1: Photo of SBN42 annealed samples on a paper with words "*Processus de démixtion dans les verres*". The samples were annealed at different temperature (T_a=600 ℃, 650 ℃ and 700 ℃) for different durations (t_a=2h, 4h, 6h, 18h and 24h).

Figure II-1.1 reveals the effects of annealing temperature and time on sample transparency. Examining this photo, one sees that the samples remain transparent (the sentence "Processus de démixtion dans les verres" can easily be read) when T_a=600 ℃ for all t_a. Annealing samples at T_a=650 ℃ for short times ($t_a \lesssim$4h), the samples remain transparent. However, increasing annealing time ($t_a \gtrsim$6h) causes the samples to become "milky". Increasing annealing temperature to T_a=700 ℃ makes the SBN42 glass samples lose their transparency very quickly ($t_a <$2h). This is evidenced by the words under the samples, as they become hard to read for $t_a \lesssim$6h and fully obscured for $t_a \gtrsim$18h. The origins of the observed opalescence may be the coursing of secondary amorphous phase [172] or the formation of crystals [186, 78]. The attenuation of light due to scattering in an APS glass or glass-ceramic depends upon the difference in refractive index of different phases [115].

After annealing, optical microscope images provides a quick means to characterize the samples and preliminary judgement of crystallization. However, the surface polish can hinder the observation of the samples. Hence, the samples were snapped in two, forming two dynamic fracture surfaces. Studying these fracture surfaces by optical microscope reveals some structural information concerning the samples. Figure II-1.2 shows optical microscope images taken with a Leica microscope (Leica DMLM). The magnification of the images is 50×. Figure II-1.2 (a) and (b) show the optical microscope images of SBN42-650C-06h-s and SBN42-650C-24h-s fracture surfaces. Dirt and sodium bubbles on the surfaces can be observed. Apart from these features, the surfaces are rather flat. Figure II-1.2 (c) and (d) show the images of SBN42-700C-06h-s and SBN42-700C-24h-s fracture surfaces. Clearly, these samples are different from the other ones, as a special conic shaped structure appears on both samples. For SBN42-700C-06h-s, the conic sizes are about 17 μm; and for SBN42-700C-06h-s, the size is about 36 μm. In addition, the density of the conic structures increases with the annealing time, as observed on the fracture surface. One can hypothesized that the

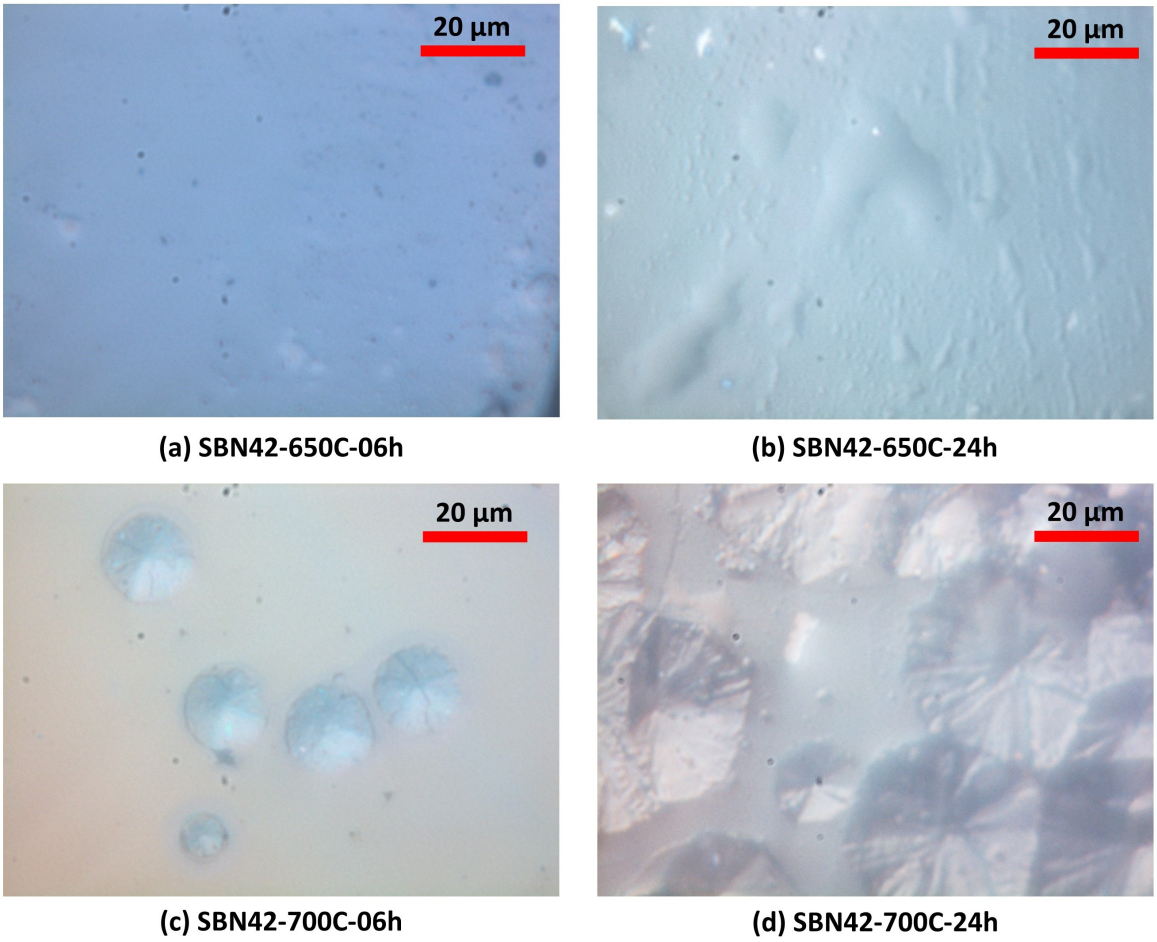

Figure II-1.2: Optical microscope images (50×) on the fracture surfaces of (a) SBN42-650C-06h-s, (b) SBN42-650C-24h-s, (c) SBN42-700C-06h-s and (d) SBN42-700C-24h-s.

conic structures are crystals. To confirm this guess, both RAMAN spectroscopy and XRD characterizations were invoked. These results are in Section II-1.2 (XRD characterizations) and Section II-1.3 (Raman analysis).

To confirm the appearances of APS in the samples annealed at T_a=600 and 650 ℃, high-resolution microscopes were invoked and the results are presented in the following two sub-sections. The first section shows the mesoscopic phase separation as evidenced by an AFM. The next section reveals TEM results, which aid in studying the boron and silicon atomic distributions in the different phases.

II-1.1.1 AFM characterizations on SBN42 pristine and APS samples

Atomic Force Microscopy (AFM) provides an excellent tool to probe phase separation in SBN glasses, when greater than a few nm [55, 265]. When dealing with APS glasses, literature frequently evidences a rather standard protocol [55, 265, 119], which is similar to the techniques used for fabricating porous glasses from APS glasses (see Section 1.2). First, as

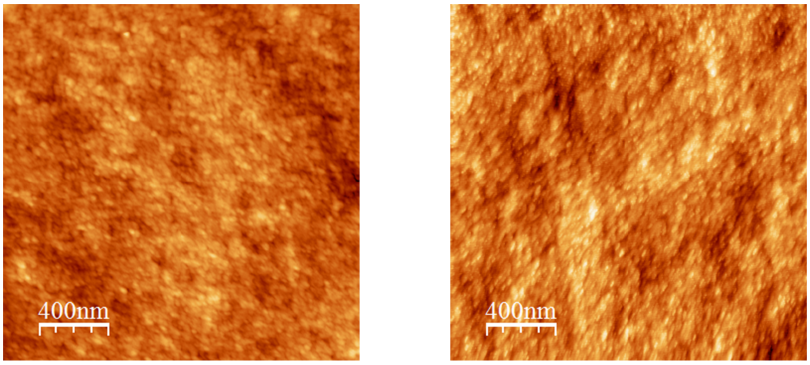

Figure II-1.3: AFM images of pristine SBN42 glass samples after being broken into two pieces. Panel (a) without and panel (b) with chemical treatment, chemical treated in HCl at 60°C for 30 mins [7]).

above, they snap the samples in two, forming two dynamic fracture surfaces. These samples undergo a chemical treatment procedure to leach out the B-rich and Na-rich phases (if exists) from the samples and leaving behind a silica rich phase [68, 149]. Herein samples are immersed in 3N HCl solution at 60 °C for 30 minutes [1].

Generally, there is no APS in SBN42-pristine samples due to the rapid quench. Figure II-3.1 depicts the pristine structure captured via an AFM before (Figure 2.6 7 (a)) and after (Figure 2.6 (b)) leaching. Neither sample revealed any inhomogeneity. Hence, pristine SBN42 samples do not display APS before nor after leaching.

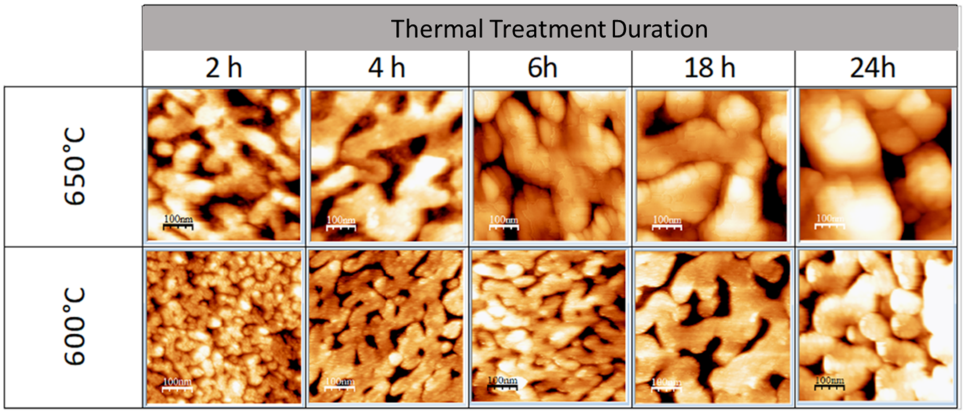

Figure II-1.4: AFM images of SBN42 after annealing at 600°C and 650°C for different times and after chemical treatment (immersion in HCl 3N at 60 °C for 30 minutes) [7].

Now let us turn to the SBN42-600C-s and SBN42-650C-s sample series. Initially, samples surfaces were scanned with an AFM. Imaging these annealed samples before leaching did not reveal the underlying structure. However, leaching (chemical treatment in HCl acid) unveiled a rich structure. Figure II-1.4 displays AFM images of SBN42 after annealing and chemical

[1]The operations in this section were done by an intern student, Rémy Baniel, at the University of Rennes as prep-work to the PhD. I continued the post-analysis of the data during my thesis.

treatment. Recalling leaching removes the B-rich and Na-rich phases, the remaining structure concerns the Si-rich phases. This series of images confirms APS in SBN42 after annealing. The 3D network geometry of these phases resembles that of a spinodal decomposition; Elmer [67] also evidenced this using a SEM. Visually comparing the images in Figure II-1.4, the phase separation evolves clearly with T_a and t_a. For a fix temperature T_a, the structure coarsens as annealing time t_a increases. Post (*i.e.* after annealing and after leaching) AFM image analysis enables a description of the growth of the Si-rich zone. This is done using the following protocol:

1. Drawing a line across the width of the Si-rich zone;
2. Measuring the width of the zone;
3. Repeating steps 1 and 2 for a total of ten width measurements for each sample;
4. Averaging the widths provides an estimated phase size L.

Figure II-1.5 (a) displays average widths of the Si-rich phase with respect to the annealing time t_a. The circles correspond to T_a=600 ℃, and inverted triangles to T_a=650 ℃. Examining this figure, one sees that increasing the annealing temperature T_a increases the phase separation process. Independent of T_a, the phase growth slows down with increasing t_a and has a tendency to saturate. Annealing times greater than 24h are required to reach APS equilibrium. Assuming a power law function to describe the evolution of the phases, one gets:

$$600\ ℃ : L = 0.18 \times t_a^{0.55} \tag{II-1.1}$$

$$650\ ℃ : L = 3.16 \times t_a^{0.36} \tag{II-1.2}$$

where L is the Si-rich phase size in nm and t_a is the annealing time in s. Figure II-1.5 (a) indicates the fits for samples T_a = 600 ℃ and T_a = 650 ℃ by blue and red dashed lines, respectively.

Recalling Section 2.2.2.2 several authors [75, 55, 265] state that spinodal APS growth should be proportional to the cubic root of t_a. Hence, assuming that the evolution of the phase size depends on the cubic root of t_a, the phase evolution is:

$$600\ ℃ : L = -33.68 + 2.87 \times t_a^{1/3} \tag{II-1.3}$$

$$650\ ℃ : L = -9.80 + 4.58 \times t_a^{1/3} \tag{II-1.4}$$

Figure II-1.5 (b) indicates the fits for samples T_a = 600 ℃ and T_a = 650 ℃ by blue and red dashed lines, respectively.

It is worth noting that both fittings follow the data well. Considering the linear fitting with $t_a^{1/3}$, the slope associated with T_a=650 ℃ fitting curve is nearly twice as large as the slope for T_a=600 ℃. In general, the phase evolution in SBN42 samples is consistent with literature. Either can be used for predicting the phase sizes of different annealing time for T_a=600 and 650 ℃.

To conclude, AFM images of SBN42 annealed samples after leaching evidence the occurrence of spinodal decomposition. The phase evolution as a function of different annealing

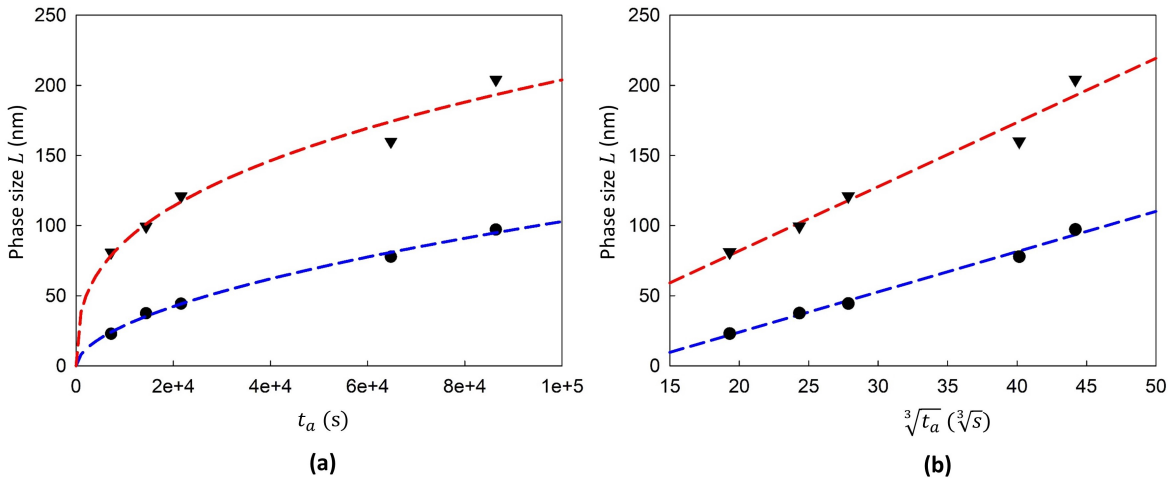

Figure II-1.5: (a) Plot of the average phase widths L as a function of the annealing time t_a. (b) Plot of the average phase widths as a function of $t_a^{1/3}$. The circles correspond to T_a=600 ℃ and their fit corresponds to the blue dashed line. The inverted triangles correspond to T_a=650 ℃ and their fit corresponds to the red dashed line. Equation (II-1.2) and (II-1.4) presents the fitting curve functions.

times is consistent with literature. Considering the annealing temperature 600 ℃, the phase size at t_a=18h is about two times larger than t_a=4h. As a result, these two annealing protocols were selected for SCC (Stress Corrosion Cracking) investigations (Chapter II-3).

II-1.1.2 TEM characterizations on SBN42 APS sample

AFM techniques provide an excellent tool quantify the sizes of the APS domains; however, it is not well suited to examine the composition of the phases. Transmission Electron Microscopy (TEM) characterizations aid in confirming the morphology of APS and clarifying the element distribution in the different phases. The SBN42-600C-18h-t annealing condition was chosen for this observation. For comparison purposes, the SBN42-pristine-t sample also underwent TEM characterization.

TEM characterization sends a beam of electrons through a specimen. As the beam passes through the sample, it interacts, and this interaction provides information on the elements in the sample. A TEM specimen needs to be rather thin (about 100 nm) for electrons to traverse a sample with minimum energy loss. Sample preparation follows these steps:

1. Cut into pieces - maximum 3 mm diameters;
2. Polishing until the thickness of pieces reduces to 150 μm;
3. Re-polish until the thickness of pieces reduces to 30 μm;
4. Put the small pieces in ionic-thinning device.

The manipulations in this section invokes the platform of THEMIS in University Rennes 1 with the aid of Ludivine Rault. Additionally, EFTEM (Energy Filtered TEM) has also been performed for illustrating the boron and silicon atomic distribution in different phases. The source of electrons is LaB6. The electrons acceleration voltage is 200 kV.

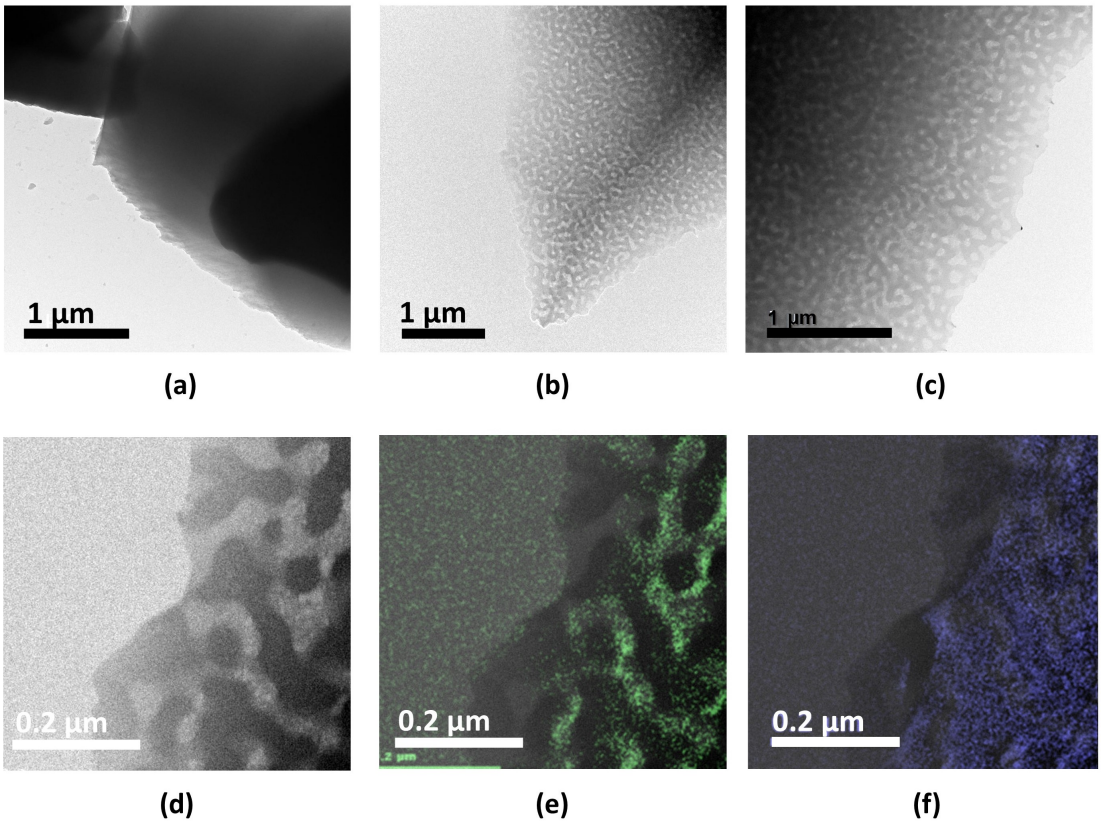

Figure II-1.6: (a) EFTEM zero loss image of SBN42-pristine-t. (b)-(d) EFTEM zero loss images of SBN42-600C-18h-t. (e) B (green) energy-filtered images of image (d). (f) Si (blue) energy-filtered images of image (d).

Figure II-1.6 (a) shows the EFTEM zero loss image of SBN42-pristine-t pieces after the special preparation. The image does not reveal any special morphology and the glass is homogeneous. On the other hand, EFTEM zero loss images of SBN42-600C-18h-t (Figure II-1.6 (b)-(d)) reveal a rich structure with variation of color darkness. The differences of chemical composition and density between different phases induce the contrast in these images. The light and dark color areas reveal the same spinodal APS morphology shown by the AFM images in Section II-1.1.1. Figure II-1.6 (e) and (f) display respectively the boron and silicon atomic distribution in Figure II-1.6 (d). According to these two maps, boron atoms concentrate in the light areas, while the silicon distribution is more homogeneous. Even so, the silicon atomic distribution is slightly less in the light areas. Hence, it can be deduced that the light color areas are B-rich phases and darker colored areas are Si-rich phases.

Additionally, it is worth noting that some "bubbles" of lighter color exist inside the B-rich phases, which might be the evidence of the existence of third phase. However, no observation has exhibited directly the third-phase because of its tiny size. More investigations should be carried out to search for a third phase and determine the chemical compositions of the different phases.

II-1.2 XRD characterizations on SBN42 samples

Section II-1.1 discussed the possibility of crystallization as the source of the opacity when T_a=700 ℃. In order to confirm the crystallization of the samples and determine their crystal structure, XRD (X-ray Diffraction) has been invoked. It should be noted if the crystals are too small, in size or density, they would elude XRD and remain undetected [199]. Hence, SBN42-700C-24h-s sample were chosen for this characterization, since the conic structures in Figure II-1.2 are the largest. If crystals exist, they should be the largest and most numerous in SBN42-700C-24h-s, making them easier to detect.

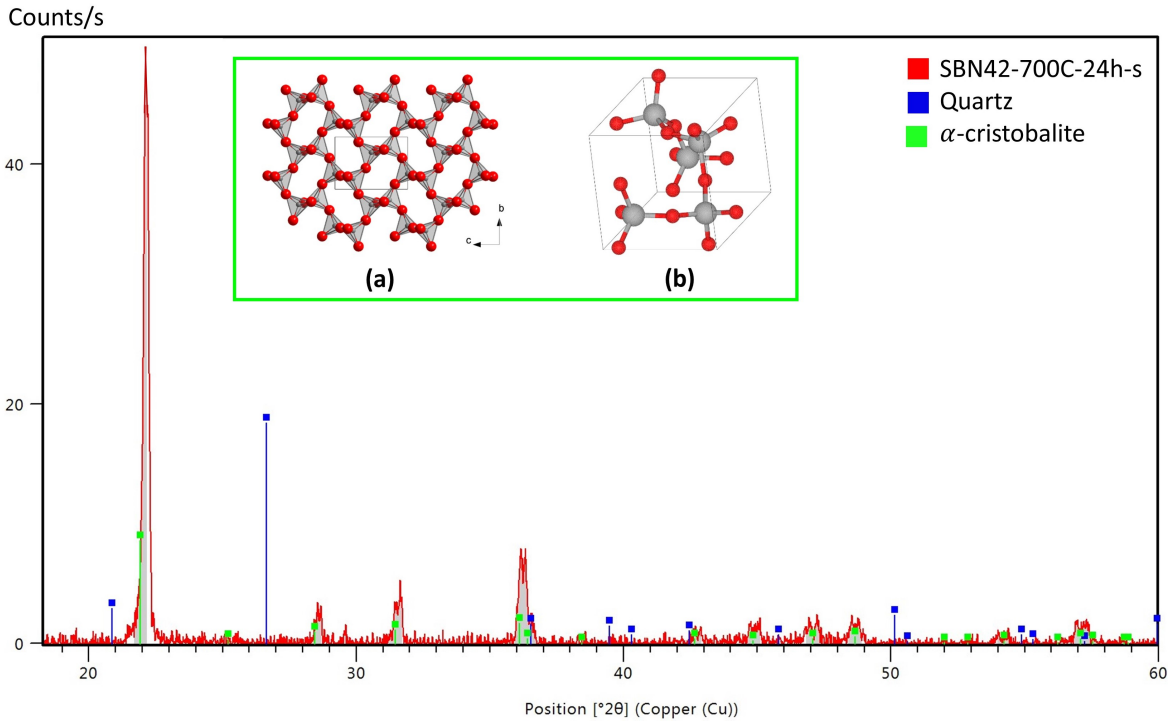

Figure II-1.7: XRD of SBN42-700C-24h-s (red line) with peak positions of quartz structure (blue rectangles) and of α-cristobalite structure (green rectangles). Embedded (a) silica α-cristobalite atomic arrangement; (b) silica α-cristobalite structure unit [51].

Figure II-1.7 displays the XRD results of SBN42-700C-24h-s. Along with the SBN42-700C-24h-s XRD pattern the image displays peak positions of the quartz structure (blue rectangles) and of α-cristobalite structure (green rectangles) found in the RRUFF database [205]. The sharp peak in the XRD data indicates crystallization in SBN42-700C-24h-s. To determine the structure of these crystals, data was compared with databases containing different crystal structures of silica, boron oxide and sodium oxide. The comparison between the XRD pattern and the reference lines evidences that the crystal formed in the SBN42-700C-24h-s corresponds to silica α-cristobalite (the atomic structure of which is shown by the embedded images (a) and (b) in Figure II-1.7). Beyond this, no other crystal structure is found according to the XRD pattern. The formation of pure silica crystals for SBN42 annealed at T_a=700 ℃ (1) enhances the theory of phase separation, (2) one of those phases

should be rich in silica, and (3) Na^+ ions should tend to be in the B-rich phase.

II-1.3 Raman characterizations on SBN42 samples

As shown in Section II-1.1, spinodal decomposition occurs in SBN42 samples annealed at 600 and 650 ℃ for all annealing times t_a. AFM images in Section II-1.1.1 reveal meso-scale $(10 - 100\ nm)$ structural changes. In order to study the short-range structural changes during APS, Raman analysis have been carried out on pristine and small samples. During Raman analysis, the interaction between the laser spot and the material concerns a small volume of sample. Thus, either fracture surfaces or polished surfaces can be used for Raman characterizations. These characterizations were done in NIMBE (CEA-Saclay, IRAMIS) with Arianna Filoramo for pristine DCDC samples and in University Rennes I by Alain Moreac for small samples.

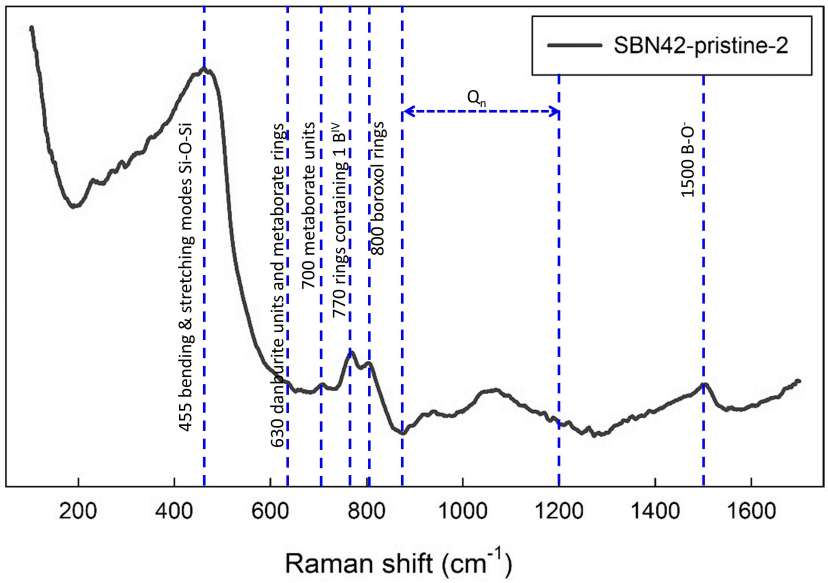

Figure II-1.8: Raman spectrum on fracture surface of SBN42-pristine-2. Blue dashed lines are for the eye and indicate several traditional RAMAN responses found in literature.

Figure II-1.8 shows the Raman spectrum on SBN42-pristine-2 fracture surfaces after SCC experiment. Recalling that Section 3.2.2 presents contributions of different structures to Raman spectra for low sodium content ($R_{SBN} < 0.5 + 0.25K_{SBN}$) glasses. There is the traditional broad band between $300 - 500\ cm^{-1}$ with pure silica peaking around $430\ cm^{-1}$. This peak corresponds to the stretching and bending modes of Si-O-Si. Here, the broadband peaks at $455\ cm^{-1}$. In the mid-range frequency, there is a peak around $630\ cm^{-1}$ attributed to daburite units and metaborate rings, and a small peak around $700\ cm^{-1}$ for metaborate units. These two peaks are hardly to be distinguished in the figure; thus, metaborate units may not exist in SBN42 as its R_{SBN} is less than $0.5 + 0.0625K_{SBN}$. Next, there are two closely located peaks centered at $770\ cm^{-1}$ and $805\ cm^{-1}$, corresponding to the six-membered borate rings with one or two B[IV] and the vibration of boroxol rings, respectively. Between

900 cm^{-1} and 1200 cm^{-1}, there is a broad band, attributed to the Q_i structures in the glass. The last broad band identified here extends from $\sim$ 1300 to $\sim$ 1550 cm^{-1} which is corresponds to various responses from the borate units and specifically the 3-coordinated units [277]. The spectrum obtained here is consistent with those found in literature about SBN glasses concerning similar chemical compositions. [82, 266].

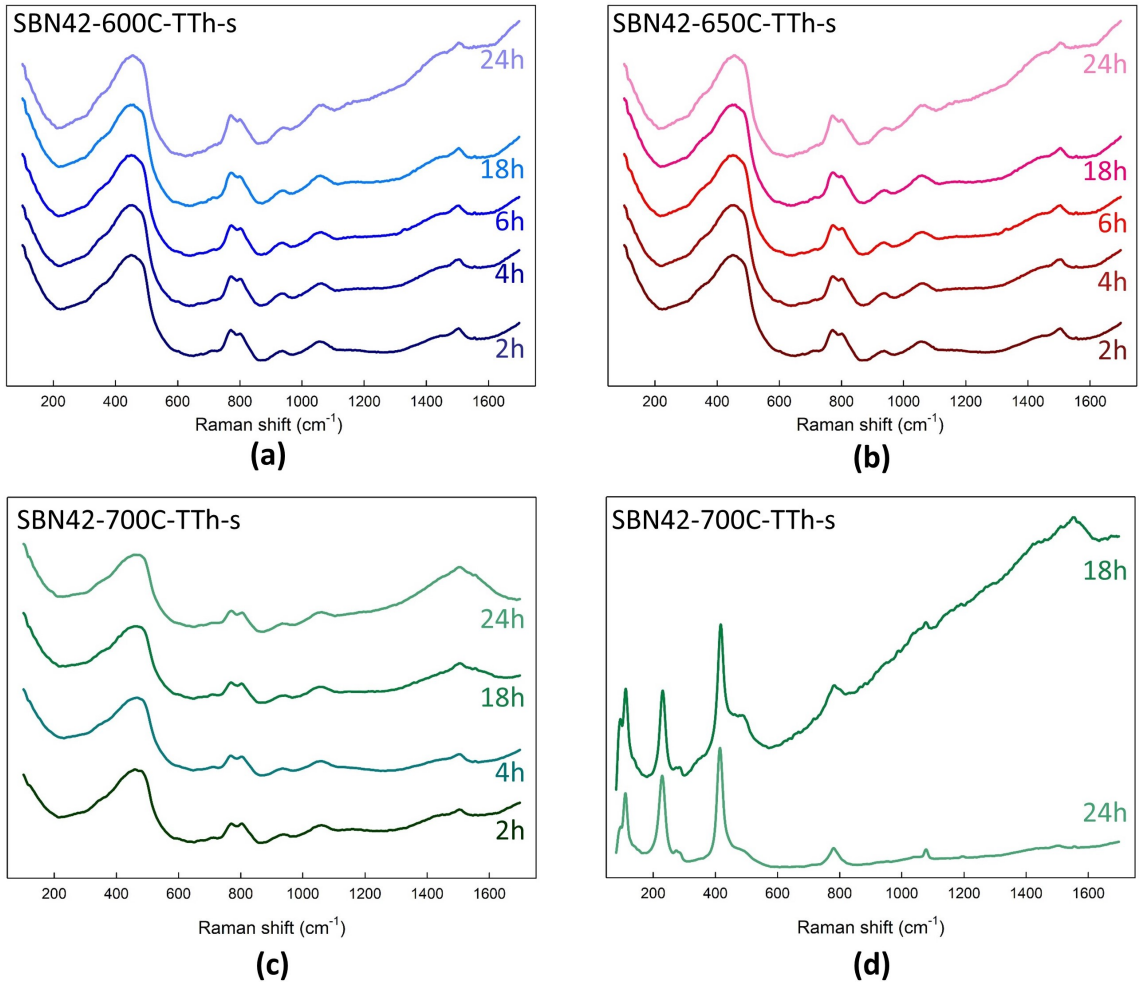

Figure II-1.9: Raman spectra of APS-SBN42 samples annealed at different temperature for different times: (a) 600 ℃; (b) 650 ℃; (c) amorphous structure of 700 ℃; and (d) crystal structure of 700 ℃.

Figure II-1.9 shows the Raman spectra for the small SBN42 samples annealed at different temperatures T_a for different times t_a. Comparing the spectra of samples annealed at T_a=600 and 650 ℃ (Figure II-1.9 (a) and (b)), no significant shifting of peaks can be observed. Moreover, the Raman signals are similar for these APS glasses and their pristine counterpart. Hence, Raman analysis for these samples does not indicate significant structure changes. Nonetheless, this is not surprising, as RAMAN characterizations for micro-heterogeneous material depend on the size of the laser spot. The diameter of the laser spot is several μm. Assuming the depth of sampling is on the same order [204], the volume of sampling is significantly larger than the order of phase separation. Hence, the laser spot is too large

to detect local structural variations between different phases. The Raman spectra obtained herein should be considered as an average of structural information of the different phases. This is coherent with White's investigation [266], who found that phase separation with small phase sizes has little to no characteristic signature in the Raman spectrum.

Now let us consider samples annealed at 700 ℃. From XRD, it is known that these samples undergo crystallization; hence, the Raman analysis are separated as I could visually select the areas for which I collected the Raman spectra. Figure II-1.10 depicts an image from the microscope of the Raman and indicates the two zones of analysis: amorphous and crystal areas.

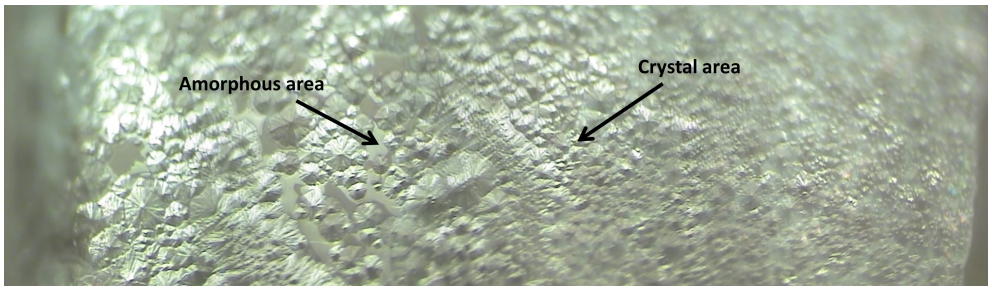

Figure II-1.10: Microscopic image of SBN42-700C-24h-s for choosing Raman characterization positions.

Figure II-1.9 (c) depicts the RamanN spectra for the amorphous areas for SBN42-700C samples for different t_a. For the most part, the spectra in the SBN42-700C samples resemble spectra in Figures II-1.9 (a) and (b). However, there is a noteworthy difference in SBN42-700C-24h-s. The last broad band identified extending from 1300 to 1550 cm^{-1} increases significantly. This is coherent with an increase in boroxol rings. For the amorphous structure, the spectra are similar to the Raman spectra for T_a=600 and 650 ℃.

Figure II-1.9 (d) depicts the RAMAN spectra when focusing on the crystalline areas (see Figure II-1.10) for SBN42-700C-18h-s and SBN42-700C-24h-s. These samples were selected due to the large fraction of crystals. The Raman spectra responses are clearly different from the amorphous areas on these samples and are dominated by three sharp peaks. They appear at low frequency ranges and are centered at 110, 230 and 415 cm^{-1}. Additionally, two small peaks exists at 780 and 1080 cm^{-1}. This five-peak Raman spectrum corresponds exactly to the Raman spectrum of α-crystoballite structure [144]. Thus, it is confirmed that there is crystallization, type α-crystoballite, in the SBN42 samples annealed at 700 ℃. Recalling that the amorphous areas do still provide a significant amorphous-like Raman spectrum, the glasses still have a Si-rich phases in the amorphous structure, and further annealing the sample will generate a larger fraction of crystals.

In general, Raman spectroscopy is not a well-suited technique for evidencing the short-range structure changes due to APS at sub-μm length scales. Nevertheless, it can reveal the structural heterogeneity of larger length scales, such as large-size APS (APS in SBN96, see Section III-1.1.2) crystal structures embedded in an amorphous media.

II-1.4 Solid-state NMR on SBN42 APS samples

This section concerns NMR characterizations on pristine and select annealing protocols for SBN42. Table II.1 lists the samples for NMR experiments, they include SBN42-pristine (-d and -p), SBN42-600C-0.5h (-d), SBN42-600C-02h (-d), SBN42-600C-18h (-d and -p), and SBN42-700C-24h (-p). Section 3.2.1 details sample preparation for disk and powder samples.

II-1.4.1 ^{11}B NMR spectra

II-1.4.1.1 ^{11}B MAS and MQMAS NMR spectra

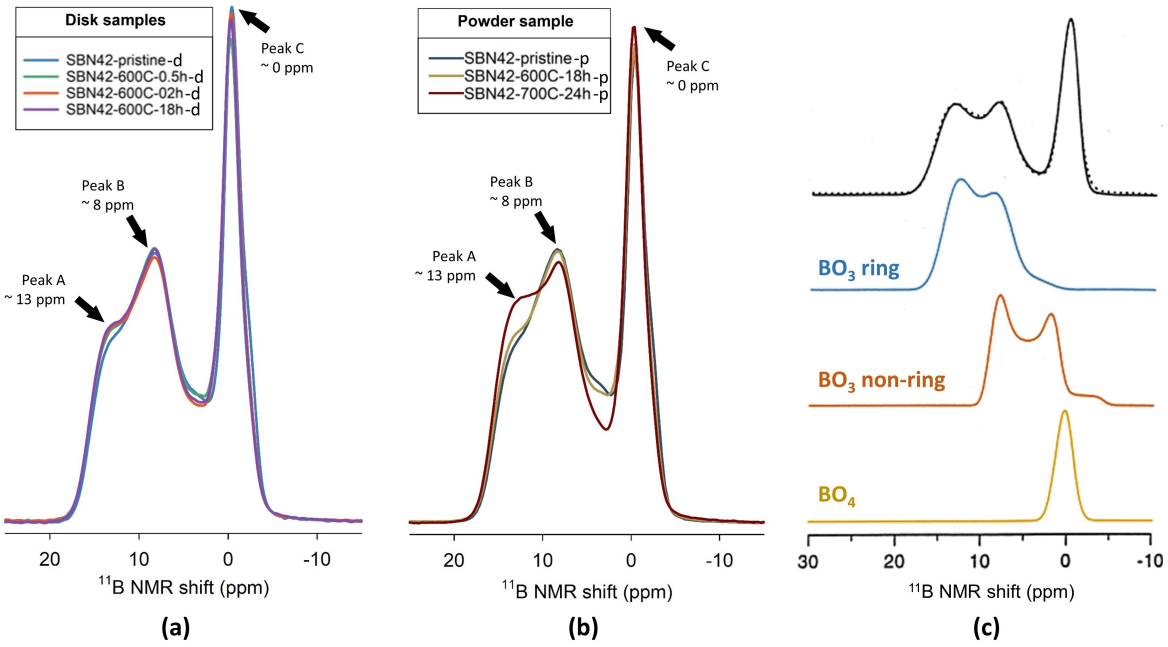

Figure II-1.11: Experimental ^{11}B MAS spectra of SBN42 pristine and annealed samples: (a) disk samples and (b) powder samples; (c) Typical deconvolution of the ^{11}B MAS NMR line shapes of a typical sodium borate glass: the dots in the top trace represent the experimental spectrum and the solid curve is the simulation. The simulation is the sum of three different contributions: BO_3 ring (blue), BO_3 non-ring (orange) and BO_4 (yellow) structures [132].

^{11}B MAS NMR experiments provides information on the glass structure via revealing the boron environment, including BO_3 ring and non-ring units, and BO_4 units. Grinding a bulk sample into powders increases the sample's surface area and brings some minor effects to the NMR spectra. However, powder sample are advantageous over their bulk counterparts, as more material can be put in the rotor for analysis. Hence, Figure II-1.11 separates the ^{11}B MAS spectra of SBN42 pristine and APS samples by sample geometry: Panel (a) disks and Panel (b) powder. Comparing these spectra, annealing the SBN42 samples leads to some slight variations on the height of the different peaks. To be accurate, ^{11}B MAS NMR spectra are composed of the sum of three components: BO_3 ring and non-ring units, and BO_4 units. Figure II-1.11 (c) display the typical line shapes of the three components:

- BO_4 units concern a narrow peak centered around 0 *ppm* (yellow curve).
- The BO_3 non-ring curve is bimodal (orange curve), also called second-order quadrupolar powder line shape. It has one peak centered at about 8 *ppm* and the other at 2 *ppm*. The whole resonance is centered at 5 *ppm*.
- The BO_3 ring units are also characterized by a broad bimodal curve (blue curve) with one peak centered at around 13 *ppm* and the other at 8 *ppm*. The whole resonance is centered around 10 *ppm*.

It is worth noting that for each sample, the position and the line shapes of these components are determined from the slices of 3QMAS spectra (Figure II-1.13). For all the spectra, signals from BO_3 and BO_4 structural groups are well resolved.

Figure II-1.11 (a) concerns NMR spectra for the disks for constant T_a with varying t_a. Comparing the spectra, a slight increase in Peak A (as indicated in Figure II-1.11) occurs after annealing at 600 ℃. The height of this peak is nearly independent of the annealing time. Additionally, a small hump exists in the valley between Peak B and Peak C for the pristine sample. However, it disappears for $t_a > 0.5$h. Considering Peak C, generally its height decreases slightly with increasing t_a. The exception is the spectrum of SBN42-600C-0.5h, which dips to the lowest Peak C height (afterwards SBN42-600C-2h is higher than SBN42-600C-0.5h and is located between the pristine and 18 h). A potential explanation is at the beginning of the APS process, the structure changes drastically with phase nucleation (which will be discussied in Section 4.1.1).

Figure II-1.11 (b) concerns NMR spectra for the powder samples. In this series of test, the T_a changed (pristine, 600 ℃ and 700 ℃) and long annealing times t_a were selected (0h, 18h and 24h respectively). Considering the powder samples, differences between the SBN42-pristine-p and SBN42-600C-18h-p resemble that of the disk samples (only minor differences exists between the powder and disk spectra). However, the SBN42-700C-24h-p spectrum differs significantly from that of the other two powder samples. As seen previously (by XRD in Section II-1.2 and by Raman in Section II-1.3), annealing the samples at 700 ℃ for 24h induces some crystallization in SBN42. Additionally, the crystals formed in this glass are α-cristobalite and the boron network remains amorphous. Compared to the other powder samples, SBN42-700C-24h has a higher Peak A, a lower Peak B and a higher Peak C.

^{11}B MAS NMR spectra line shape changes reveal variations in the B atoms local environment. Based on Figure II-1.11 (c), Peak A is attributed uniquely to BO_3 ring units, while Peak B includes the contribution of BO_3 ring and BO_3 non-ring. Annealing SBN42 samples results in a growth of Peak A and a decrease of Peak B. This indicates that the fraction of BO_3 ring units increases and BO_3 non-ring units decreases after annealing. A quantitative analysis will be introduced below to obtain more information on the NMR spectra.

Probing the boron environment reveals the populations of different boron structure, including BO_3 non-ring and ring units and BO_4 units. Fitting data in Figure II-1.11 (a) and (b) reveals the area fractions of the three components. This area concerns the fraction of different units. Figure II-1.12 shows a bar chart concerning the fraction of different boron structures (red shaded part concerns BO_3 ring, blue shaded part concerns BO_3 non-ring and green part concerns BO_4) for different samples. The chart shows that the fraction of BO_4 structures (green part) does not vary significantly before and after annealing. On the

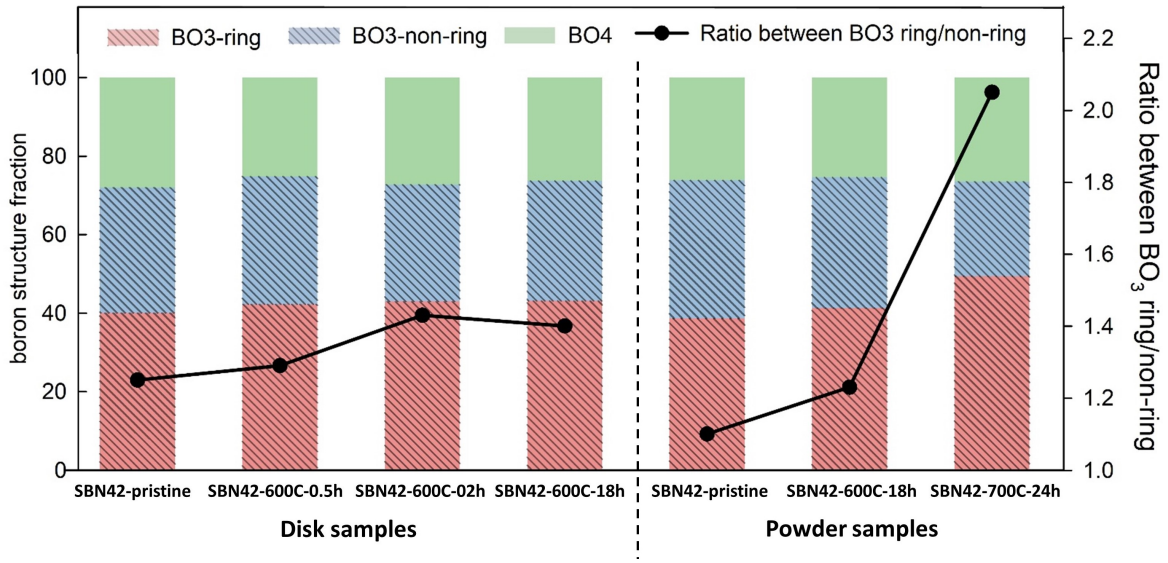

Figure II-1.12: Bar chart on the populations of boron structures in SBN42 pristine and APS glasses from ^{11}B MAS spectra (Y axis on the left side), and line chart on the ratio between BO_3 ring and non-ring fraction (Y axis on the right side).

other hand, annealing increases the BO_3 ring unit fraction compared to the pristine sample. Moreover, there is a significant change in the relative populations of ring and non-ring BO_3 species. The line in Figure II-1.12 indicates an increase in the ratio between BO_3 ring and non-ring fractions. This is especially highlighted for the SBN42-700C-24h powder sample. The structural rearrangements of the boron atoms into rings is consistent with the formation of a B-rich phase. Considering pure B_2O_3 (see Section 2.2.1), literature exemplifies that about 75% of boron atoms are in rings and about 25% providing the interconnection [127, 134, 243]. Comparing this to the increasing ratio between BO_3 ring and non-ring fractions, one deduces the formation of a B-rich phase. Additionally, longer annealing times and higher annealing temperatures increase the BO_3 ring fraction.

To obtain more detailed structural information, ^{11}B 3QMAS (Triple-Quantum MAS) spectra were collected. This technique produces two-dimensional (2-D) spectra generally displayed as contour plots. The projections of a 2-D spectrum in the two directions provide a MAS spectrum and an isotropic spectrum (a second-order quadrupolar broadening). Figure II-1.13 (a) shows the 2D ^{11}B 3QMAS spectrum of SBN42-pristine-p as an example. The BO_3 and BO_4 contours are well separated and indicated in the figure. The contours indicated by a $*$ concerns the spinning sideband from the BO_4 peak induced by the finite spinning frequency.

Figure II-1.13 displays the isotropic projection of the 3QMAS spectra for the three powder samples. The line shape for different units correspond to different peaks marked by the black dash lines. These spectra confirmed the results seen above: there is an increase of BO_3 ring units and a decrease of BO_3 non-ring units after annealing, especially in SBN42-700C-24h-p. Beyond this, a small shoulder (pointed out by the black arrow on Figure II-1.13 (b)) occurs around -5 *ppm* for SBN42-pristine-p, which makes the peak at 0 *ppm* asymmetric.

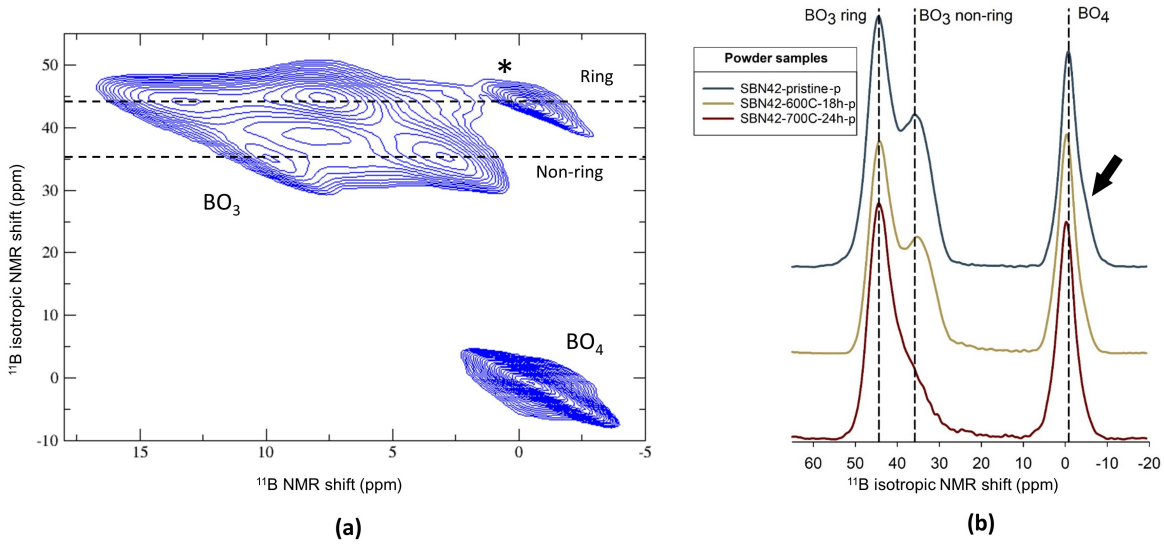

Figure II-1.13: (a) 2D ^{11}B 3QMAS spectrum of SBN42-pristine-p; (b) Isotropic spectra of the powder samples, including SBN42-pristine-p, SBN42-600C-18h-p and SBN42-700C-24h-p.

This shoulder disappears after annealing. Some studies consider that the BO_4 structures actually correspond to two different peaks: one at 0 *ppm* and the other at -5 *ppm*. Du and Stebbins [62] attributed the peak centered at 0 *ppm* to danburite structures (4-coordinated Boron tetrahedron with three silicon (4-coordinated) and one boron (4-coordinated) atoms as next-nearest neighbors, see Table A.2). They also ascribed the more negative peak (herein centered near -5 *ppm*) to correspond to the reedmergnerite structure (4-coordinated Boron tetrahedron with 4 silicon (4-coordinated) atoms as next-nearest neighbors, see Table A.2). More negative isotropic chemical shifts indicate an increase in the connectivity between B and Si [18]. Comparing the three spectra in Figure II-1.13, the peak position around 0 *ppm* shifts slightly to more positive values and becomes more symmetric for longer annealing times and higher annealing temperatures. This indicates that there is an annihilation of reedmergnerite units after annealing, and B atoms tend to leave the silica network during annealing. This is consistent with the formation of a pure silicate crystal for SBN42-700C-24h, with B[IV] having a less tendency to be "caged" in the Si-rich phase.

In general, ^{11}B MAS and 3QMAS spectra on SBN42 pristine and annealed samples indicate some structure changes. They are consistent with the fact that APS, and even crystallization, occurs in the samples.

II-1.4.1.2 ^{11}B-^{11}B DQNMR

The above section presented the ^{11}B MAS and 3QMAS spectra of different SBN42 samples. In addition, Double Quantum (DQ) ^{11}B experiments have been performed. Based on the homonuclear dipolar interactions, signals of dipolar homonuclear couplings can be separated and other signals can be filtered out by designing special pulse sequences [279]. Thus, ^{11}B DQ NMR spectra reveal predominantly the signals from ^{11}B-^{11}B pairs, when the two boron

atoms are spatially close to each other (*i.e.* boron atoms who are next to nearest neighbors sharing an oxygen atom). However, these spectra remain too complex to analyze in depth since these are signals of second-order quadrupolar broadening in addition to the chemical shift distribution due to disorder [47]. My discussions herein are qualitative and concern shape changes of the projections on the DQ dimension (*i.e.* NMR shift of ^{11}B-^{11}B pairs excited by a specific pulse sequence for correlating close boron atoms).

Nomenclature used in this section reflects NMR nomenclature. Hence, a brief summary is warranted. B[III]-B[III] refers to two 3-coordinated boron atoms who are spatially close to each other (*i.e.* they share an oxygen atom). B[IV]-B[IV] refers to two 4-coordinated boron atoms who are spatially close to each other (*i.e.* they share an oxygen atom). B[III]-B[IV] refers to one 3-coordinated boron connected to one 4-coordinated boron atoms via a common oxygen atom.

Figure II-1.14 shows the ^{11}B-^{11}B DQNMR spectra of the three powder samples with the DQ dimension projection. The single quantum (SQ) dimension reveals similar information as ^{11}B MAS spectra. The red dotted lines mark the positions of Peak A, Peak B and Peak C seen in Figure II-1.11. These 2D spectra evidence the presence of all three B[III]-B[III], B[III]-B[IV] and B[IV]-B[IV] interactions with different contours. The contribution of these three different interactions on the DQ projections are filled by different colors: orange shaded area centered at 4 *ppm* for B[III]-B[III]; green shaded area centered at 0 ppm for B[III]-B[IV]; and blue shaded area centered at -4 *ppm* for B[IV]-B[IV].

Considering the DQ projection of SBN42-pristine-p (Figure II-1.14 (a)), it consists of a broad band from -2 to 6 *ppm* and a peak centered at -4 *ppm*. The contributions of B[III]-B[III] and B[III]-B[IV] construct a broad band from -2 to 6 *ppm* with a shoulder around 4 *ppm*. Comparing pristine and annealed samples, the broad band from -2 to 6 *ppm* decomposes into different peaks for the annealed samples, and the B[III]-B[III] and B[III]-B[IV] contributions are well separate. For SBN42-600C-18h-p (Figure II-1.14 (b)), there are two clear peaks centered at -4 and 1 *ppm*, and a shoulder at -1 *ppm*. Additionally, the peak centered around 1 *ppm* possesses a bimodal shape, and the orange shaded area has several fluctuations. For SBN42-700C-24h-p (Figure II-1.14 (c)), there are three dominate peaks centered at -4, 1 and 5 *ppm*, and a shoulder at -1 *ppm*.

Comparing the two annealed samples, more B[III]-B[III] interactions exist in SBN42-700C-24h-p. Recalling that SBN42-700C-24h-p undergoes crystallization of α-cristobalite, the boron atoms are pushed out of the Si-rich zone. According to ^{11}B MAS spectra, there are more BO_3-ring in these annealed samples. The growth of the 5 *ppm* peaks (orange areas in Figure II-1.14) signals an increase in B[III]-B[III] connections. This indicates that the fraction of B atoms in the B-rich phase in SBN42-700C-24h-p is higher than SBN42-600C-18h-p. Beyond this, the -4 *ppm* peak concerning B[IV]-B[IV] remains clear for the annealed samples. Thus, it is hypothesized that Na^+ ions tend to stay in the B-rich phases. The notion that Na^+ ions tend to remain with the B-rich phases will be investigated in Section II-1.4.2.2.

In general, ^{11}B DQ NMR spectra reveal some information about the ^{11}B-^{11}B spatial interactions for different types of B (including B[III] and B[IV]). The formation of B-rich phase leads to a higher interconnectivity between B atoms (with an O atoms in between), especially concerning B[III] units forming ring structures. ^{17}O NMR analysis are expected to be performed in the future to provide more information about the network linkages, including

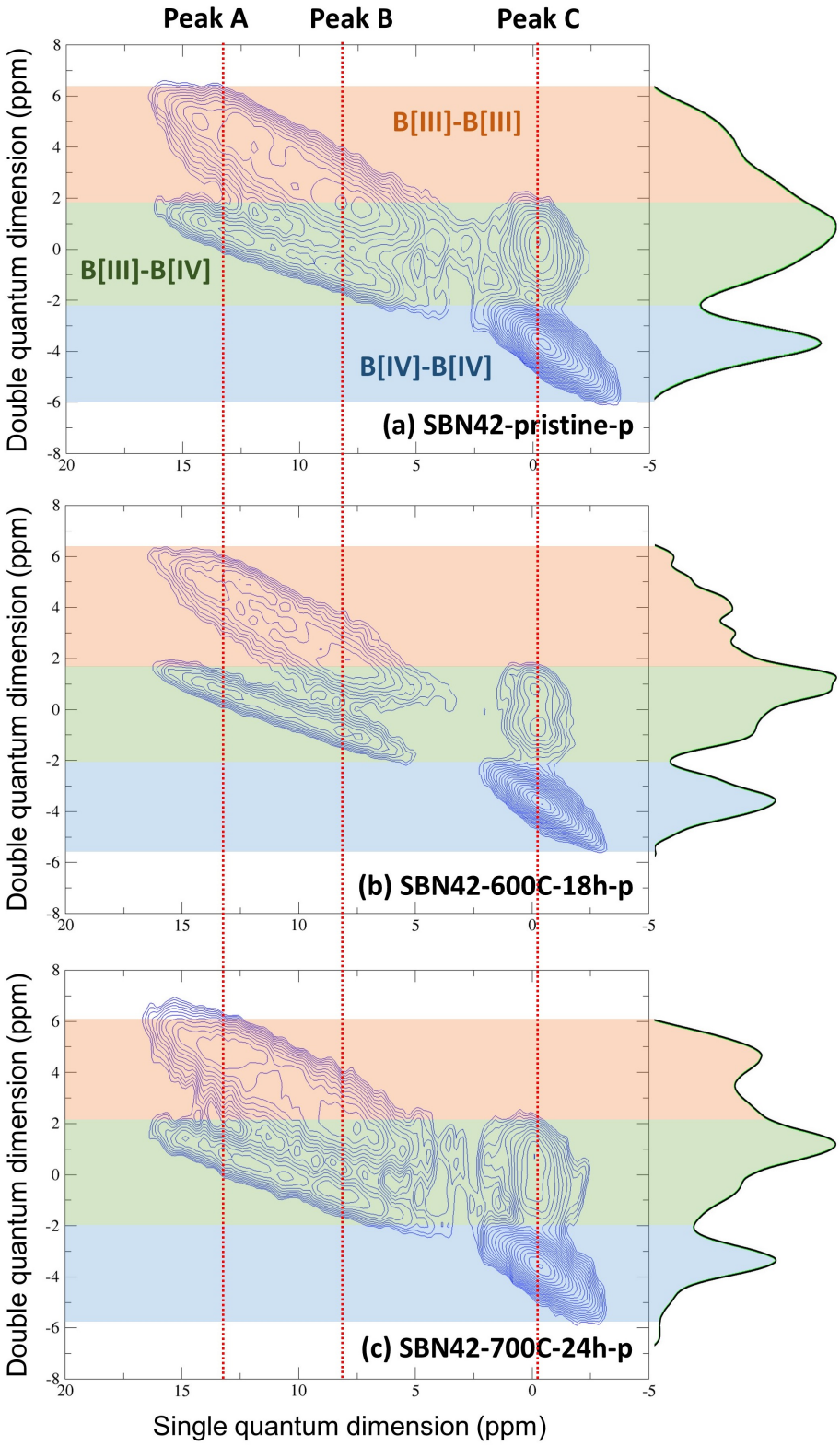

Figure II-1.14: Experimental ^{11}B-^{11}B DQMAS spectra of powder samples with projection of DQ dimension: (a) SBN42-pristine, (b) SBN42-600C-18h, (c) SBN42-700C-24h. Orange shaded area concerns B[III]-B[III], green shaded area concerns B[III]-B[IV], blue shaded area concerns B[IV]-B[IV].

Si-^{17}O-Si, Si-^{17}O-B and B-^{17}O-B connections.

II-1.4.2 ^{23}Na

II-1.4.2.1 ^{23}Na MAS

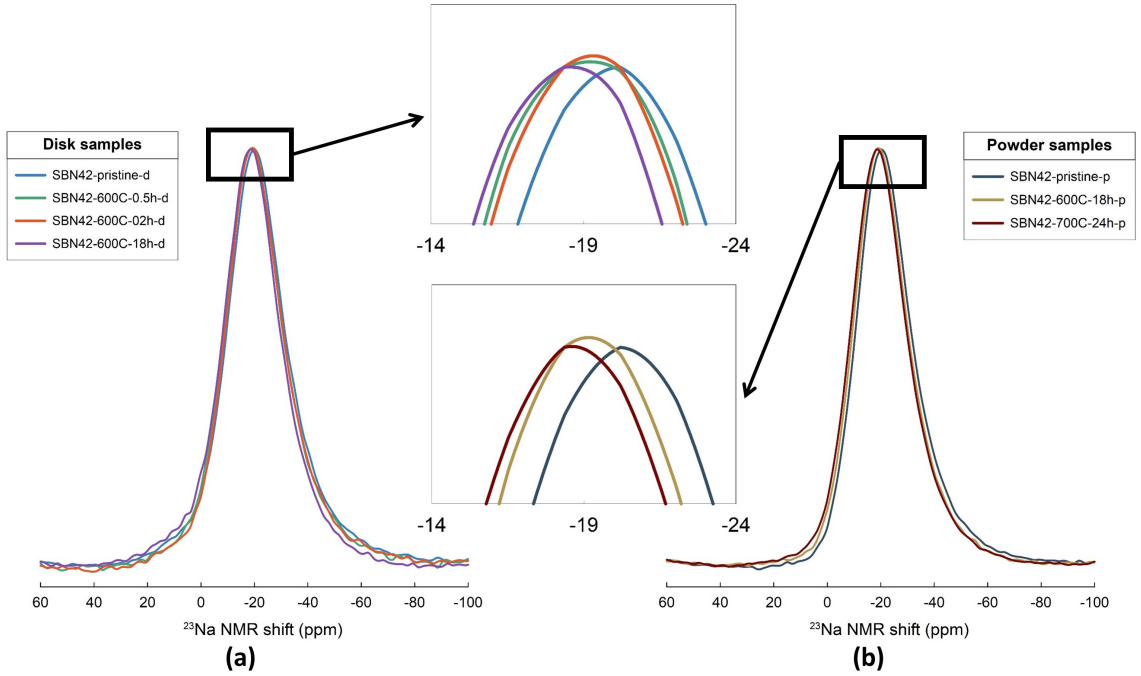

Figure II-1.15: Experimental ^{11}Na MAS spectra of SBN42 samples with the magnification of peaks: (a) disk samples; (b) powder samples.

Looking at single-phase SBN glasses, changing the chemical composition of the glass causes the sodium to act in different fashions. For relatively low amounts of Na_2O in SBN glasses, Na_2O acts as a charge compensator to BO_4 units. For relatively high amounts of Na_2O in SBN glasses, Na_2O acts as a network modifier (creating NBO atoms) depolymerizing the silica and, sequentially, boron network [30, 58, 76, 33]. ^{23}Na MAS NMR experiments provide information on the sodium atoms environment in the glass structure. When Na^+ ions are working as a network compensator, the ^{23}Na MAS NMR will have a negative shift. On the other hand, when the Na^+ ions are working as network modifiers, the ^{23}Na MAS NMR shifts to more positive values.

In phase-separated glasses, ^{23}Na MAS NMR spectra shifts can provide an idea of the changing role (if any) of Na_2O in a SBN glass. Figure II-1.15 depicts the ^{23}Na MAS spectra for SBN42 pristine and APS samples. All the peaks have a similar shape – single broad peak. This line shape is reflective of a broad distribution of NMR parameters (structural disorder and electric field gradients), because first-coordination sphere of Na is ill defined (in contrast to former atom such a Si or B) [45]. Additionally, these peaks possess negative values, indicating the Na^+ ions act as charge compensator in SBN42. These Na^+ ions charge

compensate for tetrahedral boron units, *i.e.* BO_4. This phenomenon confirms the previous assumption (originating from $R_{SBN} < 0.5$) all oxygen atoms are bridging in these glasses.

Considering the peak position with annealing temperatures, the peak position for the disk samples (Figure II-1.15 (a)) slightly shifts to positive values with increasing annealing time t_a at constant annealing temperature T_a = 600 °C. Similar phenomenon occurs for the powder samples with increasing annealing temperature T_a. The peak position of SBN42-700C-24h-p is on the left side, the peak of SBN42-pristine-p is on the right side, and the peak of SBN42-600C-18h is between them. This slight shifting in the peaks could indicate that the Na^+ ions have a tendency to work as network modifiers in the samples after annealing as compared to the pristine sample. Moreover, the peak position depends slightly on T_a and t_a. Nonetheless, the shift in the peak is small and probably inconsequential. To determine if it is consequential, more research would be needed.

II-1.4.2.2 ^{23}Na{^{11}B} and ^{11}B {^{23}Na} REDOR NMR experiments

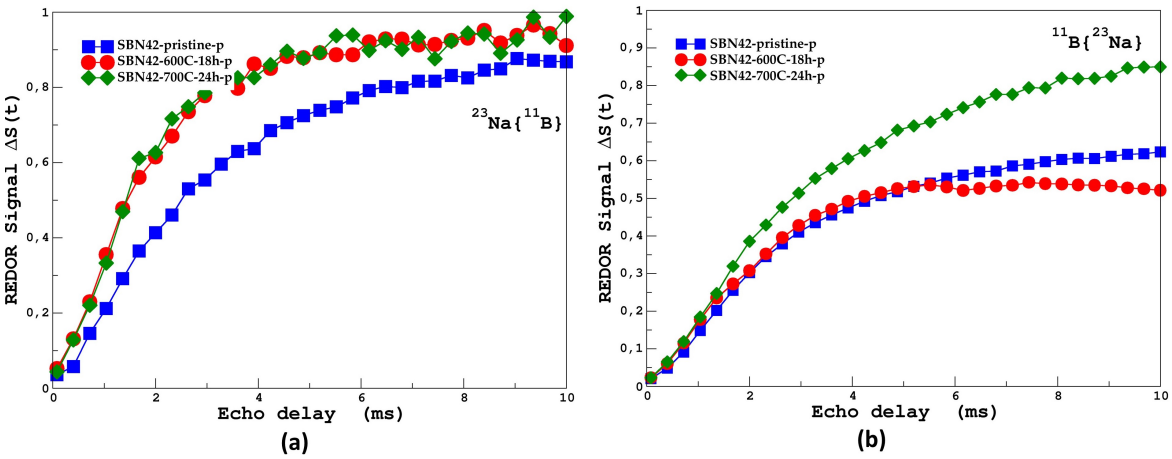

Figure II-1.16: (a) ^{23}Na{^{11}B} REDOR and (b) ^{11}B {^{23}Na} REDOR curves for SBN42 pristine and annealed powder samples.

^{23}Na{^{11}B} and ^{11}B {^{23}Na} rotational echo double resonance (REDOR) NMR has been used to probe the spatial proximity between ^{11}B and ^{23}Na species in glasses. The REDOR signals tend to saturate for longer echo delay. For a M {N} REDOR experiment, the initial slope (from 0 to $2-3$ ms), reflects the strength of dipolar interactions, while the saturation values indicates the fraction of M atom possessing a N atoms in their close vicinity. Figure II-1.4.2.2 depicts ^{23}Na{^{11}B} and ^{11}B {^{23}Na} REDOR experimental results for SBN42 powder pristine and annealed samples.

Figure II-1.16 (a) depicts the ^{23}Na{^{11}B} REDOR results. Considering short echo delays, the annealed samples are similar and higher than pristine sample. This indicates that the Na^+ ions have stronger dipolar interactions with B after annealing [132]. For long echo delays, the pristine sample (blue squares) appears to be still increasing, thus saturation has not been achieved. However, the saturated values should be higher than 0.8 (the highest value on the curve), and it is predicted to be close to 1 in the case of an ideal pulse sequence.

On the other hand, the curves of the two annealed samples saturation near 1. In general, for these three glasses, almost every Na^+ ions is near a B atom. Combining the analysis of ^{23}Na MAS, Na^+ ions work as charge compensators in these glasses, forming BO_4. The $^{23}Na\{^{11}B\}$ REDOR curves are consistent with the previous analysis.

Figure II-1.16 (b) shows the ^{11}B $\{^{23}Na\}$ REDOR results. The SBN42-pristine-p (blue squares) appears to be still increasing for long echo delays, thus saturation has not been achieved. However, it does appear that the saturation value should be well below 1, and probably around ~ 0.6. SBN42-600C-18h-p (red circles) does saturate at 0.5. SBN42-700C-24h-p sample (green diamonds) is not well saturated too, but the saturation value should be near 0.85. Hence, the ^{11}B $\{^{23}Na\}$ REDOR experiments reveal a changing environment around the B atoms in different samples. In SBN42-pristine-p and SBN42-600C-18h-p, about half of the boron atoms have a neighboring Na^+ ion, where as 85% for SBN42-700C-24h-p. To determine if there is difference between SBN42-pristine-p and SBN42-600C-18h-p, more experiments are needed, as the curves really follow one another initially. However, the increase in SBN42-700C-24h-p is significant.

To explain this phenomenon, Janssen and Eckert [132] proposed a model for describing the local environment of Na^+ ions in sodium borate (BN) glasses. It is said that for the sodium borate glasses with $R_{BN} > 0.2$, the Na^+ ion coordination is approximately 5-6 with nearest neighbors being oxygen atoms connected to 6-10 boron units [132]. Moreover, each Na^+ ion has one BO_4 unit in the vacancy for charge compensation. Hence, in addition to this BO_4 unit, there are a number of BO_3 units in the vicinity of the Na^+ ion.

Herein, I am dealing with SBN glasses rather than BN glasses, but similar circumstances should occur since the Na_2O concentration is low. Recalling that the fraction of BO_4 in this glass measured by ^{11}B MAS NMR is 26.5% (implying 73.5% of the boron atoms are BO_3 units). Additionally, according to ^{11}B-^{11}B DQNMR spectra in Section II-1.14, there are B[III]-B[IV] couplings in these samples. Thus, Na^+ ions (or at least some of them) should be in close proximity to both a BO_4 unit and BO_3 units. In SBN42-pristine-p and SBN42-600C-18h-p, one Na^+ ion is in general located near one BO_4 unit and one BO_3 unit. On the other hand, in SBN42-700C-24h-p, one Na^+ ion is in general located near one BO_4 unit and two BO_3 units. This increase is possibly due to a well-formed B-rich phase with a higher Na^+ ion concentration.

II-1.4.3 ^{29}Si MAS spectra

^{29}Si MAS NMR in SBN glasses displays generally a spectrum with a curve of one or more peaks [165, 190]. In multi-component silicate glasses, the ^{29}Si chemical shifts are sensitive to the second-neighbor environments [18, 165], including Si-O-Si, Si-O-B[III], Si-O-B[IV], *etc.* For SBN glasses, ^{29}Si MAS NMR provides insights into the polymerization of the glass network through the determination of the Q_i populations [165]. In addition, the existence of Si-O-B can result in a broadening and shifting of the peaks [18].

As analyzed in previous sections, the SBN42 glasses should have limited, if any, NBO atoms. Hence, the silica network ideally only concerns Q_4 structures, with n Si or $(4-n)$ B atoms (where n ranges from 0-4) as next to nearest neighbors, coined $Q_4(n\text{Si}, (4-n)\text{B})$. These environments contribute to the ^{29}Si MAS spectra. For pure silica $Q_4(4\text{Si})$, NMR responses a

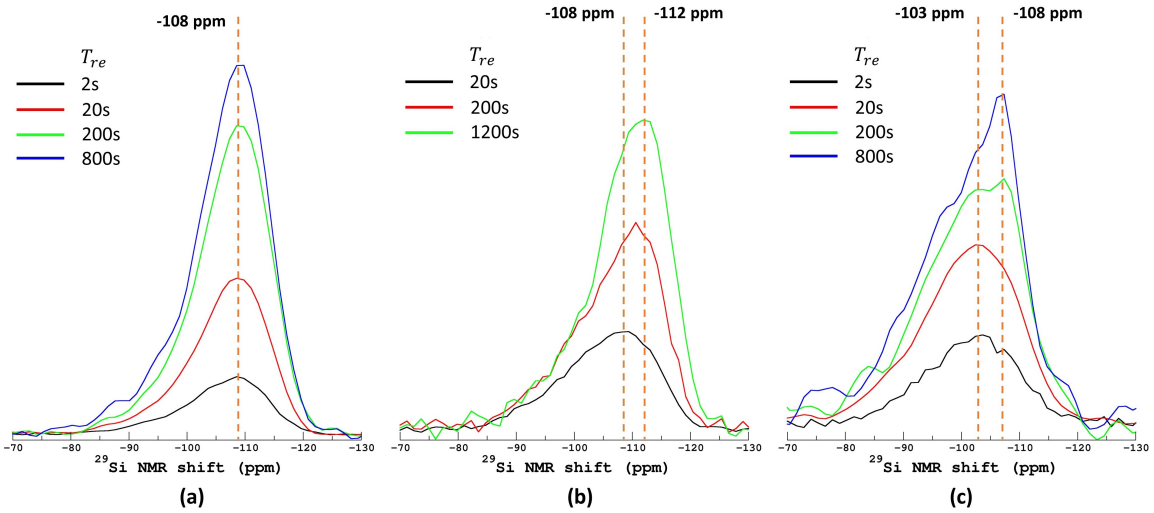

Figure II-1.17: Experimental ^{29}Si MAS spectra of SBN42 powder samples with different recovery delays T_{re}: (a) SBN42-pristine-p; (b) SBN42-600C-18h-p; and (c) SBN42-700C-24h-p.

peak at -110 *ppm* [190]. For SBN glasses, the Q_4(3Si, B) environment correspond to a more positive values [190].

^{29}Si MAS NMR has been used to measure the spin-lattice relaxation time T_1 of ^{29}Si in glasses [168]. Normally, single relaxation behavior is expected. However, non-homogeneous distributions of the same Q_4 type structure could result in two different T_1 values [187]. Thus, changing the recovery delay T_{re} potentially varies the NMR spectra. Comparing the spectra provides insights on nano-scale heterogeneity in the glass: if the sample is homogeneous, short and long T_{re} provide the same MAS spectrum line shape (*i.e.* all underlying component relax in the same way); if the sample is not homogeneous in regards to the spatial distribution of $Q_4(n\text{Si}, (4-n)\text{B})$, evolution of spectra can be observed with increasing T_{re}. Herein, the ^{29}Si NMR experiments were done with a pre-saturation, *i.e.* saturate the silicon magnetization (to zero). Then a variable delay is allowed for the magnetization to recover before its observation (90° pulse).

Figure II-1.17 shows the ^{29}Si MAS spectra response for powder samples with different T_{re}. Considering the SBN42-pristine-p sample (Figure II-1.17 (a)), increasing T_{re} only results in the peak growth (*i.e.* no peak position shifting). This indicates that the pristine sample is rather homogeneous. For the APS SBN42-600C-18h-p sample, the peak is centered at -108 *ppm* for $T_{re} = 20s$ and shifts to -112 *ppm* for $T_{re} = 1200s$. Similar phenomena occur for the SBN42-700C-24h-p spectra, where the peak shifts from -103 *ppm* to -108 *ppm* with increasing T_{re}. These spectra change with T_{re} indicate the inhomogeneity in composition of SBN42 annealed samples.

Let us assume that the spectra with long T_{re} indicates the peak position after a full relaxation of ^{29}Si. Compared to the pristine sample (Figure II-1.17 (a)), the peak of SBN42-600C-18h-p (Figure II-1.17 (b)) possesses a more negative value, signifying that there is: (1) a reduction of Q_4(B) contribution and (2) less Na^+ in the silicate network [190]. This is due to the decomposition of sample into Si-rich and B-rich phases after annealing. The

connections between silicate Q_4 units and boron units are consequently separated.

Considering the SBN42-700C-24h-p spectra ((Figure II-1.17 (c))), this sample undergoes crystallization of α-cristobalite. The peak around -108 *ppm* becomes sharp compared to the other two samples. This is due to the crystal structures, which are known to peak around -110 *ppm* for α-cristobalite [201]. Additionally, the distribution of the peak is from -120 to -80 *ppm*, indicating that there is still a significant amorphous silicate network structure in the sample. Nevertheless, T_1 of ^{29}Si in glasses is on the order of hours [232, 168]. Obtaining the full intensity of the ^{29}Si spectra costs a lot of time. Increasing the T_{re} would provide a more quantitative analysis.

II-1.5 Structure summary

During my thesis, I have performed a number of different experiments to investigate the structure of SBN42 pristine and annealed samples. As indicated at the beginning of Part II, annealing SBN42 pristine samples leads to phase separation. AFM imaging evidenced the occurrence and morphology of APS in SBN42 annealed samples. TEM images and NMR spectra aid in confirming the formation of B-rich phases.

Additionally, the special conic structures seen on samples with T_a=700 ℃ are confirmed to be crystals, specifically α-cristobalite. In the ToughGlass project, the partners are interested in the stress corrosion cracking (SCC) behavior of amorphous-amorphous structures. Hence, the annealing temperatures will be kept low for SCC tests.

Chapter II-2

Physical characterizations on SBN42

Contents

In this chapter, I will present the physical characterizations results of SBN42 pristine and APS samples. These characterizations concern not only the small samples in Figure II-1.1, but also the DCDC samples (Double Cleavage Drilled Compression) on which I have performed the SCC experiments.

II-2.1 Density of SBN42 samples

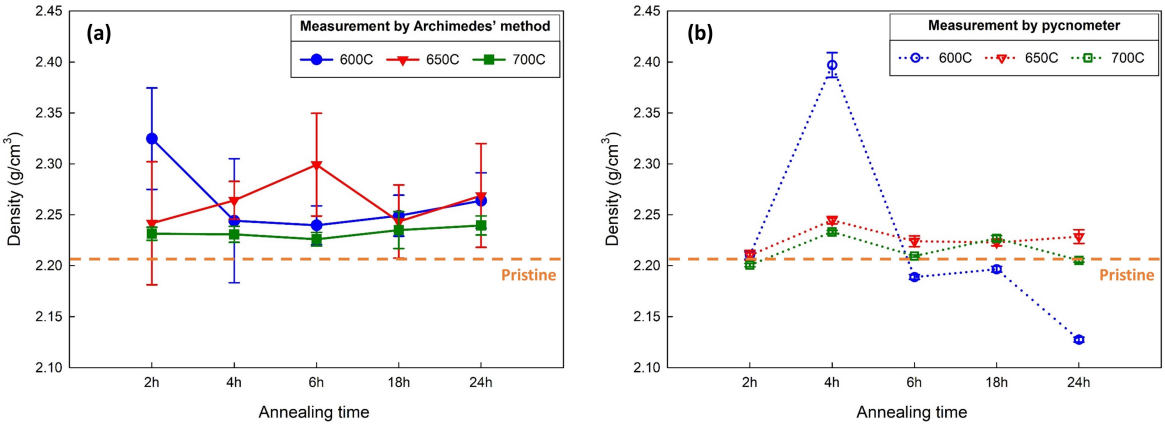

Figure II-2.1: Density of SBN42 annealed small samples in Figure II-1.1 (blue circles for 600 °C, red inverted triangles for 650 °C and green rectangles for 700 °C) and of pristine sample (orange dashed line) from the same batch (*i.e.* SBN42-pristine-1 and SBN42-pristine-2): (a) measurement by Archimedes' method, (b) measurement by pycnometer. Error bars correspond to one standard deviation.

This section presents the density measurement of SBN42 samples, including the small samples and DCDC samples. The techniques invoked herein concern Archimedes' method (see Section 3.3.1). For the small samples (Figure II-2.1 (a)), the measurements were performed in University of Rennes (see Figure A.1 (b) in Appendix A.1). For the DCDC samples

(Table II.1), I did the Archimedes' measurements with an in-house equipment (see Figure A.1 (a) in Appendix A.1).

Additionally, samples in Figure II-1.1 are rather small (about 0.01 cm^3). Hence, these samples were sent to Micromeritics France for performing the density measurements via an AccuPyc II 1340 pycnometer with the 0.1 cc sample cell. This non-destructive technique utilizes gas (helium herein) displacement to measure the volume of our samples. For each sample, the measurements were performed 5 times by Archimedes' method and 10 cycles by the pycnometer. Figure II-2.1 depicts the density of small samples measured by different methods along with the error bars. Comparing these two methods, the Archimedes' equipment provides a significantly larger error than the results obtained by the pycnometer. Hence, the calculation of elastic moduli in Section II-2.2 concerns the values measured by pycnometer.

Considering the density of SBN42 small samples with respect to the t_a and T_a (Figure II-2.1), the values obtained via Archimedes' method range between $2.20 - 2.35$ g/cm^3, and those by pycnometer range between $2.10 - 2.40$ g/cm^3. Let us first look at the results obtained by Archimedes' method. The orange dashed line on Figure II-2.1 indicates the average of SBN42-pristine-1 and SBN42-pristine-2, which are from the same batch as the small samples. The data points of the annealed samples fluctuate above this line, indicating that the annealed samples have a tendency to have a higher density compared to the pristine sample.

Turn to the pycnometer results, data concerning T_a=650 and 700 °C fluctuate slightly above the pristine sample. This indicates that these samples may have a slightly higher density. Concerning T_a=600 °C, there are larger fluctuations with the annealing time. It is worth noting that the density measured by different methods are different and the deviation is up to 0.15 g/cm^3 for SBN42-600C-04h-s. Based on these results, no specific trend can be obtained due to the APS structures.

Density measurements were also performed on the DCDC samples after SCC experiments (see Section II-3.1) and the results are presented in Table II-2.1. Since the DCDC samples are larger than the small samples, the measurement should be more accurate. Compared to the small samples, there are less data fluctuations. For the samples from the same batch, the values are within the error bars, thus one cannot eliminate that they are the same. No trend can be summarized concerning the effects of APS.

II-2.2 Moduli of SBN42 samples

This section presents the elastic moduli measurement of SBN42 samples, including Young's modulus E, bulk modulus K, shear modulus G, and Poisson's ratio ν. The technique invoked herein is ultrasonic echography (see Section 3.3.2). It should be noted, the calculations invoke the density values measured via AccuPyc II 1340 pycnometer.

Figure II-2.2 depicts the moduli and Poisson's ratio of SBN42 small samples with respect to the annealing time and temperature. Considering the results in Figure II-2.2, for the four parameters, there are data fluctuations around the orange dashed lines corresponding to pristine samples.

Table II-2.1: Density measured by Archimedes' method via an in-house equipment (Appendix A.1) and elastic moduli of SBN42 DCDC samples along with the error bars.

Sample name	ρ (g/cm^3)	K (GPa)	G (GPa)	E (GPa)	ν
Batch 0					
SBN42-pristine-1	2.24 ± 0.05	36.6 ± 1.1	24.4 ± 0.5	60 ± 2	0.228 ± 0.008
SBN42-pristine-2	2.20 ± 0.05	35.7 ± 1.2	24.1 ± 0.5	59 ± 2	0.22 ± 0.01
Batch 1					
SBN42-pristine-4	2.10 ± 0.05	34.4 ± 1.1	23.8 ± 0.2	58.0 ± 1.5	0.219 ± 0.006
SBN42-600C-18h-1	2.16 ± 0.05	33.6 ± 1.2	24.3 ± 0.6	59 ± 2	0.209 ± 0.011
Batch 2					
SBN42-pristine-5	2.18 ± 0.05	37.4 ± 1.0	24.0 ± 0.1	59.3 ± 1.4	0.236 ± 0.004
SBN42-600C-04h-1	2.17 ± 0.05	37.3 ± 0.9	23.0 ± 0.1	57.2 ± 1.3	0.245 ± 0.002
SBN42-600C-04h-2	2.15 ± 0.05	33.8 ± 1.4	22.9 ± 0.8	56 ± 3	0.223 ± 0.015
SBN42-600C-18h-2	2.17 ± 0.05	35.0 ± 1.1	24.4 ± 0.5	59 ± 2	0.22 ± 0.01
SBN42-pristine-6	2.14 ± 0.05	33.7 ± 1.2	23.0 ± 0.6	56 ± 2	0.222 ± 0.012
Batch 3					
SBN42-pristine-7	2.15 ± 0.05	32.6 ± 1.0	22.1 ± 0.4	54.1 ± 1.7	0.223 ± 0.009
SBN42-pristine-8	2.11 ± 0.05	31.4 ± 0.9	21.7 ± 0.3	53.0 ± 1.4	0.219 ± 0.006

Additionally, I measured the moduli and Poisson's ratio of the DCDC samples. Table II-2.1 presents the results by batches. In general, same batch provides similar results (within the error bars). The except is **Batch 2**. The two samples annealed at T_a=600 ℃ for t_a=4h, they possess different K and ν. As the elastic moduli are linked to fracture behavior, the differences herein reflect on the differences in fracture surfaces roughness after SCC experiments, which will be discussed in Section II-3.3.

In summary, based on the results, density and elastic moduli of annealed samples do not show specific trend with respect to annealing temperatures T_a and annealing times t_a. MD simulations may aid in filling this gap.

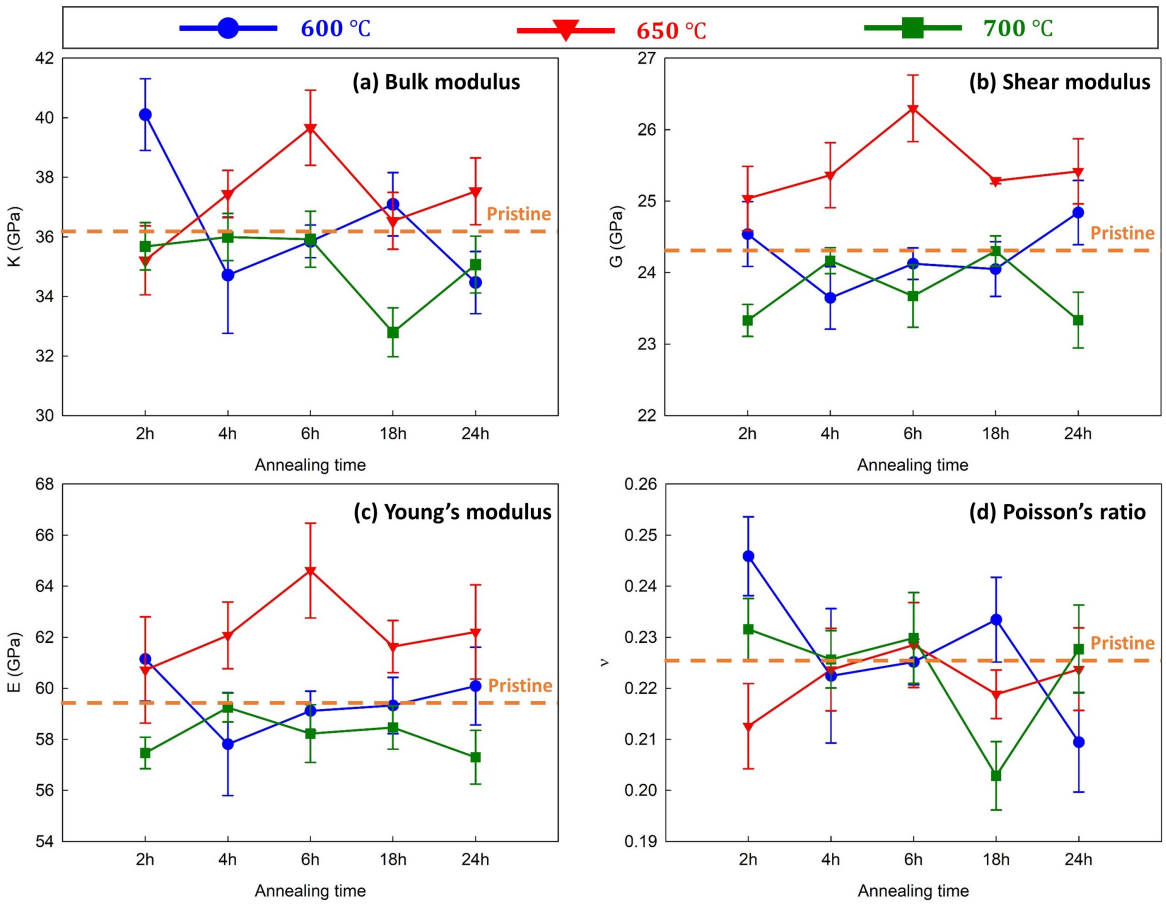

Figure II-2.2: Elastic moduli of SBN42 small samples in Figure II-1.1 (blue circle for 600 °C, red inverted triangle for 650 °C and black rectangle for 700 °C) and of pristine sample (orange dashed line) from the same batch (*i.e.* SBN42-pristine-1 and SBN42-pristine-2).

Chapter II-3

SCC experiments on SBN42

Contents

This chapter concerns SCC tests of SBN42 pristine and APS samples along with the post-mortem fracture surfaces analysis. Section II-3.1 details stress corrosion cracking (SCC) experimental results on SBN42 pristine and APS samples. The stress corrosion cracking section is broken into four sub-sections. The first subsection presents SCC results of pristine samples [1]. The subsequent subsections present the SCC results of the annealed samples by batch. Grouping samples by batches is advantageous for several reasons. First, Section II-2.2 reveals some fluctuations in the elastic moduli and the Poisson's ratio, which are linked to variations in fracture behavior [10, 13, 14, 230]. Additionally, minor differences in manipulation during sample elaborations cannot be avoided. This may lead to the differences in fictive temperature of the as-fabricated samples, and thus influence the SCC behavior of glasses [147, 148, 163]. Moreover, minor fluctuations in the final chemical compositions are possible between batches. Finally, grouping them by batches facilitates the discussion concerning their general behavior. Post-mortem fracture surface analysis will performed on the samples after SCC experiments (Section II-3.2 and Section II-3.3). RMS calculation (Section II-3.3.1) and structure function analysis (Section II-3.3.2) reveal the effects of APS structure on the fracture surfaces roughness.

[1] In addition to SBN12 samples used for testing the experimental setups, **Batch 0** of SBN42 was also used. However, improper placement of the hygrostat cause incorrect monitoring and poor humidity control inside the experimental chamber. Additionally, the second sample had to be stooped due to the spring 2020 lockdown. Hence, the results of SBN42-pristine-1 and SBN42-pristine-2 were rejected. Additionally, unexpected damage occurred during SBN42-pristine-3 experiments; and the SBN42-pristine-7 pre-crack was too long (about 4.5 mm). Hence, the results of these two samples were also rejected.

II-3.1 Stress corrosion cracking experiments on SBN42 pristine and APS samples

This section presents the studies of SCC (Stress corrosion cracking) behavior on SBN42 pristine and APS samples. Section 3.4.1.1 details the experimental setup with the Deben loading machine and DCDC samples. All experiments presented herein have a controlled humidity of $40 \pm 0.5\%$ and temperature of 19 ± 1 °C.

II-3.1.1 Pristine samples

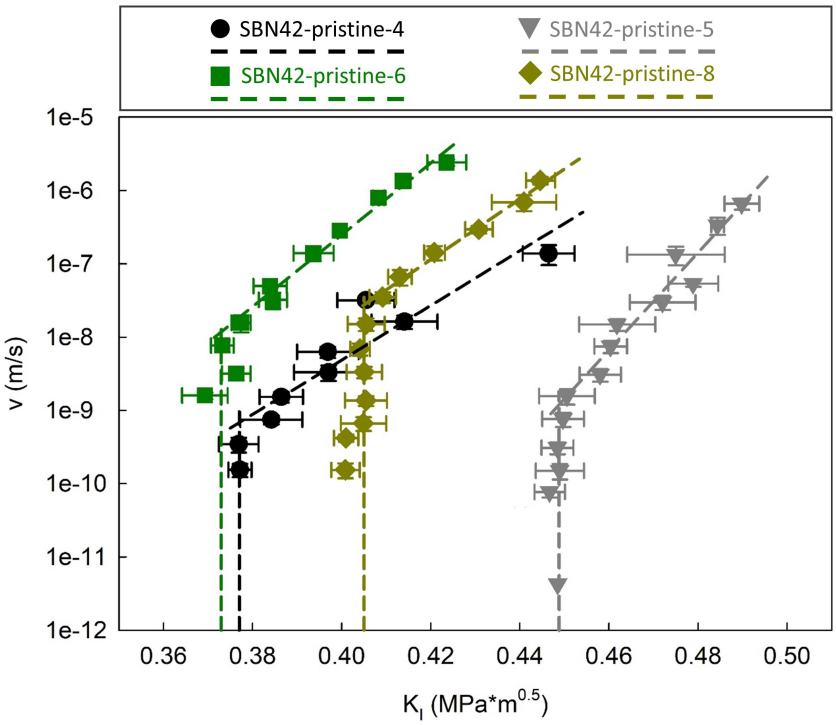

Figure II-3.1: Stress corrosion cracking curves of SBN42 pristine samples – SBN42-pristine-4 (black circles), SBN42-pristine-5 (grey inverted triangle), SBN42-pristine-6 (dark green rectangles) and SBN42-pristine-8 (dark yellow diamonds) along with the error bars and the fitting curves shown by dashed lines.

First, let us focus on the pristine samples to understand the batch effects. Figure II-3.1 shows the SCC results for SBN42 pristine samples: SBN42-pristine-4 (black circles), SBN42-pristine-5 (grey inverted triangle), SBN42-pristine-6 (green rectangles) and SBN42-pristine-8 (dark mustard diamonds). These pristine samples have no visible signs of APS in their structures. Figure II-3.1 exemplifies Region 0 (K_E) and Region I for each pristine sample.

Considering the general position of curves, the data points of SBN42-pristine-4, SBN42-pristine-6 and SBN42-pristine-8 are grouped together where as SBN42-pristine-5 sits to the right of the others. This indicates that SBN42-pristine-5 is more resistant to SCC compared

to the other pristine samples.

The vertical lines in Figure II-3.1 indicate the environmental limits K_E for each sample, and Table II-3.1 enumerates them. Considering the three samples grouped together (SBN42-pristine-4, SBN42-pristine-6 and SBN42-pristine-8), averaging the K_E gives $K_E = 0.385 \pm 0.014 MPa \times m^{0.5}$. Additionally, the error bar between these three samples is clearly less than the error bar found between SBN12 samples. However, the K_E of SBN42-pristine-8 is about 0.06 $MPa \times m^{0.5}$ larger than this average value. Considering a 95% confidence interval, SBN42-pristine-5 is statistically different from the others.

Turning to Region I. There are two well-known techniques to characterize the relation between v and K_I: Wiederhorn's exponential law β $(d(log(v))/dK_I)$ [268] and Maugis' power law n $(d(log(v))/d(log(K_I)))$ [174]. Table II-3.1 presents the estimated slopes of the fitting curves indicated by dashed lines on Figure II-3.1 for the four pristine samples. Similar to Region 0, the three samples grouped together (SBN42-pristine-4, SBN42-pristine-6 and SBN42-pristine-8) possess similar slopes, especially when considering the values of n. On the other hand, SBN42-pristine-5 has a significantly higher the slope. The SCC behavior of this sample is rather different from the other three samples.

Table II-3.1: Estimated values of β (exponential laws), n (power laws) and K_E from the data points in Figure II-3.1 for SBN42 pristine samples.

Sample name	β	n	$K_E(MPa \times m^{0.5})$
SBN42-pristine-4	37 ± 6	36 ± 5	0.3770 ± 0.0001
SBN42-pristine-5	66 ± 6	72 ± 6	0.449 ± 0.001
SBN42-pristine-6	50 ± 3	45 ± 2	0.373 ± 0.003
SBN42-pristine-8	41 ± 2	40 ± 2	0.4050 ± 0.0005

To conclude the experimental results of SBN42 pristine samples, the SCC behavior of SBN42-pristine-4 and SBN42-pristine-6 are very similar, with similar K_E values and slopes of Region I. Compared to these two samples, the curve of SBN42-pristine-8 has a slight shifting (0.03 $MPa \times m^{0.5}$) and similar slope. It is worth noting that the fabrication protocol of SBN42-pristine-8 (Protocol B) is different from the other three pristine samples (Protocol A). Considering the error bars, these samples should be considered similar. On the other hand, SBN42-pristine-5 is an outliner with data points clearly separated from the other three samples and a significantly higher environmental limit, β value, and n value.

Considering the difference between SCC test, generating APS in different batches may have varying effects on the glass structure and thus on the SCC behavior. Thus, the following analysis probes the batches separately.

II-3.1.2 Batch 1

Let us consider the results of **Batch 1** – SBN42-pristine-4 and SBN42-600C-18h-1. First, let us recall **Batch 1** fabrication protocol concerns Protocol A (Section 3.1). Figure II-3.2 shows the SCC results for these two samples. Visually the data points are in the same general area; however, the curves appear significantly different. For SBN42-pristine-4, there is a clear K_E

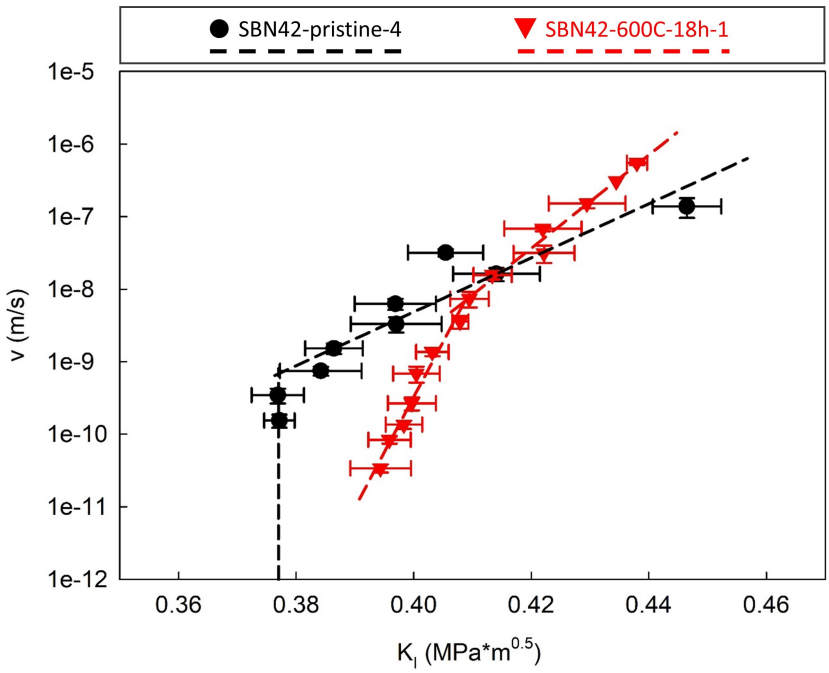

Figure II-3.2: Stress corrosion cracking curves of **Batch 1** – SBN42-pristine-4 (black circles) and SBN42-600C-18h-1 (red inverted triangles) along with the error bars and the fitting curves shown by dashed lines.

and Region I, and the line shape resembles the two lowest regions in Figure 2.11. Considering the curve of SBN42-600C-18h-1, no Region 0 can be observed. For comparison purposes, it should be assumed to be less than 0.3944 $MPa \times m^{0.5}$ (the data point with the lowest K_I in the curve). Additionally, the curve for the APS sample can be separated into two parts: v less than and greater than 10^{-8} m/s. For each part, a linear relationship between $log(v)$ and K_I can be determined. Henceforth to distinguish the two Region I, the one corresponding to lower (higher) velocities will be call Region I-L (Region I-U) and fitting parameters for this region will be marked with a superscript "L" ("U").

Table II-3.2: Estimated values of β (exponential laws), n (power laws) and K_E from the data points in Figure II-3.2 for SBN42 samples of **Batch 1**. The superscript "L" corresponds to Region I-L and "U" corresponds to Region I-U. The cross over between the upper and lower regions is $v \sim 10^8$ m/s for SBN42.

Batch 1	β^U	β^L	n^U	n^L	$K_E(MPa \times m^{0.5})$
SBN42-pristine-4	37 ± 6	–	36 ± 5	–	0.3770 ± 0.0001
SBN42-600C-18h-1	64 ± 4	152 ± 15	63 ± 4	140 ± 14	–

Table II-3.2 presents the fitting parameters concerning the environmental limits and Region I for **Batch 1**. As no clear environmental limit was revealed for SBN42-600C-18h-1, no conclusions can be drawn between the two samples. Now turning to Region I. For simplicity, the slope of SBN42-pristine-4 is put in the column with the "U" superscript.

SBN42-600C-18h-1 has been broken up into lower and upper parameters. Comparing the slopes between the two samples, both slopes of SBN42-600C-18h-1 are higher than SBN42-pristine-4. The two SCC curves are in similar area and they intersect at $v \sim 2 \times 10^{-8}\ m/s$. Interestingly, this is also the turning point for separating the upper and lower part of Region I for SBN42-600C-18h-1. For $v < 2 \times 10^{-8}\ m/s$, the APS sample is more resistant to SCC than the pristine sample (as the APS sample is on the right side of the pristine sample); while for $v > 2 \times 10^{-8}\ m/s$, the pristine sample has better SCC behavior (as the APS sample is on the left side of the pristine sample).

The results of **Batch 1** indicates two Region I in SBN42 APS glasses. This will be elaborated in the general discussion in Section 4.1.2. The data points of the two samples correspond to similar K_I ranges. However, both slopes of SBN42-600C-18h-1 are higher than SBN42-pristine-4. Comparison of SCC behavior between the two samples depends on the crack propagation velocity v.

II-3.1.3 Batch 2

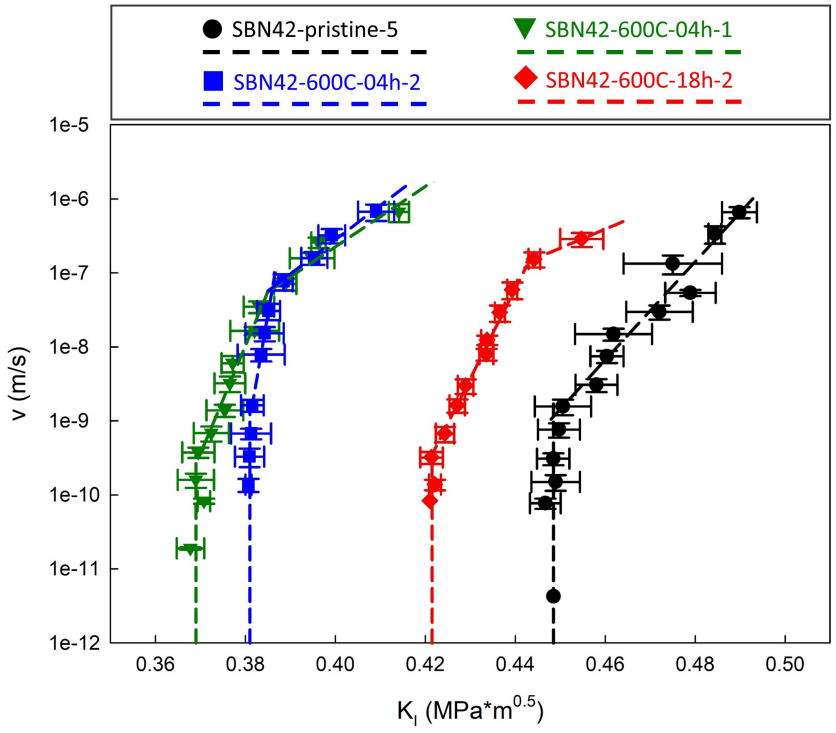

Figure II-3.3: Stress corrosion cracking curves of **Batch 2** – SBN42-pristine-5 (black circles), SBN42-600C-04h-1 (green inverted triangle), SBN42-600C-04h-2 (blue rectangles) and SBN42-600C-18h-2 (red diamonds) along with the error bars and the fitting curves shown by dashed lines.

Now let us consider the results of **Batch 2**. Batch 2 follows the same fabrication protocols as **Batch 1**, Protocol A (Section 3.1). This batch includes four samples – SBN42-pristine-5, SBN42-600C-04h-1, SBN42-600C-04h-2 and SBN42-600C-18h-2. Figure II-3.3 shows the SCC results for these samples along with the fitting curves.

Visually the data points are not in the same general area, with the exception of SBN42-600C-04h-1 and SBN42-600C-04h-2, which have similar annealing protocols (annealed for the same duration, but not at the same time). Additionally, the curves appear significantly different for different annealing protocols. The curves of three APS samples sit on the left side of SBN42-pristine-5. This signifies that the APS samples in **Batch 2** are more susceptible to SCC than the pristine sample. The two samples annealed at T_a=600 ℃ for t_a=4h are in the same area. However, the SBN42-600C-18h-2 curve shits to the right side of the two SBN42-600C-04h samples. This implies an increase in the glasses SCC behavior.

For all **Batch 2** samples, the environmental limits K_E can be identified (Table II-3.2) and are indicated by the vertical lines in Figure II-3.3. The environmental limit of SBN42-pristine-5 is greater than the APS samples. The environmental limit of SBN42-600C-04h-1 and SBN42-600C-04h-2 should be considered the same as they are within the error bar of the experimental setup. Lastly, SBN42-600C-18h-2 sits between the pristine and the two SBN42-600C-04h samples.

Table II-3.3: Estimated values of β (exponential laws), n (power laws) and K_E from the data points in Figure II-3.3 for SBN42 samples of **Batch 2**. The superscript "U" corresponds to Region I-U and "L" corresponds to Region I-L. Error bars correspond to standard deviations of data fits in data points in Figure II-3.3. Due to the minor differences between the experimental setups, which lead to shifting in the full SCC curve, K_E has an additional uncertainty of 0.025 $MPa \times m^{0.5}$.

Batch 2	β^U	β^L	n^U	n^L	$K_E(MPa \times m^{0.5})$
SBN42-pristine-5	66 ± 6	–	72 ± 6	–	0.449 ± 0.001
SBN42-600C-04h-1	41 ± 7	146 ± 12	38 ± 6	127 ± 11	0.369 ± 0.001
SBN42-600C-04h-2	46 ± 5	353 ± 2	43 ± 5	311 ± 2	0.3810 ± 0.0002
SBN42-600C-18h-2	26	121 ± 5	27	121 ± 5	0.4215 ± 0.0005

Now turning to Region I. Like SBN42-600C-18h-1 in **Batch 1**, APS samples display two slopes in Region I. Table II-3.3 presents the slopes of the fitting curves indicated by dashed lines on Figure II-3.3. The use of superscripts are the same as those of **Batch 1**. For simplicity, the slope of SBN42-pristine-5 is put in the column with the "U" superscript. Considering the two SBN42-600C-04h samples, one discovers that the slopes of Region I-U are similar within error bars and the curves coincide. However, the Region I-L of SBN42-600C-04h-2 (blue dashed line) is steeper in comparison with SBN42-600C-04h-1 (green dashed line). It is worth noting that these two samples were not annealed at the same time. At the beginning of annealing, APS commences and there are significant compositional changes in the samples. For short time annealing, minor difference in manipulations (the exact annealing time t_a and temperature T_a) during the annealing procedure may induce large differences in the glass structure. Post-mortem fracture surface analysis reveal differences between these two samples. Generally, the data points are located in the same area. The SCC behavior of these two samples are similar. Considering the effects of APS on Region I, increasing the annealing time from 4h to 18h leads to a decreases in the slopes of both Region I-L and Region I-U. Interestingly, the slope of SBN42-pristine-5 is in between of the slopes of Region I-L and Region I-U for all APS samples.

In summary, **Batch 2** is similar to **Batch 1** as both have two Region I for SBN42

APS samples. Annealing the samples for short time (4h) makes the curve shift to left side compared to the pristine samples. Longer-time annealing (18h) shift the curves to the right side compared to the 4h-annealed samples. In addition, the slopes of two Region I decreases as annealing time increases. These effects may be linked to the kinetics of spinodal decomposition, which will be discussed in the general discussion in Section 4.1.1.

II-3.1.4 Batch 3

The last batch of SBN42 samples concerns a large batch, from which there are 6 DCDC samples [2] were cut. Additionally, it is worth noting that the fabrication protocol of **Batch 3** is not the same as the other batches. Protocol B (Section 3.1) allows fabrication of larger sample batches and the as-fabricated glasses are visually more homogeneous compared to **Batch 1** and **Batch 2** (no visible wavy lines in the samples due to imperfect mixture). The results of **Batch 3** concern 3 samples – SBN42-pristine-8, SBN42-600C-04h-3 and SBN42-600C-18h-3.

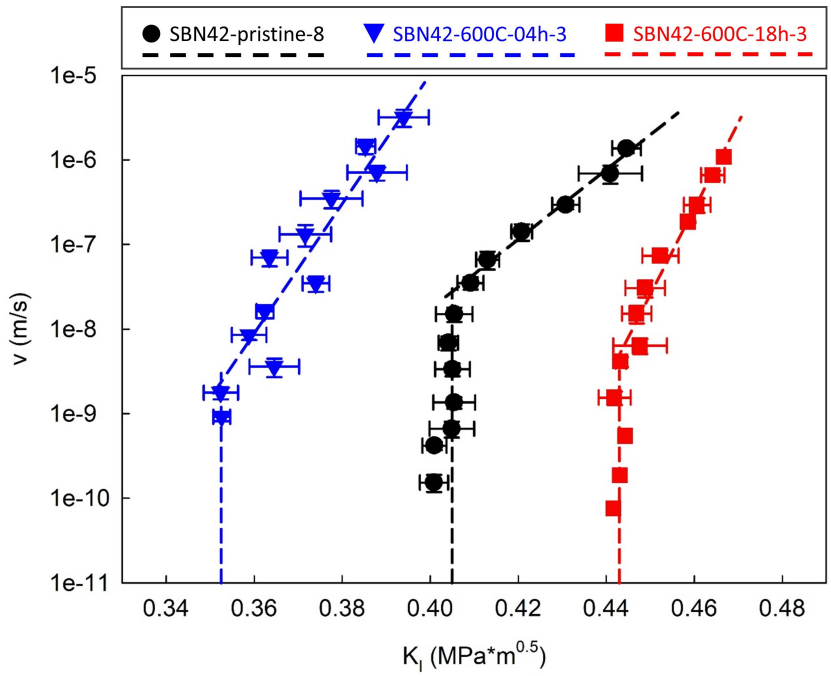

Figure II-3.4: Stress corrosion cracking curves of **Batch 3** – SBN42-pristine-8 (black circles), SBN42-600C-04h-3 (blue inverted triangle) and SBN42-600C-18h-3 (red rectangles) along with the error bars and the fitting curves shown by dashed lines.

Figure II-3.4 shows the SCC results for these samples along with the fitting curves. Let us first consider the general positioning of the SCC curves. Figure II-3.4 depicts the SBN42-pristine-8 data set as black circles. It should be recalled from Section II-3.1.1, this sample concerns the group of pristine samples located in the same region. Looking at the

[2] Four samples have been used and two are remained for further tests. The data of SBN42-pristine-7 was rejected as the pre-crack was too long; and hence, it will not be presented.

general positions of the annealed samples, SBN42-600C-04h-3 (blue inverted triangles) sits on SBN42-pristine-8 left side, and SBN42-600C-18h-3 (red squares) sits to the right side of SBN42-pristine-8. All three curves are well separated for Batch 3.

For all **Batch 3** samples, the environmental limits K_E can be identified (Table II-3.4) and are indicated by the vertical lines in Figure II-3.4. SBN42-600C-18h-3 possesses the highest K_E, SBN42-600C-04h-3 possesses the lowest, and the K_E of SBN42-pristine-8 is in between them. The phenomenon of **Batch 3** herein is similar to **Batch 2**: (1) annealing the sample for short time (T_a=600 ℃, t_a=4h) shifts the SCC curve to the left side; and (2) longer annealing time (T_a=600 ℃, t_a=18h) shifts the curve to right side compared to the short t_a. Unlike **Batch 2**, the SBN42-600C-18h-3 is on the right side of SBN42-pristine-8. Hence, SBN42-600C-18h-3 is more resistant to SCC compared to its pristine counterpart. This is a good signal and accord with our research goal – to enhance the SCC behavior of glasses with APS structure.

Table II-3.4: Estimated values of β (exponential laws), n (power laws) and K_E from the data points in Figure II-3.4 for SBN42 samples of **Batch 3**.

Batch 3	β	n	$K_E(MPa \times m^{0.5})$
SBN42-pristine-8	41 ± 2	40 ± 2	0.4050 ± 0.0005
SBN42-600C-04h-3	77 ± 10	67 ± 8	0.3525 ± 0.0001
SBN42-600C-18h-3	102 ± 8	106 ± 8	0.443 ± 0.001

Considering Region I, all **Batch 3** samples only have one clearly defined slope in Region I. This is different from **Batch 1** and **Batch 2**, which have upper and lower zones of Region I. Considering the transition between Region 0 and Region I, the data points have some fluctuations. Thus, one can hypothesize two different scenarios: (1) only one Region I exists for these APS samples, or (2) the slopes between the two Region I are too similar to be distinguished and are hidden by data fluctuations.

Table II-3.4 presents the slopes (β for Wiederhorn's exponential law [268] and n for Maugis' power law [174]) of the fitting curves for the samples in **Batch 3**. Comparing the slopes of Region I, the slopes for the APS samples are higher than the pristine sample. Additionally, longer annealing times leads to an increase of slopes. Recalling that for the samples of **Batch 2**, annealing longer time results in a decrease of slopes for both Region I-L and Region I-U. Hence, the increase of slopes for **Batch 3** are opposites of **Batch 2** results. However, the fabrication protocols are different for these two batches. This may induce the differences in fictive temperature of the as-fabricated samples, and thus influence the SCC behavior of glasses [147, 148, 163].

II-3.1.5 Summary

SCC results of 3 SBN42 batches have been presented above. In summary, annealing samples to form APS glasses clearly affects their SCC behavior. The positioning of the SCC curve depends on the underline glass structure. Additionally, **Batch 1** (Figure II-3.2) and **Batch 2** (Figure II-3.3) revealed two different slopes in Region I for APS samples. The curves of

Batch 2 also reveal clear environmental limits. **Batch 3** did not uncover two Region I, rather only Region I-U and the environmental limit were detected. A general discussion (Section 4.2) of the phenomena will occur after the presentation of APS SBN96 results (Part III).

II-3.2 Evolution of fracture surfaces with APS structure of SBN42

After SCC experiments, the DCDC samples are broken into two pieces. Post-mortem analysis of facture surfaces aid in understanding how the material breaks. AFM imaging provides high-resolution images to study the topography of fracture surfaces. FigureII-3.5 shows the AFM height sensor images of the fracture surfaces of size $500 \times 500\ nm^2$ (first row) and $10 \times 10\ \mu m^2$ (second row) for SBN42 **Batch 2** and **Batch 3** samples, including pristine (left column), 600C-4h (middle column) and 600C-18h (right column) samples. It should be noted that these are as formed fracture surfaces, *i.e.* no post chemical treatment was done.

Let us first look at the small size images ($500 \times 500\ nm^2$), the topography of SBN42 fracture surfaces is rather different from the homogeneous glasses. Looking back at SBN12 (Figure I-2.2), the color scale for the topography is four time larger for SBN42 than SBN12. This is interesting as SBN42-pristine-5 and SBN42-pristine-8 are considered homogeneous as are SBN12 samples, yet the fracture surfaces of SBN42 pristine samples are much rougher than SBN12 samples. Section II-3.3.1 confirms this visual assessment via RMS calculations. Additionally, differences exists between **Batch 2** and **Batch 3**. At first glance, the fracture surfaces of **Batch 2** do not reveal an APS structure. However, **Batch 3** seems to display a slight APS structure, but it is difficult to quantify.

To quantify the phase sizes L, the small images were used ($500 \times 500\ nm^2$). Section II-1.1.1 presents the technique for acquiring the phase sizes L. However, there is a slight modification for SCC fracture surfaces concerning post-mortem washing. Frequently, the phase sizes were revealed directly (*i.e.* without the need of any post-treatment), or only a slight alcohol wash was needed (immersing in alcohol + ultrasound bath for 5 min, repeat two times). Table II-2.1 presents the estimations of phase size L. As the estimated phase size L vary between batches, the phase separation dynamics may not be the same between batches. Thus, the local interaction between crack front and material should also differ, resulting in different SCC behaviors.

Examining the $10 \times 10\ \mu m^2$ images (note that they have the same color scale as the $500 \times 500\ nm^2$ images), the fracture surfaces roughen with increased annealing time for all batch series. Comparing the samples with the same annealing protocol (the same column), **Batch 2** images appear rougher than **Batch 3**. Post processing these AFM images provides quantitative information, including RMS calculation and structure function analysis. The following subsections detail these results.

II-3.3 Post-mortem analysis on fracture surfaces

This section presents the post-mortem analysis on SBN42 fracture surfaces. RMS calculation and structure function analysis were performed on the $10 \times 10\ \mu m^2$ AFM images. Table II-3.5 presents the estimated phase sizes, RMS and structure function parameters (ℓ, ν, A and θ) for SBN42 samples of different batches.

II-3.3.1 Evolution of fracture surface roughness

RMS calculations were performed on the $10 \times 10\ \mu m^2$ AFM images for all batches. Table II-3.5 presents the results concerning the average of at least four sets of images for statistics.

Considering the pristine samples, the RMS of SBN42-pristine-4, SBN42-pristine-6, SBN42-pristine-7 and SBN42-pristine-8 fluctuate around 3 nm. However, the SBN42-pristine-5 RMS is larger than the other four pristine samples. Recalling that for SCC results (Figure II-3.1), the SBN42-pristine-5 is an outliner with data points clearly separated from the other pristine samples and it possesses a significantly higher environmental limit, β value, and n value. It is interesting to compare SBN42-pristine-5 results with Barlet's results [10, 14]. She found an increasing RMS, K_E, β value, and n value with increasing [Na_2O] (mol%). It is well known that [Na_2O] in glasses will delay the onset of crack propagation; hence, causing a shift in the K_E [218]. Due to the shifting of K_E, the crack front has more stored energy; hence, the crack front propagates through the weakest links thus increasing the RMS, β value and n value [104]. One could be tempted to use this explanation; however, [Na_2O] increases the depolymerization of a glass. Ideally, SBN42-pristine-5 has no NBO atoms; hence, the polymerization should be high in the glass. To understand better the crack path in SBN42-pristine-5, more detailed short-range structure investigations are needed.

Comparing the samples in **Batch 1** and **Batch 3**, the RMS values increase with the increase of T_a, thus with the increase of APS phase sizes. This is consistent with the literature reviewed in Section 2.4.3.1: the existence of secondary phase can change the crack path and makes the fracture surfaces rougher since the local interaction differs while the crack front encounters different phases. Additionally, it is in lines with the idea that the crack front follows the weakest path [104]. As the APS phase sizes increases, this effect is more significant.

Concerning **Batch 2**, the RMS increases between the pristine sample (SBN42-pristine-5) and the one annealed at 18h (SBN42-600C-18h-2). However, SBN42-600C-04h-1 and SBN42-600C-04h-2 has a mixed response even though their SCC behaviors are similar. Within one standard deviation of the calculations, SBN42-pristine-5 and SBN42-600C-4h-2 have similar RMS values, while SBN42-600C-18h-2 and SBN42-600C-04h-1 have similar RMS values. Considering other results, $t_a \sim$ 4h appears to be a changeover in the dynamics of the phase growth (see Section 4.1.1 for more details). At this point, it is hard to reach any conclusions concerning **Batch 2**. To understand better the crack paths, more detailed short-range structure investigations are needed.

Table II-3.5: Estimation of phase size (L), RMS and structure function analysis on $10 \times 10\ \mu m^2$ AFM images ($v \sim 10^{-9} - 10^{-6}\ m/s$) of SBN42 samples.

Sample name	$L\ (nm)$	RMS (nm)	$\ell\ (nm)$	ν	A	θ
Batch 1						
SBN42-pristine-4	0	2.6 ± 0.2	19 ± 3	0.35 ± 0.02	0.58 ± 0.03	0.20 ± 0.03
SBN42-600C-18h-1	50	8.8 ± 0.8	35 ± 6	0.40 ± 0.02	0.51 ± 0.03	0.40 ± 0.09
Batch 2						
SBN42-pristine-5	0	4.8 ± 1.1	21.1 ± 1.1	0.41 ± 0.06	0.48 ± 0.09	0.34 ± 0.12
SBN42-600C-04h-1	42	7.3 ± 0.9	36 ± 3	0.42 ± 0.02	0.47 ± 0.02	0.34 ± 0.03
SBN42-600C-04h-2	34	4.4 ± 0.7	23 ± 5	0.41 ± 0.02	0.49 ± 0.03	0.28 ± 0.03
SBN42-600C-18h-2	52	7 ± 2	49 ± 12	0.44 ± 0.05	0.44 ± 0.08	0.25 ± 0.06
SBN42-pristine-6	0	3.4 ± 0.4	11.6 ± 1.5	0.38 ± 0.05	0.53 ± 0.07	0.38 ± 0.05
Batch 3						
SBN42-pristine-7	0	3.5 ± 0.1	13.6 ± 1.4	0.36 ± 0.02	0.55 ± 0.03	0.38 ± 0.06
SBN42-pristine-8	0	3.2 ± 0.6	13 ± 2	0.37 ± 0.03	0.54 ± 0.05	0.35 ± 0.09
SBN42-600C-04h-3	45	5.4 ± 0.5	38 ± 2	0.352 ± 0.006	0.573 ± 0.009	0.211 ± 0.014
SBN42-600C-18h-3	77	9.5 ± 1.1	76 ± 3	0.37 ± 0.02	0.55 ± 0.03	0.20 ± 0.01

II-3.3.2 Effects of APS on structure function of SBN42 fracture surfaces

Like SBN12, the fracture surfaces of SBN42 are consistent with the structure function models [9]. Table II-3.5 presents the average values computed with more than four AFM images on each sample.

Let us first consider the meso-structure length scale ℓ, which is linked to the size of heterogeneities, *i.e.* different phases for APS glasses. Considering the pristine samples, the fabrication protocols have some effects on the values of ℓ:

- SBN42-pristine-4 and SBN42-pristine-5, which were fabricated by following Protocol A, have similar ℓ values, $\sim 20\ nm$;
- SBN42-pristine-6, SBN42-pristine-7 and SBN42-pristine-8 which were fabricated by Protocol B, have similar ℓ values, $\sim 13\ nm$.

Samples following Protocol B have a significantly lower ℓ value. Recalling that ℓ for SBN12 samples is 13 nm and SBN12 is considered a homogeneous glass. Hence, comparing SBN12 with SBN42 pristine samples, Protocol B provides a better elaboration method for forming a more homogeneous glass. For SBN42 APS samples, ℓ increases with the estimated phase size L. This will be further discussed in combination with the results of SBN12 and SBN96 in Section 4.2.2.

Turning to Poisson's ratio ν, ν estimated from the structure functions are higher than the results from ultrasonic echography (Section II-2.2, $\nu \sim 0.22 - 0.25$). In general, ν varies between batches, but it remains similar for the same batch. **Batch 1** appears to be an exception at first glance; however, one cannot eliminate that they are the same within a 99%

confidence interval ($\sim$ 2.5 standard deviation). Additionally, no specific effects due to APS structure can be deduced based on the data.

Considering the disorder contrast θ, compared to the homogeneous glass, *i.e.* SBN12, the values for SBN42 are significantly higher. For **Batch 2** and **Batch 3**, annealing the samples tends to decrease θ; while for **Batch 1**, the annealed sample possesses a higher θ compared to the pristine sample. Based on the results, it is difficult to summarize the effects of APS on θ. However, θ is generally less than 0.4 for SBN42 samples, while it can be up to 4 according to literature [9]. These values are rather small, which indicates that the distributions of micro-structure are rather random in the glasses.

To summarize, APS have some effects on the fracture surfaces roughness. AFM images show that the fracture surfaces of APS samples are significantly rougher in comparison with the pristine glasses. Post-mortem analysis show that fracture surfaces roughness increases with the phase size, which will be discussed with the results of SBN12 and SBN96 in Section 4.2.2.

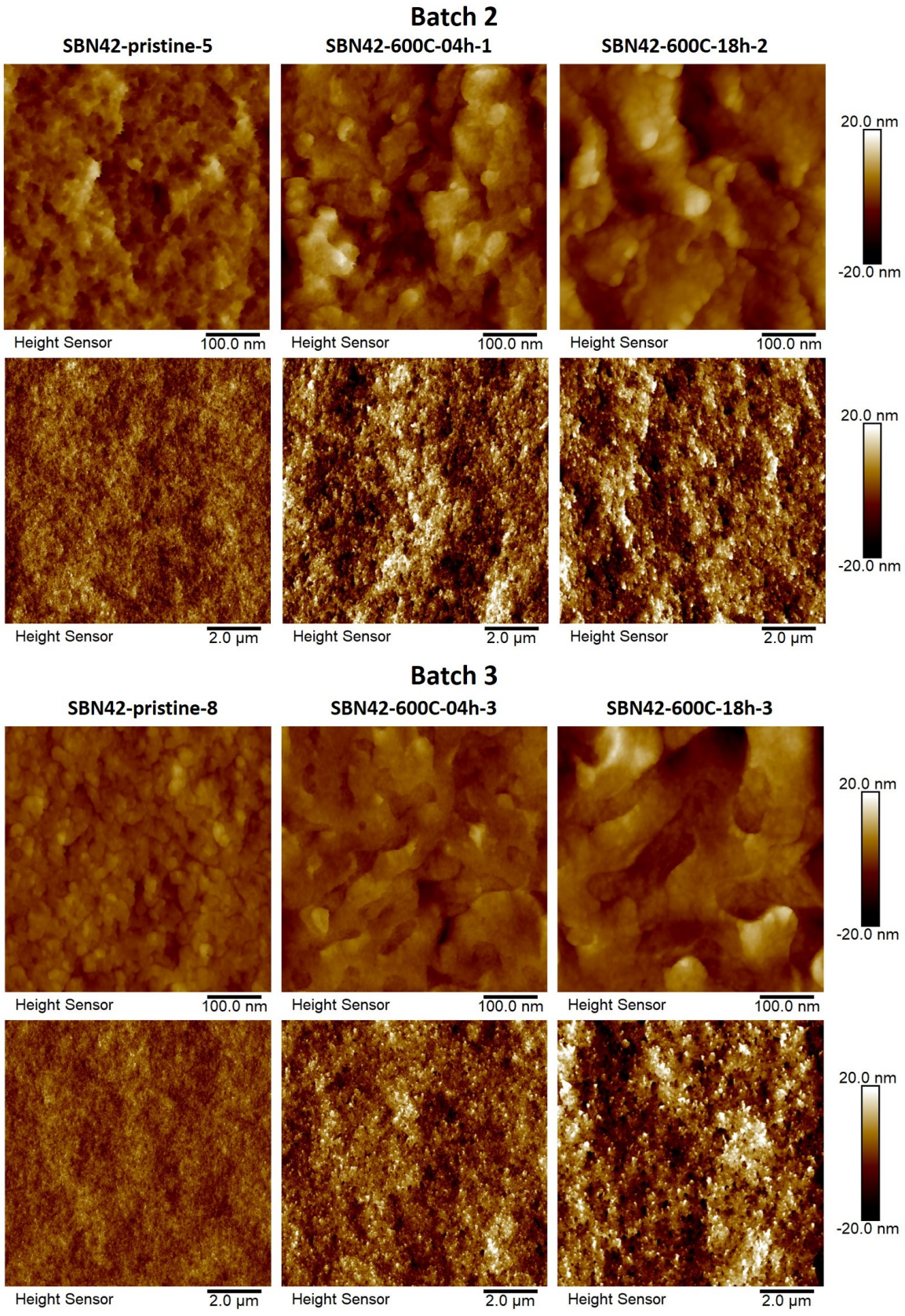

Figure II-3.5: AFM height sensor images on the fracture surfaces of SBN42 samples for **Batch 2** and **Batch 3**, of size $500 \times 500\ nm^2$ for the first row and $10 \times 10\ \mu m^2$ for the second row. The color bars remain the same all the images.

Part III

Investigations on SBN96 samples

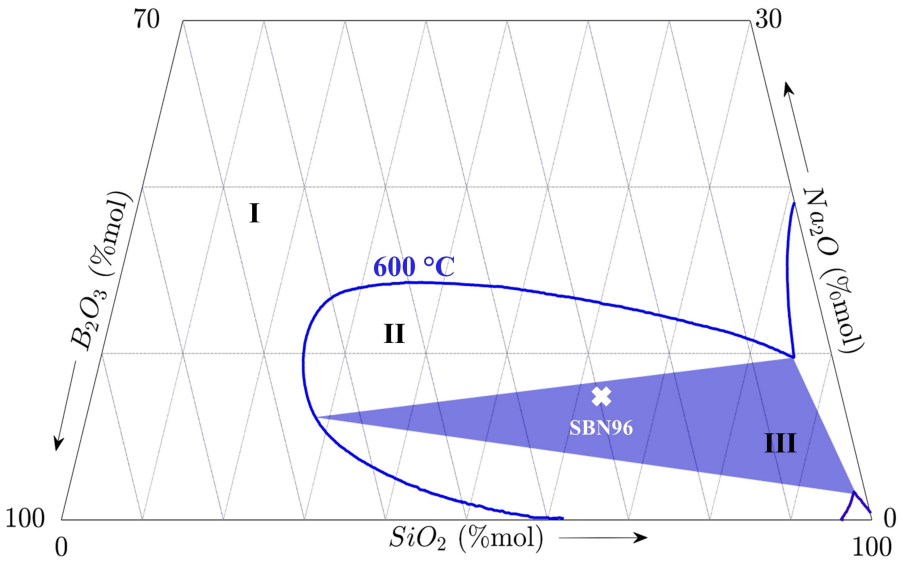

Figure III.1: Immiscibility diagram posed by Haller [106] for SBN systems at 600 ℃ with the location of SBN96 marked by the white cross.

In this part, I am going to present the results of SBN96, of which the chemical composition is 62.9SiO_2-29.6B_2O_3-7.5Na_2O (in mol%). Like SBN42 (Part II), this glass system is within the hypothesized three-phase area at 600 ℃as indicated in Figure III.1. Compared to SBN42, SBN96 has similar Na_2O fraction but a higher B_2O_3 fraction; thus a lower SiO_2 fraction. For SBN96, the values of K_{SBN} and of R_{SBN} are respectively 2.1 and 0.25. Thus, according to literature (Section 2.2.1), there should be no NBO atoms in SBN96.

The primary goal with studying SBN96 was to understand how APS alters SCC behaviors for a different chemical composition. As such the rather complete battery of test (structural, physical, mechanical and fracture tests) which SBN42 went through will not be invoked for SBN96. Like SBN42, SBN96 samples were annealed to provoke APS. The annealing conditions for SCC investigations remain the same as SBN42: pristine samples, T_a=600 ℃ and t_a=4h and 18h. Table III.1 lists the names of SBN96 samples along with the tests they underwent.

This part of the manuscript is organized as follows. Chapter III-1 presents structural and physical property characterizations of SBN96. Section III-1.1.1 concerns the general morphology of the samples, including naked-eye opalescence, optical microscopy imaging and AFM imaging. Section III-1.1.2 zooms in on the structural properties and presents Raman spectra for SBN96 pristine and annealed samples. Sections III-1.2 concerns the physical properties if SBN96, including density and elastic moduli measurements. Chapter III-2 presents SCC experiments and fracture surface analysis on SBN96 pristine and APS samples.

Table III.1: Sample list of SBN96 and tests they underwent.

Sample name	Fabrication protocol	Characterizations
Small samples		
SBN96-550C-04h-s SBN96-550C-18h-s SBN96-600C-04h-s SBN96-600C-18h-s SBN96-650C-04h-s SBN96-650C-18h-s	Protocol C	Density, Elastic moduli
DCDC samples		
SBN96-pristine-1 SBN96-600C-04h	Protocol C	Microscope, Density, Raman, Elastic moduli, SCC, AFM
SBN96-pristine-2	Protocol C	Density, Elastic moduli, SCC, AFM
SBN96-600C-18h	Protocol C	Microscope, Density, Elastic moduli, Raman

Chapter III-1

Structural characterizations and physical properties

Contents

To better understand the results of SCC tests, the general morphology at the micro- and meso- scales of APS-SBN96 samples needs to be considered. This section first examines a series of samples used to quantify and qualify the general morphology of the phase-separated zone in SBN96. These studies will invoke optical microscopy imaging and atomic force microscopy (AFM) imaging (Section III-1.1.1). Subsequently, Section III-1.1.2 reveals structural variations as seen by RAMAN analysis. Lastly, the physical properties of SBN96 (density and elastic moduli) are presented in Section III-1.2.

III-1.1 Structural characterizations on SBN96

III-1.1.1 General morphology of SBN96 APS samples

t_a \ T_a	550 °C	600 °C	650 °C
4h	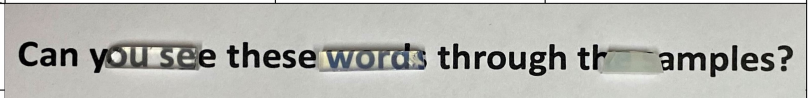		
18h			

Figure III-1.1: Photo of SBN42 annealed samples on a paper with words “Can you see these words through the samples?”. The samples were annealed at different temperatures (T_a=550 °C, 600 °C and 650 °C) for different durations (t_a=4h and 18h).

To examine the general morphology of APS-SBN96 and how it evolves with annealing protocols, a number of small samples were fabricated. Patrick Houizot in University Rennes I fabricated these small samples with Protocol C (Section 3.1). They were cut into small pieces and each pieces underwent a specific annealing protocol. An individual samples annealing temperature T_a was set to either 550 ℃, 600 ℃, or 650 ℃, and annealing duration t_a was also prescribed: 4h or 18h. Each sample underwent a single annealing procedure. The minimal and maximum annealing temperature were lowered by 50 ℃ for SBN96, in comparison with SBN42. The reason for choosing lower annealing temperatures concerns the change of the glass transition temperature (T_g) with the chemical composition. As indicated at the beginning of Part III, SBN96 has a lower SiO_2 fraction, a higher B_2O_3 fraction, and a similar Na_2O fraction compared to SBN42. According to literature [224], this induces a decrease of T_g and the deviation is estimated to be 50 ℃. Additionally, the SBN96-600C-18h DCDC sample was warped during annealing. Hence, the high annealing temperature of 700 ℃ may lead to melting of samples and would not have been suitable.

Optical microscope images

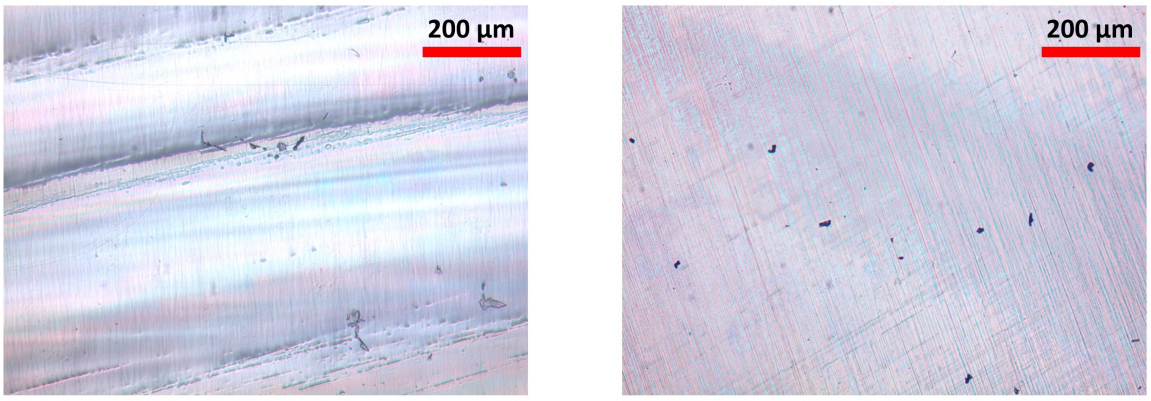

Figure III-1.2: Optical microscope images (5×) on the polished surfaces of SBN96-pristine-1 (a) and SBN96-600C-18h (b).

Figure III-1.1 reveals the effects of annealing temperature and time on the transparency of SBN96 samples. Looking at this image, one sees that the samples remain transparent when T_a=550 ℃ since the sentence "Can you see these words through the samples?" remains visible. For the two samples annealed at 600 ℃, the phenomenon is similar to that of SBN42-650C: the samples remain transparent for t_a=4h and becomes "milky" for t_a=18h. While annealing at 650 ℃, the SBN96 sample becomes fully opaque for t_a=4h and 18h. Recalling that the opalescence of APS samples is linked to the phase size. Compared to SBN42-700C samples (II-1.1), the kinetics of SBN96-650C is faster, since SBN96-650C-04h-s is more opaque than SBN42-700C-04h-s.

Like SBN42, microscope observations were performed on the polished surfaces to exclude the occurrence of crystallization in SBN96 DCDC samples before the SCC experiments.

Figure III-1.2 shows the 5× microscope images on SBN96-pristine-1 and SBN96-600C-18h. Surfaces resemble standard polished surfaces (small damages and scratches due to polishing are visible); however, no conic shape structures occur. This allows a preliminary judgement that crystallization did not occur or at least the crystals are too small to be visualized in the samples at T_a=600 ℃ and $t_a \leq$ 18h. Raman analysis in the next section further confirm this judgement.

AFM images

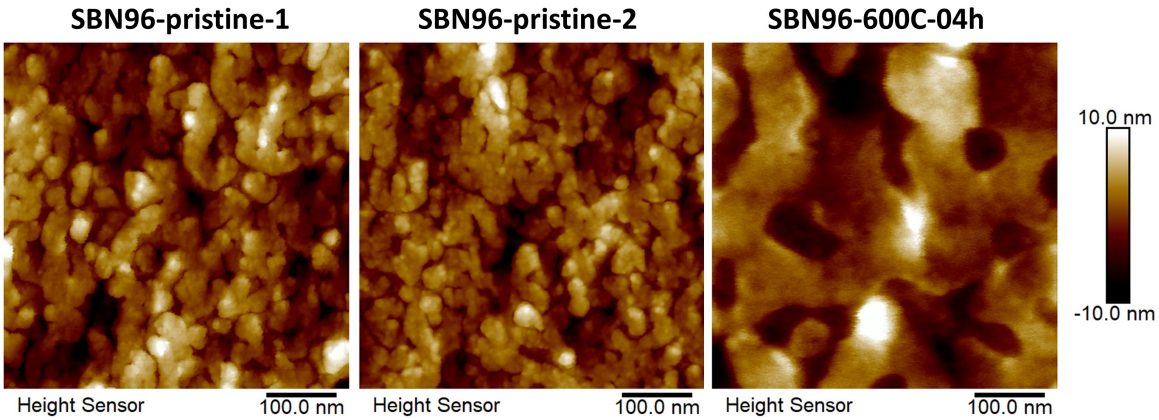

Figure III-1.3: AFM height sensor images on fracture surfaces of SBN96 DCDC samples of size $500 \times 500\ nm^2$. The color bar remains the same for each image.

Figure III-1.3 shows AFM height sensor images of the fracture surfaces (size $500 \times 500\ nm^2$) on the SBN96-pristine-1 (left column), SBN96-pristine-2 (middle column) and SBN96-600C-04h (right column) samples. These surfaces concern SCC fracture surfaces without any chemical treatment and will be further discussed in Section III-2.2. These images reveal that all the three samples display spinodal structural decomposition. It is worth noting that SBN42 pristine samples does not reveal APS structures (Figure II-3.1 in Section II-1.1.1). However, the SBN96-pristine fracture surface topographies indicate that APS exists before annealing. Compared to the pristine samples, there is a significant coarsening of phases during annealing. The phase sizes estimated from these images are 37 nm and 90 nm for SBN96-pristine and SBN96-600C-04h sample respectively.

Lastly, in the strict sense, SBN96-pristine-1 and SBN96-pristine-2 are not "pristine" samples without APS structure. They are called pristine samples because they are as fabricated, *i.e.* no annealing. Fabrication protocols requires additional development to eliminate the occurrence of APS in the as fabricated samples. SBN96-600C-04h has a significant increase in the amount phase separation after annealing.

III-1.1.2 Structural characterizations on SBN96 via RAMAN

Similar to SBN42, annealing SBN96 pristine samples should generate APS or even crystallization in the glasses. From SBN42 analysis, Raman characterizations plus optical visualizations provided the best method for identifying crystals. As my objective in my thesis is to

characterize SCC in APS glasses without crystals, I will only use Raman characterizations plus optical visualizations to ensure that crystals are absent from SBN96 samples. Raman characterizations can also reveal changes in structural properties, which will be considered.

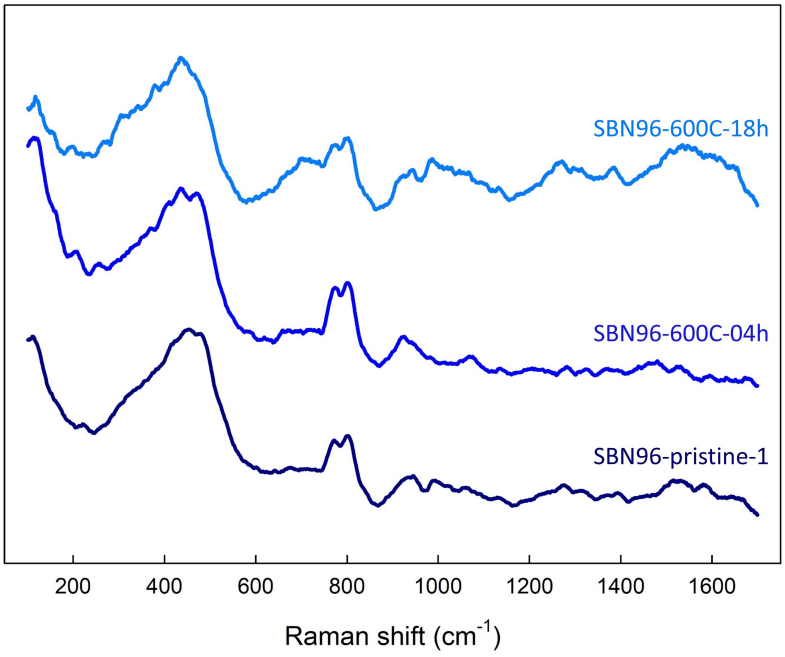

Figure III-1.4: Raman spectra of SBN96 pristine and annealed samples.

Raman characterizations were performed on the fracture surfaces of SBN96-pristine-1 and SBN96-600C-04h (to be discussed in Section III-2.1) and the polished surface of SBN96-600C-18h. These characterizations were done in NIMBE (CEA-Saclay, IRAMIS) with Arianna Filoramo on a homemade Raman spectrometer.

Ideally as R_{SBN}<0.5, there are no NBO atoms in SBN96. According to literature (Section 2.2.1), the SBN96 structural units should be similar to SBN42 but fractions should vary. Figure III-1.4 depicts Raman spectra of SBN96 pristine and annealed samples. It should be noted that the SBN96-pristine-1 has significantly more averaging, hence it is less noisy that the spectra on the annealed samples. Section 3.2.2 details the contributions to the spectra and they include:

- the broad band between $300 - 500\ cm^{-1}$ for the stretching and bending modes of Si-O-Si;
- small peak/bump at $630\ cm^{-1}$ concerning danburite or metaborate rings;
- peak at $700\ cm^{-1}$ attributed to metaborate units;
- bimodal peaks at $770\ cm^{-1}$ and $805 cm^{-1}$ concerning six-membered borate rings with one or more B[IV] and the vibration of boroxol rings, respectively;
- broad band between $900 - 1200\ cm^{-1}$ for the Q_i structures;
- broad band of between $1300 - 1660\ cm^{-1}$ attributed to B[III] units.

Unlike SBN42, SBN96 Raman spectra reveal significant differences after annealing. The features of the Raman spectra, which change with increasing annealing times t_a are:

1. The broad band between $300 - 500\ cm^{-1}$ widens slightly to lower frequencies.
2. There is a significant variation in the Raman spectra between $550 - 850\ cm^{-1}$.
3. There is a significant increase of the broad band between $900 - 1200\ cm^{-1}$.
4. There is an increase and clear splitting of the broad band between $1200 - 1600\ cm^{-1}$.

Now, let us compare the spectra for SBN96-pristine-1 and SBN96-600C-04h. Concerning the first point, this could imply larger SiO_2 rings. However, due to the noise in the spectra, it is hard to reach a conclusion. Concerning the third and last point, the spectra responses between $850\ cm^{-1}$ and $1700\ cm^{-1}$ are inconclusive due to the noise in the measurement. On the other hand, between SBN96-pristine-1 and SBN96-600C-04h there is a clear change in the Raman spectra shape between $625 - 850\ cm^{-1}$ (second point above). The response increases, and a shoulder appears between $700 - 770\ cm^{-1}$. Literature indicates that the shoulder could be due to metaborate units (rings and/or chains) [275, 57], boron rings with a BO_4 unit [275], O atom bridge between two B[III] atoms [152] and O atom bridge between one B[III] and one B[IV] [152]. It should be noted that if metaborate units are formed; the glass should have NBO atoms [152].

Increasing the annealing time from 4h to 18h results in large changes in Raman response. The shoulder between $700 - 770\ cm^{-1}$ grows into a broad peak. Additionally, the spectrum at high frequencies develops several broad bands, $1200 - 1400\ cm^{-1}$ and $1400 - 1600\ cm^{-1}$. According to literature [277], this scenario corresponds to a high sodium fraction in the borate network ($R_{SBN} > 0.5 + 0.25K_{SBN}$). Moreover, there is an increase in the broad band between $900\ cm^{-1}$ and $1200\ cm^{-1}$, especially between $980\ cm^{-1}$ and $1100\ cm^{-1}$. This zone is traditionally related to Q_i units in SBN glasses. However, Raman spectra in [277] revealed a growth of small peak at $1000\ cm^{-1}$ while increasing the sodium content in sodium borate glasses. One can hypothesize that the appearance of the two bands at high frequency ranges, the peak growth at $1000\ cm^{-1}$ and the growth of the shoulder between $700 - 770\ cm^{-1}$ are correlated. Combining all these changes, the glass could have NBO atoms on metaborate (BO_3 units with two bridging oxygen atoms and one NBO atom) units (rings and/or chains), and potentially pyroborate (BO_3 units with one bridging oxygen atom and two NBO atoms) structures [33].

Recalling that R_{SBN} of SBN96 is only 0.25. However, the SBN96 Raman spectra reveal the potential existence of NBO atoms in the borate network after annealing. One could hypothesize that local regions of sodium rich clusters exist in the boron-rich phase(s). NMR experiments should shed some light on this, and these types of experiments are planned for the future.

III-1.2 Physical properties of SBN96

Density and elastic moduli measurement were performed on SBN96 samples. The results are presented in this section.

III-1.2.1 Density

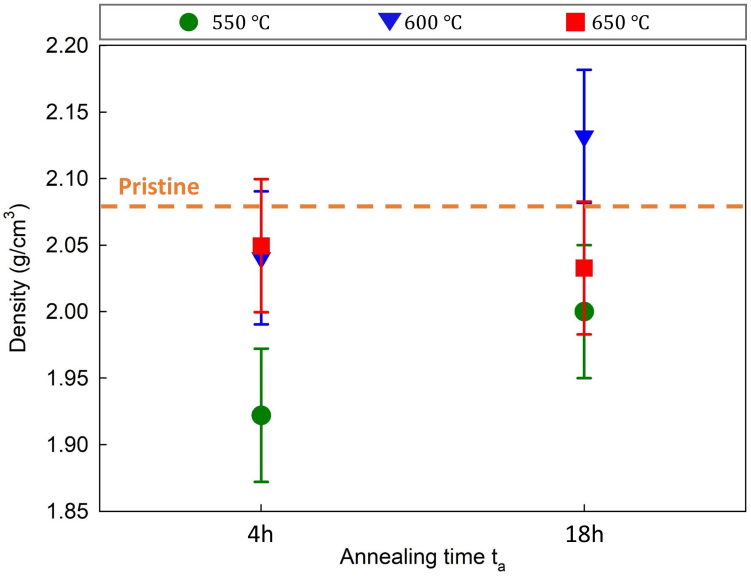

Figure III-1.5: Density of SBN96 small APS samples for different T_a (550 °C (green circles), 600 °C (blue inversed triangles) and 650 °C (red rectangles)) for different t_a (4h and 18h). Orange dashed line indicates the average density of two SBN96 pristine DCDC samples (Table III-1.1).

Density measurements herein invokes Archimedes method via the in-house equipment (Figure A.1). Since the samples are highly phase separated, emerging the sample in water risks washing out one or more phases. Thus, the measurements were only performed once for each sample. Based on previous measurements and considering the sample sizes, the measurements by Archimedes methods herein have uncertainties of about 0.05 g/cm^{-3} (Section 3.3.1).

Density measurements were performed on the SBN96 small samples in Figure III-1.1. Figure III-1.5 depicts the results with respect to the annealing time and temperature. Additionally, the dashed line indicates the average density of the two SBN96 pristine DCDC samples. Table III-1.1 presents the density measurements of various SBN96 DCDC samples, pristine and APS samples. For the DCDC samples, the measurements were done after SCC experiments. While for SBN96-600C-18h, the measurement concerns the complete DCDC sample.

In general, these results (including small samples and DCDC samples) indicate that the APS samples tend to have a lower density compared to pristine samples (with the exception of SBN96-600C-18h). However, due to the large uncertainties $\sim 0.05\ g/cm^{-3}$ (or even up to 0.1 g/cm^{-3} according to SBN42 density measurements (Figure II-2.1)), it is difficult to conclude the effects of APS on the density of SBN96 samples.

III-1.2.2 Elastic moduli

Techniques presented in Section 3.2.2 are invoked here to access the elastic moduli of SBN96 small and DCDC samples (Table III.1). Elatic moduli calculations invoke the density values

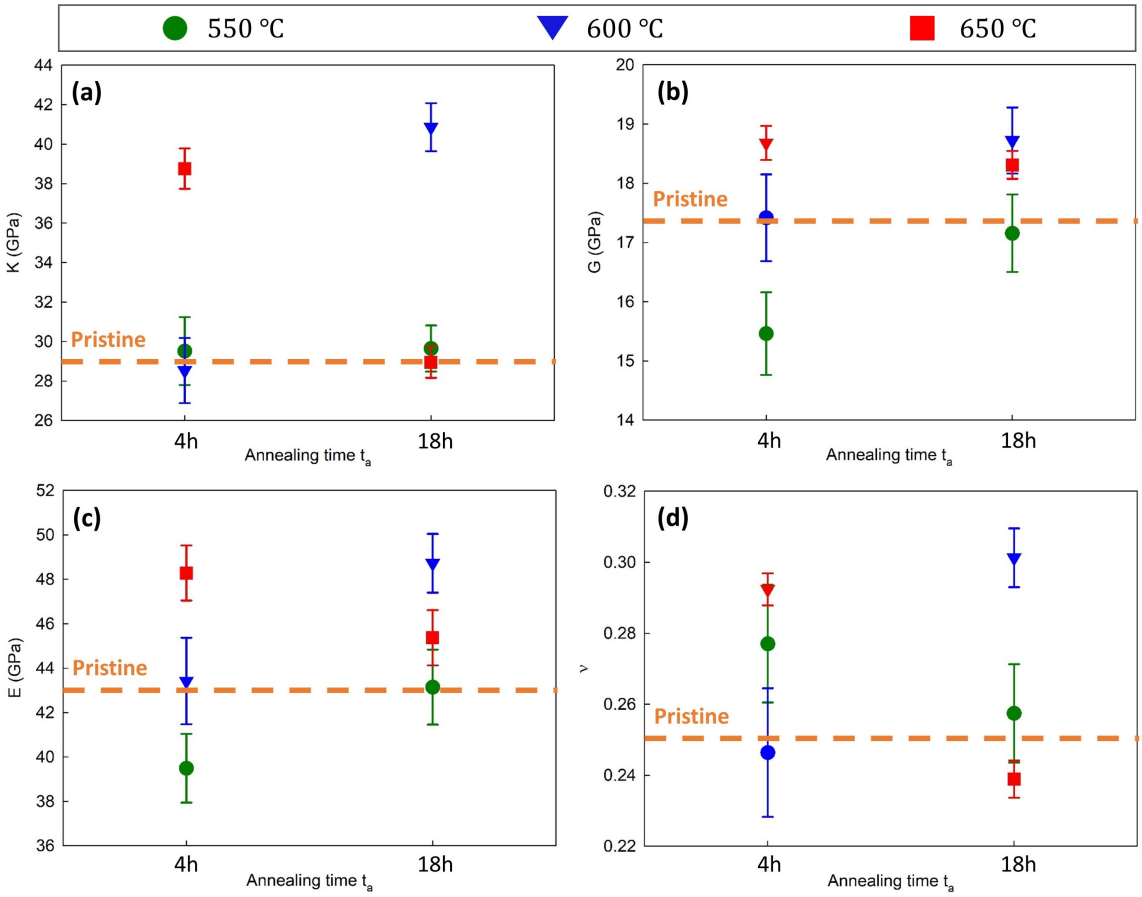

Figure III-1.6: Elastic moduli of SBN96 small APS samples for different T_a (550 °C (green circles), 600 °C (blue inversed triangles) and 650 °C (red rectangles)) with respect to t_a (4h and 18h). Orange dashed line indicates the average moduli of two SBN96 pristine DCDC samples (Table III-1.1). The uncertainties are estimated via Appendix A.2.

presented in the above section. Table III-1.1 complies the density, elastic moduli and Poisson's ratio calculations for SBN96 DCDC samples. Figure III-1.6 depicts the moduli and Poisson's ratio of SBN96 small samples with respect to the annealing times and temperature. Additionally, the dashed line indicates the average moduli/Poisson's ratio of the two SBN96 pristine DCDC samples. The results of APS samples fluctuate around the values of pristine samples. Both the density and acoustical wave techniques add error to the elastic moduli techniques. Hence, no trends with APS and moduli can be deduced at this time.

Table III-1.1: Density and elastic moduli of SBN96 DCDC samples.

Sample names	ρ (g/cm^3)	K (GPa)	G (GPa)	E (GPa)	ν
SBN96-pristine-1	2.08 ± 0.05	29.7 ± 0.9	18.0 ± 0.4	45.0 ± 1.3	0.247 ± 0.007
SBN96-pristine-2	2.06 ± 0.05	27.8 ± 0.7	16.51 ± 0.02	41.3 ± 1.0	0.252 ± 0.002
SBN96-600C-04h	1.95 ± 0.05	25.1 ± 0.9	17.0 ± 0.4	41.6 ± 1.5	0.223 ± 0.010
SBN96-600C-18h	1.94 ± 0.05	29.4 ± 0.8	16.8 ± 0.08	42.2 ± 1.1	0.261 ± 0.002

Chapter III-2

Stress corrosion cracking of SBN96

Contents

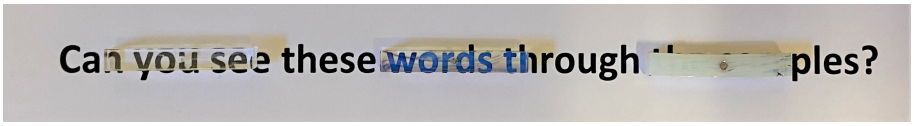

Figure III-2.1: SBN96 DCDC samples for SCC experiments on a paper with words "Can you see these words through the samples?". Left: SBN96-prisitne-2; middle: SBN96-600C-04h; right: SBN96-600C-18h.

Figure III-2.1 shows the DCDC samples of SBN96 for SCC experiments. APS due to annealing leads to sample opalescence (see Section III-1.1.1). SBN96 samples underwent the same annealing protocols as SBN42 for SCC tests, including pristine, and T_a=600 ℃ for t_a=4h and 18h. Results herein concern one batch of SBN96. Additionally, the SBN96-600C-18h sample was visibly warped after annealing; thus, it could not be used for SCC tests. (However, its shape was acceptable for density and moduli measurements.) Hence, the results in this chapter concern SBN96-prisitne-1, SBN96-prisitne-2 and SBN96-600C-04h.

III-2.1 SCC experiments on SBN96

This section presents the SCC experiments on SBN96 pristine (SBN96-pristine-1 and SBN96-pristine-2) and APS samples (SBN96-600C-04h). The three samples herein are from the same batch. During the SCC experiments, the temperature was controlled at 18.5 ± 0.5 ℃ and the humidity was controlled at $40.0 \pm 0.5\%$. Figure III-2.2 shows the experimental results along with the fitting curves for the three samples. It is worth noting that the range of K_I for the data points is from 0.24 to 0.32 $MPa \times m^{0.5}$. Recalling that the range for SBN12 and SBN42 is $[0.35, 0.50]$. At first glance, compared to SBN12 and SBN42, SBN96 samples are more susceptible to SCC.

First, consider the general position of SCC curves of different samples. The curve of SBN96-600C-04h sits to the right side of the two pristine samples, which signifies that the

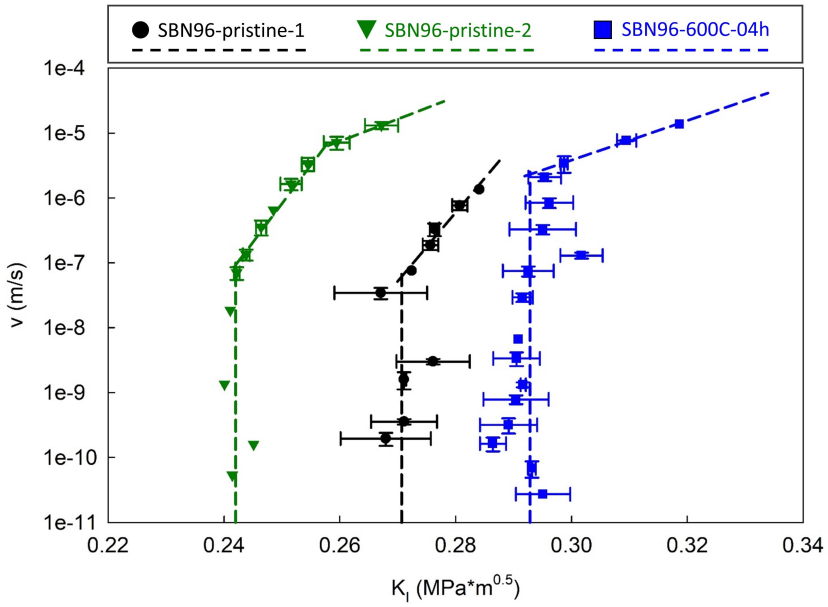

Figure III-2.2: Stress corrosion cracking curves of SBN96-pristine-1 (black circles), SBN96-pristine-2 (green inverted triangle) and SBN96-600C-04h (blue rectangles) along with the error bars and the fitting curves shown by dashed lines.

annealed sample is more resistant to SCC than the pristine samples. It is worth noting that post-mortem fracture surface analysis by AFM (Section III-1.1.1) evidences some APS structures in the pristine sample along with more significant APS in the annealed samples (Figure III-1.3). During the annealing process, there is compositional changes and phase coarsening. APS structural changes induce SCC strengthening for SBN96 samples.

Table III-2.1: Estimated values of β (exponential laws), n (power laws) and K_E from the data points in Figure III-2.2. The superscript "U" corresponds to Region I-U and "L" corresponds to Region I-L. Due to the minor differences between the experimental setups, which lead to shifting in the full SCC curve, K_E has an additional uncertainty of 0.025 $MPa \times m^{0.5}$.

Sample names	β^U	β^L	n^U	n^L	$K_E(MPa \times m^{0.5})$
SBN96-pristine-1	–	106 ± 12	–	68 ± 7	0.271 ± 0.003
SBN96-prisitne-2	34	119 ± 20	21	68 ± 5	0.242 ± 0.002
SBN96-600C-04h	30.5 ± 1.3	–	21.7 ± 0.7	–	0.293 ± 0.004

The vertical lines in Figure III-2.2 indicate Region 0, *i.e.* the environmental limit K_E, and Table III-2.1 presents the estimated K_E values. Considering Region 0, there is a horizontal shift of 0.03 $MPa \times m^{0.5}$ between the two pristine samples. Similar shifts existed for SBN12 (Section I-2.1 [10]); thus, this should be seen as the error between experimental setups. Considering Region 0 of SBN96-600C-04h, it sits to the right side of both SBN96-pristine samples. Hence, it has a tendency to have a higher threshold limit for crack propagation to commence.

Region I is a bit more interesting. First, let us examine the pristine samples. Experimen-

tal data points reveal two Region I for SBN96-pristine-2, while only one for SBN96-pristine-1. As there are two slopes for SBN96-pristine-1, the slope of Region I-L is marked with a "L" superscript, and the one of Region I-U is marked with a "U" superscript (This follows the same nomenclature as in Part II). It should be noted that the Region I-U concerns $v > 8\times10^{-6}\ m/s$ and SBN96-pristine-1 propagation velocity was not high enough to reach Region I-U. Hence, it probably exists, but was missed in this experiment.

Table III-2.1 provides the slopes in Region I. Both the upper and lower regions have been fitted with Wiederhorn's exponential law (equation (2.29)) and Maugis' power law (equation (2.30)). For the two pristine samples, the slopes for Region I-L are similar within the uncertainties of the calculations. Considering Region I-U for SBN96-pristine-2, the Maugis' power law exponent n^U is greater than 20. Thus, according to [6], this region should be controlled by stress corrosion and considered as a second Region I rather than a Region II. (See Section II-3.1.5)

Upon inspection, Region I for SBN96-600C-04h looks different from its annealed counterparts. In this sample, two different regions can be distinguished: (1) for $v > 2 \times 10^{-6}\ m/s$, log(v) shows linear relationship with K_I; and (2) for $v < 2 \times 10^{-6}\ m/s$, there is a significant fluctuation of data points. Unlike the two pristine samples, only one dominate slope exists in Region I for SBN96-600C-04h. For simplicity, the slopes of Region I in SBN96-600C-04h will be marked with a "U" superscript as the velocity is high ($v > 2 \times 10^{-6}\ m/s$). For $v < 2 \times 10^{-6}\ m/s$, data will be considered as Region 0. Region I-L either does not exist for SBN96-600C-04h or is hidden in the fluctuation of data points. It is interesting to take note that the point, where the environmental limit meets up with the lower part of Region I, has a velocity $v \sim 2 \times 10^{-6}\ m/s$. This is in stark contrast to the pristine samples where Region 0 and Region I-L meet at about $1 \times 10^{-7}\ m/s$. On the other hand, the velocity corresponding to the turning point between Region I-L and Region I-U of SBN96-pristine-2 is about $7 \times 10^{-6}\ m/s$. This value is similar to the turning velocity between Region 0 and Region I-U for SBN96-600C-04h. Moreover, comparing Wiederhorn's exponential law and Maugis' power law for Region I-U in SBN96-pristine-2 and SBN96-600C-04h, one discovers that they are similar, especially the power law slopes. Hence, the coarsening of the phase in SBN96 does not modify the slopes in Region I-U, rather it shifts the full curve to the right side of its pristine counterparts.

In general, annealing in this sample causes an increase in the glass SCC resistance. Additionally, annealing may prevent the Region I-L to occur and causes the glasses to move directly from the environmental limit to Region I-U. A general discussion of the phenomena concerning SBN42 and SBN96 occurs in Section 4.2.

III-2.2 Post-mortem analysis on fracture surfaces

Like SBN12 and SBN42, AFM characterizations were performed for post-mortem fracture surface analysis. Figure III-2.3 shows the fracture surface AFM height sensor images of size $1 \times 1\ \mu m^2$ (first row) and $10 \times 10\ \mu m^2$ (second row) on the SBN96-pristine-1 (left column), SBN96-pristine-2 (middle column) and SBN96-600C-04h (right column) samples. Small-scale images ($500 \times 500\ nm^2$) in Figure III-1.3 and Figure III-2.3 top row ($1 \times 1\ \mu m^2$)

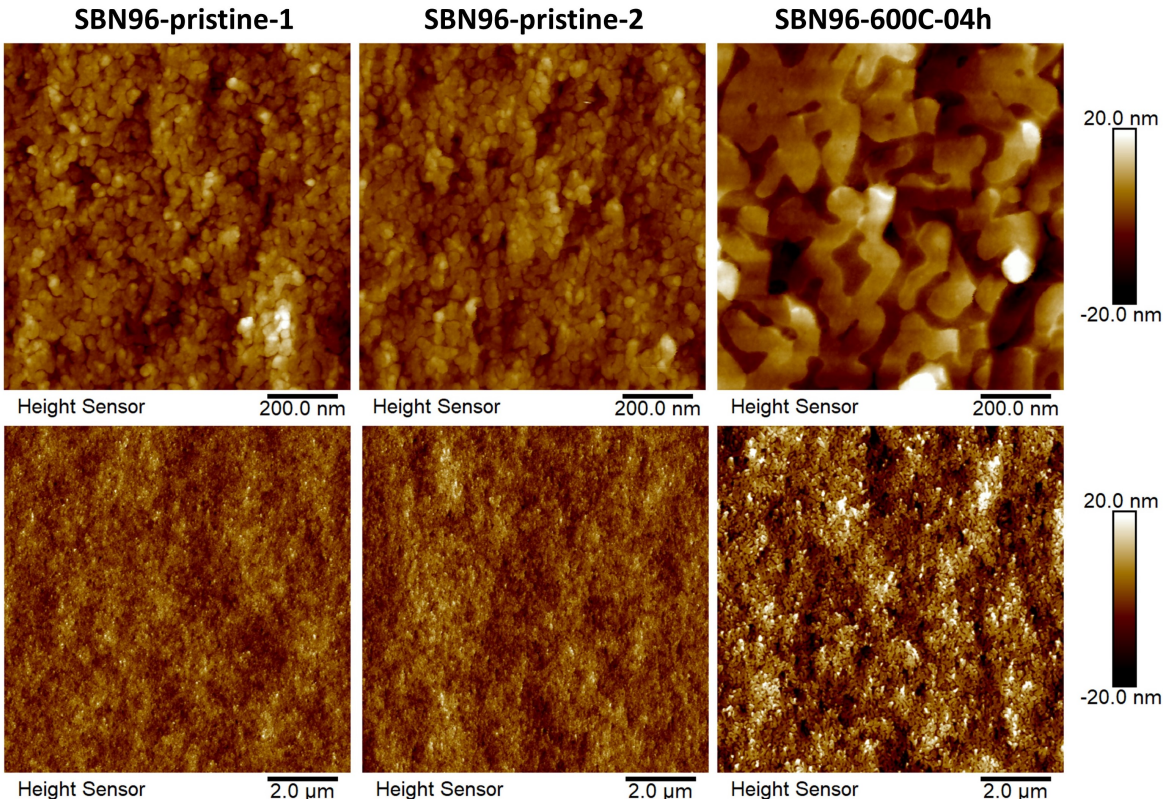

Figure III-2.3: AFM height sensor images on the fracture surfaces of SBN96 samples of size $1 \times 1\ \mu m^2$ for the first row and $10 \times 10\ \mu m^2$ for the second row. The color bars remain the same for each row.

reveal that all the three samples display spinodal decomposition structure. The phase sizes estimated from these images are 37 nm and 90 nm for SBN96-pristine and SBN96-600C-04h samples respectively. It is noteworthy that these surfaces are SCC fracture surfaces, not dynamic fracture surfaces, and they are without HCl acid treatment (Section II-1.1.1 uses chemical treatment to reveal the structure of SBN42). One hypothesis proposed to explain this phenomenon is that the crack propagation tends to circumvent one of the phases, possibly Si-rich phase as it has a higher chemical durability and more resistant to SCC [241]. The crack front turns for circumventing "obstacles", resulting in the display of "obstacles" on the fracture surfaces.

Examining the large size images, with the same color scale, the two pristine samples display similar topographies. On the other hand, SBN96-600C-04h is significantly rougher than the pristine samples. Post processing these images provides quantitative information, including RMS calculation and structure function parameters. The following sections detail these results.

III-2.2.1 Evolution of fracture surface roughness

RMS calculations were performed on post-mortem fracture surfaces. The AFM image sizes were $10 \times 10\ \mu m^2$. At least five sets of images were taken on each sample for statistics.

Table III-2.2: Estimation of phase size, RMS and structure function analysis on $10 \times 10\ \mu m^2$ AFM images of SBN96 samples.

Sample name	$L\ (nm)$	RMS (nm)	$\ell\ (nm)$	ν	A	θ
SBN96-pristine-1	40	4.0 ± 0.7	19 ± 8	0.40 ± 0.02	0.49 ± 0.03	0.37 ± 0.14
SBN96-pristine-2	33	4.5 ± 0.7	20 ± 3	0.42 ± 0.03	0.47 ± 0.05	0.36 ± 0.06
SBN96-600C-04h	90	8.0 ± 0.5	39 ± 6	0.42 ± 0.06	0.46 ± 0.10	0.35 ± 0.05

Table III-2.2 presents the results.

For the two pristine APS samples, their RMS values are within the error bars; hence, one cannot eliminate that they are the same, and the RMS is about 4 nm. Considering SBN96-600C-04h, the RMS value is approximately twice larger than the pristine samples, $\sim$ 8 nm. Similar to SBN42, the coarsening of phases results in an increase of the RMS value, indicating rougher fracture surfaces. However, one annealing condition is not enough to deduce the relationship between RMS, phase sizes and annealing time t_a. Fracture surface analysis on samples with different annealing conditions are required.

III-2.2.2 Structural function analysis on fracture surfaces

Structural function analysis on fracture surfaces of SBN96 samples after SCC tests were performed. Herein, I used $10 \times 10\ \mu m^2$ AFM height sensor images for calculating the structure functions and related parameters (protocol outlined in Section 3.4.2.3). Like SBN12 and SBN42, the fracture surfaces of SBN96 are consistent with the structure function models [9]. Table III-2.2 presents the average values computed with more than 5 AFM images for each sample.

Let us first consider the meso-structure length scale ℓ, which is linked to the size of the heterogeneities, *i.e.* different phases. Like the RMS of fracture surfaces, the values of ℓ are similar for the two pristine samples. On the other hand, ℓ for SBN96-600C-04h is approximately twice that of pristine samples. Likewise, the phase sizes (see Section III-1.1) estimated from SBN96-600C-04h AFM images (90 nm) is nearly twice that of the SBN96-pristine samples (37 nm). As mentioned above, the crack propagation tends to circumvent one of the phases. For SBN96 samples, annealing causes a doubling of the phase size visually on fracture surfaces and a doubling of ℓ values.

The remaining parameters, ν, A and θ do not vary significantly with annealing (differences with annealing are within one standard deviation). Like SBN12 and SBN42, the Poisson's ratio ν estimated from the structure functions are higher than the results from ultrasonic echography (Section III-1.2, $\nu \sim 0.23 - 0.30$). For the parameter $A \in [1/3, 1]$, the values are rather small, indicating an anisotropy in the sample. The values of θ are small, indicating that the distributions of microstructure are rather small and random in SBN96 samples.

In general, the difference of structure functions between pristine and annealed samples is mainly from the differences of ℓ, *i.e.* from the change of phase size. I hypothesis that one of the phases work as "obstacles" in the glasses to inhibit the crack propagation. The growth of this phase enhances this effect and results in a higher SCC resistance of the annealed sample.

To conclude this part, SBN96 pristine and annealed samples display APS structures. Annealing induces the coarsening of phases and potential occurrence of NBO atoms in borate network. Additionally, the SBN96 annealed samples has a better SCC performance compared to the pristine samples. This is accompanied by rougher fracture surfaces and a larger length scale ℓ.

Chapter 4

General discussion

Contents

The goal of my PhD is to study the APS structure in SBN glasses and to understand the effects of APS on SBN glass properties, especially SCC behavior. I have investigated three SBN glass systems (SBN12, SBN42 and SBN96), two of which undergo APS. The three parts above present the experimental results by glass type. This chapter concerns a general discussion on the three SBN glasses. Their results will be compared and contrasted in seeking a more general scenario.

4.1 Effects of APS on stress corrosion cracking behavior

As presented in the introduction of this thesis, I aim at studying the effects of APS structure on SCC behavior in SBN glasses. My results show that annealing samples to form APS glasses clearly affects their SCC behavior. Some common phenomena can be observed from the SCC curves of SBN42 and SBN96 samples. They will be discussed in the following subsections.

4.1.1 APS kinetics and its effects of shifting SCC curves

APS structure in the samples results in a shifting of the SCC curves. Recalling that the results of SBN42 **Batch 2** and **Batch 3** reveal several common points:

1. Annealing the samples for short times ($\lesssim$4h) makes the curve shift to left side in comparison with the pristine samples;
2. Further annealing the samples ($\gtrsim$18h) shifts the curves to the right side compared to samples annealed for short times. Moreover, for **Batch 3**, the sample annealed for long times (SBN42-600C-18h-3) has a better SCC behavior than its pristine counterpart (SBN42-pristine-8) does.

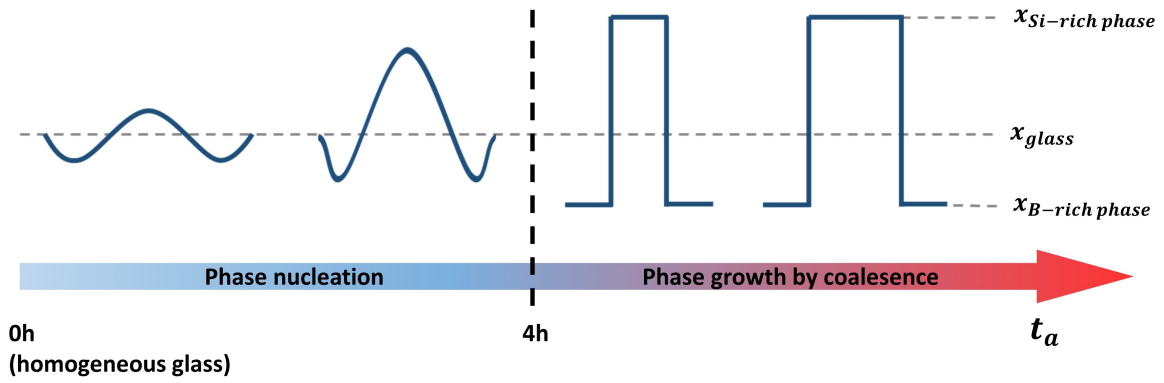

Figure III-4.1: Schematic of the evolution of concentration profiles of phases for SBN42 spinodal decomposition [7, 263].

In other words, small size APS structures make the samples more susceptible to SCC; and larger APS structures tends to re-enhance the SCC resistance. In some instances, the APS glass outperforms their pristine counterparts (*e.g.* **Batch 3**).

To explain this effect, a hypothesis concerning the kinetics of APS (based on [7, 263]) is proposed. First, recall that SBN42 decomposes into Si-rich phases and B-rich phases. According to Baniel's investigation [7] on SBN42 samples, the physical properties (more specifically, Young's Modulus and damping) fluctuate significantly during the first 4 hours of annealing; and then they stabilize with slight drifts. I hypothesize these fluctuations correspond to the large changes in the local chemical composition during these first 4 hours. These chemical composition changes should be linked to the nucleation of the Si-rich and/or B-rich phases. After 4 hours, the chemical compositions of different phases stabilize, and the dominate evolution is the merger and growth of the phases. This increases the size of the APS zones. This hypothesis is further enhanced by NMR results, which evidence significant changes in the borate network between SBN42-pristine-d, SBN42-600C-0.5h-d and SBN42-600C-2h-d (Figure II-1.11). The structure evolves between SBN42-600C-2h-d and SBN42-600C-18h-d, but less significantly.

Considering these phenomena, Figure III-4.1 provides a schematic of the evolution of the concentration profiles with respect to time for SBN42 proposed herein. Glasses start out homogeneous. During the first four hours of annealing, nucleation of the Si-rich and/or B-rich phases occurs. As revealed in Figure II-1.1, the subsequent 4h to 18h causes the growth of Si-rich phase. Let us not forget, the first 4 hours of annealing negatively impacts the SCC behavior, with a better SCC performances when t_a increases from 4h to 8h.

Hence, one can conjecture the SBN42 are in a transient state for $t_a < 4h$ and the phase chemical compositions have not yet reached an equilibrium. Additionally, the zones are rather small and localized, thus the interface formation is not complete. In this instance, the network of interfaces do not aid in inhibiting the crack propagation. Even worse, the phases in this transient state possess a worse SCC behavior compared to the homogeneous pristine sample. Freezing glasses by dropping their temperatures in this zone ($t_a < 4h$) leads to a glass with poor SCC performances.

On the other hand, one can conjecture the SBN42 reaches an equilibrium in the phase chemical compositions for $t_a \gtrsim 4h$. During this time period, phases grow and merge forming complex 3-D structures. Thus, the network of interfaces aid in inhibiting the crack propagation by working as crack front barriers. This results in enhancing the SCC behavior compared to samples annealed for $t_a \lesssim 4h$.

The APS kinetics in SBN96 are faster in comparison with SBN42. SBN96-pristine samples have small-size phase separations ($\sim$ 40 nm), which are similar to SBN42-600C-04h samples. Also, the phase size of SBN96-600C-04h ($\sim$ 90 nm) is similar to SBN42-600C-18h samples ($\sim$ 80 nm). Raman spectra of SBN96 reveal significant borate network changes concerning BO_3 units after annealing. Nonetheless, SBN42 Raman spectra do not show differences in the borate network, yet NMR spectra do. Considering the phase size, it is predicted that SBN96-600C-04h is near a phase compositional equilibrium (*i.e.* the phases are evolving by "Phase growth by coalescence" in Figure III-4.1). In this case, the SCC results of SBN96 are consistent with SBN42, as continuing to anneal after the formation of the secondary phase causes an increased SCC performance.

Literature [229] studying the effects of APS on fracture toughness show similar conclusion. Recalling Figure 2.15 in Section 2.4.2, spinodal decomposition structure aids in increasing the fracture toughness, and the binodal decomposition structure has negative effects [229]. Thus the results herein can be summarized as:

- Short annealing times provide spinodal decomposition in transient states. The zones are rather small and localized, which resembles the binodal decomposition structure to some extent. These rather small and localized zones weaken the SCC response of the glass.
- Long annealing times provide well-formed complex 3-D networks of spinodal APS in the glass. This structure aids in enhancing the glass SCC behavior.

4.1.2 Existence of two slopes in Region I for APS samples

APS samples of SBN42 **Batch 1** (Figure II-3.2), **Batch 2** (Figure II-3.3) and the SBN96-pristine samples (Figure III-2.2) revealed two different slopes in Region I, designated Region I-L for the lower velocity region and Region I-U for the higher velocity region. Simmons [241] studied phase-separated glasses of similar chemical compositions (see Figure 2.17). His results also revealed two slopes for v between 10^{-9} m/s and 10^{-4} m/s. His explanations concern the glass corrosion mechanisms and are summarized here. More specifically, the mechanism for glass corrosion in Region I consists of a proton-alkali ion exchange. This occurs rapidly to form a dealikalized surface layer around the crack front. The glass chemical durability controls this layer formation: the thickness and the formation rate of the layer decreases with increasing glass durability. As the crack propagation velocity slows down, the layer becomes thicker and ion diffusion is inhibited. The corrosion is then controlled by the matrix dissolution, resulting in Region 0. Simmons attributed the occurrence of the two different slopes to the low chemical durability of the samples [241]. He provided two explanations [241]: (1) the chemical attack in the glass is sufficient to cause an increase in the crack tip radius; or (2) the dealikalized surface is large enough to inhibit the ion diffusion.

Simmons tended to attribute the low velocity region to Region 0.

SCC results herein are not in full agreement with Simmons opinion [241] as three zones are clearly evidenced: environmental limit (*i.e.* K_E or Region 0), Region I-L, and Region I-U. Simmons [241] did not evidence the environmental limit as seen herein (vertical lines seen in Figure II-3.3 and Figure III-2.2). In short, his two regions resemble Region I-L and I-U herein, but he aligns Region I-U with the traditional Region I ($10^{-9}\ m/s < v < 2{\times}10^{-7}\ m/s$), and Region I-L with Region 0 ($2\times10^{-7}\ m/s < v < 10^{-4}\ m/s$). It is probable that Simmons' investigation should have an environmental limit (as evidenced by vertical lines in Figure II-3.3 and Figure III-2.2 herein). However, his lowest velocity corresponds to $v \gtrsim 10^{-9}\ m/s$, while the transition points between Region 0 and Region I correspond to $v \lesssim 10^{-9}\ m/s$. The experiments of Simmons were not slow enough to evidence the K_E values.

One may want to attribute Region I-U to Region II; however, it is unlikely that Region I-U corresponds to Region II. First, the Region I-U slope is rather high (in general greater than 20). According to Atkinson *et al.* [6], for the region to be controlled by diffusion of atmosphere water molecules (Region II), the value of n should be less than 10. Although not seen herein, Simmons [241] expects a collapse of the data when Region II is reached, and the Region II plateau is around $10^{-4}\ m/s$ with a RH = 50% (it should be noted similar values were found by Wiederhorn for soda-lime glasses [268]). Considering this, the second slope should be considered as a second Region I rather than a Region II. Hence, the two regions showing a linear relationship between $log(v)$ and K_I are both considered as Region I. The discussion below takes into consideration the three zones: environmental limit, Region I-L, and Region I-U.

Looking at the three different zones. For the highest velocity zone, the slopes of Region I-U are similar to what are seen in literature for a traditional Region I [10]. Additionally, Region 0 (K_E) are typically characterized by vertical lines [10] (as evidenced in Figure II-3.3 and Figure III-2.2). Region I-L is somewhat novel (as people have seen it before but associated it with K_E [241]) in this study. This slope is significantly higher than the slope in Region I-U. To explain the occurrence of two Region I, local interaction between the crack front and the material should be considered and corrosion mechanisms aid in the explanations.

Recalling that APS samples are inhomogeneous at the meso-scale ($10 - 100\ nm$), and SBN42 is decomposed into Si-rich and B-rich phases after annealing (see Chapter II-1). Additionally, Na^+ ions preferentially stay in the B-rich phase. During crack propagation at rather low v ($10^{-10}\ m/s - 10^{-8}\ m/s$ herein), the effects of different phases are significant. Recalling that there is the formation of dealikalized surface layer around the crack front during SCC. This process, *i.e.* the formation rate and the layer thickness, differs as the crack front encounters different phases. It is possible that the dealikalized layer is thick enough to provide a Region 0 in one phase, while the other phase is still in Region I. This would result in a transition between the traditional Region 0 and Region I (Region I-U herein), thus the occurrence of Region I-L. For faster crack propagation in Region I-U ($10^{-8}\ m/s < v < 10^{-5}\ m/s$ herein), the dealikalized layer(s) interacting with the different phases are thin and the effects of different phases are less significant. This hypothesis is enhanced with the results from Simmons [241] as all the APS samples annealed at different T_a for different t_a collapse to the same Region II plateau.

With the above analysis, APS structures result in two slopes in Region I. Nonetheless, some of the APS samples (SBN42 **Batch 3** APS samples and SBN96-600C-04h) reveal only one slope. It should be noted for both SBN42 **Batch 3** APS samples and SBN96-600C-04h, there are some fluctuations of data points. Hence, Region I-L may exist but is hidden in the data fluctuations of these samples. Nonetheless, this infers that the regions are not significantly differentiated from the others and the below scenarios can be hypothesized.

For SBN42 APS samples of **Batch 3** (Figure II-3.4), the turning points between Region 0 and Region I correspond to low velocities, similar to the transition between Region 0 and Region I-L. In other words, Region I-L and Region I-U merge into a traditional Region I. This indicates that for this sample, the formation of the dealikalized layer is similar in the different phases in this velocity region. Recalling that the fabrication protocol of **Batch 3** is different from the other batches. The chemical composition of different phases may also differ with the same annealing protocol. This results in different SCC behaviors.

Considering SBN96-600C-04h, the turning point corresponds to a high v, similar to the transition between Region I-L and Region I-U. In this case, Region I-L transforms into Region 0. As shown in Figure III-1.3, the APS structure are well formed. One of the phases may have significantly better SCC performance compared to the others, so that the crack front cannot propagate while interacting with this phase. This would inhibit the crack front propagation even though the environment can still interact with the weaker phase(s). Thus, the SCC behavior of the sample is dominated by this well-performing phase, and has a high velocity turning point between Region 0 and Region I.

In general, APS structure in glasses may lead to the occurrence of two slopes in Region I. Additionally, it may have other effects depending on the SCC performances of different phases. However, the chemical composition of individual phases are difficult to measure (or deduce) as they are at nanometer scales. Molecular dynamic (MD) simulations would help in understanding the interaction of crack front with different phases, thus providing explanations on the effects of APS on glass SCC behavior.

4.1.3 Effects of APS on slopes changing in Region I

The coarsening of APS in glasses results in slope changes in Region I. However, these effects are contradictory:

- SBN42 **Batch 1** and **Batch 3**: long-time annealing leads to an increase of slopes compared to pristine and/or short-time annealed samples;
- SBN42 **Batch 2**: annealing longer time results in a decrease of slopes for both Region I-L and Region I-U.

First, recall Section II-3.1.1 shows that the pristine **Batch 2** sample is statistically an outliner from the other pristine samples. Although **Batch 1** and **Batch 2** were elaborated with the same protocol, they were not fabricated at the same time. Additionally, the **Batch 3** fabrication protocol was different. Hence, the chemical composition of different phases may differ slightly between batches. Thus, the effects of APS on slopes differ between batches. Interestingly, for SBN96 samples, the slope of Region I-U for SBN96-pristine-2 (with APS of size $\sim 37\ nm$) is similar to the slope of Region I for SBN96-600C-04h (with APS of size

$\sim 90\ nm$). For SBN96 samples, the coarsening of APS does not change the slopes for high velocity region ($v > 7 \times 10^{-6}\ m/s$).

Recalling Barlet's thesis [10], she studied the impact of electronic irradiation on the SCC behavior of SBN12 (59.6SiO_2-23.9B_2O_3-16.5Na_2O in mol%) and SBN14 (70.0SiO_2-15.8B_2O_3-14.2Na_2O in mol%). Her results reveal curve shifting and slope changes in Region I after electronic irradiation: for SBN12, the slope increases and K_E decreases slightly; for SBN14, the slope decreases and K_E increases by 0.33 $MPa \times m^{1/2}$. Additionally, the fracture surface roughness (*i.e.* RMS) increased with these changes. It is worth noting that the chemical compositions of SBN12 and SBN14 are close to immiscibility area of SBN glasses (Figure 2.4). Interestingly, the results on high sodium content glasses [10], which are further away from miscibility gap, do not reveal significant differences on SCC behavior and fracture surface roughness. Furthermore, it is interesting to note structural changes in theses glasses. The Raman spectra for SBN12 and SBN14 change after electron irradiation; however, the high sodium content glasses did not change much. These spectra reveal changes in the borate network (linked to the BO_3 units) after electron irradiation along with some other changes in the silicate network. Herein, I also showed significant changes in the borate network (linked to the BO_3 network) after annealing (via NMR for SBN42 and Raman for SBN96). Thus, post treatment (*i.e.* annealing and irradiation) of low sodium glasses plays on the structural arrangement, which plays on the SCC performance, rendering the glasses more or less susceptible to SCC. Additionally, post-treatment can alter the slopes in Region I, either increasing or decreasing them. Nevertheless, based on the current results, it is difficult to summarize the effects of post treatment procedures on the environmental limit nor the slopes in Region I. Further SCC experiments on similar glasses with varying chemical compositions would aid in understanding this.

In summary, APS structure influences SCC behaviors of SBN glasses. It leads to the occurrence of a second Region I at low crack propagation velocities, and the general location of SCC curve shifts with APS. Our results show that the 3-D complex network formed during long annealing times aids in enhancing SCC behavior. Further SCC experiments are required to confirm these results. Performing MD simulations would help in understanding local interactions between the crack front and different phases, thus providing explanations for these effects.

4.2 Effects of APS on fracture surface roughness

AFM imaging provides high-resolution topography of fracture surfaces. Comparing the results between pristine and APS samples of SBN42 and SBN96, APS structure significantly affects the fracture surface roughness. For both SBN42 and SBN96, direct observations on AFM images reveal that increasing the annealing time t_a leads to an increase of fracture surfaces roughness. Post-mortem analysis including RMS calculations and structure function analysis have been performed on $10 \times 10\ \mu m^2$ AFM height sensor images. This section compares and contrasts results for the three glasses.

4.2.1 Effects of APS on RMS

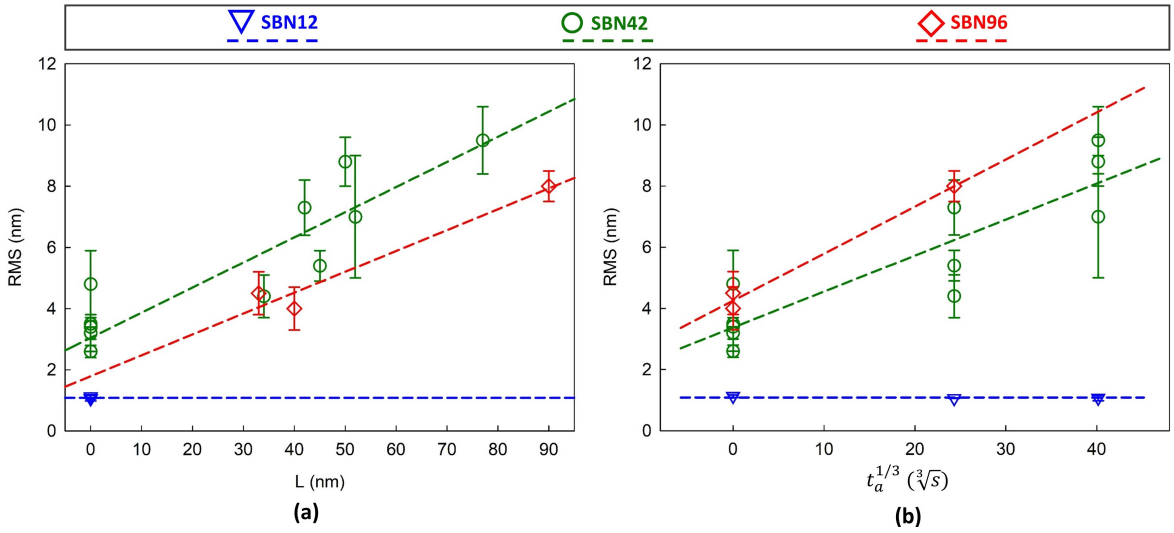

Figure III-4.2: Evolution of RMS with respect to (a) estimated phase size L and (b) the cubic root of annealing time $t_a^{1/3}$. Data in the figures concern SBN12 (blue inverted triangles), SBN42 (green circles) and SBN96 (red diamonds) along with the fitting curves indicated by dashed lines.

RMS calculations provide a traditional technique for surface analysis. Herein, the APS structure is characterized by the estimated phase sizes L. For homogeneous glasses (*i.e.* SBN12 pristine and annealed samples, and SBN42 pristine samples), L is 0. Figure III-4.2 (a) depicts the evolution of the RMS with L for the three glass systems. Additionally, literature (Section 2.2.2.2) and my results (Figure II-1.5 in Section II-1.1.1) evidence the phase size L grows as the cubic root of the annealing time $t_a^{1/3}$. Figure III-4.2 (b) presents the RMS evolution as a function of $t_a^{1/3}$. It is worth noting that even though SBN42-pristine (see Section II-1.1.1) are considered ideally homogeneous glasses (*i.e.* $L \sim 0\ nm$), the RMS values are significantly higher than SBN12 (which is outside the phase separation area and the RMS does not vary with t_a) samples. Generally, the RMS increases as a function of L. Additionally, as the phase size L growth is proportional to $t_a^{1/3}$, the RMS increases as a function of $t_a^{1/3}$ (Figure III-4.2 (b)). Nonetheless, the fracture surface roughness does depend on the underline chemical composition. By fitting the data points in Figure III-4.2, the following relationships can be extracted:

SBN12 (blue dashed lines in Figure III-4.2):	$RMS = 1.09 \pm 0.03$
SBN42 (green dashed lines in Figure III-4.2):	$RMS = 3.04 + 0.08 \times L$
	$RMS = 3.37 + 0.12 \times t_a^{1/3}$
SBN96 (red dashed lines in Figure III-4.2):	$RMS = 1.79 + 0.07 \times L$
	$RMS = 4.25 + 0.15 \times t_a^{1/3}$

where RMS and L are in nm, and t_a is in s.

The results show that for samples outside the phase separation area, the glasses remain homogeneous and RMS does not vary much before/after annealing; yet for APS SBN glass system, the RMS of fracture surfaces is proportional to phase size L and to the cubic root of the annealing time $t_a^{1/3}$. For a fixed phase size, the SBN96 RMS value is lower than SBN42, which means that the fracture surfaces of SBN96 are flatter. On the other hand, for a same annealing protocol, the SBN96 RMS value is greater than SBN42 since the APS kinetics of SBN96 are faster. Due to data fluctuations as presented in Figure III-4.2, more SBN42 and SBN96 samples are required to verify this relationship.

4.2.2 Effects of APS on fracture surfaces structure function model

Structure function analysis is rather novel for characterizing fracture surfaces. The fracture surfaces of all the samples during my thesis fit the structure function models [9]. It is worth noting that these are the first results proving the reliability of these structure function models on experimental fracture surfaces. Recalling the output parameters by fitting the structure function models are Poisson's ratio ν (or A as a function of ν, equation (I-2.1)), microstructure length scale ℓ, and disorder strength θ [9].

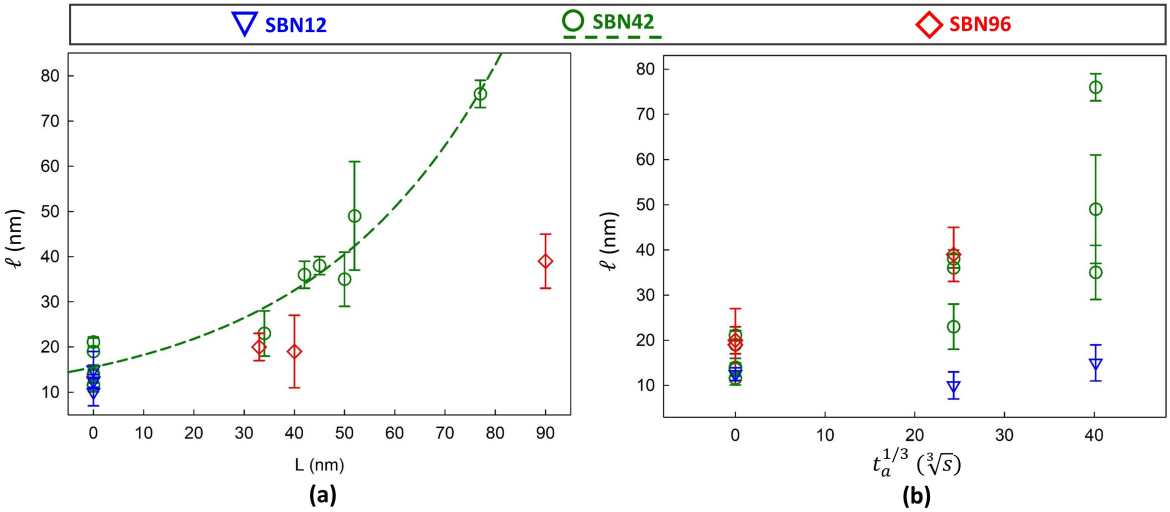

Figure III-4.3: Evolution of microstructure scale ℓ with respect to (a) estimated phase size L and (b) the cubic root of the annealing time $t_a^{1/3}$. Data in the figures concern SBN12 (blue inverted triangles), SBN42 (green circles) and SBN96 (red diamonds) along with the fitting curves indicated by dashed lines.

Figure III-4.3 shows the evolution of microstructure length scale ℓ with L and $t_a^{1/3}$ for the three glass systems, including pristine and annealed samples. For the homogeneous samples (*i.e.* SBN12 pristine and annealed samples, and SBN42 pristine samples), the heterogeneity comes from potentially ring size dispersion [264] or the imperfect mixture of the silicate and borate network. The ℓ values for the non-APS samples are lower than 20 nm. For APS samples, ℓ are generally higher compared to the non-APS samples. For SBN12, annealing does not vary ℓ. Considering the SBN42 and SBN96 data points, ℓ increases with increasing phase size L and $t_a^{1/3}$. For SBN42, the evolution of ℓ with respect to L is clearer as shown

in Figure III-4.3 (a). Fitting the SBN42 microstructure length scale ℓ as a function of phase size L, one obtains the following relation (indicated by the green dashed line in Figure III-4.3 (a))

$$SBN42: \ \ell = 6.8 + 8.8 \times exp(0.027L) \tag{4.1}$$

Hence, for SBN42, the microstructure length scale ℓ (in nm) increases exponentially with respect to the phase size L (in nm).

On the other hand, the evolution of SBN96 is not possible to deduce as I only have 3 samples. Nevertheless, SBN96 can be compared to SBN42. Figure III-4.3 depicts the microstructure length scale ℓ as a function of the phase size L. In this figure, SBN96 data points are below the fitting curve for SBN42. This signifies that when SBN42 and SBN96 possess the same phase size, the microstructure length scale ℓ of SBN96 is smaller. However, for SBN96, three samples are not enough to deduce the relationship between ℓ and L. More experiments are needed to qualify and quantify the relationship.

Considering the Poisson's ratio ν, no specific effects can be observed due to the APS structure. The values are rather similar for the samples from the same batch. However, the values estimated from the structure functions (about 0.33-0.45) are universally higher than the values measured by ultrasonic echography (about 0.22-0.26) for the three glass systems. Nonetheless, the values estimated herein are still considered reasonable, as the calculation of the Poisson's ratio ν via the structural function models invoke several hypothesis and are idealistic [9]. Different assumptions proposed during the calculations can increase errors. Another noteworthy difference is the length scale over which the Poisson's ratio are estimated: micro-scale for structure function analysis and macro-scale for echography measurements. In summary, ultrasonic echography techniques are a standard method for measuring elastic moduli, while post-mortem fracture surface analysis provides a reasonable value for ν (within the range [0,0.5]) to confirm the reliability of structural function models.

Turning to θ, the standard deviation of the Gaussian function for simulating the random spatially distributed component of a solid. For SBN12, θ is lower than 0.2, while for SBN42 and SBN96, θ ranges from 0.2 to 0.4. Generally, for the three glass systems, the θ values are rather low as it can be up to 4 according to literature [9]. However, no other specific effects can be observed due to APS structure.

In summary, APS structure alters the fracture surfaces properties, *i.e.* RMS and L. Our results show that RMS is proportional to the APS phase size. Additionally, the samples herein provide first results concerning the structure function models on experimental fracture surfaces. The microstructure scale ℓ obtained by fitting the structure function models was found to increase exponentially with APS phase size. More experiments are needed to verify the relation between APS structure and fracture surfaces roughness.

Chapter 5

Conclusion and outlook

Amorphous phase separation (APS) is a dominant feature of the sodium borosilicate (SBN) glass phase diagram. It effects the glass properties, including structure, physical and mechanical properties. However, the effects of APS on the SBN glass SCC performance remain poorly understood. Hence, the goal of my PhD was to study the APS structure in SBN glasses and to understand the effects of APS on SBN glass properties, especially SCC behavior. During my PhD, I have investigated three sodium borosilicate (SBN) glass systems including SBN12, SBN42 and SBN96 (Table 1.1 and Figure 1.2). Among them, SBN12 is outside the phase separation area; SBN42 and SBN96 are within the hypothesized three-phase immiscibility area [106].

Annealing can easily generate APS for glasses falling within the immiscibility area. Experiments herein confirm that spinodal decomposition occurs in SBN42 and SBN96 annealed samples. For SBN42, for a fixed annealing temperature T_a, the evolution of the Si-rich phase size is proportional to the cubic root of annealing time $t_a^{1/3}$. Increasing the annealing temperature speeds up the APS process. Additionally, elevated annealing temperatures of T_a=700 ℃ provide the energy necessary to form α-cristoballite. Raman and XRD evidence this crystallization. As my goal was to study the effects of APS on SBN glass SCC properties, annealing at 700 ℃ was not dwelled on. However, these samples aid in understanding the general morphology changes in the boron network.

NMR characterizations were performed to probe the short-range order of SBN42 annealed samples. ^{29}Si MAS spectra confirm the nano-scale heterogeneity due to annealing. ^{11}B MAS and 3QMAS spectra reveal an increase of BO_3 ring units and a decrease of BO_3 non-ring units in annealed samples. This is consistent with the formation of B-rich phases due to APS. According to REDOR experiments, Na^+ ions preferentially stay in the B-rich phase. However, understanding the evolution of the Si-rich phase is beyond the work of this thesis. To better grasp its evolution, new studies should be undertaken to examine its evolution, including NMR tests on samples enriched with ^{29}Si isotopes.

For SBN96, the as-fabricated, *i.e.* pristine, samples are already phase separated. Raman spectra reveal huge evolution of the borate network in SBN96 annealed samples. Compared to SBN42, it has a faster APS kinetics. Additional tests with varying annealing times and temperatures will aid in uncovering the dynamics of phase separation in SBN96 samples. NMR characterizations on these glass samples may reveal interesting results as the 3-D APS network are well formed.

SCC tests via the Deben machine and DCDC samples were performed on SBN12, SBN42 and SBN96 pristine and annealed samples. The experiments on SBN12 aided in testing the new equipment and the reliability of the set-up. Considering the SCC results for SBN42

and SBN96, APS structure significantly influences the SCC behavior. First, the existence of APS leads to the occurrence of two different slopes in Region I. One possible explanation is that for rather low velocity crack propagation, there are different local interactions as the crack front encounters different phases. However, based on the results, no specific rules can be obtained concerning how APS plays on the slopes in Region I. Further SCC experiments may help in developing a general rule, and MD simulations may help in understanding the underline physics.

Secondly, the APS sizes promote shifting in SCC curves. For SBN42, small-size APS makes the glass more susceptible to SCC compared to the pristine samples. Further annealing the samples generates a 3-D complex APS network; this enhances the SCC performances compared to short-time annealed samples. SBN96 results reveal similar effects. In some cases, APS glasses outperform their pristine counterparts. Generally, well-formed 3-D complex APS networks aid in enhancing SCC behavior in SBN glasses.

SCC behavior and fracture surfaces roughness are related. Post-mortem fracture surface analysis aid in understanding the fracture of glasses. After SCC test, an Atomic Force Microscope (AFM) captures the evolution of fracture surfaces with annealing times. APS structures have some effects on the fracture surfaces roughness. AFM images show that the fracture surfaces of APS samples are significantly rougher in comparison with the homogeneous glasses. It is found that RMS is proportional to the APS phase size. Additionally, the samples herein provide first proof of the validity of the structure function models on experimental fracture surfaces. The output parameters of the structure function models include microstructure length scale ℓ, Poisson's ratio ν, and disorder strength θ. The microstructure scale ℓ was found to be related to APS structure, and it increases exponentially with APS phase size. Poisson's ratio ν from this method does not provide a precise estimation of the macro-scale Poisson's ratio, rather the value is a reasonable estimate (within the range [0,0.5]) which aids in confirming the reliability of structural function models. Additionally, ν and θ do not evidence a specific trend with APS.

In conclusion, my research shows that APS significantly influences the SCC behavior in SBN glasses. However, a glass's susceptibility to SCC depends on a number of factors, including fabrication protocol, annealing protocol, *etc.* The morphology and the local chemical composition of phases play an important role on glass SCC behavior. My investigations herein concern two chemical compositions within the hypothesized three-phase area and two annealing protocols. Structural characterizations aid in understanding the borate network, but experiments specifically designed (including fabricating enriched ^{29}Si glasses for NMR studies) to capture the evolution of the silica network would be useful. Additionally, sub-micrometer tests to uncover the local chemical composition measurement would be interesting; however, they remain experimentally challenging. Lack of comprehension on the microstructure brings difficulties in understanding the local interactions between the crack front and the different phases during SCC. Molecular dynamic (MD) simulations would help in filling this gap. Additionally, studies on APS kinetics are important. Controlling the APS morphology by changing the chemical composition, annealing temperature and annealing time is not only useful for basic science investigations, but also has industrial significance in the fabrication of special porous glasses. Considering the SBN phase diagram, there are still many other chemical compositions and different annealing protocols remain to be studied.

To enhance SCC performances by APS structure, more investigations are required.

Appendices

A.1 Density measurement equipment by Archimedes' method

This appendix shows the images of the equipment used for measuring the glass density by Archimedes' method. Figure A.1 shows the density measurement equipment invoked during my thesis, including (1) a homemade equipment (Figure A.1 (a)) in my laboratory and (2) a balance with a density kit (Figure A.1 (b)) in IPR in University of Rennes. For the two scales, the accuracy is 0.1 mg.

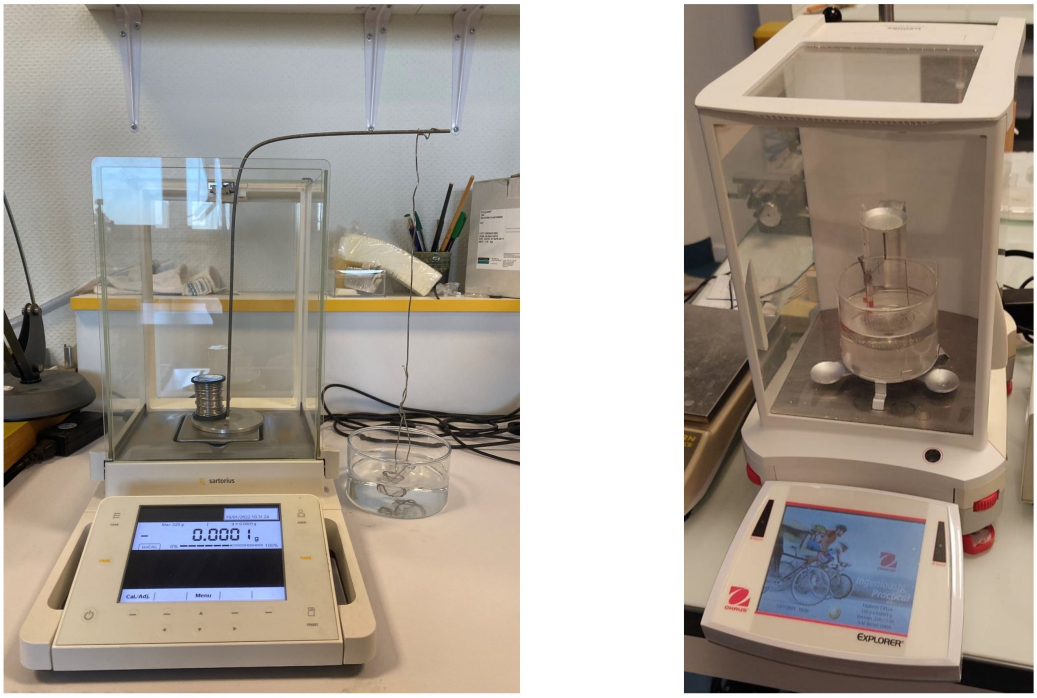

Figure A.1: Density measurement equipment by Archimedes' method: (a) Homemade equipment with a Satorius balance; (b) Explorer Analytical Analytical Balance EX124 with a density kit. The accuracy of the balances are 0.1 mg.

A.2 Estimation of elastic moduli uncertainties

Elastic moduli measurements rely on ultrasonic echography techniques. The moduli and Poisson's ratio are calculated via equations (3.7) - (3.6). Generally, the measurements of propagation velocities of acoustic waves in the samples possess some uncertainties, δv_L and δv_T. Since the calculations of moduli invoke the density results, the errors of density $\delta\rho$ add to the moduli errors. Using the propagation of uncertainties [252], the estimation of moduli uncertainties δM (with M signifying the moduli) from δv_L, δv_T and $\delta\rho$ can be expressed by the following equations:

$$(\delta E)^2 = \left[\frac{3v_L^2 - 4v_T^2}{(v_L/v_T)^2 - 1}\delta\rho\right]^2 + \left[\rho\frac{2v_L}{((v_L/v_T)^2 - 1)^2}\delta v_L\right]^2 + \left[2\rho\frac{-8v_L^2v_T^2 + 4v_T^4 + 3v_L^4}{v_T^3((v_L/v_T)^2 - 1)^2}\delta v_T\right]^2 \tag{A.1}$$

$$(\delta\nu)^2 = \left[\frac{v_L v_T^2}{(v_L^2 - v_T^2)^2}\delta v_L\right]^2 + \left[\frac{-v_T v_L^2}{(v_L^2 - v_T^2)^2}\delta v_T\right]^2 \tag{A.2}$$

$$(\delta K)^2 = \left[(v_L^2 - 4/3v_T^2)\delta\rho\right]^2 + 2\rho v_L\delta v_L)^2 + (8/3\rho v_T\delta v_T)^2 \tag{A.3}$$

$$(\delta G)^2 = (v_T^2\delta\rho)^2 + (2v_T\rho\delta v_T)^2 \tag{A.4}$$

In the above equations, δv_L and δv_T correspond to the standard deviations of measured longitudinal and transverse wave speeds. $\delta\rho$ is the uncertainties of density measurement: for Archimedes' method, it is 0.05 g/cm^{-3}; for pycnometer measurement, it concerns the standard deviations of measured values.

A.3 SCC data averaging

Section 3.4.1 details the measurement of the crack propagation velocity v and the calculation of the stress intensity factor K_I. Literature presents the results of SCC curves for different glass systems [241, 269, 271]. However, rarely did they present the error bars for the data (except for [14]) nor the method for data treatment. As I took images day and night, there was a significant amount of data. Hence, a method for smoothing the SCC data was developed during my PhD. After obtaining the v and K_I for a SCC experiment, the data treatments can be performed by following these steps:

1. Sort the v from smallest to largest. During this process, the v and its corresponding K_I should be grouped together. The v sort is expanded to the K_I.
2. Average the data and calculate the error bars. Herein, since there should be linear relationship between $log(v)$ and K_I [268], I based my averaging on the values of v. For v values between $10^{-Z} \leq v \leq 10^{-(Z-1)}$ m/s, I average the v for $[10^{-Z}, 2.15 \times 10^{-Z}]$, $[2.15\times10^{-Z}, 4.64\times10^{-Z}]$ and $[4.64\times10^{-Z}, 10^{-(Z-1)}]$ and their corresponding K_I values (2.15 is obtained from $10^{1/3}$ and 4.64 is obtained from $10^{2/3}$). Standard deviations for v and K_I can be also calculated. This provides three data points along with their error bars on the SCC curve for v between 10^{-Z} and $10^{-(Z-1)}$ m/s. Herein, Z is integer from 6 to 11.
3. Some outliners exist in the data; hence, this step aids in reducing them. Theoretically, for similar v values, the corresponding K_I should be similar. After separating the data into different ranges, v within a certain range should have similar K_I values. Hence, if they are more than one standard deviation away from the averaged values, they are considered outliners and are rejected.

4. Repeating Step 2 provides the average v and K_I along with their uncertainties.

This data treatment provides the averaged data points and the error bars for v and for K_I. Additionally, it aids in eliminating outliners.

A.4 Basic structure units in SBN glass system

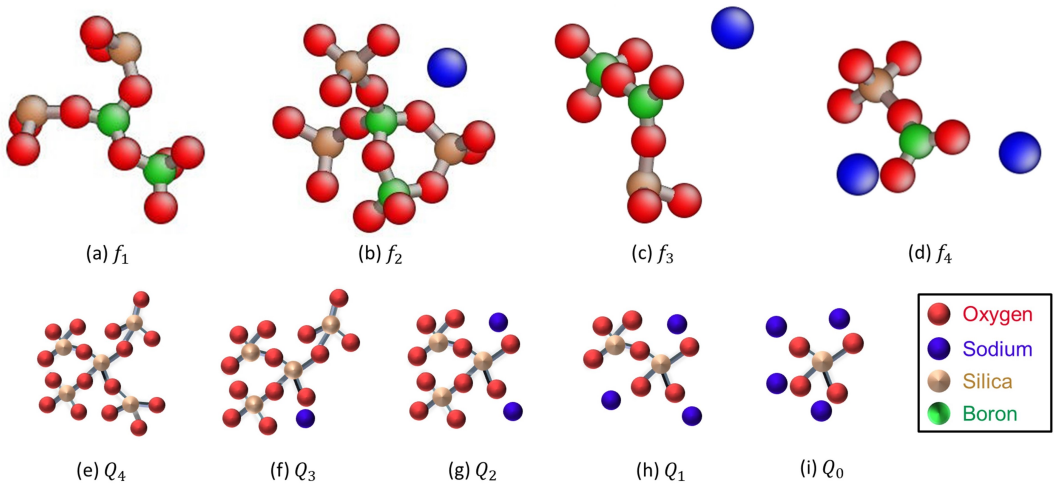

Figure A.2: Borate and silicate structural units in SBN glasses, of which the names are listed in Table A.1. B in green; Si in yellow; Na in blue; O in red. [11, 217]

This appendix presents complementary details about the structural units in Section 2.2.1. Table A.2 presents the names, chemical compositions and structure sketches of different borate units [258, 10]. Table A.1 lists the fraction names of borate and silicate units and their atomic structure sketches are displayed in Figure A.2. In the tables, NBO is the abbreviation of "Non-bridging oxygen"; and BO is the abbreviation of "Bridging oxygen".

Table A.1: Chemical composition and structure description of borate and silicate units in SBN glasses.

Fraction	**Structure units**
f_1	$BO_{3/2}$ group with 3 BO atoms
f_2	$BO_{4/2}$ group with 4 BO atoms
f_3	$BO^{-}_{4/2}$ group with 1 NBO and 2 BO atoms
f_4	$BO^{-2}_{5/2}$ group with 2 NBO and 1 BO atoms
Q_4	$SiO_{4/2}$ tetrahedrons with 4 BO atoms and no NBO atom
Q_3	$SiO^{-}_{5/2}$ tetrahedrons with 1 NBO and 3 BO atoms
Q_2	$SiO^{-2}_{6/2}$ tetrahedrons with 2 NBO and 2 BO atoms
Q_1	$SiO^{-3}_{7/2}$ tetrahedrons with 3 NBO and 1 BO atoms
Q_0	SiO^{-4}_{4} tetrahedrons with 4 NBO atoms and no BO atom

Table A.2: Chemical composition and structure description of borate units in SBN glasses of low soda content. [258, 10]

Borate units	**Chemical composition and description**	**Structure sketch**
Boroxol ring	$3/2(B_2O_3)$ (B[III] ring)	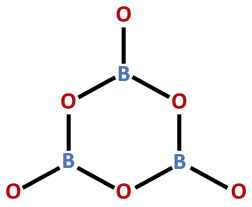
Pentaborate	$1/2(Na_2O{\cdot}5B_2O_3)$ (One B[IV] and four B[III], all BO atoms)	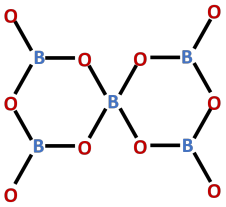
Diborate	$Na_2O{\cdot}2B_2O_3$ (Two B[IV] and two B[III], all BO atoms	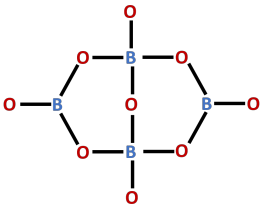
Triborate	$1/2(Na_2O{\cdot}3B_2O_3)$ (One B[IV] and two B[III], all BO atoms)	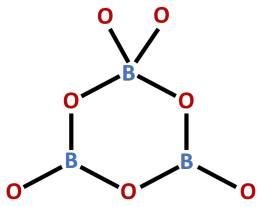
Reedmergnerite	$1/2(Na_2O{\cdot}B_2O_3{\cdot}8SiO_2)$ (One B[IV] bounded to four silica tetrahedra, noted B[IV](4Si))	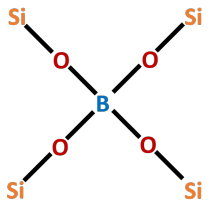
Danburite	$2B_2O_3{\cdot}3SiO_2$ (One B[IV] bounded to one B[IV] and three silica tetrahedra, noted B[IV](3Si,B))	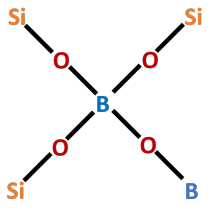

A.5 DCDC sample sizes

Table A.3: Size of SBN12, SBN42 and SBN96 DCDC samples

DCDC sample name	Length (mm)	Width (mm)	Height (mm)	Hole diameter (mm)
SBN12-prisitne	25.01 ± 0.02	5.000 ± 0.005	4.990 ± 0.005	1.0050 ± 0.0008
SBN12-600C-04h	25.118 ± 0.004	5.030 ± 0.005	5.040 ± 0.005	1.0140 ± 0.0004
SBN12-600C-18h	24.958 ± 0.007	5.008 ± 0.007	5.010 ± 0.005	1.0180 ± 0.0008
SBN42-pristine-1	25.59 ± 0.01	4.80 ± 0.01	3.99 ± 0.02	0.90 ± 0.02
SBN42-pristine-2	25.55 ± 0.01	4.74 ± 0.01	3.96 ± 0.08	0.92 ± 0.01
SBN42-pristine-3	24.82 ± 0.03	4.046 ± 0.005	4.070 ± 0.005	1.103 ± 0.008
SBN42-pristine-4	25.02 ± 0.01	4.052 ± 0.004	4.090 ± 0.006	1.061 ± 0.009
SBN42-600C-18h-1	25.26 ± 0.02	4.078 ± 0.004	4.078 ± 0.007	1.08 ± 0.01
SBN42-pristine-5	24.66 ± 0.02	4.02 ± 0.01	4.006 ± 0.005	1.05 ± 0.02
SBN42-600C-04h-1	25.170 ± 0.006	3.998 ± 0.007	4.018 ± 0.004	1.057 ± 0.02
SBN42-600C-04h-2	25.420 ± 0.004	4.058 ± 0.004	3.824 ± 0.008	1.011 ± 0.006
SBN42-600C-18h-2	26.558 ± 0.007	4.042 ± 0.004	4.026 ± 0.005	1.051 ± 0.006
SBN42-pristine-6	26.366 ± 0.005	4.032 ± 0.007	4.012 ± 0.004	1.068 ± 0.005
SBN42-pristine-7	25.306 ± 0.005	4.048 ± 0.004	4.120 ± 0.005	0.973 ± 0.006
SBN42-pristine-8	25.95 ± 0.01	4.064 ± 0.005	4.116 ± 0.005	1.10 ± 0.02
SBN42-600C-04h-3	26.218 ± 0.007	4.026 ± 0.008	4.140 ± 0.005	1.000 ± 0.005
SBN42-600C-18h-3	26.282 ± 0.004	4.058 ± 0.004	4.082 ± 0.004	1.09 ± 0.03
SBN96-pristine-1	25.498 ± 0.007	4.11 ± 0.01	4.183 ± 0.005	0.977 ± 0.004
SBN96-pristine-2	24.97 ± 0.01	3.84 ± 0.02	4.006 ± 0.005	1.01 ± 0.01
SBN96-600C-04h	25.662 ± 0.007	3.794 ± 0.005	4.03 ± 0.01	0.926 ± 0.009

A.6 Stress corrosion cracking data of SBN12 annealed samples

During the SCC experiments on SBN12 annealed samples, the behaviors of samples are out of expectation. When conducting SCC tests of SBN12-600C-04h, unexpected damage occurred and the samples partially "exploded" at the end of the test. Upon examining the samples afterwards, optical microscopy imaging revealed bubbles and/or impurities distributed inside the sample (Figure A.3), which were unseen beforehand. These bubbles and/or impurities can largely influence the stress distribution and crack motion. Annealing this sample can amplify these effects and causes unexpected damage on the sample. Blue triangles in Figure A.4 show the SCC data points of SBN12-600C-04h without averaging. There is a large fluctuation of K_I values ranging from 0.30 to 0.45 $MPa \times m^{0.5}$ and no linear relationship can be observed between $log(v)$ and K_I. The determination of SCC slopes in Region I and of K_E values

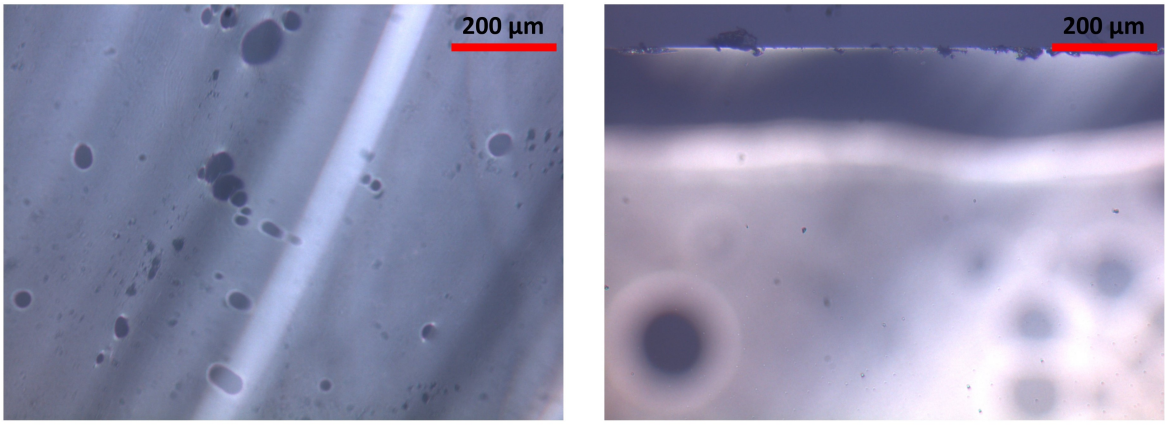

Figure A.3: Optical microscopes images on the fracture surfaces of SBN12-600C-04h with large amount of bubbles or impurities insides the sample.

becomes impossible.

Considering SBN12-600C-18h, an unexpected horizontal crack appeared while the crack length was about 3 mm, causing an explosion of sample, breaking into top and bottom. Figure A.4 also presents the SCC results of this sample without averaging (red diamonds). The data points of SBN12-600C-18h display a potential linear relationship between $log(v)$ and K_I before the explosion of the sample. However, unseen damage might exist before the explosion, which disturbs the K_I calculation. This set of data is still rejected from the main text due to the unexpected explosion happened in the sample.

Despite the unavailable SCC curves, both samples had an accessible SCC post-mortem fracture surfaces. It is hypothesized that these surfaces should not be significantly different from the pristine counterpart. Section I-2.2 presents the fracture surface properties and shows this hypothesis is valid.

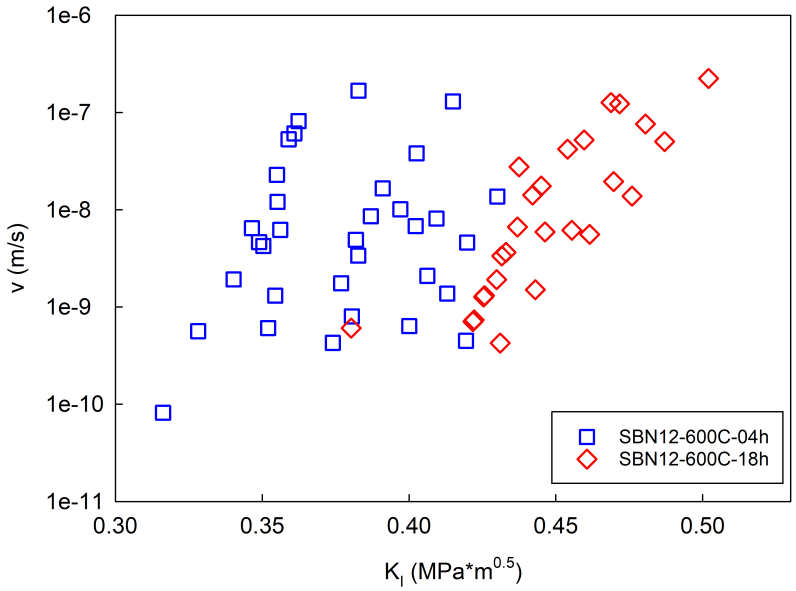

Figure A.4: SCC data points without averaging of SBN12-600C-04h (blue triangles) and SBN12-600C-18h (red diamonds).

Bibliography

[1] Case studies in the X-ray diffraction of ceramics. In M. Pomeroy, editor, *Encyclopedia of Materials: Technical Ceramics and Glasses*, pages 560–577. Elsevier, Oxford, 2021. ISBN 978-0-12-822233-1. doi: https://doi.org/10.1016/B978-0-12-818542-1.00005-9. (Cited on page 44.)

[2] D. H. Agarwal, P. M. Bhatt, and A. M. Pathan. Development of portable experimental set-up for AFM to work at cryogenic temperature. *AIP Conf. Proc.*, 1447:531–532, 2012. doi: 10.1063/1.4710113. (Cited on page 54.)

[3] C. N. Ahlquist. On the interaction of cleavage cracks with second phase particles. *Acta Metall.*, 23(2):239–243, 1975. doi: 10.1016/0001-6160(75)90189-3. (Cited on pages 30 and 35.)

[4] T. L. Anderson. *Fracture mechanics: fundamentals and applications*. CRC press, 2017. ISBN 9781498728140. (Cited on page 26.)

[5] H. Arribart and D. Abriou. Ten years of atomic force microscopy in glass research. *Ceram. - Silik.*, 44(4):121–128, 2000. URL `https://www.ceramics-silikaty.cz/2000/pdf/2000_04_121.pdf`. (Cited on page 54.)

[6] B. K. Atkinson and P. G. Meredith. The theory of subcritical crack growth with applications to minerals and rocks. *Fracture mechanics of rock*, 2:111–166, 1987. (Cited on pages 133 and 140.)

[7] R. Baniel. Synthèses et caractérisations de verres a séparation de phases dans le système ternaire $sio_2 - b_2o_3 - na_2o$, 2018. (Cited on pages 75, 79, 82 and 138.)

[8] G. Bao and Z. Suo. Remarks on crack-bridging concepts. *Appl. Mech. Rev.*, 45(8): 355–366, 1992. doi: 10.1115/1.3119764. (Cited on page 29.)

[9] J. Barés, M. Barlet, C. L. Rountree, L. Barbier, and D. Bonamy. Nominally brittle cracks in inhomogeneous solids: From microstructural disorder to continuum-level scale. *Front. Phys.*, 2:70, 2014. ISSN 2296-424X. doi: 10.3389/fphy.2014.00070. (Cited on pages 37, 56, 67, 69, 70, 115, 116, 135, 144 and 145.)

[10] M. Barlet. *Evolution of mechanical properties of silicate glasses: Impact of the chemical composition and Effects of irradiation*. PhD thesis, École Polytechnique, 2014. (Cited on pages 4, 5, 14, 16, 41, 47, 59, 60, 61, 62, 63, 65, 66, 67, 105, 114, 132, 140, 142, 155 and 156.)

[11] M. Barlet, A. Kerrache, J.-M. Delaye, and C. L. Rountree. SiO_2-Na_2O-B_2O_3 density: A comparison of experiments, simulations, and theory. *J. Non-Cryst. Solids*, 382:32 – 44, 2013. ISSN 0022-3093. doi: 10.1016/j.jnoncrysol.2013.09.022. (Cited on pages 4, 12, 14, 16, 21, 22 and 155.)

[12] M. Barlet, J.-M. Delaye, M. Gennisson, R. Caraballo, B. Boizot, B. Bonamy, and C. L. Rountree. Influence of electronic irradiation on failure and hardness properties of pure silica glasses. *Procedia Mater. Sci.*, 7:286–293, 2014. doi: 10.1016/j.mspro.2014.10.037. (Cited on pages 4 and 14.)

[13] M. Barlet, J.-M. Delaye, T. Charpentier, M. Gennisson, D. Bonamy, T. Rouxel, and C. L. Rountree. Hardness and toughness of sodium borosilicate glasses via Vicker's indentations. *J. Non-Cryst. Solids*, 417-418:66–79, 2015. doi: 10.1016/j.jnoncrysol.2015.02.005. (Cited on pages 4, 14, 32 and 105.)

[14] M. Barlet, J.-M. Delaye, B. Boizot, R. Caraballo, S. Peuget, and C. L. Rountree. From network polymerization to stress corrosion cracking in sodium-borosilicate glasses: Effect of the chemical composition. *J. Non-Cryst. Solids*, 450:174 – 184, 2016. ISSN 174184. doi: 10.1016/j.jnoncrysol.2016.07.017. (Cited on pages 4, 14, 15, 16, 60, 61, 62, 67, 105, 114 and 154.)

[15] R. A. Barrio, R. Kerner, M. Micoulaut, and G. G. Naumis. Evaluation of the concentration of boroxol rings in vitreous by the stochastic matrix method. *J. Phys. Condens. Matter*, 9(43):9219, 1997. doi: 10.1088/0953-8984/9/43/008. (Cited on page 14.)

[16] P. Benigni. CALPHAD modeling of the glass transition for a pure substance, coupling thermodynamics and relaxation kinetics. *Calphad*, 72:102238, 2021. doi: 10.1016/j.calphad.2020.102238. (Cited on page 13.)

[17] J. Bernstein. *Polymorphism in Molecular Crystals 2e*, volume 30. International Union of Crystal, 2020. ISBN 9780199655441. (Cited on page 2.)

[18] N. Bisbrouck, M. Bertani, F. Angeli, T. Charpentier, D. de Ligny, J.-M. Delaye, S. Gin, and M. Micoulaut. Impact of magnesium on the structure of aluminoborosilicate glasses: A solid-state NMR and Raman spectroscopy study. *J. Am. Chem. Soc.*, 2021. doi: 10.1111/jace.17876. (Cited on pages 43, 93 and 98.)

[19] G. G. Boiko, N. A. Bokov, et al. Small-angle scattering and scattering of visible light by sodium-silicate glasses at phase separation. *J. Non-Cryst. Solids*, 5(1):41–54, 1970. doi: 0.1016/0022-3093(70)90195-X. (Cited on page 16.)

[20] B. Boizot, G. Petite, D. Ghaleb, B. Reynard, and G. Calas. Raman study of β-irradiated glasses. *J. Non-Cryst. Solids*, 243(2):268–272, 1999. ISSN 0022-3093. doi: 10.1016/S0022-3093(98)00822-9. (Cited on page 44.)

[21] D. Bonamy, S. Prades, L. Ponson, D. Dalmas, C. Rountree, E. Bouchaud, and C. Guillot. Experimental investigation of damage and fracture in glassy materials at the nanometre scale. *Int. J. Mater. Prod. Technol.*, 26(3-4):339–353, 2006. ISSN 0268-1900. doi: 10.1504/IJMPT.2006.009474. (Cited on page 27.)

[22] D. Bonamy, S. Prades, C. L. Rountree, L. Ponson, D. Dalmas, E. Bouchaud, K. Ravi-Chandar, and C. Guillot. Nanoscale damage during fracture in silica glass. *Int. J.*

Fract., 140(1-4):3–14, 2006. ISSN 0376-9429. doi: 10.1007/s10704-006-6579-2. (Cited on pages 27 and 29.)

[23] R. Bormann, F. Gärtner, and K. Zöltzer. Application of the CALPHAD method for the prediction of amorphous phase formation. *Journal of the Less Common Metals*, 145:19–29, 1988. doi: 10.1016/0022-5088(88)90258-5. (Cited on page 13.)

[24] E. Bouchaud, G. Lapasset, J. Planes, and S. Naveos. Statistics of branched fracture surfaces. *Phys. Rev. B*, 48(5):2917–2928, 1993. ISSN 0163-1829. doi: 10.1103/PhysRevB.48.2917. (Cited on page 36.)

[25] D. Bouttes. *Micro-tomographie d'un borosilicate de baryum démixé: du mûrissement à la fragmentation*. PhD thesis, ParisTech, 2014. (Cited on pages 2 and 20.)

[26] D. Bouttes, E. Gouillart, E. Boller, D. Dalmas, and D. Vandembroucq. Fragmentation and limits to dynamical scaling in viscous coarsening: An interrupted in situ X-ray tomographic study. *Phys. Rev. Lett.*, 112(24):245701, 2014. doi: 10.1103/PhysRevLett.112.245701. (Cited on pages 2 and 20.)

[27] D. Bouttes, O. Lambert, C. Claireaux, W. Woelffel, D. Dalmas, E. Gouillart, P. Lhuissier, L. Salvo, E. Boller, and D. Vandembroucq. Hydrodynamic coarsening in phase-separated silicate melts. *Acta Mater.*, 92:233–242, 2015. doi: 10.1016/j.actamat.2015.03.045. (Cited on pages 2 and 20.)

[28] D. Bouttes, E. Gouillart, and D. Vandembroucq. Topological symmetry breaking in viscous coarsening. *Phys. Rev. Lett.*, 117(14):145702, 2016. doi: 10.1103/PhysRevLett.117.145702. (Cited on page 2.)

[29] A. F. Bower and M. Ortiz. A three-dimensional analysis of crack trapping and bridging by tough particles. *J. Mech. Phys. Solids*, 39(6):815–858, 1991. doi: 10.1016/0022-5096(91)90026-K. (Cited on page 29.)

[30] P. J. Bray, S. A. Feller, G. E. Jellison Jr, and Y. H. Yun. B^{10} NMR studies of the structure of borate glasses. *J. Non-Cryst. Solids*, 38:93–98, 1980. doi: 10.1016/0022-3093(80)90400-7. (Cited on pages 16 and 96.)

[31] P. J. Bray, A. E. Geissberger, F. Bucholtz, and I. A. Harris. Glass structure. *J. Non-Cryst. Solids*, 52(1-3):45–66, 1982. doi: 10.1016/0022-3093(82)90280-0. (Cited on pages 4 and 16.)

[32] H. Brequel, J. Parmentier, G. D. Sorar, L. Schiffini, and S. Enzo. Study of the phase separation in amorphous silicon oxycarbide glasses under heat treatment. *Nanostruct. Mater.*, 11(6):721–731, 1999. doi: 10.1016/S0965-9773(99)00360-8. (Cited on page 13.)

[33] K. Budhwani and S. Feller. A density model for the lithium, sodium and potassium borosilicate glass systems. *Phys. Chem. Glasses*, 36(4):183–190, 1995. (Cited on pages 12, 14, 21, 96 and 127.)

[34] B. Budiansky, J. C. Amazigo, and A. G. Evans. Small-scale crack bridging and the fracture toughness of particulate-reinforced ceramics. *J. Mech. Phys. Solids*, 36(2): 167–187, 1988. doi: 10.1016/S0022-5096(98)90003-5. (Cited on page 29.)

[35] J.-Y. Buffiere, E. Maire, J. Adrien, J.-P. Masse, and E. Boller. In situ experiments with X-ray tomography: an attractive tool for experimental mechanics. *Exp. Mech.*, 50(3):289–305, 2010. doi: 10.1007/s11340-010-9333-7. (Cited on page 20.)

[36] D. G. Burnett and R. W. Douglas. Liquid-liquid phase separation in soda-lime-silica system. *Phys. Chem. Glasses*, 11(5):125, 1970. (Cited on pages 13 and 22.)

[37] J. W. Cahn. Phase separation by spinodal decomposition in isotropic systems. *J. Chem. Phys.*, 42(1):93–99, 1965. doi: 10.1063/1.1695731. (Cited on pages 2 and 10.)

[38] J. W. Cahn and R. J. Charles. Initial stages of phase separation in glasses. *Phys. Chem. Glasses*, 6(5):181, 1965. (Cited on page 17.)

[39] F. C. Campbell. *Phase diagrams: Understanding the basics*. ASM International, 2012. ISBN 9781615039869. (Cited on pages 8 and 9.)

[40] F. Célarié. *Dynamique de fissuration a basse vitesse des matériaux vitreux*. PhD thesis, Université Montpellier II-Sciences et Techniques du Languedoc, 2004. (Cited on page 47.)

[41] F. Celarie, S. Prades, D. Bonamy, L. Ferrero, E. Bouchaud, C. Guillot, and C. Marliere. Glass breaks like metal, but at the nanometer scale. *Phys. Rev. Lett*, 90(7), 2003. doi: 10.1103/PhysRevLett.90.075504. (Cited on page 27.)

[42] R. J. Charles. Metastable immiscibility in BaO-Li_2O-SiO_2 system. *Phys. Chem. Glasses*, 8(5):185, 1967. (Cited on pages 2 and 13.)

[43] R. J. Charles. Origin of immiscibility in silicate solutions. *Phys. Chem. Glasses*, 10 (5):169, 1969. (Cited on page 11.)

[44] R. J. Charleston et al. *Masterpieces of Glass: a world history from the Corning Museum of Glass*. HN Abrams, 1990. ISBN 0810924641. (Cited on page 1.)

[45] T. Charpentier. Mixed network formers and modifiers, borosilicate and boroaluminosilicate glasses : a NMR point of view. USTVerre, 2017. URL `https://www.ustverre.fr/site/images/Site/Cargese_2017/Charpentier.pdf`. (Cited on page 96.)

[46] T. Charpentier and D. Massiot. Nuclear Magnetic Resonance: deciphering disorder and crystallisation phenomena in glassy materials. In *From glass to crystal*, pages 291–318. EDP Sciences, 2021. (Cited on page 42.)

[47] K. Chen. A practical review of NMR lineshapes for spin-1/2 and quadrupolar nuclei in disordered materials. *Int. J. Mol. Sci.*, 21(16):5666, 2020. doi: doi.org/10.3390/ijms21165666. (Cited on page 94.)

[48] S. Cheng, C. Song, and P. Ercius. Indentation cracking behaviour and structures of nanophase separation of glasses. *Physics and Chemistry of Glasses-European Journal of Glass Science and Technology Part B*, 58(6):237–242, 2017. doi: 10.13036/17533562.58.6.040. (Cited on page 32.)

[49] M. Ciccotti. Stress-corrosion mechanisms in silicate glasses. *Journal of Physics D - Applied Physics*, 42(21):214006, 2009. doi: 10.1088/0022-3727/42/21/214006. (Cited on pages 28 and 67.)

[50] M. Ciccotti and M. George. In Situ AFM investigations and fracture mechanics modeling of slow fracture propagation in oxide and polymer glasses. *Handbook of Materials Modeling: Applications: Current and Emerging Materials*, pages 1–37, 2018. doi: 10.1007/978-3-319-50257-1_125-1. (Cited on page 36.)

[51] W. contributors. Cristobalite — Wikipedia, the free encyclopedia, 2021. URL `https://en.wikipedia.org/w/index.php?title=Cristobalite&oldid=1044663316`. Online; accessed 21-November-2021. (Cited on page 86.)

[52] A. H. Cottrell. *Theoretical structural metallurgy*. Arnold, 1960. (Cited on page 8.)

[53] Z. Cui, Y. Huang, and H. Liu. Predicting the mechanical properties of brittle porous materials with various porosity and pore sizes. *J. Mech. Behav. Biomed. Mater.*, 71:10–22, 2017. doi: 10.1016/j.jmbbm.2017.02.014. (Cited on page 3.)

[54] P. Daguier, B. Nghiem, E. Bouchaud, and F. Creuzet. Pinning and depinning of crack fronts in heterogeneous materials. *Phys. Rev. Lett.*, 78(6):1062, 1997. doi: 10.1103/PhysRevLett.78.1062. (Cited on page 36.)

[55] D. Dalmas, A. Lelarge, and D. Vandembroucq. Quantitative AFM analysis of phase separated borosilicate glass surfaces. *J. Non-Cryst. Solids*, 353(52-54):4672–4680, 2007. doi: 10.1016/j.jnoncrysol.2007.07.005. (Cited on pages 19, 20, 37, 81 and 83.)

[56] D. Dalmas, A. Lelarge, and D. Vandembroucq. Crack propagation through phase-separated glasses: Effect of the characteristic size of disorder. *Phys. Rev. Lett.*, 101(25):255501, 2008. doi: 10.1103/PhysRevLett.101.255501. (Cited on pages 36 and 37.)

[57] J. De Bonfils, S. Peuget, G. Panczer, D. De Ligny, S. Henry, P.-Y. Noël, A. Chenet, and B. Champagnon. Effect of chemical composition on borosilicate glass behavior under irradiation. *J. Non-Cryst. Solids*, 356(6-8):388–393, 2010. doi: 10.1016/j.jnoncrysol.2009.11.030. (Cited on pages 44 and 127.)

[58] W. J. Dell, P. J. Bray, and S. Z. Xiao. ^{11}B NMR-studies and structural modeling of Na_2O-B_2O_3-SiO_2 glasses of high soda content. *J. Non-Cryst. Solids*, 58(1):1–16, 1983. doi: 10.1016/0022-3093(83)90097-2. (Cited on pages 12, 14, 16, 61 and 96.)

[59] J. Deubener, M. Allix, M. J. Davis, A. Duran, T. Höche, T. Honma, T. Komatsu, S. Krüger, I. Mitra, R. Müller, et al. Updated definition of glass-ceramics. *J. Non-Cryst. Solids*, 501:3–10, 2018. doi: 10.1016/j.jnoncrysol.2018.01.033. (Cited on page 2.)

[60] W.-Y. Dong and Y.-C. Long. Preparation and characterization of preferentially oriented continuous MFI-type zeolite membranes from porous glass. *Microporous Mesoporous Mater.*, 76(1-3):9–15, 2004. doi: 10.1016/j.micromeso.2004.07.013. (Cited on page 3.)

[61] L. S. Du and J. F. Stebbins. Nature of silicon-boron mixing in sodium borosilicate glasses: A high-resolution ^{11}B and ^{17}O NMR study. *J. Phys. Chem. B*, 107(37):10063–10076, 2003. doi: 10.1021/jp0340481. (Cited on pages 15, 16 and 41.)

[62] L.-S. Du and J. F. Stebbins. Solid-state NMR study of metastable immiscibility in alkali borosilicate glasses. *J. Non-Cryst. Solids*, 315(3):239–255, 2003. doi: 10.1016/S0022-3093(02)01604-6. (Cited on pages 16 and 93.)

[63] W.-F. Du, K. Kuraoka, T. Akai, and T. Yazawa. Investigation on phase separation and crystallization in Na_2O-B_2O_3 glass system by nuclear-magnetic-resonance. *J. Ceram. Soc. Jpn*, 107(1252):1151–1155, 1999. doi: 10.2109/jcersj.107.1151. (Cited on page 16.)

[64] M. J. Duer. *Solid state NMR spectroscopy: principles and applications*. John Wiley & Sons, 2008. ISBN 9789811369650. (Cited on page 42.)

[65] H. Eckert. Spying with spins on messy materials: 60 years of glass structure elucidation by NMR spectroscopy. *Int. J. Appl. Glass Sci.*, 9(2):167–187, 2018. doi: 10.1111/ijag.12333. (Cited on page 42.)

[66] M. Edén. NMR studies of oxide-based glasses. *Annual Reports Section" C"(Physical Chemistry)*, 108(1):177–221, 2012. doi: 10.1039/C2PC90006H. (Cited on page 42.)

[67] T. H. Elmer, M. E. Nordberg, G. B. Carrier, and E. J. Korda. Phase separation in borosilicate glasses as seen by electron microscopy and scanning electron microscopy. *J. Am. Ceram. Soc.*, 53(4):171–175, 1970. doi: 10.1111/j.1151-2916.1970.tb12064.x. (Cited on pages 19 and 83.)

[68] D. Enke, F. Janowski, and W. Schwieger. Porous glasses in the 21st century—a short review. *Microporous Mesoporous Mater.*, 60(1-3):19–30, 2003. doi: 10.1016/S1387-1811(03)00329-9. (Cited on pages 2, 3 and 82.)

[69] A. G. Evans. A method for evaluating the time-dependent failure characteristics of brittle materials — and its application to polycrystalline alumina. *J. Mater. Sci.*, 7 (10):1137–1146, 1972. ISSN 1573-4803. doi: 10.1007/BF00550196. (Cited on page 30.)

[70] A. G. Evans. Perspective on the development of high-toughness ceramics. *J. Am. Ceram. Soc.*, 73(2):187–206, 1990. doi: 10.1111/j.1151-2916.1990.tb06493.x. (Cited on page 29.)

[71] A. G. Evans and T. R. Wilshaw. Quasi-static solid particle damage in brittle solids—I. Observations, analysis and implications. *Acta Metall.*, 24(10):939–956, 1976. ISSN 0001-6160. doi: 10.1016/0001-6160(76)90042-0. (Cited on page 33.)

[72] K. T. Faber and A. G. Evans. Crack deflection processes–I. Theory. *Acta Metall.*, 31 (4):565–576, 1983. doi: 10.1016/0001-6160(83)90046-9. (Cited on page 29.)

[73] K. T. Faber and A. G. Evans. Crack deflection processes–II. Experiment. *Acta Metall.*, 31(4):577–584, 1983. ISSN 0001-6160. doi: 10.1016/0001-6160(83)90047-0. (Cited on page 29.)

[74] G. P. Fafet and A. M. Fredholm. Glass-ceramic cooking plate for gas cookers, and method for making same, 1999. US Patent 5,931,152. (Cited on page 2.)

[75] X. Fan and Q. Chen. Study of phase separation in na2o-b2o3-sio2 glasses by TEM and optical diffraction. *J. Non-Cryst. Solids*, 112(1-3):232–237, 1989. (Cited on pages 19, 20 and 83.)

[76] D. Feil and S. Feller. The density of sodium borosilicate glasses related to atomic arrangements. *J. Non-Cryst. Solids*, 119(1):103–111, 1990. doi: 10.1016/0022-3093(90) 90246-I. (Cited on pages 12, 14, 21 and 96.)

[77] G. Ferlat, T. Charpentier, A. P. Seitsonen, A. Takada, M. Lazzeri, L. Cormier, G. Calas, and F. Mauri. Boroxol rings in liquid and vitreous B_2O_3 from first principles. *Phys. Rev. Lett.*, 101(6):065504, 2008. doi: 10.1103/PhysRevLett.101.065504. (Cited on page 14.)

[78] H. R. Fernandes, D. U. Tulyaganov, I. K. Goel, and J. M. F. Ferreira. Crystallization process and some properties of Li_2O-SiO_2 glass–ceramics doped with Al_2O_3 and K_2O. *J. Am. Chem. Soc.*, 91(11):3698–3703, 2008. doi: 10.1111/j.1551-2916.2008.02724.x. (Cited on page 80.)

[79] V. N. Filipovich. Some aspects of the formation of new phases in melt and glasses. *The Structure of Glass*, 5:39, 1965. (Cited on page 20.)

[80] A. Findlay. *The Phase Rule and its Applications*. Longmans, Green, 1904. (Cited on page 2.)

[81] S.-Y. Fu, X.-Q. Feng, B. Lauke, and Y.-W. Mai. Effects of particle size, particle/matrix interface adhesion and particle loading on mechanical properties of particulate–Polymer composites. *Composites Part B: Engineering*, 39(6):933–961, 2008. doi: 10.1016/j.compositesb.2008.01.002. (Cited on page 35.)

[82] T. Furukawa and W. B. White. Raman spectroscopic investigation of sodium borosilicate glass structure. *Journal of materials science*, 16(10):2689–2700, 1981. doi: 10.1007/BF02402831. (Cited on pages 16, 41, 43, 44, 61 and 88.)

[83] T. Furukawa, K. E. Fox, and W. B. White. Raman spectroscopic investigation of the structure of silicate glasses. III. Raman intensities and structural units in sodium silicate glasses. *J. Chem. Phys.*, 75:3226–3237, 1981. doi: 10.1063/1.442472. (Cited on pages 16 and 43.)

[84] F. Y. Galakhov and S. F. Konovalova. Liquation phenomena in the system alumina-silica. Communication 1. Experimental data and their discussion. *Izvestiya Akademii Nauk SSSR, Seriya Khimicheskaya*, 8:1373, 1964. (Cited on page 20.)

[85] A. K. Gangopadhyay, T. K. Croat, and K. F. Kelton. The effect of phase separation on subsequent crystallization in $Al_88Gd_6La_2Ni_4$. *Acta Mater.*, 48(16):4035–4043, 2000. doi: 10.1016/S1359-6454(00)00196-8. (Cited on page 2.)

[86] H. Gao and J. R. Rice. A first-order perturbation analysis of crack trapping by arrays of obstacles. *J. Appl. Mech.*, 56(4):828–836, 1989. doi: 10.1115/1.3176178. (Cited on page 29.)

[87] K. Ghanbari-Ahari and A. M. Cameron. Phase diagram of Na_2O-B_2O_3-SiO_2 system. *J. Am. Ceram. Soc.*, 76(8):2017–2022, 1993. doi: 10.1111/j.1151-2916.1993.tb08326.x. (Cited on page 2.)

[88] S. Gin, X. Beaudoux, F. Angéli, C. Jégou, and N. Godon. Effect of composition on the short-term and long-term dissolution rates of ten borosilicate glasses of increasing complexity from 3 to 30 oxides. *J. Non-Cryst. Solids*, 358(18-19):2559–2570, 2012. doi: 10.1016/j.jnoncrysol.2012.05.024. (Cited on page 14.)

[89] K. S. Gjerden, A. Stormo, and A. Hansen. Local dynamics of a randomly pinned crack front: A numerical study. *Front. Phys.*, 2:66, 2014. doi: 10.3389/fphy.2014.00066. (Cited on page 29.)

[90] S. Glasstone. Text-book of physical chemistry. *Van NostrandCo*, 1940. (Cited on page 2.)

[91] R. V. Gol'dstein and R. L. Salganik. Brittle fracture of solids with arbitrary cracks. *International journal of Fracture*, 10(4):507–523, 1974. doi: 0.1007/BF00155254. (Cited on page 37.)

[92] S. Gossé, C. Guéneau, S. Bordier, S. Schuller, A. Laplace, and J. Rogez. A thermodynamic approach to predict the metallic and oxide phases precipitations in nuclear waste glass melts. *Procedia Mater. Sci.*, 7:79 – 86, 2014. ISSN 2211-8128. doi: 10.1016/j.mspro.2014.10.011. (Cited on page 13.)

[93] A. Grandjean, M. Malki, C. Simonnet, D. Manara, and B. Penelon. Correlation between electrical conductivity, viscosity, and structure in borosilicate glass-forming melts. *Phys. Rev. B*, 75(5):054112, 2007. doi: 10.1103/PhysRevB.75.054112. (Cited on page 4.)

[94] G. N. Greaves and S. Sen. Inorganic glasses, glass-forming liquids and amorphizing solids. *Adv. Phys.*, 56(1):1–166, 2007. doi: 10.1080/00018730601147426. (Cited on page 14.)

[95] D. J. Green, P. S. Nicholson, and J. D. Embury. Crack shape studies in brittle porous materials. *J. Mater. Sci.*, 12(5):987–989, 1977. doi: 10.1007/BF00540982. (Cited on page 30.)

[96] D. J. Green, P. S. Nicholson, and J. D. Embury. Fracture of a brittle particulate composite. *J. Mater. Sci.*, 14(6):1413–1420, 1979. doi: 10.1007/BF00549316. (Cited on page 30.)

[97] Y. Gueguen, P. Houizot, F. Célarié, M. Chen, A. Hirata, Y. Tan, M. Allix, S. Chenu, C. Roux-Langlois, and T. Rouxel. Structure and viscosity of phase-separated BaO-SiO_2 glasses. *J. Am. Ceram. Soc.*, 100(5):1982–1993, 2017. doi: 10.1111/jace.14642. (Cited on page 2.)

[98] C. Guerra, J. Scheibert, D. Bonamy, and D. Dalmas. Understanding fast macroscale fracture from microcrack post mortem patterns. *Proceedings of the National Academy of Sciences*, 109(2):390–394, 2012. doi: 10.1073/pnas.1113205109. (Cited on page 36.)

[99] E. Guilloteau, H. Charrue, and F. Creuzet. The direct observation of the core region of a propagating fracture crack in glass. *EPL.*, 34(7):549, 1996. doi: 10.1209/epl/i1996-00493-3. (Cited on page 27.)

[100] J. P. Guin and S. M. Wiederhorn. Crack growth threshold in soda lime silicate glass: role of hold-time. *J. Non-Cryst. Solids*, 316:12–20, 2003. doi: 10.1016/S0022-3093(02)01932-4. (Cited on page 27.)

[101] J. P. Guin and S. M. Wiederhorn. Fracture of silicate glasses: Ductile or brittle? *Phys. Rev. Lett*, 92(21), 2004. doi: 10.1103/PhysRevLett.92.215502. (Cited on page 27.)

[102] J. P. Guin and S. M. Wiederhorn. Surfaces formed by subcritical crack growth in silicate glasses. *Int. J. Fract.*, 140(1-4):15–26, 2006. doi: 10.1007/s10704-006-6729-6. (Cited on page 27.)

[103] J. P. Guin, S. M. Wiederhorn, and T. Fett. Crack-tip structure in soda-lime-silicate glass. *J. Am. Ceram. Soc.*, 88(3):652–659, 2005. ISSN 0002-7820. doi: 10.1111/j.1551-2916.2005.00108.x. (Cited on pages 27 and 37.)

[104] P. K. Gupta, D. Inniss, C. R. Kurkjian, and Q. Zhong. Nanoscale roughness of oxide glass surfaces. *J. Non-Cryst. Solids*, 262(1-3):200–206, 2000. (Cited on page 114.)

[105] R. Gy. Stress corrosion of silicate glass: a review. *J. Non-Cryst. Solids*, 316(1):1–11, 2003. doi: 10.1016/S0022-3093(02)01931-2. (Cited on pages 28 and 67.)

[106] W. Haller, D. H. BlackBurn, F. E. Wagstaff, and R. J. Charles. Metastable immiscibility surface in the system Na_2O-B_2O_3-SiO_2. *J. Am. Ceram. Soc.*, 53(1):34–39, 1970. ISSN 1551-2916. doi: 10.1111/j.1151-2916.1970.tb11995.x. (Cited on pages 4, 5, 11, 12, 13, 19, 32, 59, 75, 121 and 147.)

[107] W. Haller, D. H. Blackburn, and J. H. Simmons. Miscibility gaps in alkali-silicate binaries - data and thermodynamic interpretation. *J. Am. Ceram. Soc.*, 57(3):120–126, 1974. doi: 10.1111/j.1151-2916.1974.tb10832.x. (Cited on pages 9, 11, 12 and 13.)

[108] J. Hammel and T. Allersma. Method of making thermally stable and crush resistant microporous glass catalyst supports, 1974. US Patent 3,843,341. (Cited on page 2.)

[109] J. J. Hammel. Direct measurements of homogeneous nucleation rates in a glass-forming system. *J. Chem. Phys.*, 46(6):2234–2244, 1967. doi: 10.1063/1.1841027. (Cited on page 13.)

[110] J. H. Han, N. Mattern, D. H. Kim, and J. Eckert. Phase separation and microstructure evolution of rapidly quenched Gd-Hf-Co-Al alloys. *J. Alloys Compd.*, 509:S42–S45, 2011. doi: 10.1016/j.jallcom.2010.12.210. (Cited on page 20.)

[111] K. Han, M. Ciccotti, and S. Roux. Measuring nanoscale stress intensity factors with an atomic force microscope. *Europhysics Letters*, 89(6):66003, 2010. doi: 10.1209/0295-5075/89/66003. (Cited on page 27.)

[112] Z. Hashin and S. Shtrikman. A variational approach to the theory of the elastic behaviour of multiphase materials. *J. Mech. Phys. Solids*, 11(2):127–140, 1963. doi: 10.1016/0022-5096(63)90060-7. (Cited on page 25.)

[113] J. Häßler and C. Rüssel. Self-organized growth of sodium borate-rich droplets in a phase-separated sodium borosilicate glass. *Int. J. Appl. Glass Sci.*, 8(1):124–131, 2017. doi: 10.1111/ijag.12197. (Cited on pages 13, 17 and 33.)

[114] M. Y. He, M. R. Turner, and A. G. Evans. Analysis of the double cleavage drilled compression specimen for interface fracture energy measurements over a range of mode mixities. *Acta Metall. Mater.*, 43(9):3453–3458, 1995. doi: 10.1016/0956-7151(95)00036-U. (Cited on page 47.)

[115] S. Hendy. Light scattering in transparent glass ceramics. *Appl. Phys.*, 81(7):1171–1173, 2002. doi: 10.1063/1.1499989. (Cited on page 80.)

[116] M. Hermann and U. Gottschalk. Large-scale immobilization of antibodies on porous glass carriers. *Bioforum*, 3:172, 2000. (Cited on page 3.)

[117] R. Hiesgen and J. Haiber. MEASUREMENT METHODS | Structural Properties: Atomic Force Microscopy. In J. G., editor, *Encyclopedia of Electrochemical Power Sources*, pages 696–717. Elsevier, Amsterdam, 2009. ISBN 9780444527455. doi: 10.1016/B978-044452745-5.00073-3. (Cited on page 54.)

[118] T. Höche, M. Mäder, S. Bhattacharyya, G. S. Henderson, T. Gemming, R. Wurth, C. Rüssel, and I. Avramov. $ZrTiO_4$ crystallisation in nanosized liquid–liquid phase-separation droplets in glass–a quantitative XANES study. *CrystEngComm*, 13(7):2550–2556, 2011. doi: 10.1039/C0CE00716A. (Cited on page 2.)

[119] A. Hodroj, P. Simon, P. Florian, M.-H. Chopinet, and Y. Vaills. Phase separation and spatial morphology in sodium silicate glasses by AFM, light scattering and NMR. *J. Am. Ceram. Soc.*, 96(8):2454–2460, 2013. doi: 10.1111/jace.12459. (Cited on pages 19 and 81.)

[120] M. Hoffmann, S. Kreft, G. Georgi, G. Fulda, M.-M. Pohl, D. Seeburg, C. Berger-Karin, E. V. Kondratenko, and S. Wohlrab. Improved catalytic methane combustion

of Pd/CeO_2 catalysts via porous glass integration. *Appl. Catal., B*, 179:313–320, 2015. doi: 10.1016/j.apcatb.2015.05.028. (Cited on page 3.)

[121] W. Höland, V. Rheinberger, and M. Schweiger. Control of nucleation in glass ceramics. *Philosophical Transactions of the Royal Society of London. Series A: Mathematical, Physical and Engineering Sciences*, 361(1804):575–589, 2003. doi: 10.1098/rsta.2002.1152. (Cited on page 2.)

[122] W. Höland, C. Ritzberger, V. Rheinberger, and E. Apel. Dental glass ceramics, 2010. US Patent 7,846,857. (Cited on page 2.)

[123] H. Hosono and Y. Abe. Silver ion selective porous lithium titanium phosphate glass-ceramics cation exchanger and its application to bacteriostatic materials. *Mater. Res. Bull.*, 29(11):1157–1162, 1994. doi: 10.1016/0025-5408(94)90185-6. (Cited on page 3.)

[124] P. Howell, G. Kozyreff, and J. Ockendon. *Applied solid mechanics*. Number 43. Cambridge University Press, 2009. ISBN 9780511611605. doi: 10.1017/CBO9780511611605. (Cited on page 45.)

[125] C. Huang and A. N. Cormack. Structural differences and phase separation in alkali silicate glasses. *J. Chem. Phys.*, 95(5):3634–3642, 1991. doi: 10.1063/1.460814. (Cited on page 41.)

[126] P. Hudon and D. R. Baker. The nature of phase separation in binary oxide melts and glasses. I. Silicate systems. *J. Non-Cryst. Solids*, 303(3):299–345, 2002. doi: 10.1016/S0022-3093(02)01043-8. (Cited on page 12.)

[127] I. Hung, A. P. Howes, B. G. Parkinson, T. Anupold, A. Samoson, S. P. Brown, P. F. Harrison, D. Holland, and R. Dupree. Determination of the bond-angle distribution in vitreous B_2O_3 by ^{11}B double rotation (DOR) NMR spectroscopy. *J. Solid State Chem.*, 182(9):2402–2408, 2009. doi: 10.1016/j.jssc.2009.06.025. (Cited on pages 14 and 92.)

[128] H. Inoue, A. Masuno, Y. Watanabe, K. Suzuki, and T. Iseda. Direct calculation of the physical properties of sodium borosilicate glass from its chemical composition using the concept of structural units. *J. Am. Ceram. Soc.*, 95(1):211–216, 2012. doi: 10.1111/j.1551-2916.2011.04964.x. (Cited on pages 12, 14, 21 and 22.)

[129] L. J. Jacob and H.-P. Deigner. Nanoparticles and nanosized structures in diagnostics and therapy. In H.-P. Deigner and M. Kohl, editors, *Precision Medicine*, pages 229–252. Academic Press, 2018. ISBN 978-0-12-805364-5. doi: 10.1016/B978-0-12-805364-5.00010-X. (Cited on page 43.)

[130] P. F. James. Liquid-phase separation in glass-forming systems. *J. Mater. Sci.*, 10(10):1802–1825, 1975. doi: 10.1007/BF00554944. (Cited on pages 2, 8 and 17.)

[131] A. Jan, J.-M. Delaye, S. Gin, and S. Kerisit. Molecular dynamics simulation of ballistic effects in simplified nuclear waste glasses. *J. Non-Cryst. Solids*, 505:188–201, 2019. doi: 10.1016/j.jnoncrysol.2018.11.021. (Cited on page 14.)

[132] M. Janssen and H. Eckert. ^{11}B ^{23}Na rotational echo double resonance NMR: a new approach for studying the spatial cation distribution in sodium borate glasses. *Solid State Ion.*, 136:1007–1014, 2000. doi: 10.1016/S0167-2738(00)00535-X. (Cited on pages 90, 97 and 98.)

[133] O. Jardetzky and G. C. K. Roberts. *NMR in molecular biology.* Academic Press, 2013. ISBN 0123805805. (Cited on page 42.)

[134] C. Joo, U. Werner-Zwanziger, and J. W. Zwanziger. The ring structure of boron trioxide glass. *J. Non-Cryst. Solids*, 261(1-3):282–286, 2000. doi: 10.1016/S0022-3093(99)00609-2. (Cited on pages 14 and 92.)

[135] T. C. Kaspar, J. V. Ryan, C. G. Pantano, J. Rice, C. Trivelpiece, et al. Physical and optical properties of the international simple glass. *npj Materials Degradation*, 3(1):1–15, 2019. doi: 10.1038/s41529-019-0069-2. (Cited on page 14.)

[136] Y. Kawamoto and M. Tomozawa. Prediction of immiscibility boundaries of the systems K_2O-SiO_2, K_2O-Li_2O-SiO_2, K_2O-Na_2O-SiO_2, and K_2O-BaO-SiO_2. *J. Am. Ceram. Soc.*, 64(5):289–292, 1981. doi: 10.1111/j.1151-2916.1981.tb09604.x. (Cited on page 13.)

[137] J. R. Keaton. *Young's Modulus*, pages 955–956. Springer International Publishing, 2018. ISBN 9783319735689. doi: 10.1007/978-3-319-73568-9_298. (Cited on page 45.)

[138] J. R. Keaton. *Shear Modulus*, pages 830–831. Springer International Publishing, 2018. ISBN 9783319735689. doi: 10.1007/978-3-319-73568-9_256. (Cited on page 45.)

[139] J. R. Keaton. *Bulk Modulus*, page 96. Springer International Publishing, 2018. ISBN 9783319735689. doi: 10.1007/978-3-319-73568-9_38. (Cited on page 45.)

[140] J. R. Keaton. *Poisson's ratio*, pages 728–729. Springer International Publishing, 2018. ISBN 9783319735689. doi: 10.1007/978-3-319-73568-9_225. (Cited on page 45.)

[141] G. Kermouche, E. Barthel, D. Vandembroucq, and P. Dubujet. Mechanical modelling of indentation-induced densification in amorphous silica. *Acta Mater.*, 56(13):3222–3228, 2008. doi: 10.1016/j.actamat.2008.03.010. (Cited on page 32.)

[142] S. S. Kim and T. H. Sanders Jr. Thermodynamic modeling of phase diagrams in binary alkali silicate systems. *J. Am. Ceram. Soc.*, 74(8):1833–1840, 1991. doi: 10.1111/j.1151-2916.1991.tb07796.x. (Cited on pages 2 and 13.)

[143] S. S. Kim and T. H. Sanders Jr. Calculation of subliquidus miscibility gaps in the Li_2O-B_2O_3-SiO_2 system. *Ceramics international*, 26(7):769–778, 2000. doi: 10.1016/S0272-8842(00)00018-3. (Cited on page 2.)

[144] K. J. Kingma and R. J. Hemley. Raman spectroscopic study of microcrystalline silica. *Am. Mineral*, 79(3-4):269–273, 1994. (Cited on page 89.)

[145] H.-J. Kleebe, G. Pezzotti, and G. Ziegler. Microstructure and fracture toughness of Si_3N_4 ceramics: combined roles of grain morphology and secondary phase chemistry. *J. Am. Ceram. Soc.*, 82(7):1857–1867, 1999. doi: 10.1111/j.1151-2916.1999.tb02009.x. (Cited on page 32.)

[146] E. Kleebusch, C. Patzig, M. Krause, Y. Hu, T. Höche, and C. Rüssel. The effect of TiO_2 on nucleation and crystallization of a Li_2O-Al_2O_3-SiO_2 glass investigated by XANES and STEM. *Sci. Rep.*, 8(1):2929, 2018. doi: 10.1038/s41598-018-21227-x. (Cited on page 2.)

[147] A. Koike and M. Tomozawa. Fictive temperature dependence of subcritical crack growth rate of normal glass and anomalous glass. *J. Non-Cryst. Solids*, 352(52-54): 5522–5530, 2006. doi: 10.1016/j.jnoncrysol.2006.09.023. (Cited on pages 105 and 112.)

[148] A. Koike, M. Tomozawa, and S. Ito. Sub-critical crack growth rate of soda-lime-silicate glass and less brittle glass as a function of fictive temperature. *J. Non-Cryst. Solids*, 353(27):2675–2680, 2007. doi: 10.1016/j.jnoncrysol.2007.05.006. (Cited on pages 105 and 112.)

[149] N. Koketsu, Z. Zhang, Y. Kotani, A. Sugiyama, and K. Takashima. Method for manufacturing porous glass, and method for manufacturing optical element, 2015. US Patent 9,162,920. (Cited on pages 3 and 82.)

[150] W. L. Konijnendijk and J. M. Stevels. The structure of borate glasses studied by raman scattering. *J. Non-Cryst. Solids*, 18(3):307–331, 1975. doi: 10.1016/0022-3093(75)90137-4. (Cited on page 44.)

[151] J. Krautkrämer and H. Krautkrämer. *Ultrasonic testing of materials*. Springer, 2013. ISBN 9783662106808. (Cited on page 46.)

[152] A. Kumar, S. B. Rai, and D. K. Rai. Effect of thermal neutron irradiation on gd3+ ions doped in oxyfluoroborate glass: an infra-red study. *Mater. Res. Bull.*, 38(2):333–339, 2003. doi: 10.1016/S0025-5408(02)01003-6. (Cited on page 127.)

[153] K. Kuraoka, Y. Chujo, and T. Yazawa. Hydrocarbon separation via porous glass membranes surface-modified using organosilane compounds. *J. Membr. Sci.*, 182(1-2): 139–149, 2001. doi: 10.1016/S0376-7388(00)00559-7. (Cited on page 3.)

[154] T. Lacondemine. *Initiation et propagation d'une fissure dans un composite particulaire à matrice verre : Expérimentation et analyse numérique*. PhD thesis, Université de Rennes 1, 2019. (Cited on pages 20 and 32.)

[155] M. Lane. Interface fracture. *Annu. Rev. Mater. Res.*, 33(1):29–54, 2003. doi: 10.1146/annurev.matsci.33.012202.130440. (Cited on page 32.)

[156] F. F. Lange. The interaction of a crack front with a second-phase dispersion. *Philos. Mag.*, 22(179):0983–0992, 1970. doi: 10.1080/14786437008221068. (Cited on pages 29 and 30.)

[157] L. Laurson, S. Santucci, and S. Zapperi. Avalanches and clusters in planar crack front propagation. *Physical Review E*, 81(4):046116, 2010. doi: 10.1103/PhysRevE.81.046116. (Cited on page 29.)

[158] B. Lawn. *Fracture of Brittle Solids*. Cambridge University Press, 1993. ISBN 9780511623127. doi: https://doi.org/10.1017/CBO9780511623127. (Cited on page 27.)

[159] D. D. Le Pevelen. Nir ft-raman. In J. C. Lindon, G. E. Tranter, and D. W. Koppenaal, editors, *Encyclopedia of Spectroscopy and Spectrometry (Third Edition)*, pages 98–109. Academic Press, Oxford, third edition edition, 2017. ISBN 978-0-12-803224-4. doi: https://doi.org/10.1016/B978-0-12-409547-2.12150-X. (Cited on page 43.)

[160] F. Lechenault, G. Pallares, M. George, C. L. Rountree, E. Bouchaud, and M. Ciccotti. Effects of finite probe size on self-affine roughness measurements. *Phys. Rev. Lett.*, 104 (2):025502, 2010. doi: 10.1103/PhysRevLett.104.025502. (Cited on pages 27 and 37.)

[161] F. Lechenault, C. L. Rountree, F. Cousin, J. . P. Bouchaud, L. Ponson, and E. Bouchaud. Evidence of deep water penetration in silica during stress corrosion fracture. *Phys. Rev. Lett*, 106(16):165504, 2011. doi: 10.1103/PhysRevLett.106.165504. (Cited on page 27.)

[162] A. Lesaine. *Structural and mechanical properties of dried colloidal silica layers*. PhD thesis, Université Paris-Saclay (ComUE), 2018. (Cited on page 50.)

[163] H. Li, A. Agarwal, and M. Tomozawa. Effect of fictive temperature on dynamic fatigue behavior of silica and soda-lime glasses. *J. Am. Ceram. Soc.*, 78(5):1393–1396, 1995. doi: 10.1111/j.1151-2916.1995.tb08502.x. (Cited on pages 105 and 112.)

[164] S. Lopez-Orozco, A. Inayat, A. Schwab, T. Selvam, and W. Schwieger. Zeolitic materials with hierarchical porous structures. *Adv. Mater.*, 23(22-23):2602–2615, 2011. doi: 10.1002/adma.201100462. (Cited on page 3.)

[165] H. Maekawa, T. Maekawa, K. Kawamura, and T. Yokokawa. The structural groups of alkali silicate glasses determined from ^{29}Si MAS-NMR. *J. Non-Cryst. Solids*, 127(1): 53–64, 1991. doi: 10.1016/0022-3093(91)90400-Z. (Cited on pages 16 and 98.)

[166] A. Makishima and J. D. Mackenzie. Calculation of bulk modulus, shear modulus and Poisson's ratio of glass. *J. Non-Cryst. Solids*, 17(2):147–157, 1975. doi: 10.1016/0022-3093(75)90047-2. (Cited on page 4.)

[167] A. Makishima, J. D. Mackenzie, and J. J. Hammel. The leaching of phase-separated sodium borosilicate glasses. *J. Non-Cryst. Solids*, 31(3):377–383, 1979. (Cited on page 19.)

[168] W. J. Malfait, W. E. Halter, and R. V.l. ^{29}Si NMR spectroscopy of silica glass: T1 relaxation and constraints on the si–o–si bond angle distribution. *Chem. Geol.*, 256 (3-4):269–277, 2008. doi: 0.1016/j.chemgeo.2008.06.048. (Cited on pages 99 and 100.)

[169] K. J. Måløy, S. Santucci, J. Schmittbuhl, and R. Toussaint. Local waiting time fluctuations along a randomly pinned crack front. *Phys. Rev. Lett.*, 96(4):045501, 2006. doi: 10.1103/PhysRevLett.96.045501. (Cited on page 29.)

[170] C. Marliere, S. Prades, F. Célarié, D. Dalmas, D. Bonamy, C. Guillot, and E. Bouchaud. Crack fronts and damage in glass at the nanometre scale. *J. Phys. Condens. Matter*, 15(31):S2377, 2003. doi: 10.1088/0953-8984/15/31/313/meta. (Cited on page 27.)

[171] W. P. Marshall, J. J. Hammel, H. W. Barch, R. D. Hegedus, and W. J. Robertson. Silica-rich porous substrates with reduced tendencies for breaking or cracking, 1990. US Patent 4,933,307. (Cited on page 3.)

[172] L. Martel, M. Allix, F. Millot, V. Sarou-Kanian, E. Véron, S. Ory, D. Massiot, and M. Deschamps. Controlling the size of nanodomains in calcium aluminosilicate glasses. *J. Phys. Chem. C.*, 115(39):18935–18945, 2011. doi: 10.1021/jp200824m. (Cited on page 80.)

[173] R. Martens and W. Müller-Warmuth. Structural groups and their mixing in borosilicate glasses of various compositions–an NMR study. *J. Non-Cryst. Solids*, 265(1-2):167–175, 2000. doi: 10.1016/S0022-3093(99)00693-6. (Cited on pages 14 and 16.)

[174] D. Maugis. Sub-critical crack growth, surface energy and fracture toughness of brittle materials. In *Fracture mechanics of ceramics*, pages 255–272. Springer, 1986. doi: 10.1007/978-1-4615-7026-4_20. (Cited on pages 28, 67, 107 and 112.)

[175] O. V. Mazurin. Physical properties of phase separated glasses. *J. Non-Cryst. Solids*, 95:71–82, 1987. doi: 10.1016/S0022-3093(87)80100-X. (Cited on page 22.)

[176] O. V. Mazurin and E. A. Porai-Koshits. *Phase separation in glass*. Elsevier, 1984. ISBN 9780080983653. (Cited on page 2.)

[177] O. V. Mazurin and M. V. Streltsina. Determination of tie-line directions in the metastable phase-separation regions of ternary systems. *J. Non-Cryst. Solids*, 11(3): 199–218, 1972. doi: 10.1016/0022-3093(72)90003-8. (Cited on page 13.)

[178] O. V. Mazurin, G. P. Roskova, and V. P. Kluyev. Properties of phase-separated soda-silica glasses as a means of investigation of their structure. *Discuss. Faraday Soc.*, 50: 191–199, 1970. doi: 10.1039/DF9705000191. (Cited on page 2.)

[179] V. McGahay and M. Tomozawa. The origin of phase separation in silicate melts and glasses. *J. Non-Cryst. Solids*, 109(1):27–34, 1989. doi: 10.1016/0022-3093(89)90437-7. (Cited on page 12.)

[180] P. McMillan. Structural studies of silicate glasses and meltsapplications and limitations of raman spectroscopy. *Am. Mineral*, 69(7-8):622–644, 1984. URL `http://minsocam.org/ammin/am69/am69_622.pdf`. (Cited on page 44.)

[181] J. J. Mecholsky. Toughening in glass ceramic through microstructural design. *Fracture Mechanics of Ceramics*, 6:165, 1983. (Cited on page 32.)

[182] N. Miyata and H. Jinno. Use of Vickers indentation method for evaluation of fracture toughness of phase-separated glasses. *J. Non-Cryst. Solids*, 38:391–396, 1980. doi: 10.1016/0022-3093(80)90450-0. (Cited on pages 25 and 32.)

[183] N. Miyata and H. Jinno. Strength and fracture surface energy of phase-separated glasses. *J. Mater. Sci.*, 16(8):2205–2217, 1981. doi: 10.1007/BF00542383. (Cited on pages 25, 26, 30, 31, 32 and 34.)

[184] N. Miyata and H. Jinno. Fracture toughness and fracture surface energy of lead borate glasses. *J. Mater. Sci. Lett.*, 1(4):156–158, 1982. (Cited on page 25.)

[185] N. Miyata, S. Takeda, and H. Jinno. Slow crack growth in phase-separated glasses. *J. Non-Cryst. Solids*, 95:1047–1054, 1987. doi: 10.1016/S0022-3093(87)80715-9. (Cited on pages 32 and 34.)

[186] O. C. Mocioiu, M. Zaharescu, I. Atkinson, A.-M. Mocioiu, and P. Budrugeac. Study of crystallization process of soda lead silicate glasses by thermal and spectroscopic methods. *J. Therm. Anal. Calorim.*, 117(1):131–139, 2014. doi: 10.1007/s10973-014-3652-3. (Cited on page 80.)

[187] M. G. Mortuza, R. Dupree, and D. Holland. ^{29}Si T1 relaxation in alkali silicate glasses: a method for detecting glass-in-glass phase separation. *J. Non-Cryst. Solids*, 281(1-3): 108–116, 2001. doi: 10.1016/S0022-3093(00)00440-3. (Cited on page 99.)

[188] T. M. Mower and A. S. Argon. Experimental investigations of crack trapping in brittle heterogeneous solids. *Mech. Mater.*, 19(4):343–364, 1995. doi: 10.1016/0167-6636(94)00042-F. (Cited on page 29.)

[189] R. L. Mozzi and B. E. Warren. The structure of vitreous boron oxide. *J. Appl. Crystallogr.*, 3(4):251–257, 1970. doi: 10.1107/S0021889870006143. (Cited on page 14.)

[190] T. Nanba, M. Nishimura, and Y. Miura. A theoretical interpretation of the chemical shift of ^{29}Si NMR peaks in alkali borosilicate glasses. *Geochim. Cosmochim. Acta*, 68 (24):5103–5111, 2004. doi: 10.1016/j.gca.2004.05.042. (Cited on pages 98 and 99.)

[191] D. R. Neuville, T. Charpentier, J. C. Du, Y. Z. Yue, W. Blanc, M. R. Cicconi, M. Lancry, and M. Ren. Structure characterizations and molecular dynamics simulations of melt, glass, and glass fibers. In *Fiberglass Science and Technology*, pages 89–216. Springer, 2021. doi: 10.1007/978-3-030-72200-5_2. (Cited on page 42.)

[192] J. M. Oliveira, R. N. Correia, and M. H. Fernandes. Effect of SiO_2 on amorphous phase separation of CaO-P_2O_5-SiO_2-MgO glasses. *J. Non-Cryst. Solids*, 273(1-3):59–63, 2000. doi: 10.1016/S0022-3093(00)00144-7. (Cited on page 2.)

[193] A. Osaka, N. Soga, and M. Kunugi. Elastic constants and Vickers hardness of lead borate glasses. *Journal of the Society of Materials Science, Japan*, 23(245):128–131, 1974. doi: 10.2472/jsms.23.128. (Cited on pages 25 and 26.)

[194] P. Ostojic and R. Mcpherson. A review of indentation fracture theory - its development, principles and limitations. *Int. J. Fract.*, 33(4):297–312, 1987. doi: 10.1007/BF00044418. (Cited on page 33.)

[195] G. Pallares, L. Ponson, A. Grimaldi, M. George, G. Prevot, and M. Ciccotti. Crack opening profile in DCDC specimen. *Int. J. Fract.*, 156:11–20, 2009. doi: 10.1007/s10704-009-9341-8. (Cited on pages 47 and 48.)

[196] G. Pallares, C. L. Rountree, L. Douillard, F. Charra, and E. Bouchaud. Fractoluminescence characterization of the energy dissipated during fast fracture of glass. *EPL*, 99(2):28003, 2012. doi: 10.1209/0295-5075/99/28003. (Cited on pages 27 and 69.)

[197] G. Pallares, F. Lechenault, M. George, E. Bouchaud, C. Ottina, C. L. Rountree, and M. Ciccotti. Roughness of oxide glass subcritical fracture surfaces. *J. Am. Ceram. Soc.*, 101(3):1279–1288, 2018. doi: 10.1111/jace.15262. (Cited on page 36.)

[198] W. Pannhorst. Glass ceramics: state-of-the-art. *J. Non-Cryst. Solids*, 219:198–204, 1997. doi: 10.1016/S0022-3093(97)00270-6. (Cited on page 2.)

[199] V. Pecharsky and P. Zavalij. *Fundamentals of powder diffraction and structural characterization of materials*. Springer Science & Business Media, 2008. ISBN 9780387095790. (Cited on page 86.)

[200] A. Perriot, D. Vandembroucq, E. Barthel, V. Martinez, L. Grosvalet, C. Martinet, and B. Champagnon. Raman microspectroscopic characterization of amorphous silica plastic behavior. *J. Am. Ceram. Soc.*, 89(2):596–601, 2006. doi: 10.1111/j.1551-2916.2005.00747.x. (Cited on page 32.)

[201] J. Pluth, J. Smith, and J. Faber Jr. Crystal structure of low cristobalite at 10, 293, and 473 k: Variation of framework geometry with temperature. *J. Appl. Phys.*, 57(4):1045–1049, 1985. doi: 10.1063/1.334545. (Cited on page 100.)

[202] I. G. Polyakova. Alkali borosilicate systems: Phase diagrams and properties of glasses. *Phys. Chem. Glasses*, 41(5):247–258, 2000. (Cited on page 2.)

[203] E. A. Porai-Koshits and V. I. Averjanov. Primary and secondary phase separation of sodium silicate glasses. *J. Non-Cryst. Solids*, 1(1):29–38, 1968. doi: 10.1016/0022-3093(68)90004-5. (Cited on pages 20 and 21.)

[204] R. C. Prince, R. R. Frontiera, and E. O. Potma. Stimulated raman scattering: from bulk to nano. *Chem. Rev.*, 117(7):5070–5094, 2017. doi: 10.1021/acs.chemrev.6b00545. (Cited on page 88.)

[205] R. Project. Cristobalite r060648, 2015. URL `https://rruff.info/cristobalite/R060648`. (Cited on page 86.)

[206] L. D. Pye, L. Ploetz, and L. Manfredo. Physical properties of phase separated soda-silica glasses. *J. Non-Cryst. Solids*, 14(1):310–321, 1974. doi: 10.1016/0022-3093(74)90041-6. (Cited on page 2.)

[207] G. D. Quinn and R. C. Bradt. On the Vickers indentation fracture toughness test. *J. Am. Ceram. Soc.*, 90(3):673–680, 2007. doi: 10.1111/j.1551-2916.2006.01482.x. (Cited on page 33.)

[208] E. Rädlein and G. H. Frischat. Atomic force microscopy as a tool to correlate nanostructure to properties of glasses. *J. Non-Cryst. Solids*, 222:69–82, 1997. doi: 10.1016/S0022-3093(97)90098-3. (Cited on page 54.)

[209] R. S. Raghava. Role of matrix-particle interface adhesion on fracture toughness of dual phase epoxy-polyethersulfone blend. *J. Polym. Sci., Part B: Polym. Phys.*, 25(5): 1017–1031, 1987. doi: 10.1002/polb.1987.090250504. (Cited on page 32.)

[210] V. S. Raja and T. Shoji. *Stress corrosion cracking: Theory and practice*. Elsevier, 2011. ISBN 978-1-84569-673-3. (Cited on page 28.)

[211] S. Ramanathan, D. Ertaş, and D. S. Fisher. Quasistatic crack propagation in heterogeneous media. *Phys. Rev. Lett.*, 79(5):873, 1997. doi: 10.1103/PhysRevLett.79.873. (Cited on page 37.)

[212] A. H. Ramsden and P. F. James. The effects of amorphous phase separation on crystal nucleation kinetics in BaO-SiO_2 glasses. *J. Mater. Sci.*, 19(5):1406–1419, 1984. doi: 10.1007/BF00563035. (Cited on page 2.)

[213] J. T. Randall, H. P. Rooksby, and B. S. Cooper. X-ray diffraction and the structure of vitreous solidsi. *Z. Kristallogr. Cryst. Mater*, 75(1):196–214, 1930. doi: 10.1515/zkri-1930-0114. (Cited on page 1.)

[214] H. N. Ritland. Relation between refractive index and density of a glass at constant temperature. *J. Am. Ceram. Soc.*, 38(2):86–88, 1955. doi: 10.1111/j.1151-2916.1955.tb14581.x. (Cited on page 4.)

[215] A. J. Rosakis and K. Ravi-Chandar. On crack-tip stress state: an experimental evaluation of three-dimensional effects. *Int. J. Solids Struct.*, 22(2):121–134, 1986. doi: 10.1016/0020-7683(86)90002-8. (Cited on page 27.)

[216] C. Rountree, S. Prades, D. Bonamy, E. Bouchaud, R. Kalia, and C. Guillot. A unified study of crack propagation in amorphous silica: Using experiments and simulations. *J. Alloys Compd.*, 434:60–63, 2007. doi: 10.1016/j.jallcom.2006.08.336. (Cited on page 27.)

[217] C. Rountree, W. Feng, M. Barlet, D. Bonamy, and J.-M. Delaye. Fracture properties of SiO_2-B_2O_3-Na_2O glasses: How the structure influences macroscale fracture properties. In *25th International Congress on Glass*, 2019. (Cited on page 155.)

[218] C. L. Rountree. Recent progress to understand stress corrosion cracking in sodium borosilicate glasses: Linking the chemical composition to structural, physical and fracture properties. *J. Phys. D: Appl. Phys.*, 50:34, 2017. doi: 10.1088/1361-6463/aa7a8b. (Cited on pages 4, 14, 16 and 114.)

[219] C. L. Rountree and W. Feng. SILICA and its process zone. *Int. J. Appl. Glass Sci.*, 11(3):385–395, 2020. doi: 10.1111/ijag.15113. (Cited on pages 26, 27, 36, 69 and 70.)

[220] C. L. Rountree, D. Bonamy, D. Dalmas, S. Prades, R. K. Kalia, C. Guillot, and E. Bouchaud. Fracture in glass via molecular dynamics simulations and atomic force microscopy experiments. *Phys. Chem. Glas.: Eur. J. Glass Sci. Technol. B*, 51(2): 127–132, 2010. (Cited on pages 27 and 69.)

[221] T. Rouxel. Elastic properties and short-to medium-range order in glasses. *J. Am. Ceram. Soc.*, 10:3019–3039, 2007. doi: 10.1111/j.1551-2916.2007.01945.x. (Cited on page 4.)

[222] J. C. Rowell, W. D. Phillips, L. R. Melby, and M. Panar. NMR studies of some liquid crystal systems. *J. Chem. Phys.*, 43(10):3442–3454, 1965. doi: 10.1063/1.1696498. (Cited on page 42.)

[223] E. D. Safronsky, Y. O. Roizin, and E. Rysiakiewicz-Pasek. Application of porous glasses for humidity control. *Opt. Mater.*, 5(3):217–220, 1996. doi: 10.1016/0925-3467(95) 00058-5. (Cited on page 3.)

[224] P. Sahu, M. Ali, K. T. Shenoy, S. Mohan, A. Ananthanarayanan, G. Sugilal, and C. Kaushik. Molecular dynamics simulations of simplified sodium borosilicate glasses: The effect of composition on structure and dynamics. *Phys. Chem. Chem. Phys.*, 2021. doi: 10.1039/D1CP00207D. (Cited on page 124.)

[225] L. Salvo, P. Cloetens, E. Maire, S. Zabler, J. J. Blandin, et al. X-ray micro-tomography an attractive characterisation technique in materials science. *Nucl. Instrum. Methods Phys. Res., Sect. B*, 200:273–286, 2003. doi: 10.1016/S0168-583X(02)01689-0. (Cited on pages 19 and 20.)

[226] N. Saunders and A. P. Miodownik. *CALPHAD (calculation of phase diagrams): A comprehensive guide*. Elsevier, 1998. ISBN 9780080528434. (Cited on page 13.)

[227] S. Scholes and F. C. F. Wilkinson. Glassy phase separation in sodium borosilicate glasses. *Discuss. Faraday Soc.*, 50:175–181, 1970. doi: 10.1039/DF9705000175. (Cited on page 17.)

[228] H. Scholze. *Glass: nature, structure, and properties*. Springer, 2012. (Cited on page 14.)

[229] A. K. Seal, P. Chakraborti, N. R. Roy, S. Mukerjee, M. K. Mitra, and G. C. Das. Effect of phase separation on the fracture toughness of SiO_2-B_2O_3-Na_2O glass. *Bull. Mater. Sci.*, 28(5):457–460, 2005. doi: 10.1007/BF02711236. (Cited on pages 32, 33 and 139.)

[230] P. Sellappan, T. Rouxel, F. Celarie, E. Becker, P. Houizot, and R. Conradt. Composition dependence of indentation deformation and indentation cracking in glass. *Acta Mater.*, 61(16):5949–5965, 2013. doi: 10.1016/j.actamat.2013.06.034. (Cited on page 105.)

[231] J. Selsing. Internal stresses in ceramics. *J. Am. Ceram. Soc.*, 44(8):419–419, 1961. doi: 10.1111/j.1151-2916.1961.tb15475.x. (Cited on pages 30 and 31.)

[232] U. Selvaray, K. J. Rao, C. N. R. Rao, J. Klinowski, and J. M. Thomas. MAS NMR as a probe for investigating the distribution of si o si angles in lithium silicate glasses. *Chem. Phys. Lett.*, 114(1):24–27, 1985. doi: 10.1016/0009-2614(85)85047-8. (Cited on page 100.)

[233] T. P. Seward III, D. R. Uhlmann, and D. Turnbull. Phase separation in the system BaO-SiO_2. *J. Am. Ceram. Soc.*, 51(5):278–285, 1968. doi: 10.1111/j.1151-2916.1968.tb13858.x. (Cited on page 20.)

[234] R. R. Shaw and J. F. Breedis. Secondary phase separation in lead borate glasses. *J. Am. Ceram. Soc.*, 55(8):422–425, 1972. doi: 10.1111/j.1151-2916.1972.tb11326.x. (Cited on pages 20, 21, 23 and 24.)

[235] R. R. Shaw and D. R. Uhlmann. Subliquidus immiscibility in binary alkali borates. *J. Am. Ceram. Soc.*, 51(7):377–382, 1968. doi: 10.1111/j.1151-2916.1968.tb11897.x. (Cited on page 11.)

[236] R. R. Shaw and D. R. Uhlmann. Effect of phase separation on the properties of simple glasses. I. Density and molar volume. *J. Non-Cryst. Solids*, 1(6):474–98, 1969. doi: 10.1016/0022-3093(69)90009-X. (Cited on pages 22, 23 and 24.)

[237] R. R. Shaw and D. R. Uhlmann. Effect of phase separation on the properties of simple glasses. II. Elastic properties. *J. Non-Cryst. Solids*, 5(3):237–263, 1971. doi: 10.1016/0022-3093(71)90034-2. (Cited on pages 22, 24, 25 and 26.)

[238] M. P. Shepilov, A. E. Kalmykov, and G. A. Sycheva. Liquid–liquid phase separation in sodium borosilicate glass: Ordering phenomena in particle arrangement. *J. Non-Cryst. Solids*, 353(24-25):2415–2430, 2007. doi: 10.1016/j.jnoncrysol.2007.03.019. (Cited on page 18.)

[239] G. C. Sih. Fracture toughness concept. In *Properties Related to Fracture Toughness*. ASTM International, 1976. (Cited on page 28.)

[240] G. C. Sih. Mechanics of subcritical crack growth. In G. C. Sih, N. E. Ryan, and R. Jones, editors, *Fracture Mechanics Technology Applied to Material Evaluation and Structure Design*, pages 3–18, Dordrecht, 1983. Springer Netherlands. ISBN 978-94-009-6914-8. (Cited on page 28.)

[241] C. J. Simmons and S. W. Freiman. Effects of phase separation on crack growth in borosilicate glass. *J. Non-Cryst. Solids*, 38:503–508, 1980. doi: 10.1016/0022-3093(80)90469-X. (Cited on pages 29, 35, 36, 134, 139, 140 and 154.)

[242] R. Singh. Cv raman and the discovery of the raman effect. *Phys. Perspect.*, 4(4):399–420, 2002. doi: 10.1007/s000160200002. (Cited on page 43.)

[243] A. K. Soper. Boroxol rings from diffraction data on vitreous boron trioxide. *J. Phys. Condens. Matter*, 23(36):365402, 2011. doi: 10.1088/0953-8984/23/36/365402. (Cited on pages 14 and 92.)

[244] T. F. Soules. A molecular dynamic calculation of the structure of sodium silicate glasses. *J. Chem. Phys.*, 71(11):4570–4578, 1979. doi: 10.1063/1.438210. (Cited on page 4.)

[245] Z. Strnad and P. W. McMillan. Metastable two-liquid tie lines in the soda-lime-silica system. *Phys. Chem. Glasses*, 24(3):57–64, 1983. (Cited on page 13.)

[246] Z. Strnad and P. Strnad. Calculation of metastable two-liquid tie lines in ternary glass-forming systems. *J. Am. Ceram. Soc.*, 61(7-8):283–286, 1978. doi: 10.1111/j.1151-2916.1978.tb09309.x. (Cited on page 13.)

[247] M. Suzuki and T. Tanaka. Materials design for the fabrication of porous glass using phase separation in multi-component borosilicate glass. *ISIJ Int.*, 48(11):1524–1532, 2008. doi: 10.2355/isijinternational.48.1524. (Cited on pages 2 and 3.)

[248] M. Suzuki and T. Tanaka. Thermodynamic prediction of spinodal decomposition in multi-component silicate glass for design of functional porous glass materials. *High Temp. Mater. Processes (London)*, 31(4-5):323–328, 2012. doi: 10.1515/htmp-2012-0086. (Cited on pages 3 and 13.)

[249] T. Takamori and M. Tomozawa. HCl leaching rate and microstructure of phase-separated borosilicate glasses. *J. Am. Ceram. Soc.*, 61(11-12):509–512, 1978. doi: 10.1111/j.1151-2916.1978.tb16129.x. (Cited on pages 3 and 19.)

[250] H. Tanaka and T. Araki. Spontaneous double phase separation induced by rapid hydrodynamic coarsening in two-dimensional fluid mixtures. *Phys. Rev. Lett.*, 81(2):389, 1998. doi: 10.1103/PhysRevLett.81.389. (Cited on page 20.)

[251] L. Tang, N. M. Anoop Krishnan, J. Berjikian, J. Rivera, M. M. Smedskjaer, J. C. Mauro, W. Zhou, and M. Bauchy. Effect of nanoscale phase separation on the fracture behavior of glasses: Toward tough, yet transparent glasses. *Physical Review Materials*, 2(11):113602, 2018. doi: 10.1103/PhysRevMaterials.2.113602. (Cited on page 32.)

[252] J. Taylor. *Introduction to error analysis, the study of uncertainties in physical measurements*. 1997. ISBN 0935702105. (Cited on pages 46 and 153.)

[253] P. Taylor, S. D. Ashmore, and D. G. Owen. Chemical durability of some sodium borosilicate glasses improved by phase separation. *J. Am. Ceram. Soc.*, 70(5):333–338, 1987. doi: 10.1111/j.1151-2916.1987.tb05004.x. (Cited on page 13.)

[254] T. To. *Fracture toughness and fracture surface energy of inorganic and non-metallic glasses*. PhD thesis, Université de Rennes 1, 2019. (Cited on page 14.)

[255] T. To, C. Stabler, E. Ionescu, R. Riedel, F. Célarié, and T. Rouxel. Elastic properties and fracture toughness of SiOC-based glass-ceramic nanocomposites. *J. Am. Ceram. Soc.*, 103(1):491–499, 2020. doi: 10.1111/jace.16686. (Cited on page 33.)

[256] M. Tomozawa. Liquid-phase separation and crystal nucleation in Li_2O-SiO_2 glasses. *Phys. Chem. Glasses*, 13(6):161, 1972. (Cited on page 2.)

[257] G. Toquer, C. Delchet, M. Nemec, and A. Grandjean. Effect of leaching concentration and time on the morphology of pores in porous glasses. *J. Non-Cryst. Solids*, 357(6): 1552–1557, 2011. (Cited on page 19.)

[258] G. Tricot. The structure of pyrex® glass investigated by correlation NMR spectroscopy. *Phys. Chem. Chem. Phys.*, 18(38):26764–26770, 2016. doi: 10.1039/C6CP02996E. (Cited on pages 155 and 156.)

[259] D. R. Uhlmann and A. G. Kolbeck. Phase separation and the revolution in concept of glass structure. *Phys. Chem. Glasses*, 17(5):146–158, 1976. (Cited on pages 17 and 41.)

[260] D. R. Uhlmann, M. Goldstein, S. Scholes, T. I. Barry, J. Zarzycki, et al. General discussion. *Discuss. Faraday Soc.*, 50:222–240, 1970. doi: 10.1039/DF9705000222. (Cited on page 2.)

[261] L. Van Brutzel. *Contribution à l'étude des mécanismes de rupture dans les amorphes : Étude par dynamique moléculaire de la rupture de verre de silice*. PhD thesis, Univérsité Paris VI, 1999. (Cited on page 4.)

[262] L. van Wüllen and G. Schwering. 11B-MQMAS and 29Si–{11B} double-resonance NMR studies on the structure of binary B_2O_3–SiO_2 glasses. *Solid State Nucl. Magn. Reson.*, 21(3-4):134–144, 2002. doi: 10.1006/snmr.2002.0054. (Cited on pages 14 and 16.)

[263] A. K. Varshneya. *Fundamentals of inorganic glasses*. Elsevier, 2013. ISBN 9780128162262. (Cited on pages 8, 11 and 138.)

[264] P. Vashishta, R. K. Kalia, J. P. Rino, and I. Ebbsjö. Interaction potential for SiO_2: A molecular-dynamics study of structural correlations. *Phys. Rev. B*, 41(17):12197, 1990. doi: 10.1103/PhysRevB.41.12197. (Cited on pages 14, 70 and 144.)

[265] B. R. Wheaton and A. G. Clare. Evaluation of phase separation in glasses with the use of atomic force microscopy. *J. Non-Cryst. Solids*, 353(52-54):4767–4778, 2007. doi: 10.1016/j.jnoncrysol.2007.06.073. (Cited on pages 13, 18, 19, 20, 81 and 83.)

[266] W. B. White. Investigation of phase separation by Raman spectroscopy. *J. Non-Cryst. Solids*, 49(1-3):321–329, 1982. doi: 10.1016/0022-3093(82)90128-4. (Cited on pages 16, 43, 88 and 89.)

[267] W. B. White and D. G. Minser. Raman spectra and structure of natural glasses. *J. Non-Cryst. Solids*, 67(1-3):45–59, 1984. doi: 10.1016/0022-3093(84)90140-6. (Cited on page 44.)

[268] S. M. Wiederhorn. Influence of water vapor on crack propagation in soda-lime glass. *J. Am. Ceram. Soc.*, 50(8):407, 1967. ISSN 1551-2916. doi: 10.1111/j.1151-2916.1967.tb15145.x. (Cited on pages 28, 33, 67, 107, 112, 140 and 154.)

[269] S. M. Wiederhorn and L. H. Bolz. Stress corrosion and static fatigue of glass. *J. Am. Ceram. Soc.*, 53:543–548, 1970. ISSN 1551-2916. doi: 10.1111/j.1151-2916.1970.tb15962.x. (Cited on pages 28, 33 and 154.)

[270] S. M. Wiederhorn, H. Johnson, A. M. Diness, and A. H. Heuer. Fracture of glass in vacuum. *J. Am. Ceram. Soc.*, 57(8):336–341, 1974. ISSN 1551-2916. doi: 10.1111/j.1151-2916.1974.tb10917.x. (Cited on page 28.)

[271] S. M. Wiederhorn, S. W. Freiman, E. R. Fuller, and C. J. Simmons. Effects of water and other dielectrics on crack-growth. *J. Mater. Sci.*, 17(12):3460–3478, 1982. doi: 10.1007/BF00752191. (Cited on pages 28, 33 and 154.)

[272] S. M. Wiederhorn, J. M. Lopez-Cepero, J. Wallace, J.-P. Guin, and T. Fett. Roughness of glass surfaces formed by sub-critical crack growth. *J. Non-Cryst. Solids*, 353(16-17):1582–1591, 2007. doi: 10.1016/j.jnoncrysol.2007.01.029. (Cited on page 27.)

[273] S. M. Wiederhorn, T. Fett, G. Rizzi, M. J. Hoffmann, and J. P. Guin. The effect of water penetration on crack growth in silica glass. *Eng. Fract. Mech.*, 101:3–16, 2013. doi: 10.1016/j.engfracmech.2012.04.026. (Cited on page 27.)

[274] C. Wünsche, E. Rädlein, and G. H. Frischat. Glass fracture surfaces seen with an atomic force microscope. *Fresenius' Journal of Analytical Chemistry*, 358(1-2):349–351, 1997. doi: 10.1007/s002160050426. (Cited on page 36.)

[275] A. K. Yadav and P. Singh. A review of the structures of oxide glasses by Raman spectroscopy. *RSC Adv.*, 5(83):67583–67609, 2015. doi: 10.1039/C5RA13043C. (Cited on page 127.)

[276] Z. Yang, W. Ren, R. Sharma, S. McDonald, M. Mostafavi, Y. Vertyagina, and T. J. Marrow. In-situ X-ray computed tomography characterisation of 3D fracture evolution and image-based numerical homogenisation of concrete. *Cem. Concr. Compos.*, 75:74–83, 2017. doi: 10.1016/j.cemconcomp.2016.10.001. (Cited on page 20.)

[277] T. Yano, N. Kunimine, S. Shibata, and M. Yamane. Structural investigation of sodium borate glasses and melts by Raman spectroscopy.: I. Quantitative evaluation of structural units. *J. Non-Cryst. Solids*, 321(3):137–146, 2003. doi: 10.1016/S0022-3093(03)00158-3. (Cited on pages 44, 88 and 127.)

[278] R. Youngman. NMR arlet2016p. *Mater.*, 11(4):476, 2018. doi: 10.3390/ma11040476. (Cited on page 42.)

[279] Y. Yu, B. Stevensson, and M. Edeén. Direct experimental evidence for abundant BO_4–BO_4 motifs in borosilicate glasses from double-quantum ^{1}1B NMR spectroscopy. *J. Phys. Chem. Lett.*, 9(21):6372–6376, 2018. doi: 10.1021/acs.jpclett.8b02907. (Cited on pages 41 and 93.)

[280] W. H. Zachariasen. The atomic arrangement in glass. *J. Am. Chem. Soc.*, 54(10): 3841–3851, 1932. doi: 10.1021/ja01349a006. (Cited on pages 1 and 4.)

[281] J. Zhong, D. Chen, Y. Peng, Y. Lu, X. Chen, X. Li, and Z. Ji. A review on nanostructured glass ceramics for promising application in optical thermometry. *J. Alloys Compd.*, 763:34–48, 2018. doi: 10.1016/j.jallcom.2018.05.348. (Cited on page 2.)

[282] Z. Zhou, M.-C. Wang, J. Han, F. Xu, and X. Zhao. Effect of heat treatment on $7Na_2O$–$23B_2O_3$–$70SiO_2$ glass. *Ceram. Int.*, 37(6):1769–1773, 2011. doi: 10.1016/j.ceramint.2011.01.047. (Cited on pages 16 and 41.)